MODELLING AND SIMULATION ASPECTS OF PERFORMANCE-BASED WIND ENGINEERING OF TALL BUILDINGS

GORDON HENRY CLANNACHAN

“This thesis is submitted in fulfilment of the requirements for the degree of Doctor of Philosophy in the Department of Civil Engineering, University of Strathclyde, Glasgow.”

APRIL 2012

Declaration of Authenticity

“This thesis is the result of the author’s original research. It has been composed by the author and has not been previously submitted for examination which has led to the award of a degree.”

Gordon Henry Clannachan

April 2012

Acknowledgements

The path to completing this PhD thesis was an enjoyable journey. However, it was not without its obstacles along the way. I cannot overstate the importance of the positivity and encouragement I received from my family and my partner, Nicky Pollock, through the more challenging times. My parents are an inspiration and I hope I have made them proud.

I am indebted to Dr James Lim for his part in allowing me to undertake this PhD immediately after completing my undergraduate course. I thoroughly enjoyed the opportunity and will look back fondly on my time spent at the University of Strathclyde. I have made a great friend in Andrzej Wrzesien; I will miss our conversations over morning coffee.

I would like to thank my primary supervisor, Dr Graham Copeland, for his involvement during my PhD research. I would also like to acknowledge the contribution of Dr Ian Taylor and Dr Tom Scanlon for offering their expertise while I learned how to use CFD at the early stages of my study. The role of Dr Richard Martin in maintaining the HPC facility is greatly appreciated.

Last, but by no means least, I owe a massive debt of gratitude to Professor Nenad Bićanić for providing invaluable support and advice throughout the entirety of this research. His involvement is especially appreciated since he was under no formal obligation to do so. It is difficult to imagine completing this PhD without his contribution. I dedicate my PhD thesis to this great man.

Abstract

The study is concerned with developing an adequate Performance-Based Wind Engineering (PBWE) framework for tall building design. The focus is to introduce advanced modelling and simulation techniques to improve key analysis stages, namely by using Computational Fluid Dynamics (CFD) and Computational Structural Mechanics (CSM). The clearly defined five stage PBWE framework is realised and implemented using both existing and newly developed simulation components. The performance of the developed process is explored by comparative PBWE analyses to assess the wind-induced behaviour of two tall building designs with distinctly different cross sections; a regular rectangular cross section and an irregular 'L'-shaped cross section.

The performance of CFD was primarily dependent on the turbulence model. On the basis of an extensive validation study, the Reynolds-Averaged Navier-Stokes (RANS) model was able to adequately compute the mean pressure coefficients acting on the benchmark CAARC tall building. However, its inability to sustain the atmospheric turbulence resulted in a significant under-estimation of the top floor accelerations. Hence, it was concluded that the RANS model is not suitable for competent PBWE studies. The results showed that the Large Eddy Simulation (LES) model offered the closest alternative to wind tunnel testing. However, full LES was too computationally expensive to be used for the PBWE framework, and hence a hybrid RANS-LES simulation strategy was formulated as a compromise. This was considered to offer an appropriate representation of the wind-induced pressure field without prohibitive complexities emanating from a full LES model.

The response of the regular tall building was compared for both the RANS and the LES computed wind loads. This identified that the atmospheric turbulence had a much greater affect on the response of a regular prismatic tall building than the structure-induced turbulence. Despite an increase in structure-induced turbulence, the results suggested that the response of an irregular ‘L’-shaped tall building would also be governed by atmospheric turbulence in the incident wind field.

Contents

List of Figures

List of Tables

Nomenclature

a_{peak}	peak acceleration
B	crosswind width of building
C_P	mean pressure coefficient
C_{RMS}	root-mean-square pressure coefficient
$[C]$	damping matrix
c	damping constant
c_{cr}	critical damping coefficient
c_{prob}	probability factor
D	alongwind depth of building
d	depth of interfacial layer
f	Coriolis parameter
f_i	natural frequency for mode i
H	building height
h	gradient height of atmospheric boundary layer
I_u	streamwise turbulence intensity
$[K]$	stiffness matrix
K_x	fetch factor to adjust for step change in terrain roughness
k	turbulence kinetic energy
${}^{x}L_u$	length scale of turbulence in streamwise direction
$[M]$	mass matrix
m	mass
n	frequency of vibration
P	pressure
P_0	static pressure
p'	instantaneous

Q	annual risk of exceedance
R	return period of event
St	Strouhal number
T	time duration of the event
T_i	natural period of vibration for mode i
U	mode
u_*	frictional velocity
V_z	mean wind velocity at height z
v_b	basic mean wind velocity
v_{crit}	critical wind velocity
x_H	peak resonant displacement amplitude
y	distance to the centre of the first computational cell
z	height from the ground
z_0	aerodynamic roughness length
α	dispersion
ε	turbulent dispersion rate
κ	von Karman constant
ν	kinematic viscosity
ρ	density
ζ	damping ratio
ζ_s	structural damping ratio
ζ_{so}	nominal structural damping ratio
σ^2	variance
φ	angle of latitude
Ω	angular velocity of the earth
ω	circular frequency
ω_n	natural circular frequency

1

Introduction

1.1 Scope for the Study

Advances in structural engineering often respond to our intrinsic desire to reach higher and higher and to design taller, more slender buildings. The current generation of flexible tall structures invariably have very low natural frequencies, which in turn heightens the risk of undesirable consequences due to wind-induced excitation. The field of *Wind Engineering* – particularly for tall building design – is complex and involves a broad range of uncertainties, which need to be accounted for in assessment analyses and simulations. The choice of an appropriate level of complexity depends on the context in which such an analysis takes place and it is difficult to decide a priori on an appropriate level of accuracy by considering traditional deterministic assessment methods only.

In the context of wind resistant design of tall buildings (which lie outside an established framework of understanding), choosing the highest level of complexity and precision in every possibly aspect is potentially an exaggeration and can even be misleading due to the inherent uncertainties. Accordingly, a quote from Albert Einstein seems appropriate here: *'Things should be made as simple as possible, but not simpler'*. In other words, the chosen level of complexity should be as simple as possible without failing to robustly and safely simulate the behaviour of tall buildings in wind. The probabilistic context of Performance-Based Design (PBD) is considered to offer a more rational approach to the problem. Such a framework has been established in Earthquake Engineering, however, the field of Performance-Based Wind Engineering (PBWE) is still in its infancy.

1.2 Research Aim

The present study focuses on several modelling and simulation aspects of PBWE of tall buildings. The main aim is to enhance an existing PBWE framework by considering Computational Wind Engineering (CWE) to propose improvements to the key analysis stages and to suggest the level of analysis accuracy and complexity appropriate for PBWE. Specifically, the research uses the techniques of Computational Fluid Dynamics (CFD) and Computational Structural Mechanics (CSM). In short, the former is used to model the wind field and compute the unsteady wind load histories, while the latter is used to derive the resulting dynamic response of the tall building. Clearly, consideration of wind-structure interaction phenomena, such as aeroelasticity, adds further, considerable complexities.

A further research aim is an actual realisation and implementation of the entire PBWE process and the study of two benchmark problems – the PBWE framework (using both existing and newly developed simulation components) is proposed and developed to assess the performance of two 180-metre tall building case studies. The two tall building designs have distinctly different geometry. The first tall building has a regular rectangular cross-section, while the alternative tall building has an irregular ‘L’-shaped cross-section. The comparative results from these PBWE analyses with buildings of very different configurations allow the adequacy of the intended computational enhancements to be assessed.

PBWE is thought to offer great potential to complement and/or augment traditional deterministic methods and experiments for tall building design. It is hoped that the results from this research will contribute towards developing a consistent and robust assessment framework for PBWE. Needless to say, a considerable research effort is still required to encourage the eventual transition to practical implementation.

1.3 Outline of the Thesis

The following descriptions effectively summarise the content of the thesis. Firstly, the overall purpose of the research is detailed in Chapter 2. In particular, there is a strong emphasis on achieving adequate levels of accuracy given the large number of uncertainties. An overview of the proposed five stage PBWE methodology is subsequently described in Chapter 3. An extensive CFD validation study (including Reynolds-Averaged Navier-Stokes (RANS) and Large Eddy Simulation (LES) turbulence models) is performed in Chapter 4 to establish the capabilities and limitations of CFD for modelling wind actions on tall buildings, again with the aim to determine an adequate level of complexity. The results are used to identify and propose suitable CFD modelling requirements for the PBWE framework. Chapter 5 then describes the first stage of the PBWE framework, which involves characterising a range of probabilistic wind events for the considered site wind environment. Chapters 6 and 7 detail the remaining stages of the PBWE framework for the regular and irregular tall building case studies, respectively. The discussion and conclusions are included in Chapter 8. Finally, Chapter 9 contains the recommendations for the future progression of PBWE.

2

Uncertainties in Wind Engineering and the Rationale for Appropriate Levels of Accuracy

2.1 Preamble

The Chapter details the various uncertainties associated with Wind Engineering for a particular class of structure: tall buildings. It is proposed that the probabilistic context of Performance-Based Design (PBD) could offer a rational approach for wind-resistant tall building design. Recent developments in Performance-Based Wind Engineering (PBWE) are then reviewed; the current research aims to further develop this subject.

The PBWE framework requires a modelling approach for determining the wind actions on tall buildings with an appropriate level of accuracy. The limitations of codes of practice and wind tunnel testing for the present research are described. Instead, the techniques of Computational Wind Engineering (CWE) are proposed for the PBWE framework. Both the flexibility and potential of CWE are detailed to justify its implementation for the study. Subsequently, an appropriate coupling algorithm for the wind-structure interaction analyses is discussed. Eventually, a one-way coupling algorithm is considered to provide adequate accuracy within the PBWE context.

The final stage of the Chapter is concerned with specifying clear performance (or damage) measures for PBWE. A governing serviceability limit state for tall buildings is considered to be occupant comfort; attention is thus focused on the corresponding acceleration threshold criteria.

2.2 Uncertainties in Wind Engineering

Extreme wind rivals earthquakes as the dominant lateral hazard for the built environment. Damages induced by the most severe windstorms can cause substantial direct and indirect economic losses and even human casualties (Augusti *et al.*, 2001). The assessment of the wind-induced response of modern tall buildings for satisfying ultimate and serviceability limit state requirements is made challenging by the stochastic nature and complexity of both the loading and response parameters. The problem can be discretised into the following areas: (a) wind environment; (b) structural properties; and (c) exchange zone. It is stated by Ciampoli *et al.* (2010) that uncertainties can arise from the aspects shown in Figure 2.1 and propagate through the subsequent stages of the assessment.

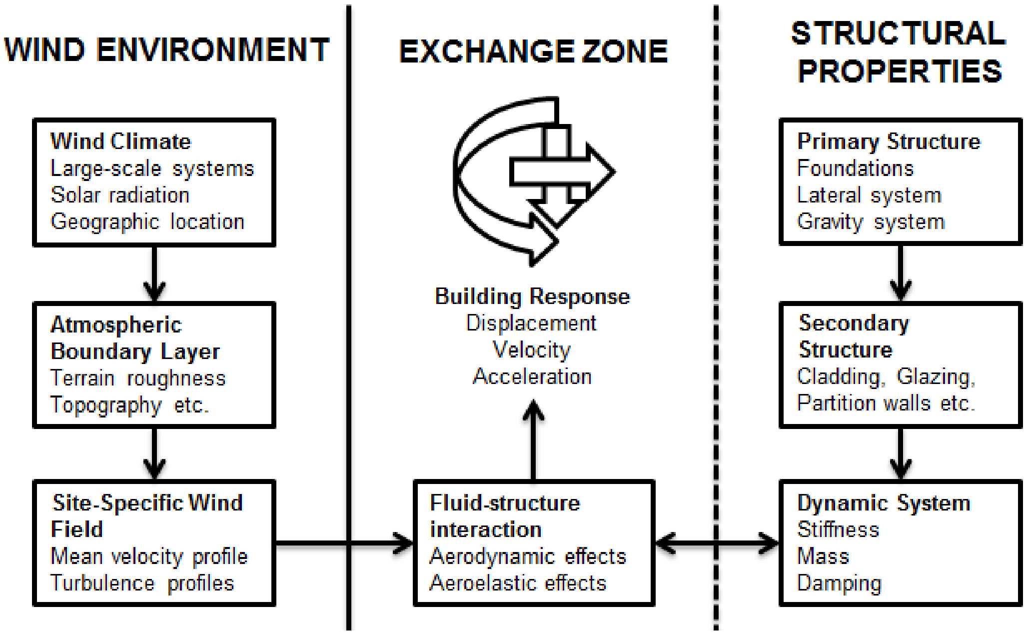

Figure 2.1. Fundamental aspects for determining wind-induced building response

Petrini (2009) classifies the uncertainties as *aleatoric*, *epistemic* or *model* uncertainties. *Aleatoric* uncertainties occur due to the stochastic nature of the magnitude and direction of the wind properties. This includes mean wind speed, gust wind speed and turbulence. *Epistemic* uncertainties arise from either a lack of data or from possible errors in acquiring data. Such uncertainties are relevant for all three areas of the problem. Finally, *model* uncertainties transpire from assumptions and approximations made – either by choice or necessity – as part of modelling the areas shown in Figure 2.1. The modelling approach could be computational, theoretical, physical or a combination of the three. The reasons as to why these aforementioned uncertainties occur are explored in more detail throughout this Section.

If these uncertainties are not handled adequately by traditional deterministic engineering design methods, then it could give rise to wind-related problems after the building is constructed. A significant cost would then be incurred from providing a suitable retrofit solution. Conversely, the uncertainties may be handled over-conservatively, resulting in the building being significantly over-designed. This would induce costs from providing unnecessary building material, or otherwise, to increase the building strength and/or stiffness.

2.2.1 Wind Environment

As stated by Holmes (2007), the site-specific wind environment consists of two main components: wind climate and atmospheric boundary layer. The wind climate describes the strong winds originating from global convective instabilities of weather systems. The differential pressure gradients are then affected by the rotation of the earth. The atmospheric boundary layer (ABL) is the region of turbulent wind flow driven by the wind climate and affected by the roughness of the earth's surface. The surface shear stress is transmitted upwards through the momentum exchange between successive layers within the ABL. The effects are progressively dissipated until the influence becomes negligible at the gradient height, z_g.

The gradient height can range between a few hundred meters to several kilometres depending on the strength of wind, terrain roughness, and angle of latitude (Simiu and Scanlan, 1986). Cook (1985) states that the typical gradient height during strong winds in the UK wind climate can be approximated to 2550 m, and hence it fully immerses the built environment. An illustrative representation of the variation in depth between typical ABL mean velocity profiles for smooth and rough terrains is shown in Figure 2.2. However, accurately characterising the vertical distribution of the incident wind field by its mean velocity and turbulence properties is a function of many upwind variables, including changes in terrain roughness and topographic features.

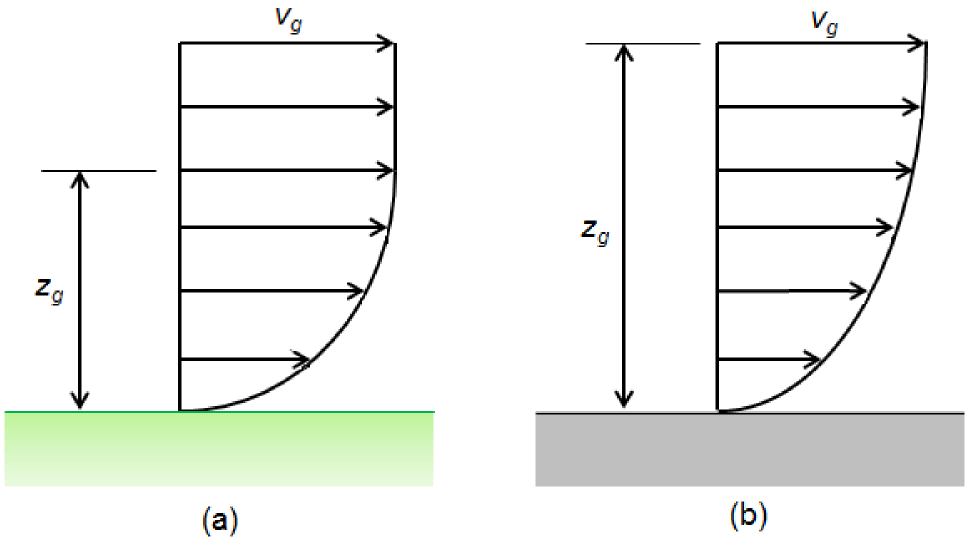

Figure 2.2. Typical mean velocity profile and gradient height for ABL in: (a) smooth terrain, i.e. open country and (b) rough terrain, i.e. town

The atmospheric turbulence is the most stochastic and uncertain quantity of the entire problem. The turbulence in the wind field contains a broad spectrum of eddies with different magnitudes and frequencies. Modern tall buildings with low natural frequencies are extremely sensitive to the effects of turbulence, and hence its spatial and temporal variation must be described as best as possible to minimise errors propagating throughout the analysis. This usually means a statistical distribution is required. However, a combination of parametric uncertainties and the apparent randomness of turbulence imply that unavoidable errors will be introduced.

For example, the UK Meteorological Office collects field measurements of hourly-mean and gust data at approximately 140 anemograph stations across the UK. The stations are almost entirely located in smooth open country terrain at a 10 metre observation level. Cook (1982), on behalf of the Building Research Establishment (BRE), performed rigorous extreme-value analysis to the maxima wind speeds to yield probability distributions for the estimated occurrence of extreme wind events. The parent wind data was found to be asymptotic to the Fisher-Tippett Type I (FTI) model. The cumulative distribution function, $P(v)$, of the extreme wind speed, v, is expressed by

$$P(v) = \exp[-\exp\{-(\alpha(v-U))\}] \tag{2.1}$$

where $1/\alpha$ and U are the dispersion and mode of the wind maxima data, respectively. The dispersion represents the spread of the distribution, and hence is a measure of variability. The mode represents the most likely value. The probability density function, $p(v)$, is then the differential of Equation 2.1 and takes the form

$$p(v) = \exp\{-(\alpha(v-U))\}\exp[-\exp\{-(\alpha(v-U))\}] \tag{2.2}$$

The corresponding probability density functions for Glasgow and London are illustrated in Figure 2.3. It can be seen that the FTI distribution has a fixed shape. The peak of the skewed distributions clearly indicates that the hourly-mean wind speeds in Glasgow are greater than London. The integral of each probability distribution is equal to 1.

In addition, it was found that the prevailing incident winds in the UK blow from a quadrant centred on west-south-west (i.e. 240° East of North) due to strong frontal depressions from the Atlantic Ocean. These winds are relatively warm and wet. The most recent statistical update is based on data records of 30 years and is the source for the prescribed 10-minute basic mean wind speeds given in the UK National Annex (NA) to BS EN 1991-1-4:2005 (British Standards Institution, 2008a).

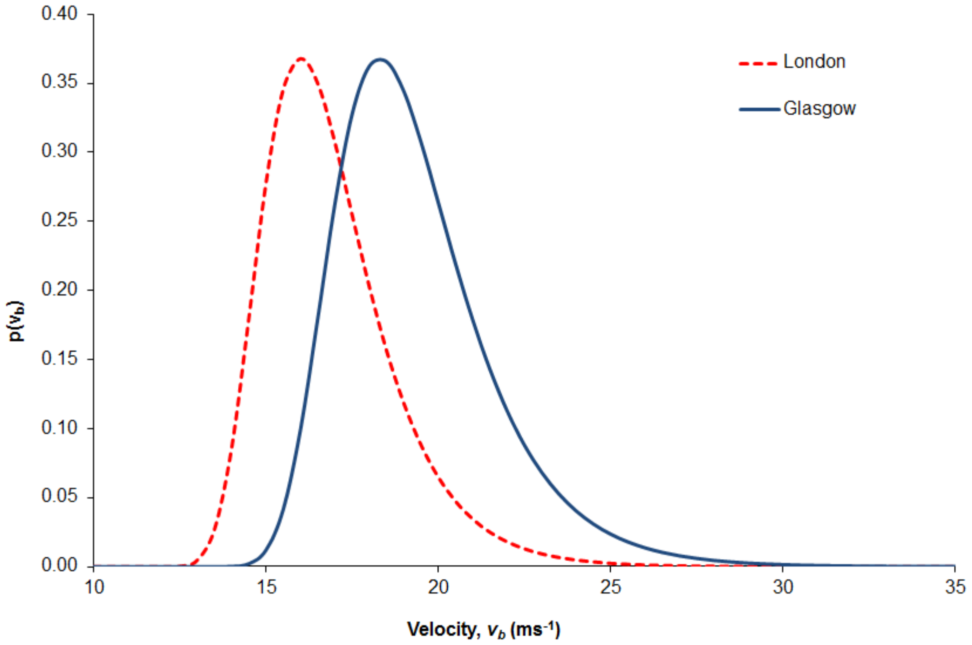

Figure 2.3. FTI probability density distribution for estimated hourly-mean wind speed in Glasgow and London

A major difficulty arises from there being a substantial lack of field measurements and limited understanding of wind flow within densely built-up town terrains. The flow characteristics over this rougher terrain are significantly more complex and unsteady than smooth open country flows. As a result it is often necessary to transpose the measured open country data using codes of practice, numerical simulations or scaled boundary layer wind tunnel tests. The lack of data gives rise to epistemic uncertainties, while model errors arise predominantly from the difficulty in schematising the turbulence in a simple and physically suitable way (Pagnini and Solari, 2002).

An insufficient array of anemometry (single observation level) often necessitates the spatial variation of the wind field to be derived from empirical engineering models, many of which assume deterministic values and a horizontally homogenous ABL. However, this ideal state can only be attained when the flow has travelled over a considerably long fetch (> 100 km) of uniform surface roughness. It is stated in PD 6688-1-4:2009 (British Standards Institution, 2009) that the proximity of the UK coastline does not allow this equilibrium condition to occur. The incident wind field for any site in the UK is likely to be affected by at least one change in upwind surface roughness (Engineering Sciences Data Unit, 2002a). To characterise the vertical variation of the wind field a rational decision must be made regarding the distance of upwind fetch to consider.

Furthermore, the feasibility of extrapolating the ground-based data to determine the wind characteristics at the upper levels of tall buildings, hundreds of metres above the ground, is questionable. Irwin (2009) recognises that there is a pertinent need for more reliable upper level wind statistics, since the response of tall buildings is very sensitive to wind speed and, often, direction.

The terrain surface roughness is commonly expressed by its aerodynamic roughness length, z_0. Uncertainties in the roughness length propagate on the mean velocity, turbulence and friction velocity, u_*. It is difficult to precisely quantify this parameter for a given site, particularly in the likely absence of sufficient measured data. Tieleman (2008) performed detailed analyses of wind data measured at several observation levels from two meteorological towers located in open country terrains. The hourly-mean velocity profiles showed occasional non-neutral patterns; the thermal effects had not been suppressed by the turbulence in the flow. It was identified that the derivation of z_0 from recorded data can be unreliable, especially if derived from only two or three observation levels. A relatively small instability in the flow at one observation level can cause a significant variation in the derived roughness parameter. It should also be noted that the value of z_0 is sensitive to potential changes to the upwind terrain during the life-cycle of the structure.

Solari and Piccardo (2001) carried out a critical review of the wide range of empirical, semi-empirical and theoretical models available to describe the longitudinal, lateral and vertical turbulence components. The reliability of these turbulence models was found to be strictly dependent on the choice of spectral equations and their parameters. It was stated that each of the available approaches involved unavoidable errors and uncertainties. The broad range of available models based on deterministic parameters could not be justified by the quality and quantity of the available data.

That the earth's climate is changing still seems a controversial topic (Colls, 2002). The primary source of climate change is considered to be man-made due to global greenhouse gas emissions from the combustion of fossil fuels. It has been argued that climate change will to some extent influence the future global wind environment. The UK Technology Strategy Board prepared a report focused on the projected effects and foreseeable challenges of climate change for the built environment in the UK (Gething, 2010). The document states that its effect on future wind loads on buildings is still unclear. It also highlights that there is very weak statistical correlation between various climate models. The report concludes that any changes to design wind speeds are best derived from statistical models based on historical field measurements rather than projections from climate models.

2.2.2 Structural Properties

The dynamic system must be modelled for the serviceability assessment of a tall building under the action of wind. The natural frequencies and mode shapes are predominantly dependent on the mass and stiffness provided by the primary structure. However, the contribution of secondary structural components, such as cladding and partition walls, and boundary conditions can be notable. An ideal evaluation of the wind-induced response of a tall building would use advanced experimental methods to derive the key structural parameters of the dynamic system. However, this is rarely feasible due to the high costs involved and a lack of time (Chopra, 2007).

The techniques of Computational Structural Mechanics (CSM) using the finite element method (FEM) or similar can be used to create complex multi-degree-of-freedom (MDOF) models of a tall building. The eigenvalues and corresponding mode shapes are solved from the formulated mass and stiffness matrices. While there are unavoidable modelling uncertainties as a result of the discretisation process and uncertain boundary conditions, it can be considered to provide a detailed estimation of the natural frequencies and mode shapes of tall buildings. The extent of agreement to full-scale data has been shown to depend on the feasibility of the modelling assumptions used to improve computational efficiency.

A structural identification study by Kim *et al.* (2009) achieved a very strong correlation between the natural frequencies obtained from detailed finite element modelling and full-scale monitoring for three reinforced concrete tall buildings in South Korea (Figure 2.4). The complexity of their numerical models was increased to improve the correlation to the full-scale data. The initial basic models were simple bare frames consisting of beam elements with lumped masses at each floor. The natural frequency results were 14% to 33% lower than measured values due to over-simplification (i.e. failing to adequately represent the mass distribution and additional stiffness provided by the floor plates). The optimum solution explicitly included the flexural stiffness of floor slabs and the effects of beam-end offsets. It also considered the influence of major secondary structural components such as plain concrete walls and cement brick walls. The error when compared against the full-scale results was reduced to a range of 2% to 7%. Consequently, the predicted building response during a typhoon event showed good agreement with measured values.

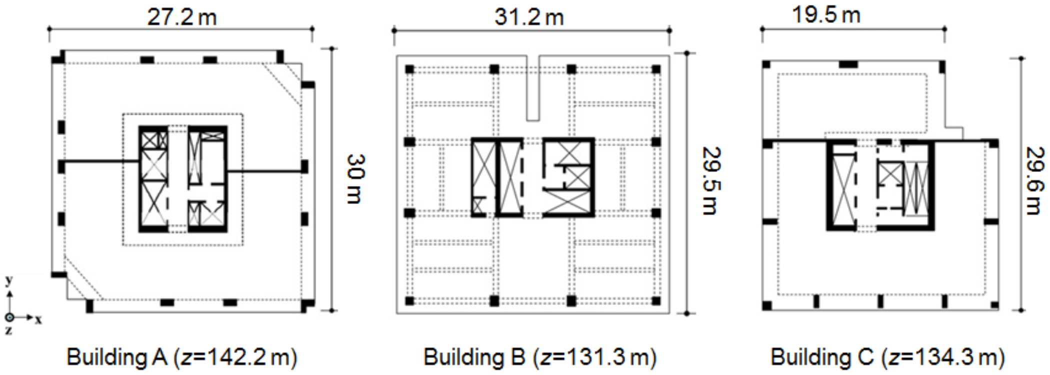

Building A (*z*=142.2 m) Building B (*z*=131.3 m) Building C (*z*=134.3 m)

Figure 2.4. Typical floor plans of three tall building modelled b Kim *et al.* (2009).

The research carried out by Campbell *et al.* (2005) found that the natural frequencies of two high-rise buildings in Hong Kong determined from full-scale measurements were higher than empirical and numerical predictions. The results supported their hypothesis that reinforced concrete buildings in Hong Kong are stiffer than similar buildings in other countries, as opposed to errors in the numerical approach. However, the implementation of inappropriate assumptions in the FE model could have contributed to the underestimated results; a detailed discussion of the FE numerical model was not provided.

As stated by Cook (1985), the most challenging dynamic characteristic to estimate at the design stage is structural damping. An accurate estimation of damping is essential to ensure serviceability and ultimate limit state criteria is satisfied. A common measure of damping is by the damping ratio, ζ, which is given in its simplest form by

$$\zeta = \frac{c}{2m\omega_n} = \frac{c}{c_{cr}} \tag{2.3}$$

where the damping constant c is the energy dissipated in a cycle of vibration, m is the mass of the system and ω_n is the natural circular frequency (rad/s). The critical damping coefficient c_{cr} represents the distinction between oscillatory and non-oscillatory response. Every engineered structure within the built environment, including tall buildings, is under-damped ($c < c_{cr}$). Hence, it will undergo oscillations when displaced from its equilibrium. The damping ratio of a tall building is typically less than 0.03 (Chopra, 2007).

However, the damping is a function of many variables such as the construction material, the form and quality of construction, the amplitude and frequency of vibration, and the internal features (Engineering Sciences Data Unit, 1990). The generalised amplitude-dependent regions are shown qualitatively in Figure 2.5. Initially, structural damping during very low amplitude oscillations exhibits little variation and is provided mainly by the construction material; typically concrete dissipates energy quicker than steel. As the amplitude increases the building components and internal walls participate and provide additional damping, shown in the nonlinear region.

Eventually, assuming no major structural damage, the dissipative action provided by the building elements reaches its maximum and the damping tends to its upper limit.

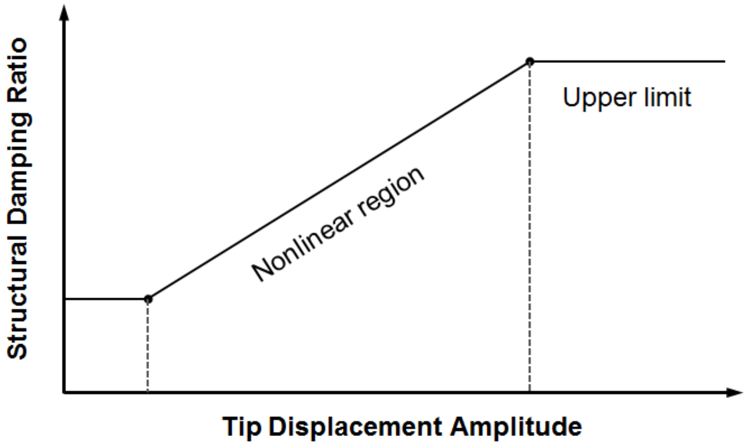

Figure 2.5.Generalised damping variation with amplitude of vibration (Li *et al.*, 2000)

Historically, the majority of full-scale measurements of damping were derived from forced vibration measurements within the initial low amplitude region. For example, Suda *et al.* (1996) conducted detailed analyses of full-scale data measured from forced vibration tests for 123 steel structures and 66 reinforced concrete structures in Japan to determine their dynamic properties. However, these results are not representative of the effects within the nonlinear damping region related to wind-induced excitation, and hence it is difficult to prescribe reliable recommendations for damping estimations at the design stage, particularly for tall buildings.

There are far fewer in-situ monitoring data of dynamic properties of tall buildings under wind-induced motion. The Chicago Full-Scale Monitoring Project was established in 2001 with an objective of addressing this shortage of data (Bashor *et al*., 2005). Initially, three tall buildings in Chicago were fitted with accelerometers, GPS devices and anemometers. The program has been extended to include tall buildings in Seoul, South Korea and Toronto, Canada. Pirnia *et al.* (2007) applied the Random Decrement Technique (RDT) to determine the dynamic characteristics of a 264 m tall building in Seoul under various wind events. It was identified that the RDT results displayed notably lower stabilising damping ratios than the design estimations. The conclusions emphasised the need for amplitude-dependent assessment frameworks for damping of tall buildings.

Ultimately, the role of damping is becoming increasingly important with growing engineering trends towards taller, more flexible tall buildings. However, there remains a large degree of uncertainty for estimating the design value for unique tall building designs due to the complex mechanisms involved and a lack of data. This uncertainty is problematic for traditional deterministic assessments of tall building designs.

2.2.3 Exchange Zone

The exchange zone defines the complex aerodynamic and aeroelastic phenomena from fluid-structure interaction (FSI) between the wind and tall building. The interaction effects cause the tall building to respond simultaneously in alongwind, crosswind and torsional directions (Chen and Huang, 2009). The biggest uncertainty is associated with modelling the complex phenomena for the dynamic response. The modelling limitations are given for codes of practice in Section 2.5, followed by wind tunnel testing in Section 2.6 and then computational methods in Section 2.7. In the meantime, the related excitation phenomena and their influence on the dynamic response of a tall building will be summarised to emphasise the complexity of the problem.

The movement of the structure is capable of influencing the dynamic properties of the structural system; this feedback is acknowledged in Figure 2.1. It has already been mentioned that the structural damping is dependent on the amplitude of vibration. In addition, the velocity of a vibrating tall building relative to the incident wind flow induces aerodynamic damping forces which can notably influence the response. A positive value of aerodynamic damping opposes the motion of the structure and extracts additional energy from the vibrating system. Conversely, a negative value of aerodynamic damping reduces the overall damping and can initiate a significant increase in the response. Additionally, prolonged exposure to strong windstorms over several years may reduce the stiffness of the structural system (Holmes, 2002).

Davenport (1998) subdivided the aerodynamic instabilities for a wind sensitive structure into the following three categories: extraneously-induced excitation; instability-induced excitation; and movement-induced excitation. Furthermore, the frequency content of the excitation source can be either narrow-band or broad-band (Holmes, 2007). In the case of narrow-band excitation, the energy is concentrated within a narrow frequency range and the tall building is likely to respond in a single natural mode. On the other hand, broad-band excitation can cause the structure to respond in a wide combination of modes determined by the amount of energy present at each natural frequency of the system and the corresponding damping.

Extraneously-induced excitation describes the buffeting action caused by the gustiness of the incident wind field. This broad-band atmospheric turbulence can be notably supplemented by vortex shedding interference effects from upwind tall buildings. This buffeting is normally the principal source of alongwind loading. However, it can also generate notable crosswind and torsional loading based on the angle of incidence and shape of the structure. Typically, when alongwind loading from atmospheric turbulence is dominant, it will cause the building to respond predominantly in its fundamental mode of vibration (Engineering Sciences Data Unit, 1990).

Instability-induced excitation covers unsteady flow phenomena such as flow separation, reattachment and vortex shedding. When flow approaches a bluff-bodied tall building normal to one of its faces it attaches to the windward face. As the flow approaches the sides and roof it cannot negotiate the sharp-edged corners and separates to form shear layers and a turbulent wake. A key loading feature is that it creates a region of strong suction at the leading edge. This can be critical for crosswind building response and the design of cladding. In addition, flow separation at these upstream corners and potential reattachment of the separated shear layers create non-uniform fluctuating pressure distributions on the side faces. The resultant torque loading can excite torsional modes of vibration and heighten occupant perception of motion. Flow reattachment on bluff bodies depends on the building shape, angle of attack and the incident turbulence (Engineering Sciences Data Unit, 2010). Consequently, the pressure in the building wake can be notably affected.

Vortex shedding occurs in the wake and is the most common form of crosswind loading. The vertical dependence of the mean wind velocity and turbulence intensity results in tall buildings being exposed to notable variations throughout their height, and hence the vortex shedding becomes less organised and the frequency is effectively broad-band (Kwok, 2007). The wind speed at which the shedding frequency coincides with the natural frequency, n_i, of the structure is called the critical wind velocity, $v_{crit,i}$ and is given by

$$v_{crit,i} = \frac{n_i b}{St} \tag{2.4}$$

where b is the crosswind dimension of the tall building and St represents the Strouhal number, a dimensionless parameter primarily dependent on the building cross-section shape. The vertical variation of the ABL mean wind velocity and the height of a tall building combine to cause the shedding to occur in fragmented, weaker vortices than occurs in low-rise buildings.

Movement-induced excitation is perhaps the most complex and refers to the self-induced aeroelastic fluid forces created by the structural motion. The main aerodynamic instabilities are galloping, flutter and lock-in (Holmes, 2007). Essentially, the occurrence of any of these mechanisms affects the structural system by introducing additional forces or negative aerodynamic damping, which increases the building response due to other excitation mechanisms. If the effects are such that the overall damping becomes zero or negative, then the amplitude of the oscillations resonate until it reaches a steady magnitude governed by the non-linearity of the aerodynamic damping.

These aeroelastic phenomena can have catastrophic consequences and are particularly pertinent for highly flexible, wind-sensitive structures such as long-span bridges and steel chimney stacks. However, these instabilities have become a very real concern for modern tall buildings and their onset should most definitely be avoided.

Literature on this complex subject is vast and is primarily based on results from boundary layer wind tunnel studies. At increased wind speeds the resulting crosswind forces often become substantially greater than in the alongwind plane. Accordingly, the crosswind dynamic response is normally critical in tall building design (Gu and Quan, 2004). However, many aspects of the tall building design can have a significant impact on the loading and response. For example, a series of 1:400 scale wind tunnel tests by Beneke and Kwok (1993) investigated the relationship between the building form and torsional loading. The triangular-shaped model was found to produce a torsional response notably greater than the rectangular, diamond and D-shaped models. In addition, the effects of eccentricity between the centre of mass and centre of stiffness was studied by Thepmongkorn and Kwok (2002). It was found that eccentricity could cause a massive increase in the resultant alongwind, crosswind and torsional responses, particularly when the centre of stiffness was located laterally or diagonally towards the leeward face. The effects of coupled translational-torsional motion magnified the resulting building accelerations at the corner of the upper floors.

It has been detailed that the interaction phenomena within the exchange zone are extremely complex. Proper consideration of the full range of excitation mechanisms is essential when determining the wind-induced building response. The problem is further complicated for intricate building shapes and asymmetric structural systems – common features in modern tall building design. This exchange zone is highly uncertain as it is also affected by uncertainties propagating from other fundamental aspects of the problem.

2.3 Performance-Based Design

Performance-based design (PBD) offers a novel probabilistic approach for handling the hazards faced by structures, rationally reducing the associated risks for both design and retrofitting strategies (Augusti and Ciampoli, 2008). The methodology of PBD requires a clear specification of the pertinent damage objectives associated with both the considered hazard and building type. The performance of the structural design must satisfy these prescribed damage objectives with an acceptable probability to control and minimise the expected losses throughout the life-cycle of the structure. The aim is to improve the decision-making process through the provision of assessment and design methods that present design options in terms that the stakeholders can clearly understand and appreciate (Deierlein *et al.*, 2003).

The concepts of PBD have developed predominantly in the field of Earthquake Engineering, where it is now regarded as a fundamental tool for risk reduction and management (Ghobarah, 2001). Over the last two decades, however, the capability offered by PBD to compliment, or even replace, traditional deterministic methods for designs involving a range of uncertainties has been recognised. This has seen a gradual increase towards extending the PBD methodologies for other extreme loading hazards such as fire (e.g., Liew, 2004) and blast (e.g., Whittaker *et al.,* 2003) events. The focus of this research is to progress the development of PBD for handling the various uncertainties in Wind Engineering for a particular class of structure; tall buildings.

2.4 Performance-Based Wind Engineering

2.4.1 Background to Performance-Based Wind Engineering

The probabilistic context of PBD suggests it is well suited to handle the various uncertainties in Wind Engineering, discussed in Section 2.2. The probabilistic performance assessment of buildings and structures subject to wind action is not a new phenomenon and has given rise to the term

Performance-Based Wind Engineering (PBWE). Past research includes a study by Unanwa *et al.* (2000) that developed a fresh approach to hurricane damage prediction through wind damage bands for low to mid-rise buildings. Also, Wen (2001) used minimum lifecycle cost criteria to achieve optimal target reliability for structures under multiple natural hazards, including wind. Additionally, Zhang *et al*. (2008) applied the probability density evolution method for the dynamic response and reliability analysis of a 20-storey frame under wind loading. Finally, van de Lindt and Dao (2009) implemented a PBWE fragility curve approach for the assessment of low-rise wood-frame buildings exposed to hurricane-type winds.

The analysis methods implemented by most of these previous PBWE studies tend to be very specific and offer a limited range of applicability with little flexibility. A collective and consistent research effort is required if PBWE is ever to develop into a readily available tool for practical engineering designs. In addition, its application for tall buildings is still very much in its infancy.

2.4.2 The Extension of the PEER Framework for PBWE

Researchers from the Pacific Earthquake Engineering Research (PEER) Centre in Berkeley developed a robust and effective framework for Performance-Based Earthquake Engineering (PBEE) (Deierlein *et al.*, 2003). The probabilistic assessment procedure consists of four main analysis stages: hazard analysis; structural analysis; damage analysis; and loss analysis. The outcome of each stage is characterised by its specific generalised variable. This PEER PBD framework offers great flexibility in that it can be adapted for a broad range of engineering hazards.

The first stage, Hazard Analysis, considers the site location and initial design characteristics to derive one or more probabilistic events for the considered hazard. The resulting hazard events are referred to as the Intensity Measure (IM) variable. This is followed by the Structural Analysis step which involves the probabilistic assessment of the structural response under each IM hazard event. The Engineering Demand Parameter (EDP) is the relevant building response measure, e.g. tip displacement, inter-storey drift, or torsional acceleration. The Damage Analysis quantifies the estimated Damage Measure (DM) as a consequence of the EDP response. Finally, the Loss Analysis translates the DM estimates into a quantifiable measure of likely losses. The Decision Variable (DV) is expressed in terms that are meaningful to the decision makers so they can decide whether the probabilistic performance of the structural design is adequate. These sequential stages and their outcomes are illustrated in Figure 2.6.

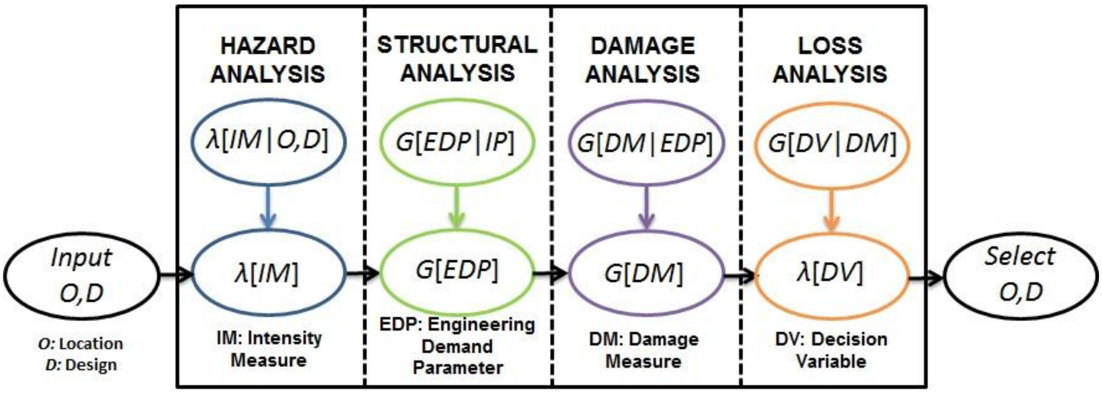

Figure 2.6. PEER framework developed for PBEE (Moehle and Deierlein, 2004)

Furthermore, it has been stated by Petrini *et al.* (2009) that the Decision Variable DV can be distinguished between two performance categories; low performance levels and high performance levels. The significant DV belonging to low performances are concerned with the consequences of damage in terms of structural integrity and human safety. On the other hand, high performance levels are related to occupant comfort and similar serviceability conditions. Thus, the costs are incurred from losses such as out-of-service time and business interruption. The chosen DV must be relevant to both the hazard and structure under consideration.

As a consequence of the associated uncertainties within each quantity, the variables are related as conditional probabilities of exceedance (Augusti and Ciampoli, 2008). In its simplest form, their combination by the total probability theorem yields the following triple integral PEER equation:

$$\lambda(DV) = \iiint G\langle DV \mid DM\rangle \cdot dG\langle DM \mid EDP\rangle \cdot dG\langle EDP \mid IM\rangle \cdot d\lambda(IM) \qquad (2.5)$$

The term $\lambda(DV)$ is a probabilistic description of the DV, such as the mean annual frequency of the DV losses (e.g. cost of repairs) exceeding a specified limiting loss (e.g. cost of building). The terms $G(DV|DM)$, $G(DM|EDP)$ and $G(EDP|IM)$, or their derivatives, are conditional probabilities relating one component of the framework to another. The final term $d\lambda(IM)$ is the derivative of the hazard curve, based on the probabilistic distribution of the intensity measure.

Progress has been made by the PERBACCO research group at the Sapienza University of Rome in extending this PEER theory to Wind Engineering problems (Paulotto *et al.*, 2004). Of course, in this adapted framework the fundamental IM hazard now refers to a range of wind events based on the site wind environment. These probabilistic events are characterised by their mean and turbulent velocity components. However, it was then recognised that an additional step was required to translate these wind speeds into corresponding wind actions based on the complex wind-structure interaction phenomena within the exchange zone. Hence, the PEER framework has been adapted and supplemented with an intermediate Interaction Analysis stage and an Interaction Parameter, IP. The revised PEER procedure is shown in Figure 2.7.

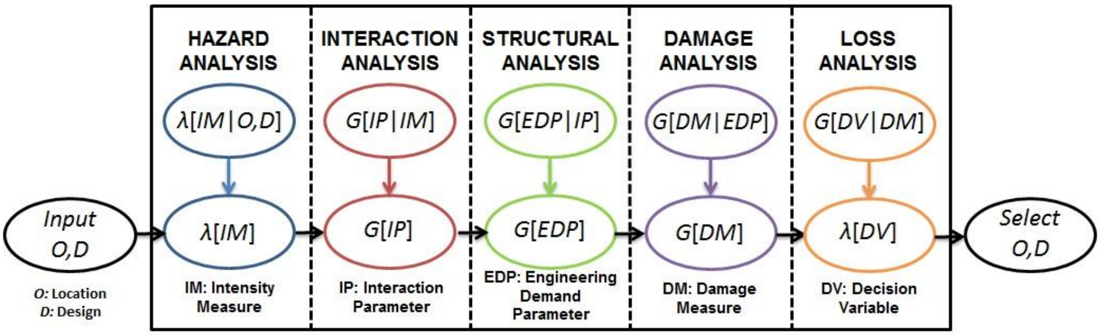

Figure 2.7. Procedure developed by PEER and adapted for PBWE (Petrini *et al.*, 2009)

Consequently, the original structural risk equation given by Equation 2.5 is modified and now takes the following form:

$$\lambda(DV) = \iiiint G\langle DV \mid DM \rangle \cdot dG\langle DM \mid EDP \rangle \cdot dG\langle EDP \mid IP \rangle \cdot dG\langle IP \mid IM \rangle \cdot d\lambda(IM) \tag{2.6}$$

The first attempt towards extending the PEER methodology to Wind Engineering was proposed by Paulotto *et al.* (2004). This was discussed in the context of a specific type of structure, namely tall buildings. It was stated that traditional vulnerability curves would not suffice for PBWE since they are not probabilistic and are generally expressed as DM vs. IM rather than the required DM vs. EDP. Therefore, an alternative fragility curve method was presented for high performance levels. This focused on business interruption losses from unacceptable occupant comfort conditions due to wind-induced excitation. An overview of the relevant recommendations revealed the uncertainty in quantifying unacceptable comfort conditions since no universally accepted criteria exist. A more rational approach was described for office buildings, which assumed people could not work if the peak acceleration on the top floor exceeded a value in the range of 4 – 10 milli-g.

The validity of this initial PBWE proposal was checked by Petrini *et al.* (2008). The framework was implemented to assess the cumulative axial fatigue damage to the hangers of a long-span suspension bridge due to wind and train transit over its 200-year design life. Attention was focused on minimising the data required to characterise the IM wind field. The 10-minute mean velocity ABL profile was represented by the horizontally homogeneous logarithmic law, while the turbulent components were characterised from ESDU 86010 guidelines (Engineering Sciences Data Unit, 2001). The wind velocity time-histories at each point of the structure were generated using the Weighted Amplitude Wave Superposition method. The fatigue damage was then estimated using a Monte Carlo simulation for 500 samples. The results indicated that the adapted framework was effective and offered great potential for future PBWE assessments.

This PEER-adapted PBWE methodology was later applied to the same long-span suspension bridge for the overall assessment of the collapse and out-of-service risks (Petrini *et al.,* 2009). The performance levels were based on limit state criteria. The serviceability limit state (high performance) was concerned with maintaining the operation of the rail and road networks, while the ultimate limit state (low performance) focused on the structural safety by flutter stability. The IM set was reduced to just one variable – the mean wind velocity at 10 metres height – and the Interaction Parameter IP was derived from deterministic aeroelastic theory. A sensitivity check on the significance of the roughness length z_0 was then conducted for a small range of z_0 values, namely 0.05 m, 0.1 m and 0.2 m. These relatively small values have a significant impact on the vertical variation of the mean wind speed and turbulence intensity. The notable differences from the resulting fragility curves identified that the uncertainty in z_0 should be incorporated as a variable for IM. The study concluded that PBWE is clearly feasible. However, it stated that better probabilistic descriptions of both IM and IP are necessary improvements to make the proposed framework more reliable.

One of the most recent extensions of this PEER-based PBWE framework was for the assessment of an offshore wind turbine design (Ciampoli and Petrini, 2010). This problem was concerned with wind flow over sea, which meant the mechanisms for characterising the IM wind environment were more straightforward than those associated with town terrains. This study included uncertainties regarding an additional environmental action, the hydrodynamic phenomena. The peak alongwind and crosswind displacements at the hub were considered as the relevant EDPs and relevant DM displacement thresholds were specified. The analyses of the structural response were carried out in the frequency domain. The study concluded that PBWE was relatively simple and effective when using ultimate or serviceability limit state damage criteria.

The literature certainly suggests that this PBWE framework offers great potential to compliment traditional deterministic methods, particularly given the large number of uncertainties. It is believed that continuing to progress this promising procedure will help to promote and develop a consistent assessment method for PBWE. The intention is that this present study will assist the eventual transition from research and development to practical implementation for tall building design and retrofitting.

The flexibility of this generalised PEER-based PBWE framework allows specific components of the procedure to be enhanced. It is evident that the current weaknesses of the framework for tall building design are associated with the representation of the IM and IP variables. It is these components that the present research intends to develop. A suitable modelling approach for enhancing both IM and IP in the probabilistic context of PBWE must be investigated.

2.5 Codes of Practice

2.5.1 Background to Codes of Practice

The most straightforward means of quantifying design wind actions on buildings is by relevant codes of practice. These codes of practice are formulated with a view to providing a solution with an acceptable balance between the overly complex reality and an oversimplified (conservative and/or unreliable) approach. They should be formed on the basis of state-of-knowledge, which includes current practices and past experiences (Mehta, 1998). As listed by Narayanan (2009a), some of the undoubted benefits from publishing codes of practice include: promoting an efficient design practice; creating a fair and impartial market place; and allowing consistent enforcement of building regulations.

Simplifying the problem for codification purposes necessitates a number of underlying assumptions to be made. The use of relevant codes of practice as a PBWE tool for predicting wind actions on tall buildings should be approached with care. It must be ensured that the conditions of its limited range of applicability are safely satisfied. In general, the quasi-static approach offered by traditional codes of practice for wind loading and response are only valid for structures that are not dynamically sensitive. Also, the complexity associated with the crosswind and torsional excitation phenomena means the response cannot be coherently related to the oncoming turbulent wind and are difficult to codify (Allsop, 2009a). Therefore, codes of practice are typically limited to alongwind building response and provide little, if any, guidance for these other axes. This is a significant limitation for the assessment of modern tall buildings.

2.5.2 Eurocode 1; BS EN 1991-1-4:2005

The Eurocodes have been developed to provide a coherent package of codes incorporating a single market of 28 countries, including the UK. The British Standards Institution (BSI) was required to withdraw all conflicting domestic standards by 31^{st} March 2010. The participating countries were obliged to provide their own National Annex (NA) to cover country-specific data and to reference non-contradictory complimentary material. As a result, the Eurocodes contain clauses that allow nationally determined parameters (NDPs) to be specified by the relevant National Annex for different climatic, geological and geographical conditions.

The relevant documentation for wind loading is BS EN 1991-1-4:2005 (British Standards Institution, 2005) which replaced the highly-regarded BS 6399-2:1997 (British Standards Institution, 2002). In addition to the National Annex (British Standards Institution, 2008a), the British Standards Institution has produced PD 6688-1-4:2009 (British Standards Institution, 2009). The Published Document provides non-contradictory complimentary information that supports BS EN 1991-1-4:2005. It offers theoretical justifications to the decisions made in the National Annex, as well as commentary on some specific sub-clauses. It is permitted to include additional data which can be used in conjunction with BS EN 1991-1-4:2005. Thus, it introduces a significant amount of guidance from BS 6399-2:1997, including procedures for assessing building forms with irregular geometry and the directional method for determining wind actions. It also provides an alternative method for dealing with vortex shedding and other aerodynamic instabilities.

However, the code of practice clearly states its gust peak factor procedure is only applicable to buildings up to a height of 200 metres. It does not provide guidance on torsional or crosswind vibrations. Furthermore, it does not deal with vibrations where more than the fundamental natural frequency is involved in the building response. Ultimately, the applicability of this code is similar to its predecessor BS 6399-2:1997; it is limited to ‘normal’ buildings and structures only. Furthermore, it is stated by Allsop (2009b) that the basic Eurocode for wind loading is based on technology that was readily available 40 years ago. The superseded British Standard BS 6399-2, despite providing more data in a more usable way, is still based on resources from the 1980s.

2.5.3 Suitability of Codes of Practice for Proposed Research

Ultimately, these major limitations suggest it would be inadvisable to use codes of practice as the primary calculation method for determining IP, even in the probabilistic setting of PBWE. Nonetheless, it may prove useful to compare the resulting codified wind pressures to an alternative, better-suited method. In addition, the Eurocode may be referenced for other parameters such as probabilistic descriptions of the basic 10-minute mean velocity for sites across the UK, detailed in Section 2.10, and the internal wind pressures within the building. Indeed, Narayanan (2009b) states that BS EN 1991-1-4:2005 offers a flexible and realistic approach for internal wind pressure which covers a range of building forms and porosity distributions. The alternative modelling methods for determining wind actions, namely wind tunnel testing and computational wind engineering, do not explicitly consider the internal wind pressure. The codified internal pressures could be used to supplement these results.

2.6 Wind Tunnel Testing

2.6.1 Background to Wind Tunnel Testing

The traditional solution for determining the wind actions and the dynamic response of buildings and structures outside the scope of current codes and standards is boundary layer wind tunnel testing. Wind tunnel testing has become an established tool for industry engineering practices and is now routinely performed as a key part of the design procedure for tall buildings. The development of advanced boundary layer wind tunnel facilities has enabled engineering boundaries to be pushed beyond what would have previously been considered impossible (Irwin, 2009).

It is normal practice to place the scaled model of the tall building on a turntable along with physical models of the significant surrounding cityscape. This allows data for a full range of wind directions to be efficiently acquired. Recent software developments, such as Google Earth, act as invaluable tools for enhancing the model detail of surrounding urban environments. Roughness blocks are positioned upstream to generate the desired mean wind velocity and turbulence characteristics for the incident ABL flow. It must be ensured that the scale of the turbulence properties, namely length scale and intensity, correspond to the scale of the structural model.

The design of super-tall buildings has encouraged an increasing trend of implementing wind tunnel methods at the initial design stage. One of the main applications has been concerned with optimising the building cross-section to reduce the crosswind loads in order to satisfy strength and serviceability requirements. Indeed, it was documented by Stansfield (2006) that the world’s tallest building, the Burj Khalifa, was practically designed in the wind tunnel. The tri-form shape of the footprint was changed throughout the height of the structure to disorganise the vortex shedding and reduce resonance effects. The structure was then tested in 12° incremental wind directions and the building orientation was aligned to the optimum direction according to the prevailing wind speeds.

2.6.2 Model Techniques in Wind Tunnel Testing

The estimated wind actions and structural responses by wind tunnel testing are generally obtained from three techniques: the high-frequency force-balance model; high-frequency pressure integration model; or the aeroelastic model. In tall building design, it is common to use a combination of these methods to provide added confidence that the final design is accurate. However, each modelling technique is not without its own difficulties and limitations.

A 6-component high-frequency force-balance (HFFB) system measures the bending and torsional moments at the base of the rigid building model to provide data of the net wind actions on the building. This method does not indicate where the high local pressure regions exist across the building envelope (Taranath, 1998). The implications of this limitation is that it is only suited for building responses in the fundamental mode. In addition, the mounted building model is required to be extremely stiff. Achieving a sufficient stiffness for slender tall building models can often be difficult. This can necessitate the tests to be performed at lower wind speeds in order to avoid resonance with the building model. The Reynolds number effects at this reduced range can become significant (Allsop, 2009a).

The high-frequency pressure integration (HFPI) technique involves positioning pressure taps throughout the envelope of a rigid building model. It is capable of providing time histories of the wind load and local peak pressures for various points on the structure. The total wind force can be determined by integrating the measured pressures. It overcomes the limitations of HFFB by being able to provide higher-order modal loads. The HFPI results can be validated by comparing the fundamental mode results against the HFFB results. For complex building designs, it may prove difficult to fit a sufficient array of pressure tabs on the building model (Irwin, 2009).

The aeroelastic model intends to model the full aeroelastic response and can be an effective tool for checking the final structural design. It employs multi-channel non-contacting displacement transducers and accelerometers for measuring the response. This technique can be accurate for aeroelastic analyses of tall buildings that behave like idealised cantilevers. However, Gu and Quan (2004) stated that the difficulties in both accounting for aerodynamic damping and manufacturing reliable aeroelastic models for tall buildings with irregular shapes contribute to the uncertainties of this test technique.

Wind tunnel blockage is a more general limitation based on the cross-section area of the wind tunnel (Allsop, 2009a). This implication dictates the scale at which the tall building can be feasibly modelled without constraining the flow. Additionally, the wind tunnel cannot account for the apparent Coriolis force due to the rotation of the earth's surface. This phenomenon could cause a significant variation between the incident wind direction at the upper and lower levels of a super-tall building. This effect will be most prominent in extreme northern and southern locations (Taranath, 1998).

2.6.3 Suitability of Wind Tunnel Testing for Proposed Research

Based on current state-of-the art, it is acknowledged that wind tunnel testing would offer the most accurate assessment of the Interaction Parameter (IP) stage in the proposed PBWE framework. However, the major difficulty for this study is that the specialist technology is not readily available. The most advanced facility in the UK is operated by BMT Fluid Mechanics (www.bmtfm.com). The commercial demand is such that there is rarely an opportunity to utilise this service for academic purposes or, perhaps more importantly, the budget to do so. Nonetheless, it has been detailed above that even these established scaled methods have their own difficulties and uncertainties.

2.7 Computational Wind Engineering

2.7.1 Background to Computational Wind Engineering

Computational Wind Engineering (CWE) describes the application of Computational Fluid Dynamics (CFD) for problems associated with the built environment. It offers a flexible modelling alternative for conducting the wind-structure interaction analyses. The potential for implementing CWE as a tool for modelling the Intensity Measure (IM) wind events and the Interaction

Parameter (IP) will be expressed in relation to the probabilistic context of the proposed PBWE PEER framework and its ability to handle uncertainties.

The implementation of CWE for practical engineering problems has received a lot of research attention over the last three decades (Huang *et al.*, 2007) and has made major progress due to the advancement of computer technology. CWE requires the numerical solution of the three-dimensional Navier-Stokes equations for high Reynolds number flows around the considered structure(s) (Swaddiwudhipong and Khan, 2000). The highly turbulent wind conditions and complex flow phenomena, mainly regarding separation and reattachment, have given rise to many difficulties in using CFD for such problems (Murakami, 1997). It is for this reason that commercial applications of CFD for the built environment has focused on areas such as pollution dispersion, natural ventilation, wind-driven rain and pedestrian comfort (Stathopoulus, 1997).

A typical CFD domain for CWE simulations using the finite volume method is shown in Figure 2.8. Basic fluid flow is solved by subdividing the domain into a continuous mesh of finite volumes before solving the governing integral equations for mass and momentum conservation. These equations can be supplemented by a variety of different turbulence models, one of which must be used for all FSI problems (Sun *et al*., 2009). At present, no single turbulence model exists that is capable of producing accurate results for all types of problem (Castro, 2003). The selection of the turbulence model has a significant bearing on both the computational cost and accuracy. Therefore, the choice of an appropriate model is normally governed by criterion such as the accessible computational power, the level of accuracy required and the amount of time available for simulations.

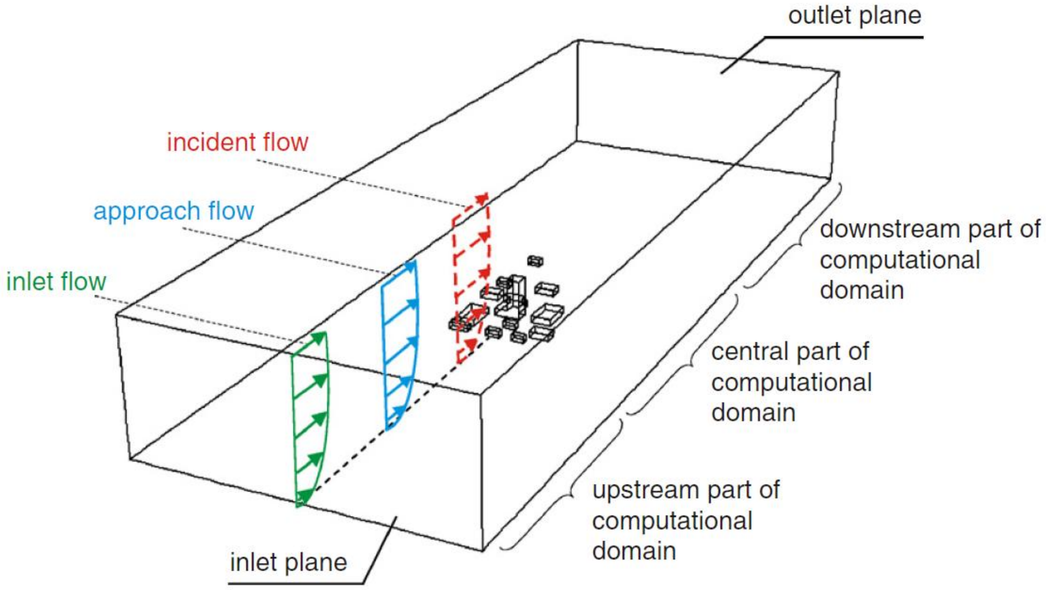

Figure 2.8. Typical CFD computational domain (Blocken *et al.*, 2007).

The most complete form of CFD is Direct Numerical Simulation (DNS). This technique calculates the direct solution of the Navier-Stokes equations for each control volume. Wind turbulence is an inherently random phenomenon and the fluctuations develop in a variety of sizes and frequencies, from large sustained gusts to small eddies. The DNS mesh must be smaller than the smallest turbulent eddy within the flow in order to accurately capture all turbulent effects. Therefore, the computational cost of DNS is high as the procedure is extremely inefficient and Knapp (2007) states that this particular method should be limited to small scale simulations with low Reynolds numbers (low turbulence).

Reynolds-Averaged Navier-Stokes (RANS) and Large Eddy Simulation (LES) are two of the leading turbulence models which create their own additional terms in the instantaneous governing equations to achieve ‘closure’. Thus, the small scales of turbulence do not require direct modelling and the computational requirement is reduced.

RANS equations control the transport of the time (or ensemble) averaged flow quantities, modelling the full spectra of the scales of turbulence. The time averaging means most of the turbulence terms in the Navier-Stokes equations of motion disappear. The remaining Reynolds stress terms are resolved using an effective viscosity called the eddy viscosity. The most popular RANS methods are the two-equation k-ε and k-ω models. This is because they are relatively simple to use, are robust and have a low computational cost (ANSYS Inc., 2009a). These empirical models solve two additional transport equations to obtain the turbulent viscosity; the kinetic energy, k, and either the turbulent dissipation rate, ε, or the specific dissipation rate, ω.

The LES turbulence model offers a transient solution that adopts a spatial filtering approach: eddies exceeding the mesh size are resolved directly in a time-dependent method whilst those smaller must be resolved by a subgrid-scale (SGS) model. Essentially, the filtering process is a mathematical manipulation of the real Navier-Stokes equations to eliminate eddies smaller than the filter criteria. The idea is to parameterise less of the turbulence but resolve this in a more complete manner. It requires a significantly finer mesh than traditional RANS simulations and the transient conditions are much more demanding. The time-step is often a whole order of magnitude smaller than RANS, and hence a large number of time steps are needed to obtain stable statistics of the flow being modelled. Thus, the computational time and required memory are far greater than RANS.

Detached Eddy Simulation (DES) has since been developed in the field of aeronautics with the intention to combine the useful features of both RANS and LES (Spallart, 2001). In this approach the simpler RANS model is used to simulate the majority of the flow, while LES is employed to the regions of separated flow. The concern with using DES for structural wind engineering applications is that the entire fluid domain could be highly turbulent. This is in contrast to aeronautic analyses involving flow around an airfoil, since the flow is not separated. Hence, it may not be applicable for highly complex unsteady flow regimes in densely built-up environments.

The choice of turbulence model is the most important parameter in CWE simulations for wind actions on buildings. However, there are many additional modelling considerations which affect the performance of CWE. For example, the numerical results for such complex turbulent flow regimes are extremely sensitive to the choice of the mesh. The near-wall mesh and other regions where the flow experiences unsteady phenomena must be resolved with a sufficiently fine grid. The total cell count for the domain must be as low as possible without compromising the accuracy of the results in order to optimise the computation time. Meanwhile, the geometry of the domain must ensure it never constrains the flow as it interacts with the opposing bluff body. In addition, the relevant tall building must be positioned in the channel such that is does not adversely affect the inflow and outflow boundary conditions.

2.7.2 Atmospheric Boundary Layer Modelling in CWE

The application of CWE as a component for the proposed PBWE framework would involve a series of simulations for the quantified IM wind events. The wind events are derived from the Hazard Analysis stage with a corresponding annual risk of exceedance. Being able to sufficiently model the intended ABL characteristics of each IM wind event is an essential prerequisite for predicting the resulting wind loads on the tall building.

Referring to Figure 2.8, the basic requirement is that the ABL flow profiles specified at the inlet are maintained through the upstream part of the domain until the incident flow meets the explicitly modelled obstructions. Modelling a horizontally homogeneous ABL flow is dependent on the boundary conditions satisfying the equations of the implemented turbulence model. However, previous studies have identified that simulations using the standard functionality of commercial CFD packages encounter great difficulty in attaining this equilibrium condition (Richards and Norris, 2011). The presence of erroneous streamwise pressure gradients would create an unintended internal boundary layer within the computational domain where the inflow conditions adapt rapidly.

Blocken *et al.* (2007) investigated the problems associated with modelling horizontally homogeneous ABL flows using wall functions in CFD. The extent of the unintended streamwise gradients were dependent on a number of variables, including the inlet ABL profiles, the turbulence model, the near-wall mesh resolution, the type of wall functions, the specified roughness height and the roughness constant. The study emphasised the critical importance of conducting empty-channel studies prior to the actual simulation of the building or obstacle. This stage allows the ABL to be monitored throughout the domain without physical disruption. A horizontally homogeneous ABL would have outflow wind characteristics identical to those specified at the inlet. It is recommended that the incident flow is monitored throughout these preliminary simulations as this corresponds to the actual flow characteristics that will be imposed on the building – these could differ significantly from the target inlet ABL profiles.

New equations to describe the inflow boundary conditions for the standard k-ε turbulence model were proposed by Yang *et al.* (2009). It was intended that the expressions would provide a better representation of a neutral equilibrium ABL in CFD. The equations are based on the assumption that the rate of production of turbulent kinetic energy is equal to the rate of dissipation, i.e., turbulence equilibrium. The study by O'Sullivan *et al.* (2011) has since reviewed this model and proposed further advances. The study recommends that the gradient of the streamwise velocity, u, the turbulent kinetic energy, k, and the turbulent dissipation rate, ε, at the top of the domain should be based on a simple extension of the shear stress, u_*. Therefore, the mean velocity gradient based on the logarithmic law (Simiu and Scanlan, 1986) becomes

$$\frac{\partial u}{\partial z} = \frac{u_*}{\kappa(z + z_0)} \tag{2.7}$$

where κ is the von Karman constant and z_0 is the aerodynamic roughness length.

Meanwhile, the gradients of the turbulent equations of Yang *et al.* (2009) are expressed by

$$\frac{\partial k}{\partial z} = \frac{1}{z+z_0} \cdot \frac{C_1}{2\sqrt{C_1 \ln\left(\frac{z+z_0}{z_0}\right) + C_2}} \tag{2.8}$$

$$\frac{\partial \varepsilon}{\partial z} = \frac{u_*^3}{\kappa (z+z_0)^2} \cdot \left[\frac{C_1}{2\sqrt{C_1 \ln\left(\frac{z+z_0}{z_0}\right) + C_2}} - \sqrt{C_1 \ln\left(\frac{z+z_0}{z_0}\right) + C_2} \right] \tag{2.9}$$

The additional terms C_1 and C_2 are constants determined by fitting the model data to measured or experimental data.

The application of these recommended boundary conditions yielded an exact simulation of a horizontally homogeneous ABL flow. The results were shown to be valid regardless of the vertical height of the domain and when the idealised and real topographic obstacles in the domain were explicitly included. It should be noted that these studies involved flows with relatively low levels of turbulence.

Research by Knapp (2007) found that the RANS *k-ε* turbulence models better sustained the inflow turbulence conditions when both the top and side boundaries were set as velocity inlets with corresponding streamwise flow components only. Attaining the neutrally equilibrium ABL boundary conditions was a rigorous, iterative process. The vertical distribution of the turbulent kinetic energy for the derived horizontally homogeneous ABL was still significantly less than the original target profile. Subsequently, this had a detrimental effect on the fluctuating component of the predicted structural wind loads.

It appears that horizontally homogeneous ABL flow can be reproduced for the standard *k-ε* model if alternative boundary conditions are implemented. However, it is unclear if this equilibrium can be attained for high turbulence or for alternative RANS turbulence models which assume non-isotropic turbulence. The problems encountered in the literature suggest that it could prove difficult to model ABL flows that are undergoing transition due to changes in the terrain surface roughness. As mentioned previously, the proximity of the UK coastline means the ABL will always be in some state of transition.

2.7.3 Structural Wind Pressure Modelling in CWE

In the UK the majority of benchmark studies to assess the performance of CFD for predicting flow patterns and wind loads on buildings have referred to basic low-rise surface-mounted cube shapes, usually exposed to wind acting normal to its face. This is chosen for two main reasons; the simplicity of the shape and the numerous experimental results available for comparison. In particular, the 6-metre Silsoe Cube was built in 1987 for the purpose of providing full-scale data for wind tunnel and CFD development (Richardson and Surry, 1992).

Knapp (2007) reviewed the recent advances in CFD turbulence modelling for structural wind engineering. The Silsoe Cube was modelled to validate these methods for predicting the flow regime and wind loads. The study was then extended to a complex grandstand. Data for a range of wind directions was obtained from a wind tunnel study. The CFD simulations of the grandstand were run at model scale (1:300). The study consisted of both steady and unsteady RANS as well as DES. The steady RANS solution could not converge due to the irregular geometry of the grandstand and inherent unsteadiness of the flow phenomena. The unsteady RANS encountered difficulty in sustaining the inlet turbulence, and hence the fluctuating component of the wind load was underestimated. In addition, it failed to accurately model flow separation and reattachment for the complex geometry. Meanwhile, the DES results showed an improvement in the prediction of mean loads and better modelled the unsteady aerodynamics. However, the conclusions stated that the slight superiority of DES was not worth the substantial increase in computational cost and further improvements are necessary. The research also identified that detailed pressure results are extremely sensitive to mesh design and refinement.

The Commonwealth Advisory Aeronautical Council (CAARC) standard tall building has been subjected to several CFD studies due to the high amount of wind tunnel data available for comparison (Obasju, 1992). The building is a flat-topped regular rectangular prism with a cross section D = 30 m by B = 45 m and height H =180 m. The steel structural system provides a fundamental natural frequency of approximately 0.2 Hz. It is worth noting that there is quite significant scatter of the measured building pressures between some of the wind tunnel laboratories, despite using the same experimental techniques (Huang *et al.*, 2007). This highlights the sensitivity of wind tunnel tests to certain key variables, most notably concerning turbulence scalability.

A comprehensive three-dimensional CFD study of the wind actions on the CAARC tall building was performed by Huang *et al.* (2007). The simulations were performed at a 1:250 scale, providing a range of Reynolds numbers identical to the wind tunnel experiment by Obasju (1992). The ABL flow was characterised by the power law equation for the mean velocity profile and relatively low turbulence intensities. The numerical time-step for LES was limited to 5 x 10^{-4} s, while the RANS k-ε models were set as 2 x 10^{-3} s. The computational time for a single physical time step (5 sub-iterations) in LES was approximately 60 s using 16 CPUs in parallel. Meanwhile, the RANS simulations only required 30.4 s using 8 CPUs. Assuming the scalability of the CFD code for parallel processing is efficient, the time for one physical time step in LES would be four times higher than RANS. In addition, the required LES time step is an order of magnitude smaller than RANS. This emphasises the massive computational cost of LES.

A summary of the results by Huang *et al.* (2007) will now be provided. The results from the LES turbulence model using the dynamic SGS kinetic energy approach provided the most accurate predictions for both the mean and fluctuating components of the surface pressures at 2/3H (= 120 m) on the tall building. Meanwhile, revisions of the RANS k-ε turbulence model offered encouraging results. However, the RANS models could only partially reproduce some of the complex flow structures. For example, the standard k-ε and k-ε with Launder and Kato (LK) modifications failed to properly model the arch vortex in the wake. The revised k-ε with Murakami, Mochida and Kondo (MMK) modifications was found to provide the best RANS model for quick solutions. The conclusions stated that the wind tunnel was still essential for investigating the wind actions on buildings and structures. Strategies for improving the performance of CFD were also suggested. This included better grid generation methods for complex geometries and more representative methods for generating inflow turbulence characteristics.

CFD simulations of the CAARC building were modelled at full-scale as part of the study by Braun and Awruch (2009). The wind flow and aerodynamic loads were predicted using the LES dynamic SGS turbulence model and a time-step $\Delta t = 6.5 \times 10^{-4}$ s. The mean and root-mean-square (RMS) pressure coefficients at heights of $1/3H$ (= 60 m) and $2/3H$ (= 120 m) were compared against the accessible wind tunnel and numerical data. The accuracy of both the mean and fluctuating parts of the structural wind loads at $2/3H$, approximately corresponding to the stagnation point, were in strong agreement with the wind tunnel data. Available measurements at $1/3H$ are far more limited. The mean pressure coefficients showed strong correlation. However, the RMS component exhibited much more noticeable discrepancies.

The Architectural Institute of Japan (AIJ) formed a working group dedicated to the field of CFD for the wind-resistant design of structures. A primary objective has been concerned with identifying the capabilities and limitations of the leading turbulence models available in CFD. On behalf of the AIJ, Tamura *et al.* (2008) published definitive guidelines on the use of CFD for wind loads on buildings. The research assessed the performance of both LES and RANS for predicting the surface pressures on a low-rise (1:1:0.5) and high-rise (1:1:4) building. These ratios are expressed as (B:D:H) where

B is the crosswind width, *D* is the alongwind depth and *H* is the height. The outputs were compared against data from wind tunnel tests. The conclusions stated that LES was essential for full wind load estimation, while RANS should be limited to calculating mean wind forces on buildings. The results lead to the development of a flow chart (Figure 2.9) to outline the procedure for predicting wind loads on structural frames using CFD. Reference to Figure 2.9 highlights that the RANS models are restricted to alongwind loads only and should be supplemented with a relevant AIJ gust effect factor.

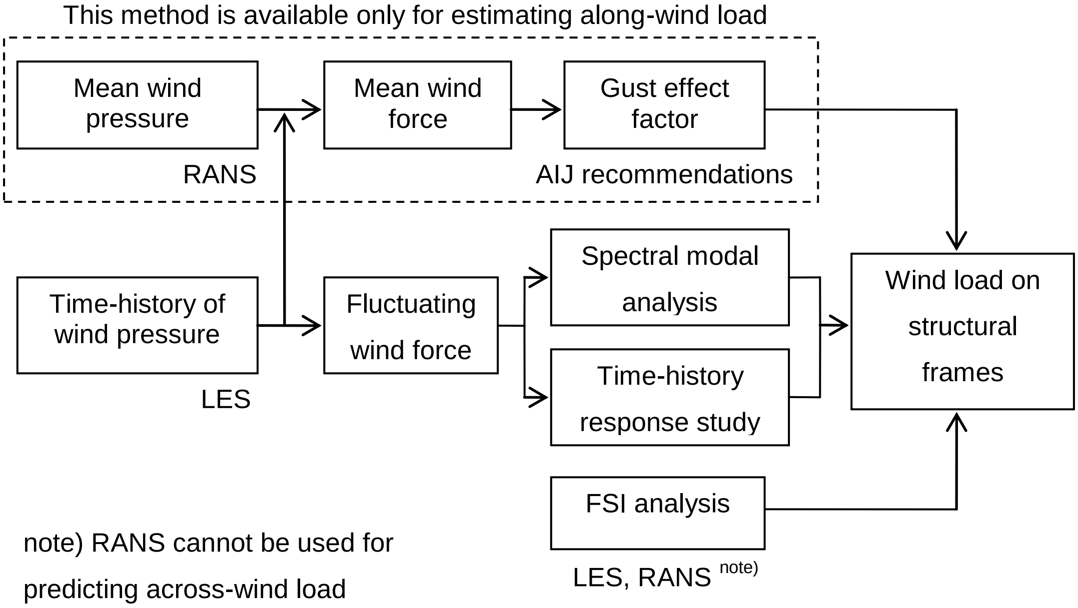

Figure 2.9. CFD procedure for wind loads on structural frames (Tamura *et al.*, 2008)

The problem becomes conceptually more complicated when the application of CFD is extended from single isolated structures to multiple building arrangements within built-up urban environments. However, Nozu *et al.* (2008) modelled the flow and building pressures in the centre of Tokyo using CFD. A combination of Geographic Information System (GIS) data and a nested grid technique enabled the city to be reproduced to a high level of detail. The study cited that a number of previous analyses had identified that LES better predicted wind flow among densely arrayed tall buildings with vortex shedding than RANS. The LES results were compared directly against field measurement data. It was found that LES was able to reproduce the local unsteady flow patterns around a target building within the urban area. Also, the simulation was capable of qualitatively predicting the distorted pressure distributions on the building surfaces. However, it proved difficult to generate an optimum mesh for buildings in urban areas since the flow regime was not predictable beforehand.

Tamura (2008) provided examples of successful applications of LES for several issues in wind engineering. This included estimations of wind loads for wind resistant building design, flows over complex topography and flows within complex city terrain. The focus was on the current state and future potential of LES for its practical implementation in wind engineering. It acknowledged that peak-type values are a key requirement for many wind engineering problems. The study concluded that LES was definitely capable of predicting accurate values that are comparable to wind tunnel data. The high computation cost was not foreseen as a long-term problem due to the continued improvement of innovative parallel programming and its user-friendly usage.

The choice of domain size and building position for CFD modelling of tall buildings in turbulent flow was considered by Revuz *et al.* (2010). The aim was to determine the optimum domain size in terms of computational cost and time. The tall building was a rectangular prism with H = 180 metres, B = 20 metres and D =10 metres. The numerical simulations were performed at a 1:200 scale. The initial geometry of a small domain was incrementally increased and the impact on the velocity field and surface pressures was studied. The practical recommendations stated that an upwind distance of 20B and downwind length of 30B were sufficient. Also, a domain height of approximately 5H should be followed. Inexplicably, there was no conclusive value stated for the crosswind width of the domain. The minimum width was 8B to either side of the building, while the maximum was 62B. The results appeared to show only minor decreases in pressure on the side face as the domain geometry was increased.

If these recommendations are implemented for the geometry of the CAARC standard tall building, i.e., H = 180 m and B = 45 m, then the resulting domain volume would be almost 4.5 times larger than that used by Huang *et al.* (2007), but only 1.2 times larger than the domain by Braun and Awruch (2009). The three domains are shown in Figure 2.10. Consequently, the number of computational cells required for this larger volume would cause an increase in the computational cost of the CFD simulations. The considerably smaller domain used by Huang *et al.* (2007) achieved encouraging results using their domain geometry. However, it should be noted that these simulations were performed at model scale, whereas Braun and Awruch (2009) ran full-scale CFD simulations.

The increased domain size proposed by Revuz *et al.* (2010) would decrease the streamwise blockage ratio, which is a measure of the area of the windward face of the building divided by the area of the streamwise plane of the domain. This would inevitably relax the top and lateral boundary constraints on the flow as it passes the building and the accuracy of the results could potentially improve. It is difficult to foresee whether this expected improvement would merit the increase in CPU time. However, it may prove that such a large domain is required for full-scale, highly turbulent CFD simulations.

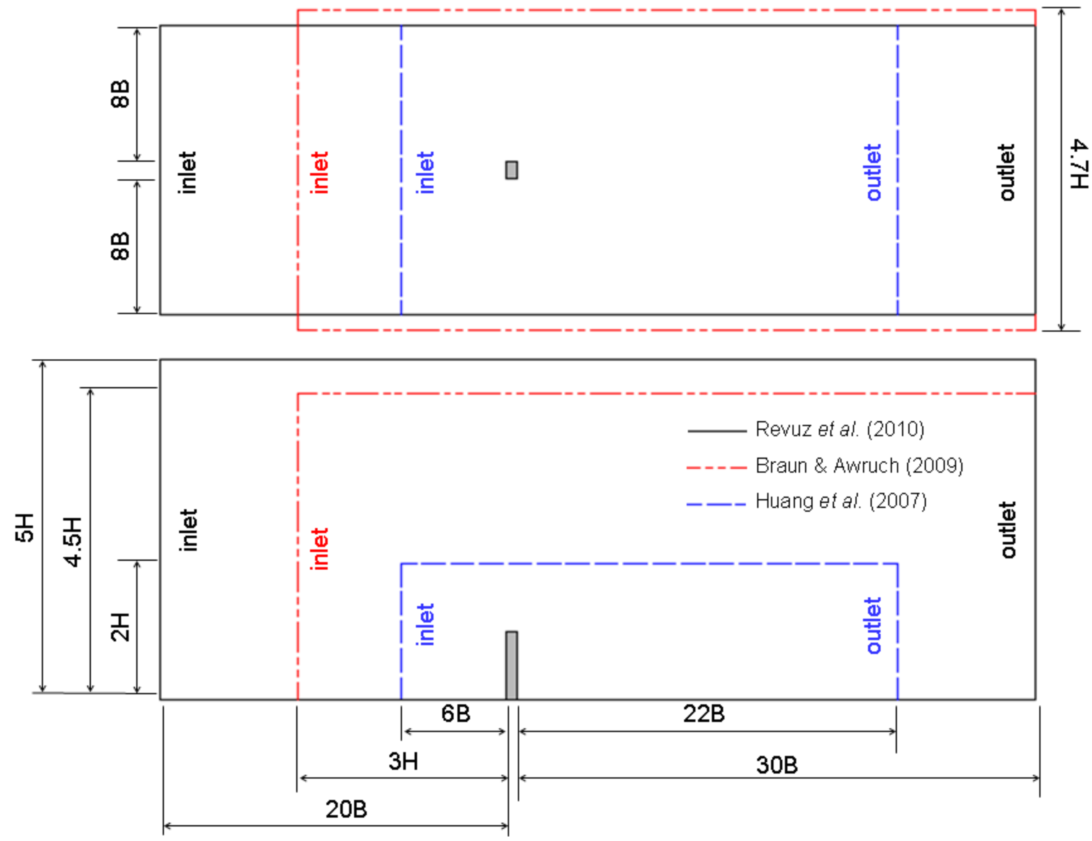

Figure 2.10. Comparison of CFD domain size for CAARC standard tall building

2.7.4 Suitability of CWE for Proposed Research

The current state-of-the-art CFD modelling methods are not in a position to replace traditional boundary layer wind tunnel testing as the primary load calculation method for structural engineering. However, the evidence from the literature suggests it can act as a complimentary tool – provided it is used within its capabilities. Cochran and Derickson (2011) conducted a historical review of the evolution of physical modelling and the current state of CWE. It was recommended that CWE should follow a similar economic and analytically rigorous path as wind tunnel testing so it can develop into a more predominant tool for wind-load assessment of buildings and structures. It is envisaged that this endeavour along with faster computers will eventually lead to CWE replacing physical scaled modelling of bluff bodies. It is apparent that CWE offers very promising potential for future improvements, and hence its progress should remain of great interest to structural wind engineers. It is this potential which has inspired the decision to implement CWE for the current research on PBWE of tall buildings.

The use of full LES demands a high computational cost and its implementation is likely to exceed the capabilities of industrial practices for many years. While it appears LES may offer the closest computational alternative to traditional wind tunnel testing, RANS is certainly the most practical in terms of computational requirements. By limiting RANS applications to mean alongwind loads, as recommended by AIJ, it is difficult to assess its value for tall building problems since it is the crosswind response that is so often critical. Nonetheless, the literature suggests that a statistically improved version of the k-ε or k-ω turbulence models which assume non-isotropic turbulence will produce the best RANS results for predicting flow features and surface pressure distributions.

A sufficient number of CFD simulations would be required to provide a probabilistic description of the PBWE building performance. The computational demand of the chosen turbulence model would have a significant bearing on the number of IM wind events that could be sampled within a practical time scale, and hence full LES may not be feasible. Perhaps the probabilistic nature of PBWE can accept the shortcomings related to CFD turbulence modelling, in particular those associated with the RANS method. However, the implications will have to be investigated.

2.8 Coupling Algorithms for Fluid-Structure Interaction

As stated in various Sections so far, a key component of the proposed PBWE framework involves creating an appropriate coupling interface to assist in the wind-structure interaction (IP) analyses. The requirement of the developed coupling algorithm is to appropriately consider the FSI phenomena involving the wind and the tall building during each IM wind event. It is intended that CFD techniques will be employed to model the wind actions and Computational Structural Mechanics (CSM) will predict the building response.

A range of different coupling algorithms are available for communicating between independent fluid and structural solvers and each has its own advantages and limitations. The coupling strategies are classified as monolithic, partitioned (or staggered) and one-way. No single coupling algorithm is ideally suited for all FSI problems; the choice depends on an appropriate level of detail and accuracy vs. uncertainty in a given simulation setting and has a significant impact on the computational demand. A basic illustrative representation of the various coupling algorithms is provided by Figure 2.11.

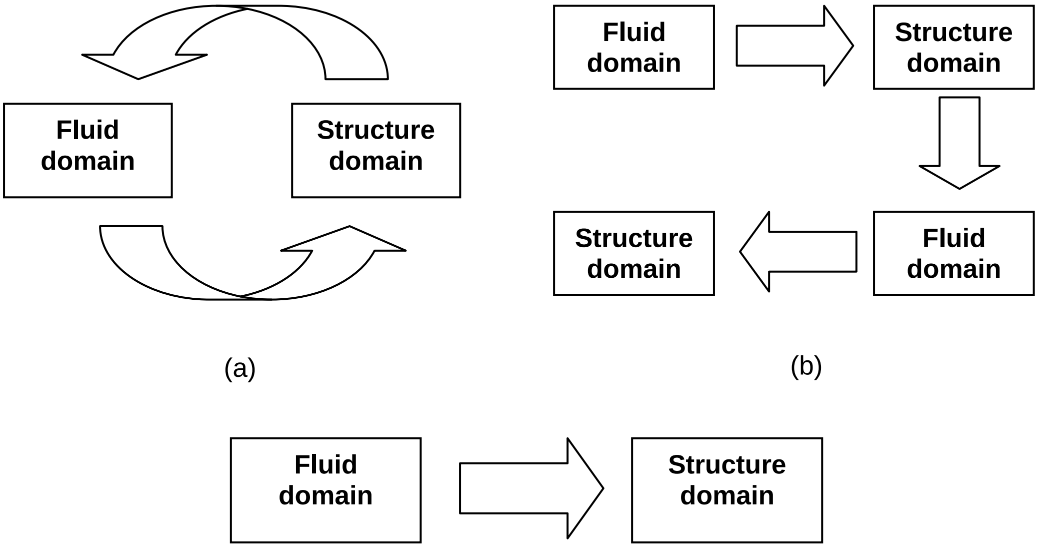

(a)

(b)

(c)

Figure 2.11. Coupling algorithms in FSI: (a) monolithic; (b) partitioned; and (c) one-way.

2.8.1 Monolithic Coupling

Monolithic coupling simultaneously discretises and solves the entire, fully coupled, set of fluid and structural governing equations within a single domain setting. Full aeroelastic effects can be considered so the assessment of the wind-induced building response would include the movement-induced excitation phenomena caused by the structural motion. However, this method is computationally very demanding and difficult to implement, particularly for multi-degree-of-freedom (MDOF) problems (Joosten, 2007). If the motion of the structure is δ_D and the dimension of the structure corresponding to this direction of motion is D then monolithic coupling is essential when $\delta_D / D \geq 1$. Examples of such engineering applications include the flutter stability assessment of a long-span bridge decks and the design of aircraft wings.

2.8.2 Partitioned Coupling

A partitioned approach independently solves each domain; it moves intermittently between the fluid and structural solver throughout the simulation. Coupling is achieved by specifying kinematic and dynamic continuity conditions between the mesh motions of each domain. The strength of coupling depends on the temporal discretisation and the number of iterations performed to achieve convergence at each transition. Such algorithms allow the use of discretisation and solution methods from well-established software for each solver (Matthies and Steindorf, 2002). The computational requirements, although still substantial, are less demanding than monolithic coupling. Lee *et al.* (2007) provide a recent example that shows it offers a great deal of potential for 2-D FSI problems. It has also displayed early signs of promise for complex 3-D FSI problems, such as the aeroelastic study by Braun and Awruch (2009) of the CAARC standard tall building using CFD for the fluid solver and FEM for the structural solver. However, Heil (2004) states that it is often difficult to ensure the overall stability and temporal convergence (sensitivity to the choice of the computational time-step size) of this method. This method is generally applied when $\delta_D / D < 1$.

2.8.3 One-Way Coupling

A one-way strategy is the simplest form of FSI coupling; it allows the fluid solver to predict a range of pressure histories before transferring these in a single step as a series of forcing functions for the structural solver to determine the dynamic response. The underlying assumption is the motion of the structure has a negligible effect on the flow pattern and thereby the algorithm does not account for aeroelastic instabilities. It must be assured that the effect of aeroelastic phenomena can be safely neglected or otherwise considered in the context of the simulation setting. This coupling method is suited to relatively stiff structures, where $\delta_D / D << 1$, and is similar to the high-frequency pressure integration technique performed in boundary layer wind tunnel experiments.

2.8.4 Coupling Algorithm for Proposed Simulation Setting

The need to simulate the IP for each of the IM wind events in the PBWE framework suggests the one-way coupling strategy is the most practical in terms of computational demand. Developing a more advanced coupling algorithm would quickly become a research objective in its own right. The one-way coupling algorithm is considered to provide adequate accuracy within the PBWE context, due to inherent complexities and uncertainties built into the more accurate coupling formats. In addition, the relative wind-induced motions of the tall buildings considered in the present study satisfy the $\delta_D / D << 1$ requirement. However, the extension of the proposed PBWE framework for the assessment of highly flexible structures such as long-span bridge decks would require an alternative coupling strategy, such as the 2-D discrete-vortex method implemented by Taylor and Vezza (2002).

2.9 Occupant Comfort Serviceability Criteria

Modern design trends and advances in engineering materials have encouraged the demand for taller, more slender buildings with low natural frequencies. This inherently flexible generation of structures are susceptible to wind-induced excitation (British Standards Institution, 1985). While lateral drift requirements may be satisfied, acceleration levels may be unacceptable (Breeze, 2011). Thus, the pertinent high performance level for PBWE of tall buildings is occupant comfort (Bashor *et al.,* 2005). The relevant DM for the PEER-based PBWE framework can therefore be set as unacceptable levels of building vibration for occupants due to excessive levels of acceleration as EDP parameters.

2.9.1 Uncertainties in Occupant Comfort Thresholds

Excessive levels of building vibration can initiate a range of human responses, from minor adverse comment to motion sickness (Taranath, 1998). The level of adverse comment depends on the return period between occurrences. Attaining such conditions would inevitably impair the occupants' working efficiency and quality of life. However, human perception and their subsequent response to wind-induced motion is essentially a subjective assessment that depends on many psychological and physiological factors. Thus, predicting occupant perception and comfort levels for a densely populated tall building becomes a difficult task. This introduces further uncertainties into tall building design and supports the development of the PBWE framework.

According to BS 6841:1987 (British Standards Institution, 1987), the relevant sources of uncertainty can be classified as either intrinsic or extrinsic. Intrinsic variables include population (age, gender, etc.), expectation and habituation, activities and building use, and body posture. Extrinsic variables relate to the wind-induced building vibration such as magnitude, frequency, duration, recurrence interval, and axis, as well as other environmental effects. The dependency of occupant comfort to these many factors means serviceability limits can never be precise (Breeze, 2011).

Studies on the influence of these uncertainties on human response to wind-induced motion are based on field experiments, surveys, motion simulators and shake table tests. Kwok *et al.* (2009) summarised past studies on human perception and occupant comfort to wind-induced vibration in tall buildings. Generally, young children are the most sensitive to vibration and male adults are the least sensitive. In addition, it was found that people are typically more sensitive to vibration when standing, as opposed to sitting or lying down.

2.9.2 Assessment Criteria for Occupant Comfort

At present, there are no universally accepted occupant comfort serviceability guidelines; this reflects the uncertainty and subjective nature of the problem. It is evident from the literature that perception of vibration is perhaps best related to the rate of change, or jerkiness, of acceleration (Bashor *et al.,* 2004). However, modern design guides typically describe satisfactory limits of wind-induced building vibration as a measure of either peak or RMS acceleration (Hicks and Devine, 2004). A basicentric co-ordinate system is commonly adopted to reference the acceleration vector, where the z-axis corresponds to the direction of the human spine (Figure 2.12). It should be noted that assessment criteria are traditionally expressed in a deterministic format (Kwok *et al.*, 2009).

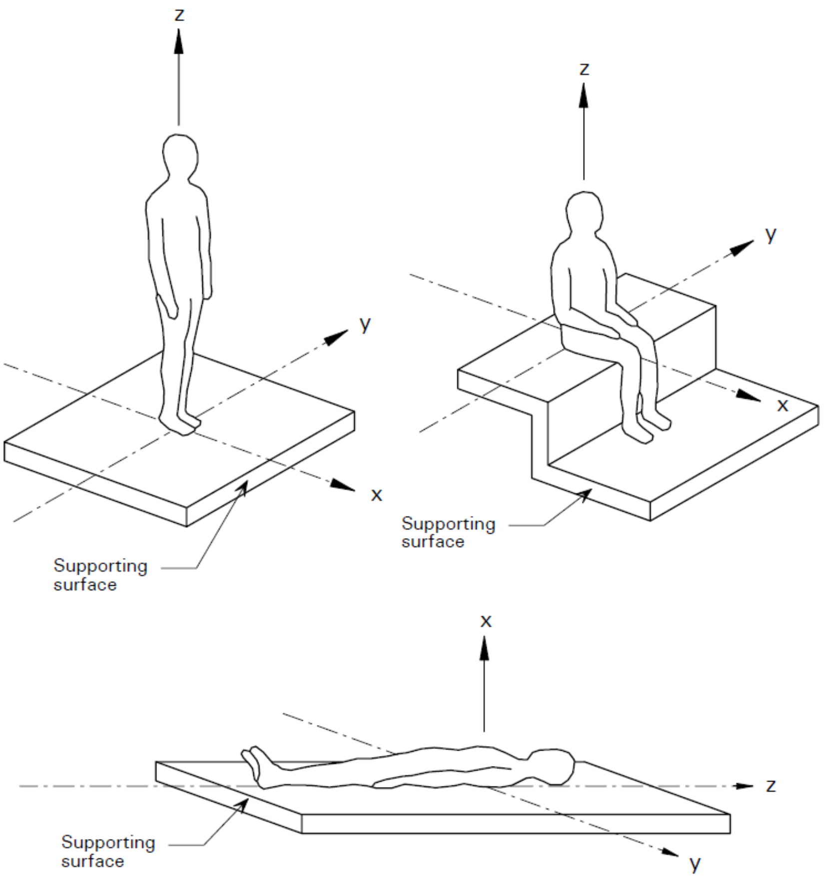

Figure 2.12. Basicentric coordinate system for vibration (Hicks and Devine, 2004)

The relevant British Standard for human response to low frequency (0.063 to 1 Hz) horizontal vibration events having duration in excess of 10 minutes is BS 6611:1985 (British Standards Institution, 1985). This falls into the fundamental frequencies of a tall building. The guide acknowledges the sensitivity of human perception to even small rotational oscillations about the vertical axis. However, it assumes that the perception of motion is initiated through sense or balance rather than visual or acoustic cues. This limitation indicates the difficulty in quantifying the influence of noise and torsional building response.

The response thresholds to wind-induced vibration are expressed in terms of frequency-dependent RMS acceleration limits for the worst 10 consecutive minutes of a wind storm with a return period of at least 5 years. The limits are specified with the intention that probably not more than 2% of the occupants on the levels undergoing the most extreme wind-induced vibration would comment adversely about the motion. It tentatively suggests that levels for a recurrence interval of one year can be obtained by applying a factor of 0.72 to the provided five year limits. This guidance is technically equivalent to ISO 6897:1984 (International Organization for Standardization, 1984). The only difference is that BS 6611:1985 refers to BS 6472 (British Standards Institution, 2008) for horizontal motion at frequencies greater than 1 Hz, while ISO 6897:1984 links to the corresponding parts of ISO 2631 (International Organization for Standardization, 1997).

In addition, the work of Melbourne and Palmer (1992) stands as one of the most commonly used criteria in UK Wind Engineering (Breeze, 2011). This research transformed the underlying methodology of BS 6611:1985. It stated that the design criteria for occupant comfort in tall buildings should be based on peak acceleration rather than RMS. The derived peak threshold acceleration, a_{peak}, was given as:

$$a_{peak} = \sqrt{2\ln nT}\left(0.68 + \frac{\ln R}{5}\right)\exp\left(-3.65 - 0.41\ln n\right) \qquad (2.10)$$

where *T* is the time duration of the event (normally 600 s), *R* is the return period in years and *n* is the natural frequency of the building in Hz.

These peak acceleration limits for a range of return periods are shown in Figure 2.13. The one and five year curves of satisfactory magnitudes of RMS acceleration for discrete frequency horizontal motion of general structures recommended by BS 6611:1985 are also illustrated. It should be noted that the limitations of BS 6611:1985 regarding the effects of torsion and noise were not specifically addressed.

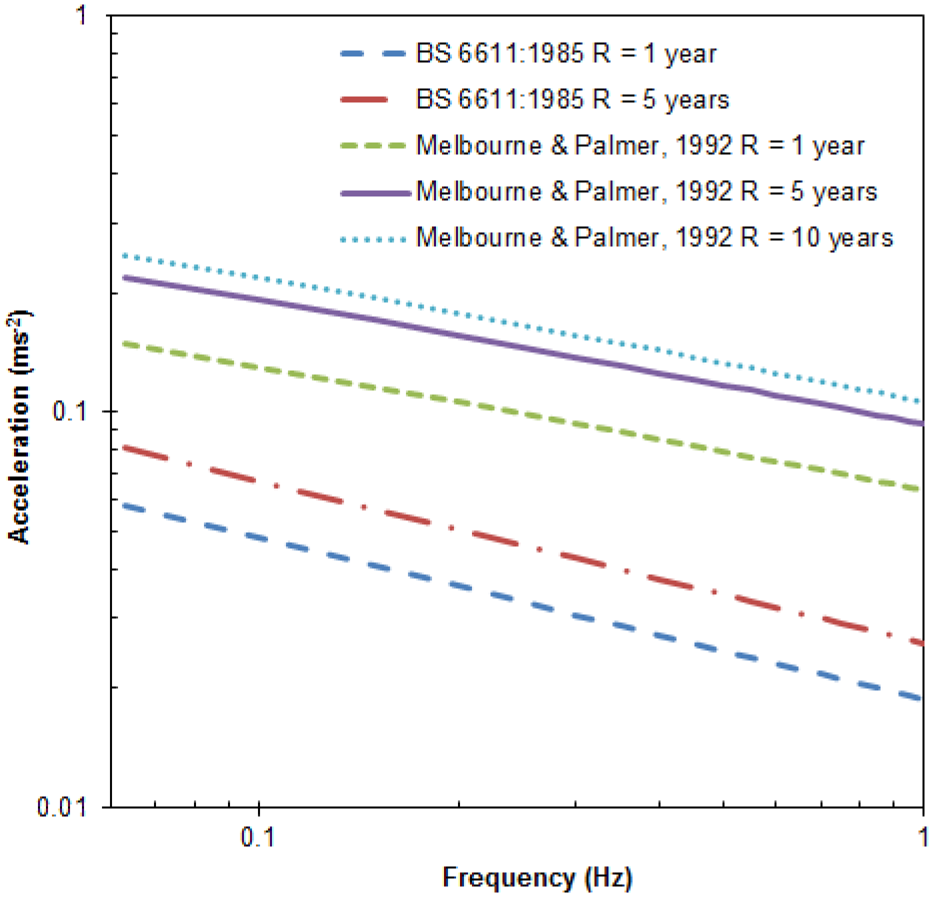

Figure 2.13. Horizontal motion limits for general buildings.

The discrepancy among the assessment criteria from various international codes of practice and guidelines was demonstrated by Kwok *et al.* (2009) for a one-year return period and is reproduced in Figure 2.14. The values were expressed in terms of peak accelerations. Therefore, the adjusted curve given for ISO 6897:1984 essentially became the Melbourne and Palmer

(1992) recommendations. It can be seen that some of the recommendations differentiate between office and residential building use, while others are based on duration of event.

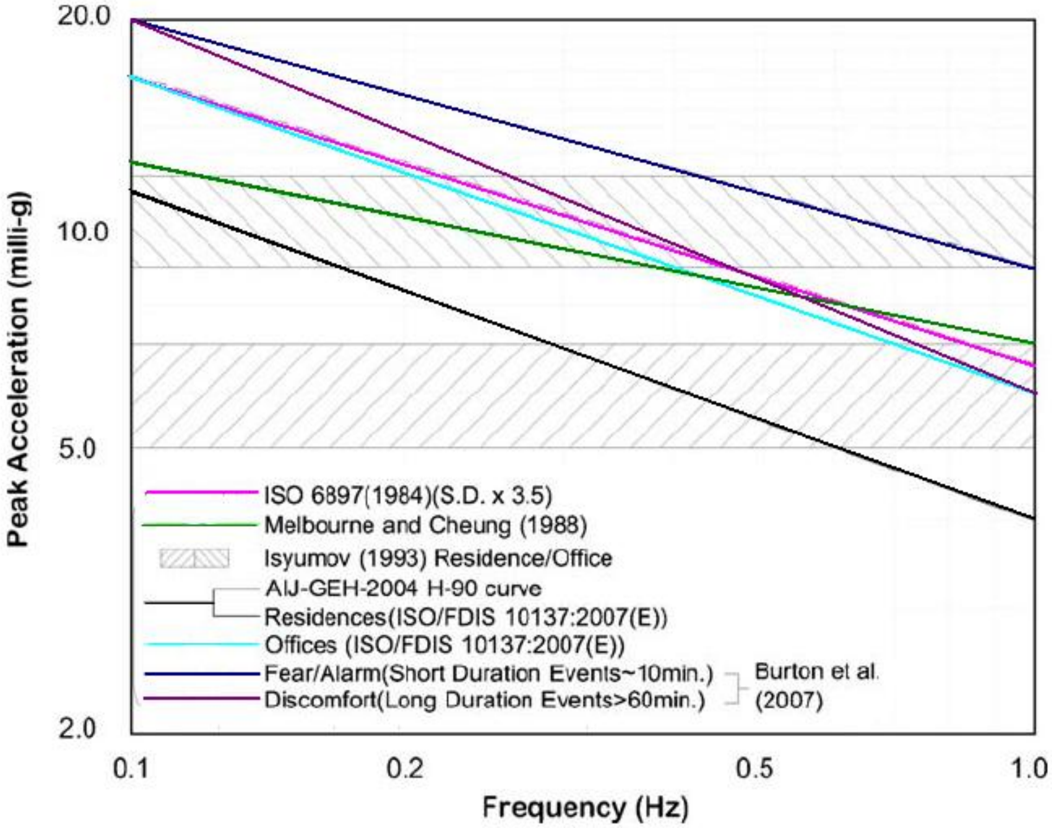

Figure 2.14. Comparison of occupant comfort serviceability criteria for a one-year return period wind storm (Kwok *et al.*, 2009)

This uncertainty was recognised in the design of the Chicago Spire (Morava *et al.,* 2010). Consequently, a full-scale show apartment was built on hydraulic pistons. This multi-degree-of-freedom motion simulator was used to represent several levels throughout the building height and the excitation input was determined by wind tunnel models. This alleviated the need for codified comfort criteria by allowing the owners to have a direct experience of the likely wind-induced motions and form their own judgements. However, this is a very impractical and costly alternative solution for tall building design.

2.10 Concluding Remarks

The Chapter has reviewed the various uncertainties associated with Wind Engineering of tall buildings. The probabilistic context of Performance-Based Design (PBD) is well suited to handle these uncertainties. Recent advances in Performance-Based Wind Engineering (PBWE) have been detailed, with particular focus on the robust and effective framework developed by the Pacific Earthquake Engineering Research Centre (PEER). The weaknesses from previous PBWE research using the PEER framework have been related to the representation of the Intensity Measure and Interaction Parameter components. The present research aims to improve these components by introducing advanced simulation techniques. However, it must be ensured that the chosen techniques provide an appropriate level of accuracy.

Based on current state-of-the-art, wind tunnel testing undoubtedly offers the most accurate modelling alternative to full-scale measurements. Nonetheless, the flexibility and potential of Computational Wind Engineering (CWE) suggest it can be feasibly used for the proposed PBWE framework. While CWE is not in a position to replace traditional wind tunnel testing, the evidence in the literature suggests it can be used as a complimentary tool – provided its limitations are understood. The most important modelling criterion appears to be related to the turbulence model chosen for the CFD simulations. An extensive CFD validation exercise would provide a better understanding of the capabilities and limitations of leading RANS and LES turbulence models in the context of the present study. This would clarify the uncertainty regarding the performance of CWE turbulence models for full-scale, high Reynolds number flows. In addition, it would quantify the CPU cost of the LES model in relation to the available computational power, which is still expected to be too impractical.

A one-way coupling algorithm is considered to provide adequate accuracy for CWE within the PBWE context. This method is similar to the high-frequency pressure integration technique performed in wind tunnel experiments. However, the proposed coupling algorithm assumes that aeroelastic effects are negligible, which is clearly not suitable for extremely flexible structures. The wind-induced motion of the considered tall buildings for the PBWE framework must satisfy this assumption.

It is apparent that the development of international occupant comfort serviceability criteria is a practical need. Until this need is addressed it offers a problem for readily specifying DM performance levels for the probabilistic PBWE framework. In the meantime, a more rational approach, as implied by Paulotto *et al.* (2004), will have to suffice. An example of such an assessment method was applied by van de Lindt and Dao (2009). A limiting performance value was specified for a range of damage states for low-rise wood-frame buildings. The performance expectation was that the exceedance (or failure) probability from the fragility curve of each damage state was less than 50%. A similar strategy should be implemented for the proposed PBWE framework using a selection of comfort thresholds with different return periods.

3

Overview of PBWE Methodology

3.1 Preamble

This Chapter summarises the methodology implemented to satisfy the research aim. The probabilistic PBWE framework for tall building design adapts the PEER-based PBWE methodology discussed in Section 2.4. The five main analysis steps are reproduced in Figure 3.1. Throughout the Chapter, the function of each step in the context of the research on tall buildings is discussed. The primary focus is to introduce advanced simulation techniques to address the weaknesses encountered in previous studies. The CWE techniques, using Computational Fluid Dynamics (CFD) and Computational Structural Mechanics (CSM), are incorporated into the PBWE framework. It is anticipated that these techniques will improve the characterisation of both the Intensity Measure (IM) wind events and the Interaction Parameter (IP) phenomena to provide a better prediction of the Engineering Demand Parameter (EDP) building response. Therefore, greater attention is concentrated on the relevant stages of the procedure, namely Hazard Analysis and Interaction Analysis. The Damage Analysis and Loss Analysis stages are discussed to a lesser extent. The Chapter concludes by introducing two contrasting tall building designs which will be assessed by the proposed PBWE framework.

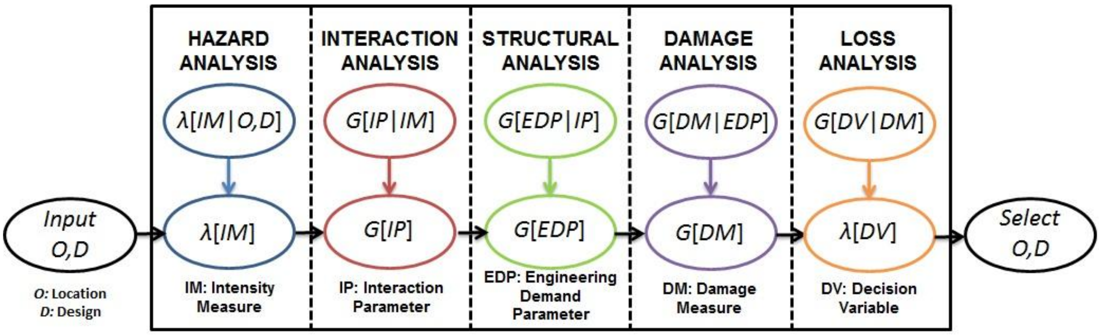

Figure 3.1. Proposed research procedure for PBWE of tall buildings

3.2 Hazard Analysis

3.2.1 Proposed Site Location

The Hazard Analysis determines the IM wind events and is fundamentally dependent on the site location for the considered tall building design. Therefore, it is assumed for the purpose of characterising a representative wind environment that the proposed tall building case studies are located in Glasgow, Scotland. The roughness category, as classified by NA to BS EN 1991-1-4:2005 (British Standards Institution, 2008a), is town terrain (Category III). The shortest upwind distance to the shoreline is approximately 50 kilometres, while the distance inside town is taken as 10 kilometres.

3.2.2 Considered Variables

The mean velocity and turbulence characteristics of the IM wind events consider two variables: the basic mean wind velocity, v_b, and the aerodynamic roughness length, z_0. The basic mean wind velocity corresponds to the 10-minute mean wind speed measured in country terrain at an elevation of 10 metres. The aerodynamic roughness length characterises the roughness for the considered town terrain at the proposed site in Glasgow. The description of the wind field in Section 3.2.4 accounts for the transition in v_b from country to town terrain. It should be noted that considering z_0 as an additional variable addresses the shortcomings of the PBWE study by Petrini *et al.* (2009), discussed in Section 2.4.2. This can account for both the uncertainty in the initial estimation of z_0 and the potential changes in the z_0 value throughout the design life of the tall building.

Basic Mean Wind Velocity, v_b

The extreme basic mean wind velocity for sites in the UK conform to a Fisher-Tippet Type I (FTI) probability distribution (Cook, 1982), as given by Equations 2.1 and 2.2. The use of these equations requires the input of the mode and dispersion parameters for the considered location. The procedure for determining the mode and dispersion for the Glasgow site utilises the information given by the UK National Annex to BS EN 1991-1-4:2005 (British Standards Institution, 2008a). This document provides a basic wind velocity map of the UK, shown in Figure 3.2, based on the Meteorological Office records mentioned in Section 2.2.1. The provided v_b values refer to country terrain at a height 10-metres above the ground.

In addition, the mapped velocities are estimated to have the annual risk of exceedance, $Q = 0.02$. This can be translated as having a return period of 50 years. The National Annex states that the mapped values can be adjusted to determine any other annual exceedance by applying the following probability factor, c_{prob}.

$$c_{prob} = \left[\frac{1 - 0.2\ln[-\ln(1-Q)]}{1 - 0.2\ln(-\ln 0.98)} \right]^{0.5} \tag{3.1}$$

where Q is the desired annual risk of exceedance for the wind event.

Although based on the FTI distribution theory, this equation does not directly deduce the mode and dispersion parameters required by the present study. Therefore, it is used to determine v_b for a substantial range of exceedance probabilities to plot the cumulative distribution function of v_b for the considered location. A best-fit analysis in MATLAB then determines the specific values of the dispersion and the mode. This full procedure is realised in Chapter 5.

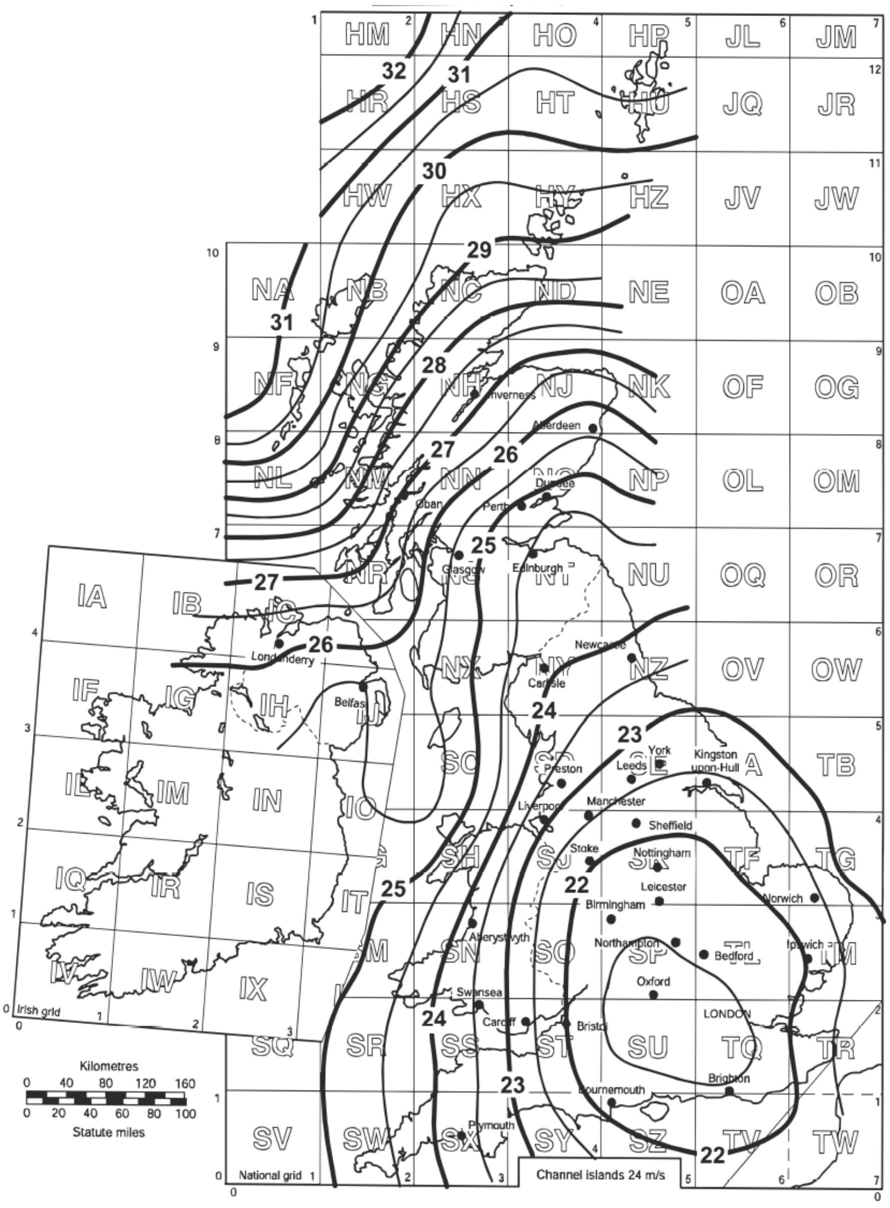

Figure 3.2. Basic 10-minute mean wind velocity $v_{b,map}$ (ms^{-1}) before altitude correction (British Standards Institution, 2008a)

Aerodynamic Roughness Length, z_0

The uncertainty in the aerodynamic roughness length is represented by a standard Gaussian probability distribution. The probability density function, $p(z_0)$, is a symmetrical distribution about a single peak and is expressed by

$$p(z_0) = \frac{1}{\sqrt{2\pi\sigma^2}} \exp\left[\frac{-(z_0 - \overline{z_0})^2}{2\sigma^2}\right] \qquad (3.2)$$

where $\overline{z_0}$ is the mean value and σ^2 is the variance of the spread. The mean corresponds to the peak of the distribution. The value of z_0 for typical town terrains is 0.3 m (British Standards Institution, 2002), and hence it is appropriate that this acts as the mean of the distribution. Meanwhile, ESDU 82026 (Engineering Sciences Data Unit, 2002a) suggests upper and lower limits for town terrains of 0.4 m and 0.2 m, respectively. The variance is enclosed between 0.2 m and 0.4 m, specified to ensure at least 97.5% probability.

3.2.3 Sampling Method

An appropriate sampling method is implemented to derive the variable combinations of v_b and z_0 for characterising the IM wind events. Common sampling techniques such as the First-Order Second-Moment (FOSM) method (Zhao and Ono, 2001) and Monte Carlo method (Lu and Zhang, 2003) are unsuitable for the proposed framework since they rely on hundreds, or even thousands, of repeated random samples to compute their results. This is impractical for this proposed PBWE framework since each IM sample would have to be modelled in separate CFD simulations. Therefore, the focus must be on generating the minimum amount of feasible samples which still provide a sufficient representation of the probability distributions.

Latin hypercube sampling (LHS) offers an efficient alternative sampling method which is well suited to the requirements of this project (Olsson *et al.*, 2003). The Latin hypercube is an arbitrary-dimensional sampling space based on the number of variables. If K represents the number of variables then the sampling space is K-dimensional. The probability distributions of each variable are divided into N equally probable intervals, where N denotes the required number of samples, or realisations. The discretised sampling space then becomes a K-dimensional grid. The basic principle is that only one sample is taken within the axis-aligned hyperplane containing it.

An example sampling process for LHS is shown in Figure 3.3 for two input variables (K = 2) and five realisations (N = 5). An initial N x K matrix P is formed, where each column of the matrix is a random permutation of whole numbers from 1 to *N.* This represents the first discretisation process and its effect on the sampling space is shown in Figure 3.3(a). An N x K matrix R of random numbers from the uniform (0,1) distribution is then created. The specific samples are obtained from the P sampling space by using the corresponding random R matrix number as a fraction indicator of where the point lies between the lower and upper limits of the considered sampling cell. This forms the final S sampling space which is illustrated in Figure 3.3(b).

A similar LHS procedure is followed for the Hazard Analysis of the proposed PBWE framework. Two variables (v_b and z_0) are considered (K = 2) and the chosen number of realisations is ten (N = 10). This determines the parametric combinations of v_b and z_0 used to characterise the IM wind events. It is acknowledged that an increased number of realisations would provide a better description of the probability distributions. However, the computational cost associated with CFD is such that it is completely impractical to simulate a higher number of sampled IM wind events.

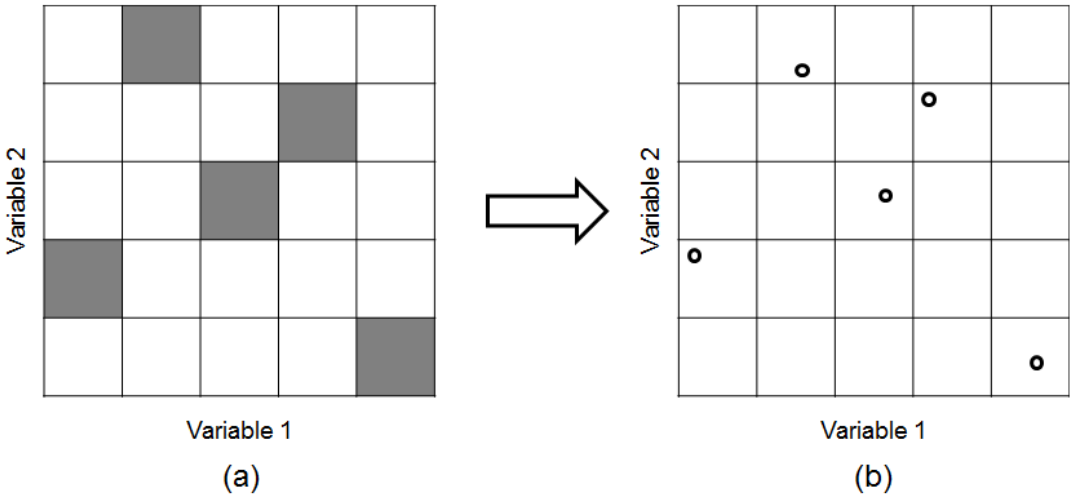

Figure 3.3. Latin hypercube discretisation process for two variables (K = 2) and five samples (N = 5), where (a) is P sampling space and (b) is S sampling space.

3.2.4 Description of Wind Field

The minimum input criteria required by CFD to sufficiently model the atmospheric boundary layer (ABL) wind field are based on the mean wind velocity, turbulence intensity and turbulence length scale. Therefore, the vertical variation of these parameters is characterised for each IM wind event using engineering models and the associated values of basic variables v_b and z_0. The turbulence intensity is a measure of the magnitude of the fluctuating velocity component compared to the mean wind velocity at the same elevation. The turbulence length scale is a characteristic to describe the size of the turbulent eddies (Wilcox, 2002).

The vertical profile of the mean velocity is determined using the ESDU 82026 (Engineering Sciences Data Unit) recommendations. The profile is based on the popular logarithmic law but it can incorporate step changes in terrain roughness upwind of the site. In its simplest form, the vertical profile of the mean wind speed is derived by

$$V_z = 2.5u_* \left[\ln\frac{(z-d)}{z_0} + \frac{34.5fz}{u_*} \right] \cdot K_x \tag{3.3}$$

The term u_* is the frictional velocity. The Coriolis parameter, f, is due to the rotation of the earth and is calculated from $f = 2\Omega\sin\varphi$, where $\Omega = 72.9 \times 10^{-6}$ rad/s is the angular velocity of the earth and the local angle of latitude, φ, for Glasgow is 0.975 radians. Therefore, the Coriolis parameter for Glasgow is 1.2×10^{-4} rad/s. The zero-plane displacement height d is the depth of the ABL interfacial layer, i.e., the region occupied by the dominant site features. For the built environment, the thickness of d depends on the average height and the plan-area density of the buildings. The typical value for built-up town terrain is between 15 to 25 m (Engineering Sciences Data Unit, 2002a). The K_x factor adjusts the equilibrium ABL for the site to account for the transition due to the upwind step change in terrain roughness. The PBWE study considers a single step change in roughness from open country (z_0 = 0.03 m) to town terrain. The open country terrain represents the location where the variable v_b was measured and the variable z_0 refers to the town terrain at the site.

The turbulence intensity and length scale are derived from ESDU 85020 (Engineering Sciences Data Unit, 2001). The streamwise turbulence intensity I_u is calculated from

$$I_u = \frac{\sigma_u}{u_*} \cdot \frac{u_*}{V_z} = \frac{7.5\eta\left[0.538 + 0.09\ln(z/z_0)\right]^p}{1 + 0.156\ln(u_*/(fz_0))} \cdot \frac{u_*}{V_z} \tag{3.4}$$

where $\eta = 1 - 6fz/u_*$ and $p = \eta^{16}$.

Meanwhile, the approximate expression for the integral length scale ${}^xL_u$ for heights up to about 300 m is given as

$${}^xL_u = \frac{A^{3/2}(\sigma_u/u_*)^3 z}{2.5K_z^{3/2}(1 - z/h)^2(1 + 5.75z/h)} \tag{3.5}$$

where $$A = 0.115\left[1 + 0.315(1 - z/h)^6\right]^{2/3} \tag{3.6}$$

and $$K_z = 0.188\left[1 - \left(1 - \frac{z}{0.39h(u_*/(fz_0))^{-1/8}}\right)^2\right]^{1/2} \tag{3.7}$$

In the above expressions, the gradient height is calculated from $h = f/6u_*$.

3.3 Interaction Analysis

3.3.1 CFD Simulations

The CFD simulations are performed using the latest version of the commercial CFD package ANSYS FLUENT (ANSYS Inc, 2009a, 2009b). This software uses the finite volume method to solve the governing integral equations. The CFD models have grids containing millions of computational cells. Therefore, the transient simulations are run on the University of Strathclyde High Performance Computing (HPC) facility. The CFD software offers an automatic partitioning feature which enables efficient parallel processing. A total of 8 CPUs are used in parallel for the simulations. The CPUs have 2.93 GHz Intel Xeon X5570 quad-core processors and each node has 12 GB of RAM. This state-of-the-art HPC has 1088 cores (i.e.

CPUs) available to users. As each core requires its own ANSYS FLUENT software license, a fair-use policy restricts the amount of CPUs that can be used for the CFD simulations.

An extensive CFD validation study is initially performed to identify the modelling requirements for the pressure-based solver. This begins with a series of empty channel studies to monitor the ABL wind characteristics. The simulations are then extended to include the CAARC tall building as an obstacle in the domain. The predicted flow patterns and wind loads are assessed. This validation exercise investigates the performance of the leading RANS and LES turbulence models and assesses the sensitivity of the results to parameters such as mesh, time-step, domain size and boundary conditions. The detailed procedure is documented in Chapter 4.

The derived modelling techniques from the validation study are then implemented for separate CFD simulations of each IM wind event from the Hazard Analysis. The characterised ABL mean wind velocity and turbulence profiles are written in C programming language as user defined functions (UDF) to be interpreted into FLUENT and used as the inlet boundary conditions. The wind characteristics are monitored at various locations throughout the domain during each simulation. In addition, a series of pressure monitors are created across the envelope of the tall building. The transient pressure histories are recorded throughout the simulations and written to an external data output file. Due to the computational costs of CFD, the PBWE assessments of the two tall building case studies only consider a single incident wind direction. The angle of attack is parallel to the most flexible axis of the structure, i.e., in the direction of the fundamental mode of vibration.

3.3.2 CSM Simulations

The analysis of the EDP structural response is predicted using the finite element (FE) method in Strand7 (Strand7, 2005a). These simulations are run on a standard desktop PC with a 3.00 GHz Intel Pentium D dual-core processor and 3.49 GB of RAM. Detailed multi-degree-of-freedom FE models of the tall building case studies are created by following the successful modelling techniques applied by Kim *et al.* (2009), discussed in Section 2.2.2. The components of the primary structure are explicitly modelled using a combination of beam and plate elements. The mesh specification is such that it optimises the computational efficiency without compromising the accuracy of the results.

The natural frequency solver uses the Sub-Space Iteration Method to derive the first *N* natural frequencies and corresponding mode shapes for the undamped structural system of the modelled tall building. It is important to ensure that all the eigenvalues converge to the specified tolerance. These eigenvalues are required for the linear transient dynamic solver.

The linear transient dynamic solver uses the modal superposition method to predict the wind-induced EDP building response for individual modes of vibration. Modal superposition is chosen instead of full system direct time integration to optimise the computational efficiency. The full system method integrates all nodal displacements at each time step. The computational cost would be extremely high if it is used for the proposed FE tall building models with thousands of nodes. The choice of the correct time step is essential to ensure that the full response of the structure is captured and the solution is numerically stable, i.e., free from divergence.

The Rayleigh damping method is implemented to derive the modal damping ratios. Chopra (2007) stated that in most cases it provides an efficient and straightforward method of modelling damping. The damping matrix [C] is assumed to be a linear combination of the mass [M] and stiffness [K] matrices of the form $[C] = \alpha[M] + \beta[K]$. The relationship between α and β and the frequency dependent damping ratio ζ is given by

$$\zeta = \frac{1}{2}\left(\frac{\alpha}{\omega} + \beta\omega\right) \tag{3.8}$$

where ζ is the critical damping ratio at frequency ω, while α and β are the stiffness and mass proportional constants, respectively. They are determined from the following equations

$$\alpha = \frac{2\omega_1\omega_2\left(\zeta_2\omega_1 - \zeta_1\omega_2\right)}{\left(\omega_1^2 - \omega_2^2\right)} \tag{3.9}$$

$$\beta = \frac{2\left(\zeta_1\omega_1 - \zeta_2\omega_2\right)}{\left(\omega_1^2 - \omega_2^2\right)} \tag{3.10}$$

To minimise error, the ω_1 and ω_2 frequencies used to characterise these damping factors are typically the lower and upper natural frequencies of the tall building that are explicitly considered in the dynamic analysis. However, the corresponding damping ratios must also be specified.

The informative Annex F of BS EN 1991-1-4:2005 (British Standards Institution, 2005) provides recommended approximate damping values for the fundamental mode of vibration for buildings and structures. The value is simply determined from the structural type and does not depend on height or vibration amplitude. For reinforced concrete buildings the damping ratio is 1.59% of critical, while for steel buildings a lower value of 0.80% is advised. However, it was demonstrated by Allsop (2009a) that these provided damping values are not always conservative. Therefore, adopting these values for dynamically sensitive tall buildings is best avoided.

ESDU 83009 (Engineering Sciences Data Unit, 1990) provides a relatively simple damping model which can be used for the assessment of the wind-induced response of tall buildings. The structural damping ratio (ζ_s) for the fundamental mode of vibration is expressed as

$$\left(\zeta_s\right) = \left(\zeta_{so}\right) + \left(\zeta'_s\right)\frac{x_H}{H} \tag{3.11}$$

The first component (ζ_{so}) is the nominal damping component provided at very small displacement amplitudes. The term (ζ'_s) represents the rate of increase of structural damping with x_H/H, where x_H is the single peak resonant displacement amplitude and *H* is the building height. This more theoretical approach is used to determine the fundamental damping ratio of the tall building case studies.

3.3.3 Coupling Interface

It was identified in Section 2.8 that a one-way coupling interface will suffice for the proposed PBWE framework for tall building assessment. This is developed as part of this research using the Visual Basic Application (VBA) code in Microsoft Excel. The VBA code is established for the interaction analysis to communicate the predicted wind actions from the CFD solution in ANSYS FLUENT into the CSM domain in Strand7.

The procedure of the one-way coupling algorithm for each IM is very similar to the high-frequency pressure integration (HFPI) technique in wind tunnel testing (Irwin, 2009). The array of pressure monitors around the building envelope in the CFD computational model writes the transient wind loads to individual output files. The VBA code post-processes and transfers these external CFD files as time-history forcing functions for the EDP analyses in Strand7. A beneficial feature of Strand7 is its Application Programming Interface (API). The API consists of a Dynamic Link Library (DLL) and a number of Header files and Include files (Strand7, 2005b). The DLL contains a number of functions that allows the Microsoft VBA coupling algorithm to execute a range of pre- and post-processing commands. The VBA subroutines specify the required linear transient dynamic solver settings and initiate the solver. Upon completion of the analysis the VBA code exports the nodal acceleration histories on the top floor for statistical post-processing.

This coupling process is repeated for all of the interaction parameter (IP) wind loading events associated with the sampled IM wind events. The conditional probability of the peak EDP top floor acceleration is related to the corresponding IM wind event. The derived EDP cumulative distribution function, or fragility curve, can then be compared against the specified DM performance expectation level to assess the adequacy of the design.

3.4 Damage Analysis

The performance expectation levels are specified for occupant comfort. The uncertainties regarding this subject have been discussed in Section 2.9. The present study does not intend to offer a solution to resolve the need for universally accepted occupant comfort criteria. Instead, a rational, if somewhat crude, approach is used to assess the adequacy of the tall building design. The Melbourne and Palmer (1992) equation, given by Equation 2.10, is used to determine the peak acceleration limits for three return periods. For the purposes of the PBWE framework, it is considered that each return period can be associated with a different Damage Measure, which is subsequently assigned a suitable limiting exceedance probability.

The Damage Measures are concerned with different levels of complaint from the building occupants, classified as: (a) minor complaint; (b) moderate complaint; and (c) major complaint. It is assumed that the PBWE framework is being implemented for office buildings. In this context, ‘minor complaint’ refers to occupants on the top floor of the building perceiving the vibration and commenting adversely about it. ‘Moderate complaint’ describes a situation where the occupants on the top floor begin to feel nauseous as a result of the wind-induced vibration levels and cannot (or refuse to) work under such conditions. Lastly, ‘major complaint’ is an extreme case that, when exceeded, induces a sense of panic for the occupants and causes them to vacate the building.

The performance criteria proposed for the Damage Analysis stage of the PBWE framework are specified in Table 3.1. The final probabilistic fragility curve of the EDP peak top floor acceleration is checked for each Damage Measure to determine the adequacy of the tall building design. This procedure is similar in principle to that implemented by van de Lindt and Dao (2009). However, their framework was developed to assess structural damage of wood-frame low-rise buildings due to wind loading; the performance criteria were related to the strength capacity of different components of the structure. Therefore, it did not involve the same level of uncertainty as occupant comfort to wind-induced vibration.

Table 3.1 Damage Measures and performance expectations for PBWE Damage Analysis

Damage Measure	Return Period	Limiting Probability
Minor Complaint	5 year	20%
Moderate Complaint	20 year	5%
Major Complaint	50 year	2%

3.5 Loss Analysis

The losses from wind damage to buildings can arise from replacing structural or non-structural components, reduced building tenancy with potential legal implications, loss of operation, loss of production, drop in property valuation, installation of mitigation measures and, in the worst instance, loss of human life. As an example, consider the potential losses emanating from wind-induced damage to the cladding of a building. The external appearance of tall buildings has evolved over the past decade, with louvers, double-skin façades and even mechanically operated sunshades becoming defining features of modern skyscrapers. These systems are often more expensive than the cost of the primary structure itself. If one or more of these cladding elements experience wind damage then the immediate direct loss would be the replacement cost. In addition, if the installation required part or full closure of the building then (depending on the building use) there is the additional cost from business interruption losses, or similar. Finally, if the cladding element detached and fell from the building then it could potentially land on a member of the public, causing serious injury or death. This last event would have major consequences.

Building insurers should be responsible for collecting and providing quantitative losses to buildings from wind damage. Whilst this has become common practice in Seismic Engineering, there is no evidence to suggest it is conducted for Wind Engineering. The current state-of-the-art is the HAZUS multi-hazard loss estimation document (HAZUS, 2012) produced by the Federal Emergency Management Agency (FEMA). The document provides a methodology to produce loss estimates for use by federal state, regional or local governments in planning for risk mitigation from earthquakes, floods and hurricanes. However, hurricanes and other tropical storms are far more intense than the frontal depressions in the UK, so the losses given in HAZUS (2012) are generally for more severe damages than would be incurred in the UK. Nonetheless, the basic principles of its Business Interruption Model have been adapted to suit this proposed PBWE framework.

The losses emanating from the ‘minor complaint’ damage measure would be small. This is a minimum performance expectation to provide a pleasant working environment for the occupants. Exceeding this damage measure may slightly impair occupants’ working efficiency but the consequences would not be very significant. A 20% probability of exceedance has been specified for this damage measure.

It is likely that the minimum losses incurred from the ‘moderate complaint’ damage measure would be the costs to cover the time of those occupants who could not work due to the level of wind-induced vibration. If, for example, the building tenant was a global engineering consultancy, then the costs would be based on the company overhead rate for their employees. There may also be additional compensation costs to the employee(s) who were adversely affected. A 5% probability of exceedance has been specified for this damage measure.

A major increase in losses could be expected from the ‘major complaint’ damage measure. If the upper levels of the building were evacuated then the costs to cover the lost time of the employees would also be incurred, but at a much larger scale. A safety inspection of the building post-evacuation may increase the business interruption to a couple of days. Such a scenario is likely to involve legal implications and a substantial compensation payment to the tenant company; they may lose work to competitors during the business interruption that cannot be recovered. A 2% probability of exceedance has been specified for this most severe damage measure.

3.6 Tall Building Case Studies

This enhanced PBWE framework is implemented to assess two alternative tall building office designs. The two 49-storey structures have similar primary structural bracing systems for resisting lateral loads. This is provided by a concrete core, incorporating the services, lifts and stairs, and perimeter columns. The storey levels directly correspond between the two designs throughout their 180-metre building heights; the typical floor heights range between 3.5 metres and 4 metres. Two 7-metre outrigger levels are present on the 11th and 30th floors to increase the lateral stiffness. The distinct contrast between these two tall building designs is the geometric shape of their cross-sections. The first design has a regular rectangular cross-section, while the other has an irregular L-shape cross-section. Consequently, these designs offer an interesting contrast in building aerodynamics and wind-induced response.

Structural members are designed to furnish approximately equal fundamental natural frequencies for the two tall building forms, while still satisfying the BS EN 1992-1-1:2004 (British Standards Institution, 2004a) code of practice criteria. This provides a useful benchmark to compare the wind-induced dynamic response of the two structures.

3.6.1 Regular Tall Building

The basic geometry of the regular tall building is based on the dimensions of the CAARC standard tall building (Obasju, 1992). This seemed a logical decision as it offered a continuation of the initial CFD validation study in Chapter 4. There is little information disclosed in the literature regarding the original steel building design, except that it provides a fundamental natural frequency of 0.2 Hz. Therefore, the primary structure was changed to the concrete design mentioned at the beginning of the Section. The typical 45 m x 30 m floor plan of this new design is shown in Figure 3.4, which clearly illustrates the core and column grid. This layout was based on satisfying an initial target efficiency ratio (net floor area / gross floor area) of 80%.

In addition, Figure 3.4 indicates the relevant angle of attack of the incident wind field that is considered for the PBWE assessment. This is parallel to the most flexible plane of the structure. The results of this PBWE study are documented in Chapter 6.

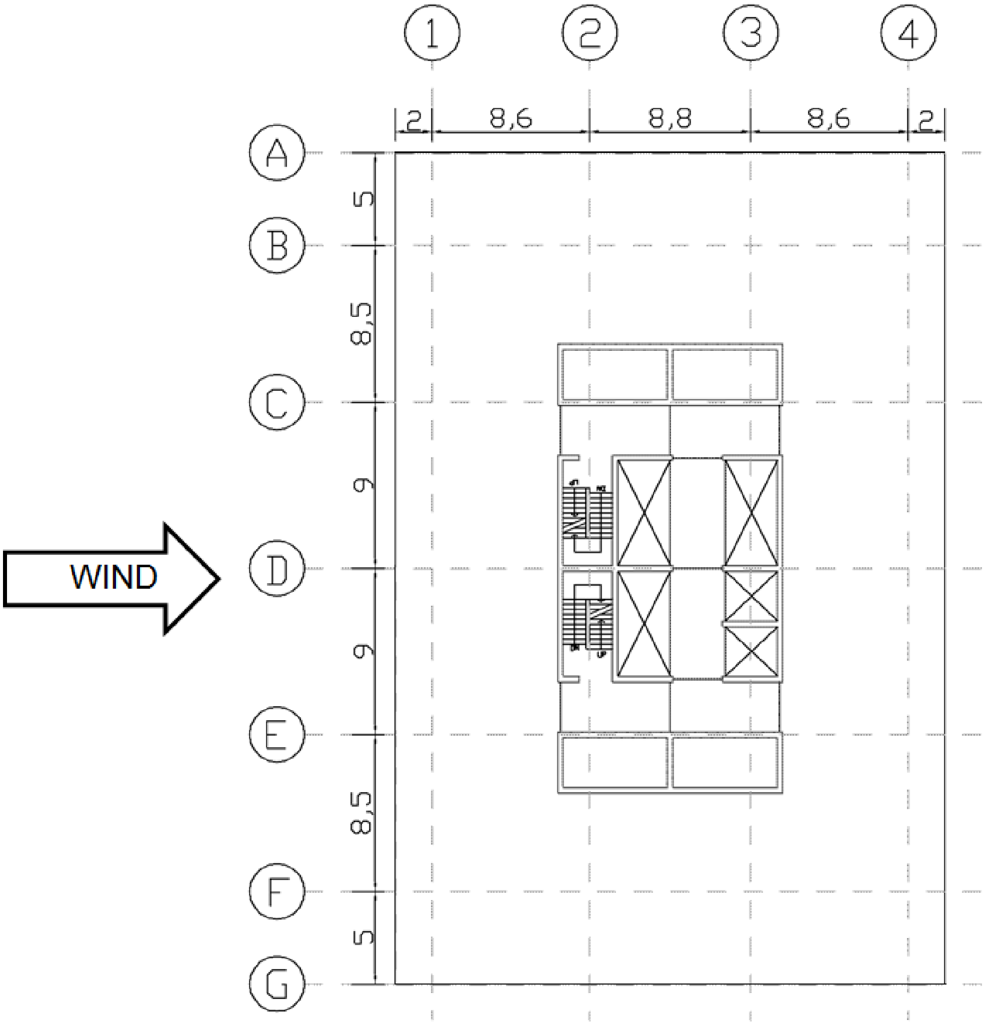

Figure 3.4. Typical floor plan of regular tall building (dimensions in metres)

3.6.2 Irregular Tall Building

The irregular structure represents a completely original tall building design created for the specific purpose of this PBWE research. The geometry of the L-shape cross-section was determined by ensuring the same gross floor area as the regular tall building was provided. Thus, the two designs would theoretically generate the same income for the building owner in terms of office lets, residential rents, etc. This provides a useful foundation to then compare the performance and suitability of the two configurations. The location of the concrete core was offset to be closer to the re-entrant corner and increase the torsional stiffness of the dynamic system. The outer geometry is 42.5 m x 42.5 m and the re-entrant edges are 20 m long. Thus, the design has a single axis of symmetry. The typical floor plan for this arrangement is shown by Figure 3.5. The eccentricity between the concrete core and the outer envelope is evident.

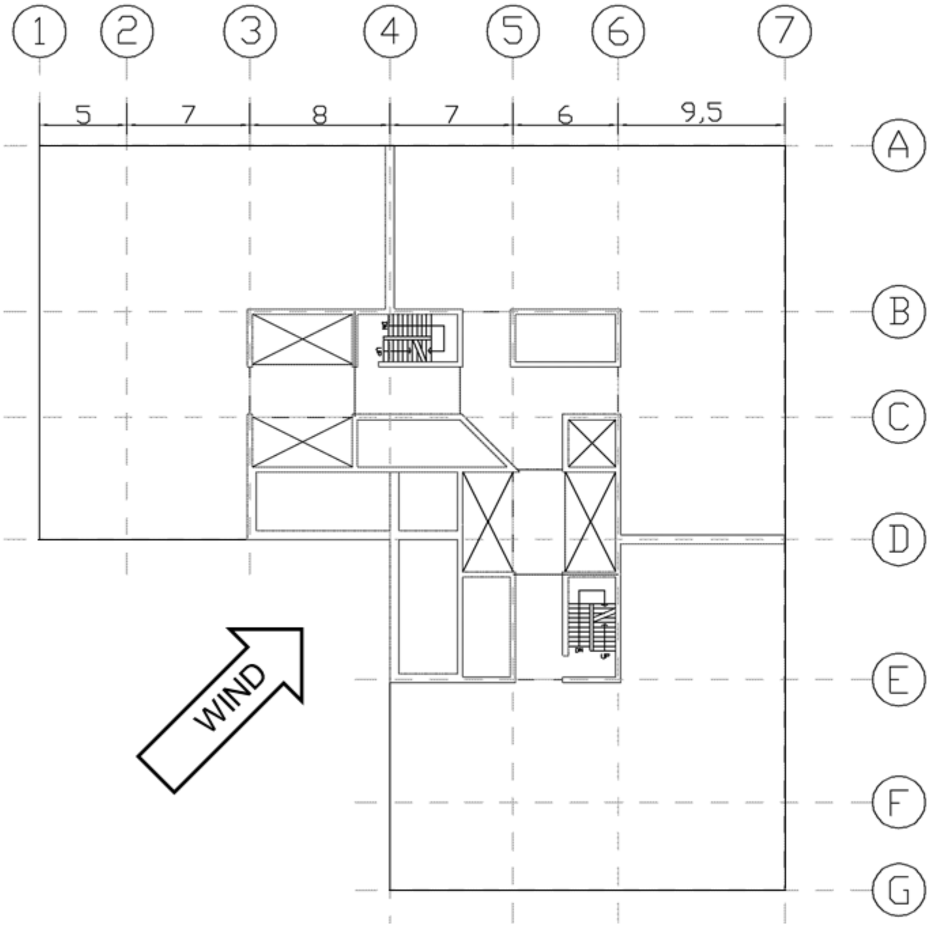

Figure 3.5. Typical floor plan of irregular tall building (dimensions in metres)

The single angle of attack that is considered for the PBWE assessment is also indicated in Figure 3.5. This is parallel with the single axis of symmetry of the structural design, which also represents the most flexible plane of the tall building. At this angle of attack the incident wind field directly encounters the re-entrant bay and exerts a high drag force on the corresponding building faces.

This new design means there are no previous wind tunnel studies or numerical results available for comparison. The BS EN 1991-1-4:2005 (British Standards Institution, 2005) quasi-static wind pressures are used to provide an assurance that the general pressure distribution predicted by CFD is accurate. The results of the PBWE study of this irregular tall building are discussed in Chapter 7.

3.7 Concluding Remarks

The Chapter has given an overview of the research methodology for the proposed PBWE analysis of tall buildings. The main aspect of the present study involves implementing advanced simulation techniques to improve the weaknesses of previous research. Specifically, the techniques of Computational Fluid Dynamics (CFD) and Computational Structural Mechanics (CSM) are implemented into the PBWE framework. It is intended that the former models the characterised Intensity Measure (IM) wind events and provides an adequate prediction of the Interaction Parameter (IP) wind loading. Meanwhile, the latter simulates the resultant Engineering Demand Parameter (EDP) response of the tall building case studies.

The procedure of the Latin-Hypercube sampling method is described, which is used to sample two considered variable distributions: the basic mean wind velocity, v_b, and the aerodynamic roughness length, z_0. The sampled combinations of v_b and z_0 are used to characterise the IM wind events. The number of samples to be obtained from the Latin-Hypercube sampling space was restricted by the computational demands of CFD versus the available computational power. Although the HPC facility at the University of Strathclyde boasts 1088 cores, the number of processors that can be used for CFD simulations is limited by the number of available FLUENT software licenses. A fair-use policy specifies a maximum of 8 CPUs can be used at any one time for CFD simulations. Since each IM wind event requires its own CFD simulation, it is impractical to sample more than 10 variable combinations. However, it is recognised that an increased number of samples would provide a better representation of the variable distributions. The full sampling procedure for the Hazard Analysis is detailed in Chapter 5.

The Damage Analysis for the PBWE assessment of two tall building case studies is based on unacceptable occupant comfort conditions from top floor peak accelerations. The limiting performance criteria are specified using the Melbourne and Palmer equation. Three performance levels are specified based on the return period of the event; each performance level has been assigned an arbitrary limiting exceedance probability. The PBWE assessment derives fragility curves for the two contrasting tall building designs. The fragility curves will be compared against the specified damage criteria to assess the adequacy of the designs. This simplified Damage Analysis is perhaps an aspect of the PBWE framework that could be improved by future research.

4

CFD Validation

4.1 Preamble

This Chapter details the extensive CFD validation study which was required to establish the appropriate complexities and modelling techniques for predicting wind actions on tall buildings. It is argued that, once the capabilities, practical limitations and adequacy of the CFD simulations are identified and understood, the methods can be extended to the PBWE assessment of the two tall building case studies.

This CFD validation study is based on the CAARC standard tall building (Obasju, 1992). The simulation strategy using ANSYS FLUENT (ANSYS Inc, 2009a) is detailed. This is followed by discussing the predicted wind characteristics from a series of empty channel CFD simulations. The study is then progressed to model the wind actions on the CAARC tall building. The pressure coefficients predicted using the RANS and the LES turbulence models are compared against previous numerical and wind tunnel studies. The performance of each turbulence model is assessed in the context of their eventual applicability and suitability for the PBWE framework.

The results validate the use of the CFD software for full-scale simulations with high Reynolds number flows. As expected, the CFD simulation using the LES model provides a better agreement with the wind tunnel data.

However, the high computational cost associated with the LES model is impractical for the PBWE framework. The limitations of the RANS model relate to its failure to sustain the atmospheric turbulence in the incident flow. It is established that the RANS model is capable of determining the mean wind pressures on the tall building, including the high suction effect from flow separation at the leading edge.

4.2 CAARC Standard Tall Building

The CAARC standard tall building is a well-suited benchmark case for the CFD validation study due to the high number of previous wind tunnel and numerical results available for comparison. As discussed in Section 2.7.3, the major results include but are not limited to those from the wind tunnel experiment by Obasju (1992), as well as those from the extensive CFD studies by Huang *et al.* (2007) and Braun and Awruch (2009). The results from the aforementioned CFD studies are described in Section 2.7.2. It should be noted that the CFD study by Braun and Awruch (2009) appears to stand as the only previously published full-scale CFD study of the wind actions on the CAARC tall building.

The CAARC tall building is a standard rectangular prism with a flat-topped roof and its dimensions are D = 30 m, B = 45 m and H = 180 m. The geometry of this simple shape is shown in Figure 4.1. The validation study considers the wind acting normal to the wider building face. This incident wind angle is referred to as $\alpha = 0°$. The majority of pressure results are measured at 2/3H (= 120 m), which approximately corresponds to the height of the stagnation point. In addition, there are measurements available at 1/3H (= 60 m). However, these results are far less well documented in open literature, appearing in only the numerical study by Braun and Awruch (2009).

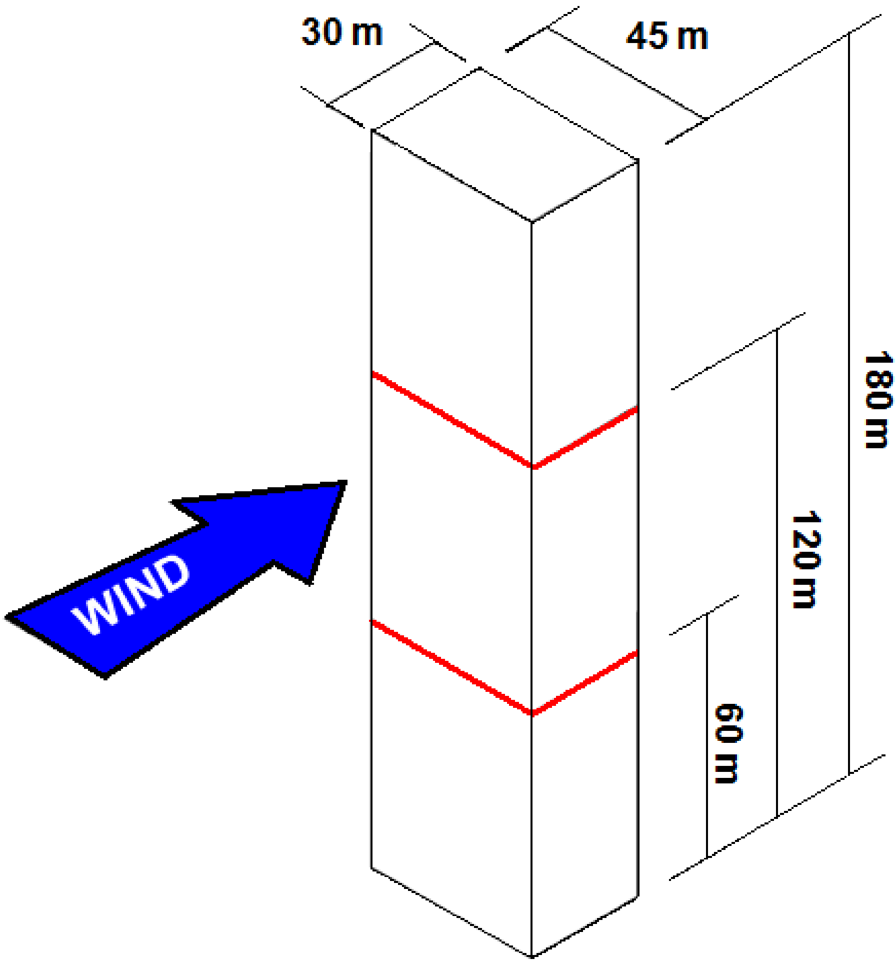

Figure 4.1. CAARC standard tall building dimensions and pressure measurement locations

The flow regime and resulting load characteristics corresponding to $\alpha = 0°$ will now be described to help interpret the results documented in this Chapter. When the incident wind meets the front face it comes to rest at approximately 2/3*H* to form the front stagnation point. This point corresponds to the maximum drag force exerted on the front face. Elsewhere on the front face the flow diverges in both the transverse and the longitudinal planes in order to flow round the tall building. The flow displaced downwards is constrained by the ground surface. When it reaches this boundary it possesses more kinetic energy than the corresponding incident wind. Subsequently, the flow travels against the original wind direction, while gradually losing energy. Once all its kinetic energy has been lost the flow comes to rest and separates from the ground. The separated flow is then forced to roll into a vortex just above the ground, before being swept around either side of the building to leave a horseshoe trail.

The flow displaced towards the sides and the roof cannot manoeuvre around the sharp corners of the leading edges. This causes flow separation to occur, which creates a region of extremely low pressure towards the leading edges of the side faces and the roof. Consequently, this causes a high suction effect at these regions. The intensity of the suction effect reduces on these faces with increasing distance from the leading edges. The separated shear layers produce an arch vortex in the near-wake. The vertical variation of the mean velocity causes the vortex shedding to occur in fragmented, weaker vortices.

4.3 CFD Modelling Strategy

4.3.1 Basic Fluid Properties

The air was modelled as a single homogenous fluid throughout the computational domain and its properties are listed in Table 4.1. The atmospheric boundary layer (ABL) wind speeds modelled in the CFD simulations were considered strong enough to provide sufficient turbulence mixing to supress the thermal effects, and hence the flow was treated as being neutrally stable. This condition applies to the majority of wind loading problems (Cook, 1982).

Table 4.1. Fluid properties used in the CFD simulations

Property	**Value**
Density, ρ	1.226 kg/m^3
Dynamic Viscosity, μ	1.785 x 10^{-5} kg/m/s
Kinematic Viscosity, v	1.456 x 10^{-5} m^2/s

4.3.2 Computational Domain and Mesh Design

The geometry of the fluid domain for the full-scale CFD simulations needs to be large enough to ensure the flow was not constrained by the lateral and top boundaries near the tall building location and that obstacle effects at the inflow and outflow were eliminated. Two domain sizes were created for the CFD validation study. The domain D2 followed the recommendations of Revuz *et al.* (2010), whilst domain D1 offered a smaller alternative. It should be noted that the normalised geometry of D1 was still significantly larger than that used in the successful 1:250 scale CFD study by Huang *et al.* (2007), as described in Section 2.7.2.

The geometries of D1 and D2 are detailed in Table 4.2 and shown in Figure 4.2. The blockage ratio is a measure of the area of the windward face of the building divided by the area of the streamwise plane of the domain. The larger downwind dimension was to allow full development of the recirculation zone in the near-wake and substantial dissipation of the vortices in the turbulent far-wake. The sensitivity of the surface pressure results to these different domain sizes was assessed and is detailed in Section 4.5.1.

Table 4.2. Details of the domain geometry

Domain	DX (m)	DY (m)	DZ (m)	Blockage
D1	535 + D + 1350	402.5 + B + 402.5	540	1.76%
D2	900 + D + 1350	585 + B + 585	720	0.93%

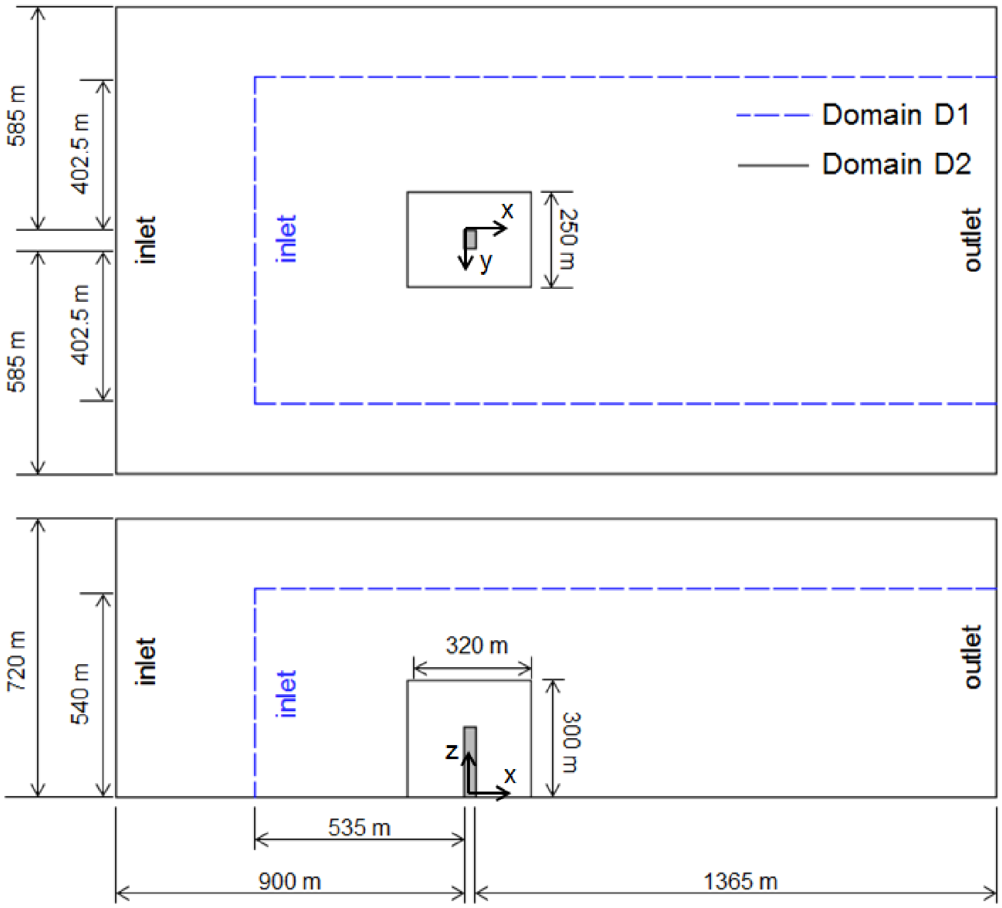

Figure 4.2. Dimensions of computational domains

As in the previous studies, the CAARC tall building was assumed to geometrically represent an isolated obstacle in the CFD domain without the explicit inclusion of surrounding topography or neighbouring buildings. In reality, this assumption is only feasible if the topography is sufficiently flat within the considered fetch. Furthermore, the height of all the surrounding buildings must be significantly lower than the height of the tall building. In other words, there should be very little difference between the height of the surrounding buildings and the zero-plane displacement height d (15 m ≤ d ≤ 25 m for built-up town terrain).

Despite the simplicity of the building shape, the generation of an optimised mesh suitable for both the RANS and the LES turbulence models was a challenging task. The number of computational cells had to be as low as possible to reduce the CPU cost. However, it had to be ensured that the results were not compromised by over-coarsening the mesh. A fine mesh is required near the building in order to adequately model the complex flow characteristics, such as separation at the leading edge and vortex formation in the near-wake. The flow features have a significant influence on the computed surface pressures on the tall building.

A nested mesh technique, similar to that used by Huang *et al.* (2007), was adopted to assist in the mesh generation. As the name suggests, the CAARC tall building was nested in a rectangular cylinder within the domain. An unstructured mesh was generated inside this ‘nest’ and a structured mesh was created for the outer domain. The key attribute of this meshing approach was that it allowed a fine mesh to be used for the near-wall regions and a suitably coarser mesh to be used in the zones far away from the tall building. This was created in the CFD pre-processor GAMBIT (FLUENT, 2007), which is part of the FLUENT software suite. The initial mesh of domain D1 was generated using this technique, as shown in Figures 4.3 and 4.4, and contains approximately 2.59 million computational cells.

The relevant external faces of domain D1 were then extruded to provide the larger geometry of domain D2. This generated a series of additional fluid volumes. The structured mesh design was simply extended into these new zones and the boundary conditions were adjusted accordingly. The initial mesh of domain D2 contains 2.96 million computational cells and is shown in Figures 4.5 and 4.6.

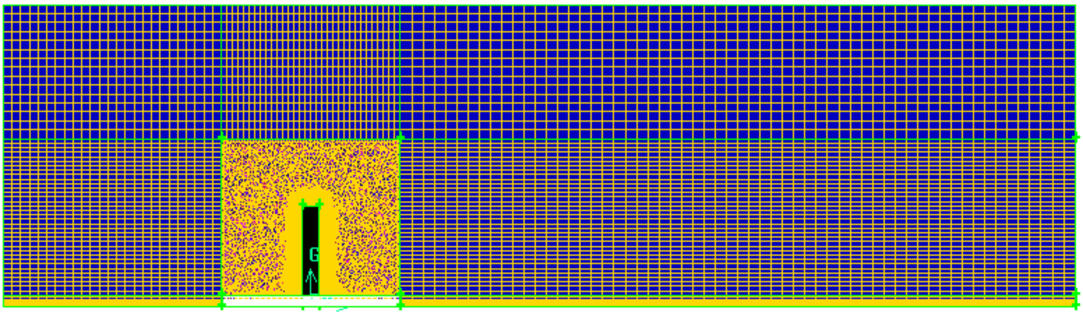

Figure 4.3. Domain 1: Initial CFD mesh in *X*-*Z* plane (flow is from left to right)

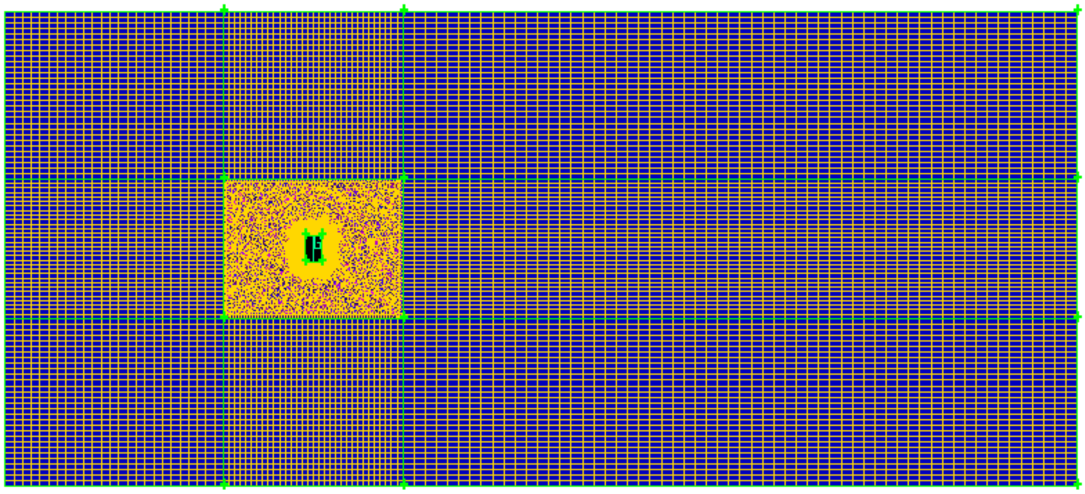

Figure 4.4. Domain 1: Initial CFD mesh in *X*-*Y* plane (flow is from left to right)

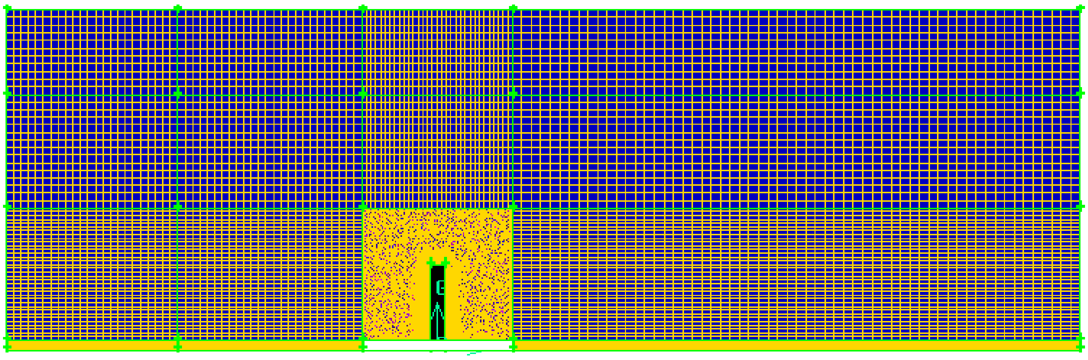

Figure 4.5. Domain 2: Initial CFD mesh in *X*-*Z* plane (flow is from left to right)

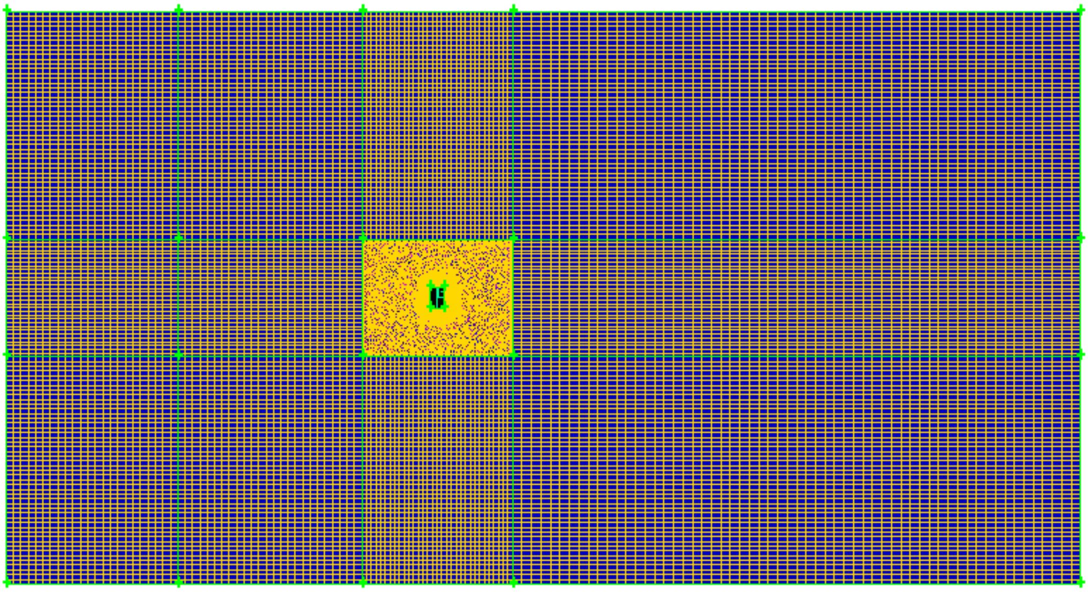

Figure 4.6. Domain 2: Initial CFD mesh in *X*-*Y* plane (flow is from left to right)

Near-wall modelling at the building faces and the ground boundary was a very important consideration during the mesh generation. The inflated boundary layer tool in the pre-processing software GAMBIT (FLUENT Inc, 2007) can be used to define the spacing of mesh node rows in the regions immediately adjacent to building surfaces. An inflated boundary layer was created from the surface of the tall building mesh and extended onto the domain floor. A mesh sensitivity study performed by Knapp (2007) identified that this inflated boundary layer meshing technique better modelled the intensity of the separation at the leading edges than a homogeneous unstructured mesh. In addition, Knapp (2007) found that the homogeneous unstructured mesh could not fully resolve the high velocity gradients in the downstream wake. The CFD study of the CAARC tall building by Huang *et al.* (2007) also applied this boundary layer method.

The inflated boundary layer within the unstructured ‘nest’ is shown in Figures 4.7 and 4.8. It should be noted that the mesh of the inflated boundary layer consists entirely of hexahedral cells. The nest volume consisted of 1.71 million cells, which represents 66% and 58% of the total number of cells in domains D1 and D2, respectively. This emphasises that the majority of computational effort for the CFD simulations is concentrated within the nest. Furthermore, the cell count in the inflated boundary layer mesh (9.95×10^5 cells) equates to 59% of the total mesh within the nest volume. This was necessary in order to resolve the complex flow interaction characteristics.

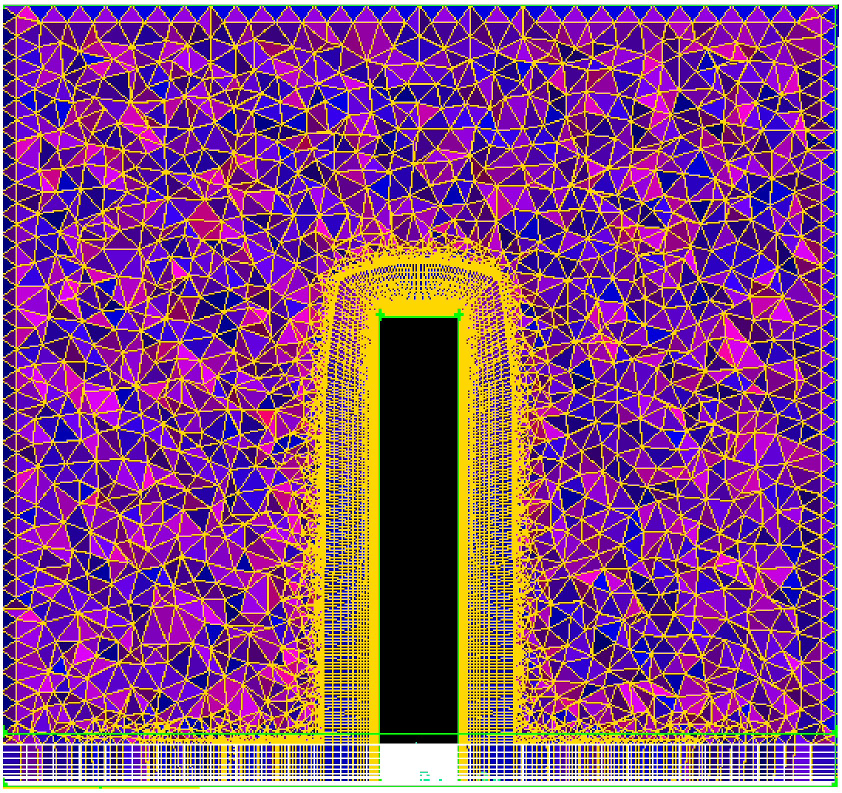

Figure 4.7. Nested mesh technique in *X*-*Z* plane at *y* = 0 m (flow is from left to right)

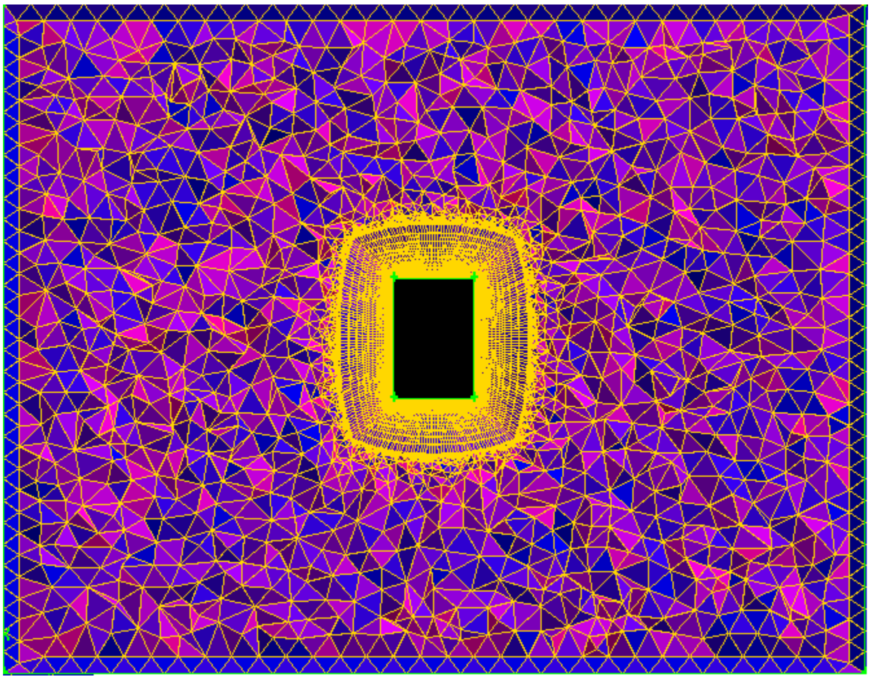

Figure 4.8. Nested mesh technique in *X*-*Y* plane at *z* = 120 m (flow is from left to right)

The details of the inflated boundary layer are summarised in Table 4.3. The enhanced wall treatment was chosen for the near-wall modelling with the intention of resolving the laminar sublayer. The near-wall meshing scheme had to satisfy certain recommendations to sufficiently resolve this region (ANSYS Inc, 2009b). Ideally, the first cell height should have provided a y^+ value of the order of 1 but never exceeded 4 or 5. This y^+ value is a dimensionless variable expressed by

$$y^+ = \frac{u_* y}{v} \tag{4.1}$$

where u_* is a wall-function friction velocity (in ms^{-1}), y is the distance to the centre of the first cell (in m) and v is the kinematic viscosity (in m^{2}s^{-1}). To satisfy this condition, a first cell height of 0.045 m (i.e., B / 1000) was specified. This is the minimum ratio recommended by Murakami (1998).

In addition, a minimum of 10 cells had to be positioned within the viscosity-affected near-wall region (Re_y < 200) to determine the mean velocity and turbulent properties. Therefore, a total of 20 mesh layers with a growth rate of 1.2 were specified.

Table 4.3. Properties of the inflated boundary layer

Property	**Value**
First row (a)	0.045 m
Growth rate (b/a)	1.2
Number of rows	20
Depth	21.239 m

The sensitivity of the results to further near-wall mesh refinement had to be investigated. This was achieved by reducing the aspect ratio, or skewness, of the boundary layer computational cells. However, Knapp (2007) detailed that it is not currently possible to achieve full mesh independence for such highly unsteady, complex flow cases. Therefore, the mesh was refined until the results converged to within an acceptable tolerance. The initial near-wall mesh at the leading edge of the windward face and roof is shown in Figure

4.9. The mesh dependence was assessed by progressively refining the initial mesh, details of which are listed in Table 4.4. The mesh intervals were distributed equally across the building face. The results of this mesh optimisation study are detailed in Section 4.5.2.

Table 4.4. Details of interval sizes for mesh sensitivity study

Mesh Design	**DX (m)**	**DY (m)**	**DZ (m)**	**Cells in Inflated Boundary Layer**
Initial	0.70	0.81	1.80	9.95×10^5
M1	0.65	0.72	1.70	1.17×10^6
M2	0.60	0.65	1.60	1.37×10^6
M3	0.54	0.60	1.20	1.95×10^6

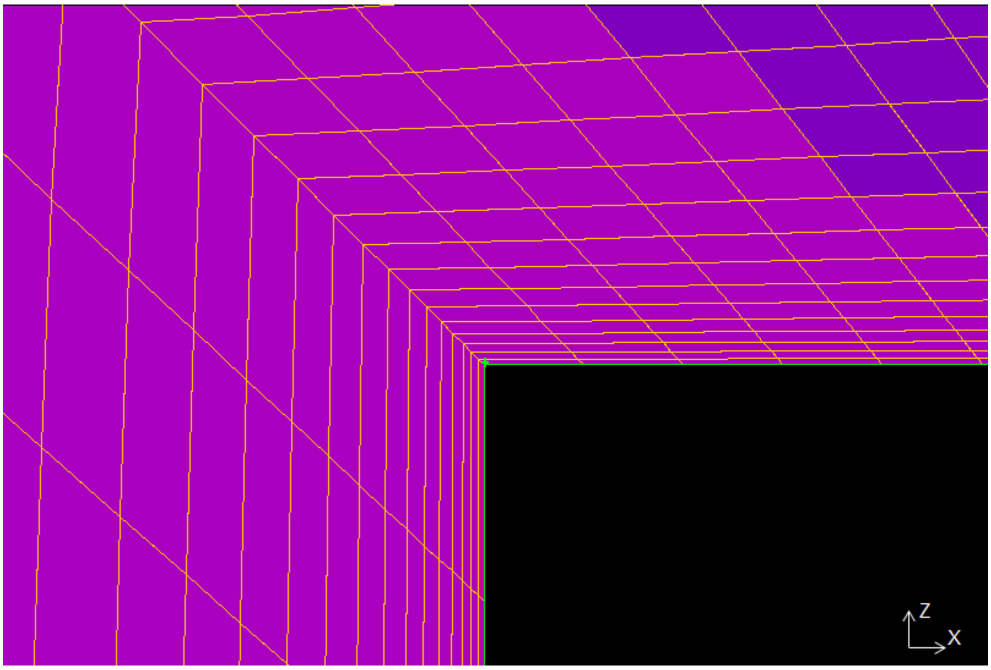

Figure 4.9. Initial near-wall mesh at leading edge of the windward face and roof in (flow is from left to right)

4.3.3 Boundary Conditions

It was important that the vertical profiles of the ABL specified at the velocity inlet in the CFD validation study were consistent with those used in the previous CFD studies by Huang *et al.* (2007) and Braun and Awruch (2009). In the full-scale CFD simulation by Braun and Awruch (2009), the reference velocity, V_{ref}, was 100 ms^{-1} at the top of the building (i.e., z = 180 m). The full-scale aerodynamic roughness length of the surrounding domain was calculated by Obasju (1992) as z_0 = 0.228 m.

The vertical profile of the mean wind velocity for this CFD validation was described by the popular logarithmic law. For the given reference values, the following expression was determined and specified at the velocity inlet

$$V_z = \frac{u_*}{0.4}\ln\left(\frac{z}{z_0}\right) = \frac{5.996}{0.4}\ln\left(\frac{z}{0.228}\right) \tag{4.2}$$

The resulting vertical profile of the mean wind velocity for the CFD validation study is shown in Figure 4.10.

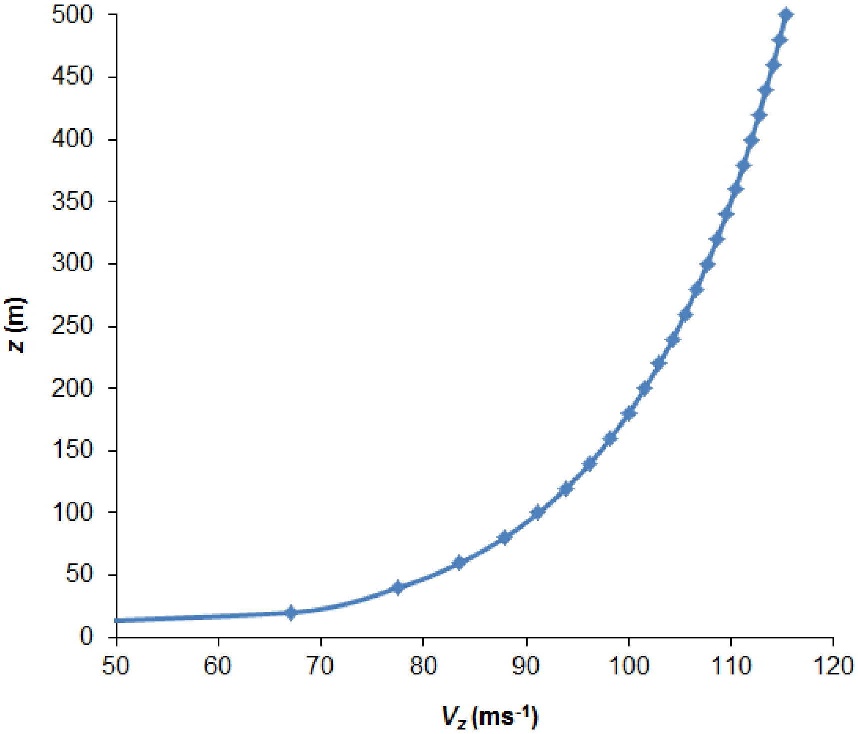

Figure 4.10. Vertical profile of mean wind velocity specified at the inlet

The turbulence intensity was then derived based on Equation 3.4 given by ESDU 85020 (Engineering Sciences Data Unit, 2001), resulting in the following equation

$$I_u = \frac{\sigma_u}{u_*} \cdot \frac{u_*}{V_z} = \frac{7.5\eta\left[0.538 + 0.09\ln(z/0.228)\right]^p}{2.918} \cdot \frac{5.996}{V_z} \tag{4.3}$$

Figure 4.11 shows the resulting target vertical profile of the turbulence intensity that was to be attained in the CFD validation study.

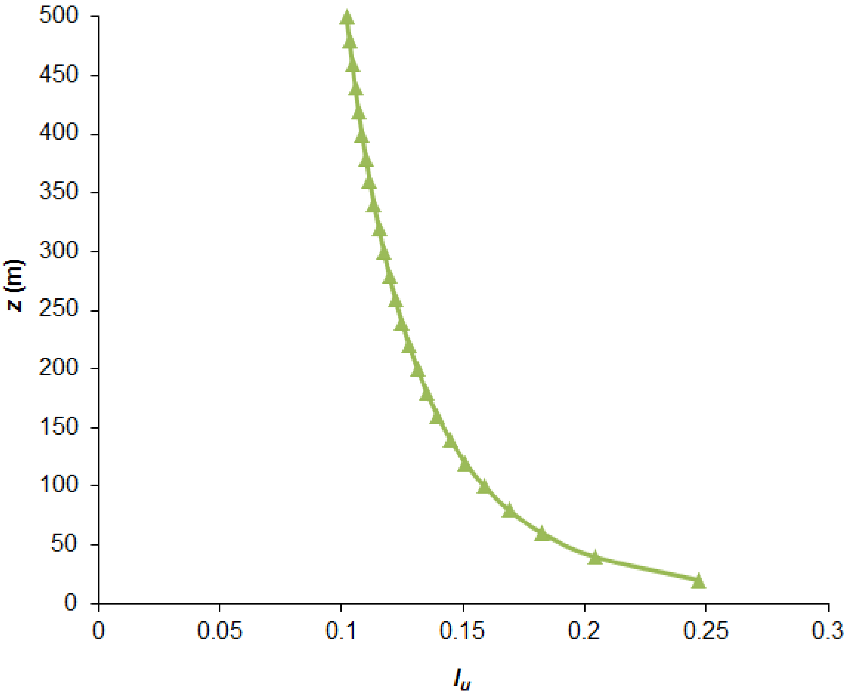

Figure 4.11. Target vertical profile of turbulence intensity

The wind tunnel experiment conducted by Obasju (1992) identified that the measured turbulence length scales were well described by the following formula

$$^{x}L_u = \frac{25 \cdot \left(z^{0.35}\right)}{z_0^{0.063}} = \frac{25 \cdot \left(z^{0.35}\right)}{0.228^{0.063}} \tag{4.4}$$

This equation represents a significantly simpler expression than was given by Equation 3.5. However, it is specific to the CAARC tall building and is not a general expression to describe the turbulence length scale. The derived vertical profile of the streamwise ${}^{x}L_u$ from Equation 4.4 is illustrated by Figure 4.12.

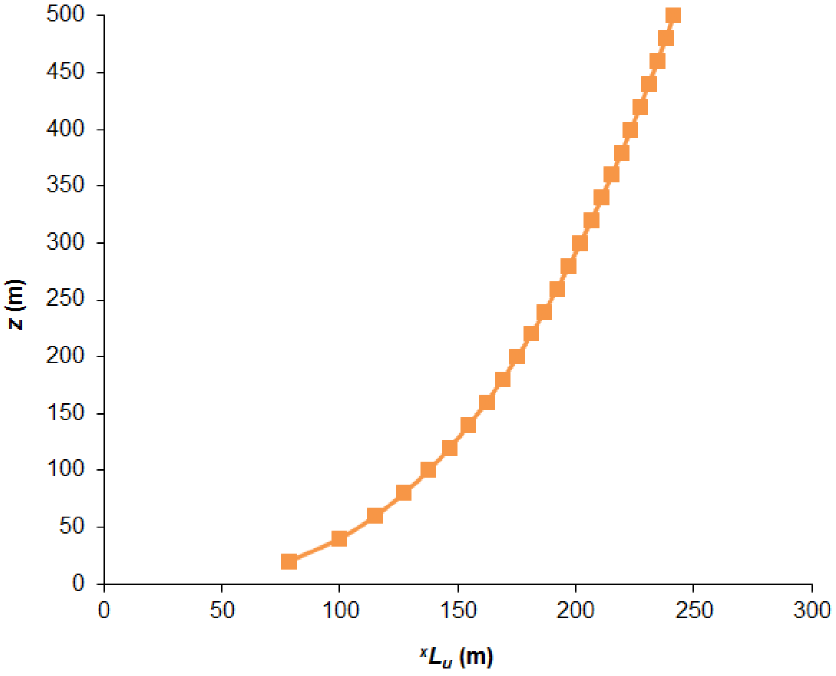

Figure 4.12. Target vertical profile of turbulence length scale

However, a difficulty arose from FLUENT not offering the facility to explicitly define UDF profiles for the turbulence intensity and length scale. Therefore, these properties had to be translated as a function of the turbulent kinetic energy, k, and its dissipation rate, ε. The relationships were established based on the expressions recommended by the FLUENT User Guide (ANSYS Inc, 2009b and references within), namely

$$k = \frac{3}{2}\left[V_{z=H} \cdot I_u\right]^2 \tag{4.5}$$

$$\varepsilon = \frac{C_\mu^{0.75} k^{3/2}}{{}^{x}L_u} \tag{4.6}$$

The parameter C_μ is a model constant and its default value for the RNG k-ε turbulence model is 0.0845 (ANSYS Inc, 2009a). The corresponding vertical profiles of k and ε are shown in Figures 4.13 and 4.14, respectively.

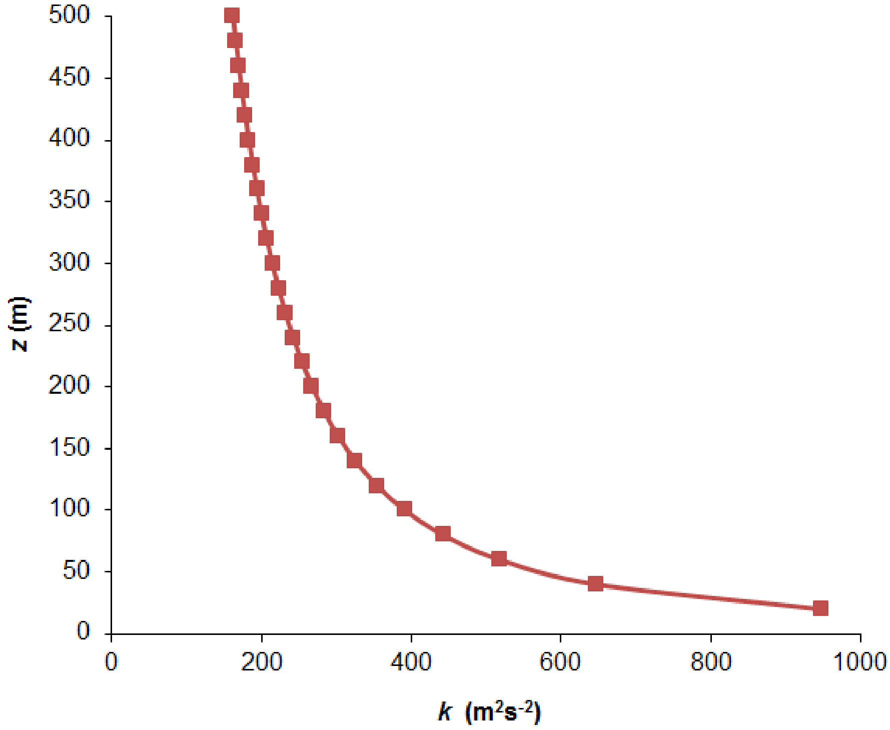

Figure 4.13. Vertical profile of turbulent kinetic energy specified at the inlet

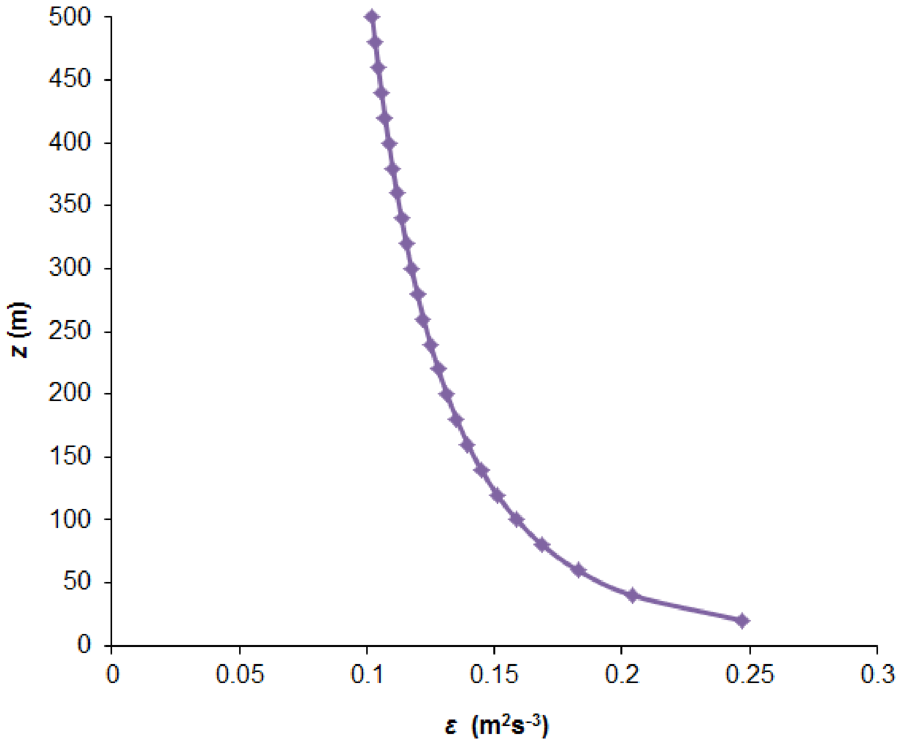

Figure 4.14. Vertical profile of turbulence dissipation rate specified at the inlet

The other boundary conditions considered in the CFD simulations were based on reviewing those used by previous CFD studies, as discussed in Section 2.7. Conditions at the top and side boundaries of the computational domains were set as additional velocity inlets with corresponding streamwise components only, since Knapp (2007) identified that this condition better simulated an equilibrium ABL flow. The outflow was defined as a pressure outlet with a 0 Pa gauge pressure and the backflow turbulence conditions were set equal to those set at the velocity inlet. These backflow conditions were required if the flow reversed direction at the pressure outlet boundary at any stage during the simulations (ANSYS Inc, 2009b). Finally, in agreement with Huang *et al.* (2007), the building surfaces and the domain floor were modelled as wall boundaries with the default no-slip shear condition.

4.3.4 Turbulence Models

It must be emphasised that the purpose of the CFD simulations was to assess the suitability of commercially available CFD methods to be used in the proposed PBWE framework. The intention was not to focus on developing new, improved turbulence models for structural wind engineering. ANSYS FLUENT has a range of turbulence models that could have been used for this CFD validation study. Rather, the main objective was to compare the performance of the RANS and the LES turbulence models for determining the wind actions on the CAARC tall building. The results were assessed in the context of PBWE.

Having reviewed the relevant literature in Section 2.7 it was apparent that a revised k-ε model would offer an improvement to the standard k-ε turbulence model. ANSYS FLUENT offers the renormalisation group (RNG) and realizable versions of the k-ε turbulence model. The RNG k-ε turbulence model has become increasingly popular for predicting bluff body aerodynamics due to its improved prediction of turbulence production and flow separation (Preveser and Holding, 2002). In addition, its convergence properties have made it a preferred option over k-ω turbulence models (Knapp, 2007). Therefore, the RNG k-ε turbulence model was chosen as the reference RANS case and was used for both the domain sensitivity and the near-wall mesh optimisation studies.

With regards to the LES turbulence model, the dynamic SGS kinetic energy model was chosen for resolving eddies smaller than the mesh size. The sub-grid scale (SGS) turbulence is modelled by accounting for the transport of the SGS turbulence kinetic energy. This is considered to be more appropriate for high Reynolds number bluff body flows than the local equilibrium assumptions used by the alternative Smagorinsky SGS models (ANSYS Inc, 2009a). Indeed, Huang *et al.* (2007) successfully implemented this dynamic SGS kinetic energy model in FLUENT for the CFD simulations of the CAARC tall building.

The performance of the above turbulence models in modelling equilibrium ABL flow in an empty computational domain is discussed in Section 4.4. The predicted mean and RMS pressure coefficients at 1/3*H* and 2/3*H* on the CAARC tall building are then compared against previous numerical and wind tunnel studies in Section 4.5.3.

4.3.5 Solver Settings

The pressure-based solver was used in FLUENT since the flow was considered incompressible. The segregated Pressure-Implicit with Splitting of Operators (PISO) algorithm was chosen as the pressure-velocity coupling method. The FLUENT User Guide (ANSYS Inc, 2009b) recommends this method for unsteady simulations and states it is particularly useful for computational models with regions of skewed mesh. The extremely small first cell height of the inflated boundary layer caused an unavoidable degree of skewness for the near-wall mesh. Therefore, skewness correction was used to improve convergence difficulties (ANSYS Inc, 2009a). The second order implicit scheme was used for temporal discretisation. The spatial discretisation was performed using the second-order upwind scheme. However, the bounded central differencing scheme was used by LES to discretise the convective terms of the momentum equations. Finally, the default Least Squares Cell-Based method was used to evaluate the gradients and derivatives for computing values of a scalar at the cell faces and secondary diffusion terms (ANSYS Inc, 2009b).

The computational time-step chosen for the CFD simulations had to be small enough to capture the inherent flow instabilities and the pressure fluctuations which would influence the dynamic structural response. Furthermore, the time-step size was dependent on the turbulence model considered. It was noted in Section 2.7 that the LES turbulence model requires a significantly smaller time-step than traditional RANS since it represents a fully transient solution. Based on the detailed investigation in Section 2.7.3, the CFD simulations using the RANS model were conducted with computational time-steps of 0.001 s, 0.01 s and 0.05 s, while the time-step for the CFD simulations using the LES model was limited to 5 x 10^{-4} s and 0.001 s. It had to be ensured that the total flow time of these unsteady CFD simulations provided sufficient data for the statistical analysis of the measured quantities.

The accuracy of CFD solutions are typically measured in terms of the solver residuals summed over all the computational cells (Knapp, 2007). The convergence criteria for the mass, momentum and turbulence residuals were set at 1 x 10^{-5}. A sufficient number of iterations per time step were computed to reduce the residuals of the governing equations towards zero and satisfy the convergence criteria.

The solver of each CFD simulation was initiated by setting the initial conditions of the cells within the entire computational domain equal to the average conditions specified at the velocity inlet. Therefore, the statistical analysis of the transient results was performed after an initial set of time-steps that allowed the unsteady solution to develop. The measurements during this ‘warm-up’ phase were discarded.

4.4 CFD Simulations: Empty Channel Study

The initial stage of the validation exercise involved a series of empty channel studies. As discussed in Section 2.7.2, Blocken *et al.* (2007) identified that this was a crucial prerequisite for any CFD study concerned with modelling wind actions on structures. The objective was to measure the incident wind field that would impact on the front face of CAARC tall building if the obstacle were to be included in the domain. This incident wind could have differed significantly from the wind properties specified at the inlet if the boundary conditions and mesh fail to model a horizontally homogeneous ABL.

The empty channel studies used the geometry of domain D1 except the space corresponding to the CAARC tall building was replaced by a fluid volume with a structured mesh. The aim was to investigate the performance of the chosen RANS and LES turbulence models in modelling an equilibrium ABL flow. Vertical arrays of monitors were created at the inlet, approach and outlet. The positioning of the approach monitors corresponded to the proposed location of the front face of the CAARC building. The monitors recorded the computed streamwise velocity, turbulent kinetic energy and turbulence intensity throughout the simulations. The results of this empty channel study were assessed in terms of their potential impact on the flow field and pressure distribution on the CAARC tall building. This study identified the capabilities and limitations of the turbulence models for modelling the IM wind events from the site hazard analysis. It was necessary that the turbulence model implemented for the PBWE framework provided a sufficient representation of the IM wind field.

4.4.1 RANS Turbulence Model

The first set of empty channel simulations were concerned with the performance of the RNG k-ε turbulence model. The C programming file containing the user-defined functions (UDF) for the vertical profiles of V_z, k and ε from Section 4.3.3 was interpreted in to FLUENT and set as the inflow boundary conditions. The relevant solver settings detailed in Section 4.3.5

were implemented. The RANS simulations were computed for time-steps of Δt_1 = 0.01 s and Δt_2 =0.001 s to assess the impact of reducing the RANS averaging time by an order of magnitude. It should be noted that Δt_2 is a time-step suitable for LES. The required number of time-steps from each simulation was based on attaining statistical data for a flow time of 240 seconds. Hence, Δt_1 required 2.4 x 10^4 steps and Δt_2 required 2.4 x 10^5 steps. In both cases, the CPU cost of a single physical time step was 6.7 seconds. Therefore, the total computation time was 44.7 hours for Δt_1 and 446.7 hours for Δt_2.

As shown in Figure 4.15, the vertical profiles of the mean streamwise velocity for Δt_1 display a very strong agreement to the target profile throughout the domain. The largest discrepancies from the target profile arise within the lower 10 metres of the domain. The results within this region produce a maximum error of just 7%. Meanwhile, all the monitors at elevations greater than 10 metres produce an error less than 1%. Similar results were computed for Δt_2.

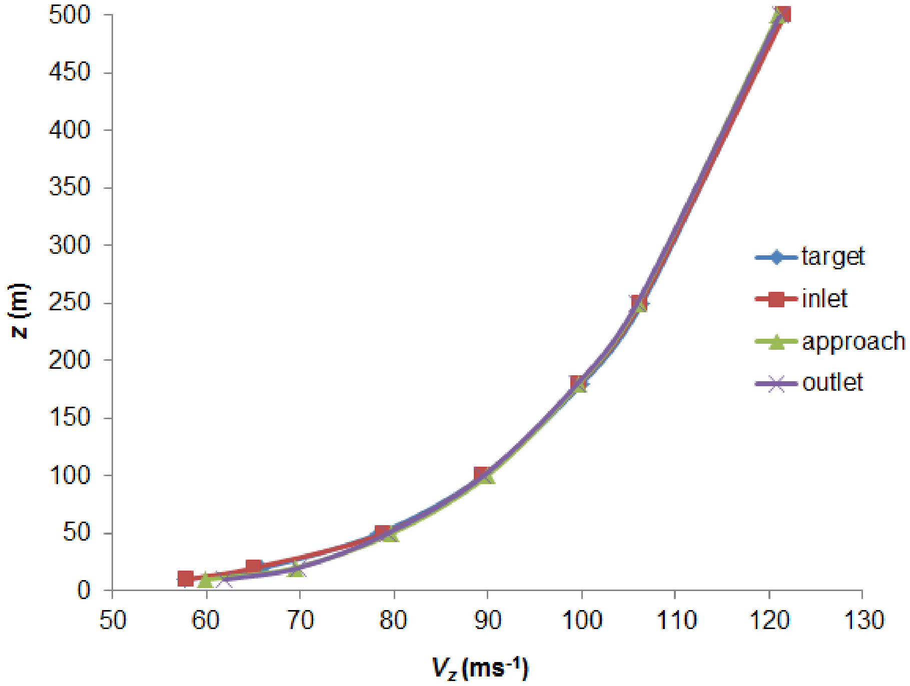

Figure 4.15. Mean x-velocity profiles for RNG *k*-ε turbulence model

However, the flow characteristics monitored for Δt_1 showed that the RANS model failed to sustain the high turbulence levels specified at the inlet. This is clearly evident from the measured profiles of turbulent kinetic energy and turbulence intensity shown in Figures 4.16 and 4.17, respectively. This outcome was expected since similar problems were documented by Knapp (2007). A similar limitation occurred for Δt_2, which identified that the shortcoming in modelling the atmospheric turbulence could not be overcome by significantly reducing the time-step for RANS time-averaging.

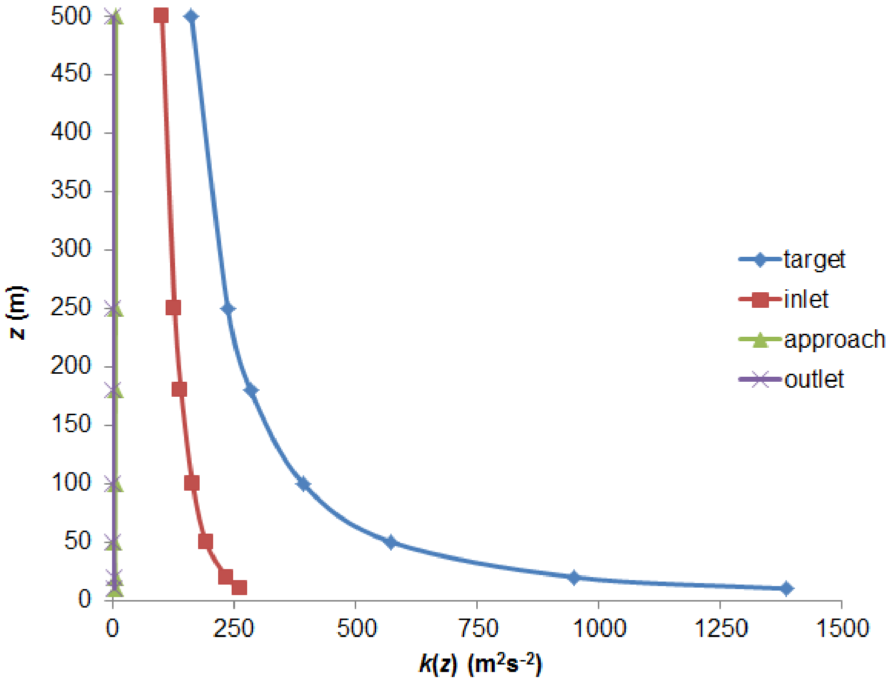

Figure 4.16. Turbulent kinetic energy profiles for RNG k-ε turbulence model

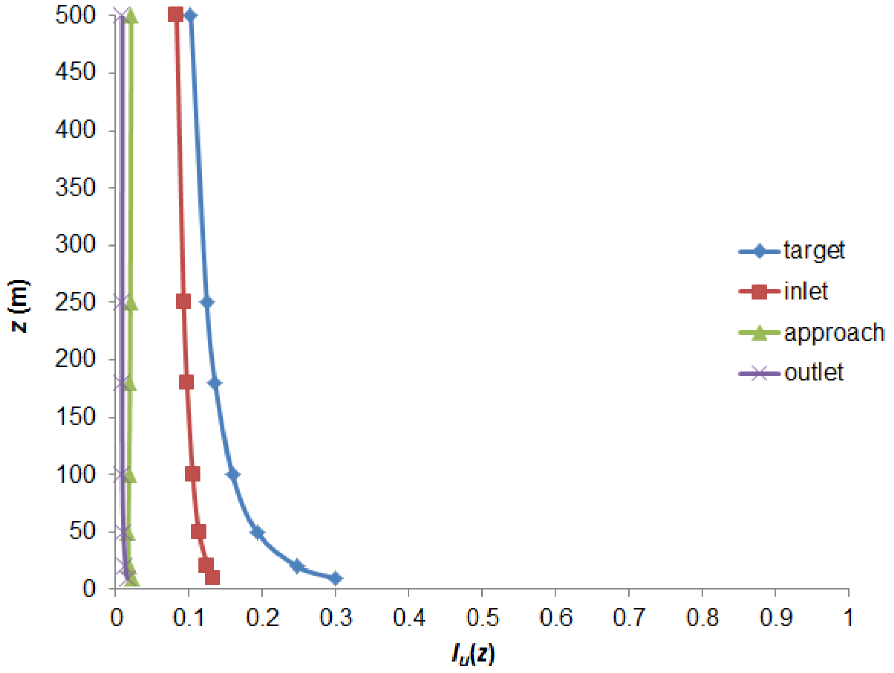

Figure 4.17. Turbulence intensity profiles for RNG *k*-ε turbulence model

It was expected that this low turbulence flow would cause a notable under-prediction of the fluctuating component measured by the pressure monitors on the CAARC tall building, particularly on the front face. In addition, the reduced turbulence in the free stream would result in a wider spread of the shear layers separated at the leading edge, producing a larger separation bubble. The *B/D* ratio of the CAARC tall building is such that high levels of turbulence in the free-stream could potentially cause flow reattachment on the side face. If flow reattachment occurred in the real high turbulence flow but was not captured by the modelled flow in RANS, then the net drag force on the back face of the CAARC tall building predicted by RANS would be higher. Conversely, if no reattachment occurred in the real high turbulence flow, then the net drag force on the back face of the CAARC tall building predicted by RANS would be lower.

4.4.2 LES Turbulence Model

The initial empty channel simulations using the LES turbulence model were run without utilising the fluctuating velocity algorithms available for generating perturbations at the inflow. This method is only suitable when the level of incoming turbulence does not have a dominant influence on the overall results (ANSYS Inc, 2009a). This condition was obviously not applicable to these highly turbulent bluff body CFD simulations. However, it provided a useful reference for when the fluctuating velocity algorithm was later used. The boundary conditions were identical to those specified in the earlier CFD simulations using the RANS model. A numerical time-step of 5 x 10^{-4} s was used and the relevant solver settings were set to those detailed in Section 4.3.5. A total of 4.8 x 10^5 steps were computed and the CPU cost of a single physical time-step was 7.0 s. This required a total computation time of 933.3 hours – over 20 times longer than RANS using Δt_1.

The measured flow properties are plotted against the target profiles in Figures 4.18 to 4.20. A strong agreement to the relevant target profile is seen for all the flow properties; slight discrepancies occur within the lower regions (z < 20 m) at the domain outlet. This is considered a consequence of backflow in the skewed cells near the domain floor and was expected to have a negligible influence on the subsequent CFD simulations involving the CAARC tall building.

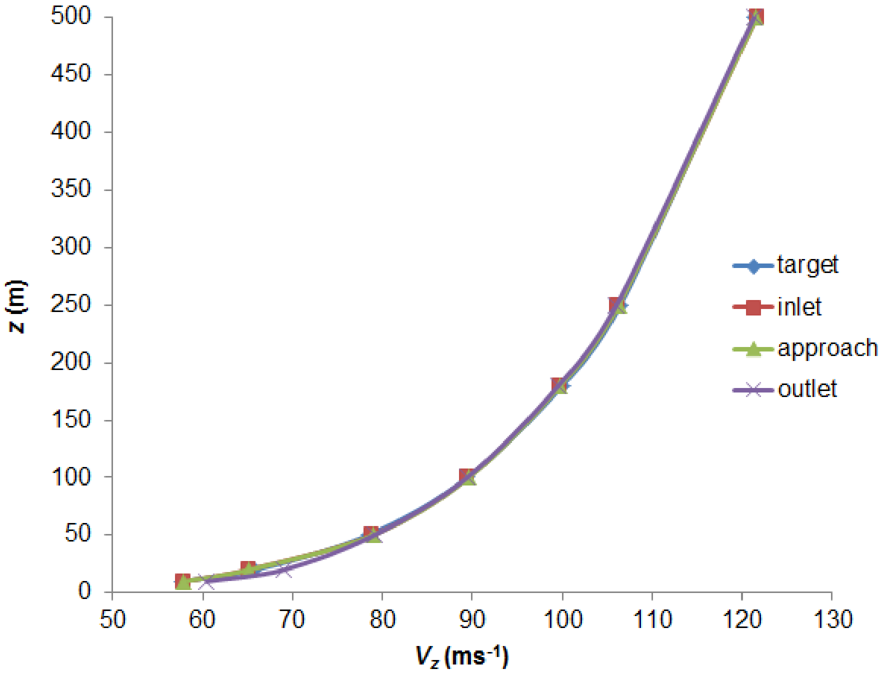

Figure 4.18. Mean x-velocity profiles for LES turbulence model with no perturbations

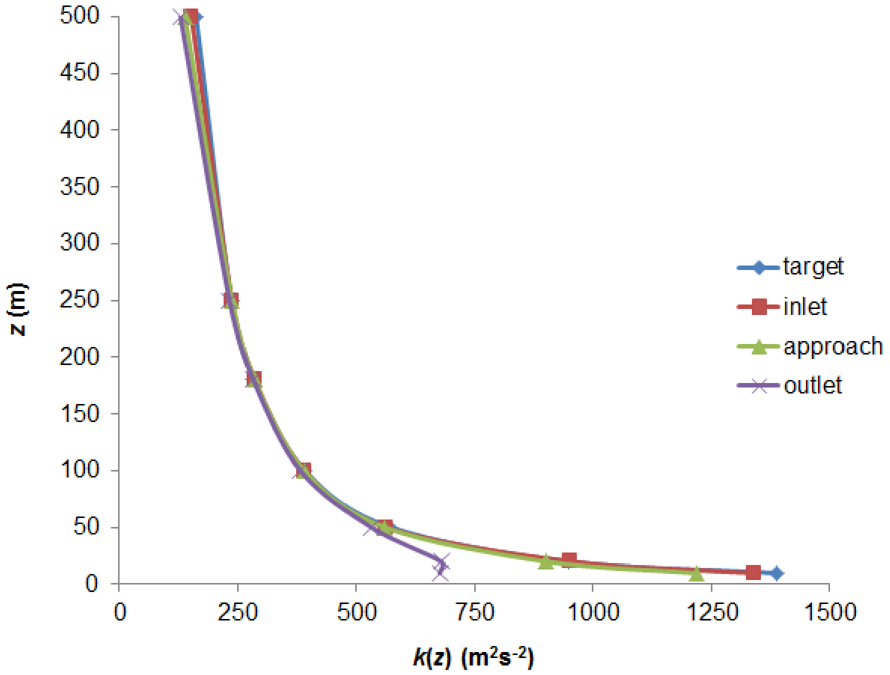

Figure 4.19. Turbulent kinetic energy profiles for LES turbulence model with no perturbations

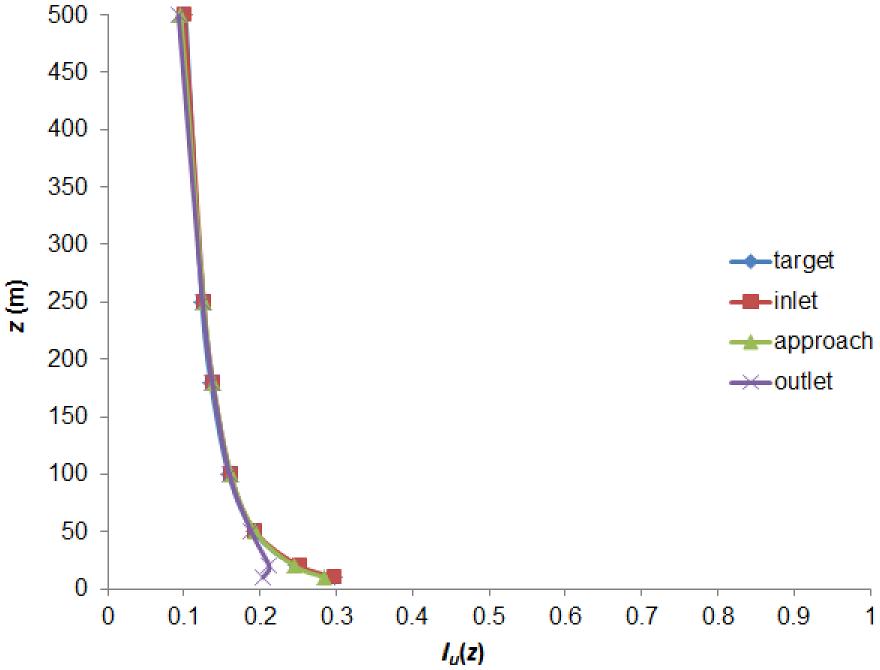

Figure 4.20. Turbulence intensity profiles for LES turbulence model with no perturbations

Perturbations were then generated at the velocity inlet using the spectral synthesizer function available for the CFD simulations using the LES model in FLUENT. This method is based on a random flow generation technique where the fluctuating velocity components are computed by synthesizing a divergence-free velocity-vector field from the summation of 100 Fourier harmonics (ANSYS Inc, 2009a). The turbulence intensity and length scale were chosen for the specification method. The values of turbulence intensity and length scale at the building height were 13.5% and 168.9 m, respectively. It was expected that the mean of the fluctuating wind data would still converge towards the target mean velocity profile, provided a sufficiently long sampling time was used.

The time-history of the streamwise velocity measured at the inlet at heights of 10 metres, 180 metres and 500 metres are shown in Figure 4.21. The corresponding mean velocity profile is shown in Figure 4.22. The statistical averaging was taken over a flow record of 240 s. As expected, the results at the inlet, approach and outlet are clearly converging towards the target mean velocity profile. The maximum variance between the mean approach velocity and the target profile was 5.4%. However, the statistical average was still adapting as the flow time increased, particularly at the outlet. A sufficiently longer record of flow time would have been required in order to achieve fully settled mean results. This was extremely impractical due to the large computational cost already spent on attaining the first 240 seconds of flow time in LES. It was recognised that failing to satisfy this prolonged averaging requirement could have adverse effects on the mean pressure coefficients later measured on the CAARC tall building.

The representation of the ABL in LES was clearly superior to RANS. This is a major reason as to why LES has better modelled the wind actions on bluff bodies. The CAARC simulations using the LES model were expected to provide a closer agreement to previous wind tunnel results. In addition, the results identified that the LES model would provide a better representation of the IM wind events for the PBWE assessment. However, this initial study also verified the impractical computational demand of LES. Therefore, the LES model was expected to be too impractical for the PBWE framework since the methodology requires several IM wind events to be simulated.

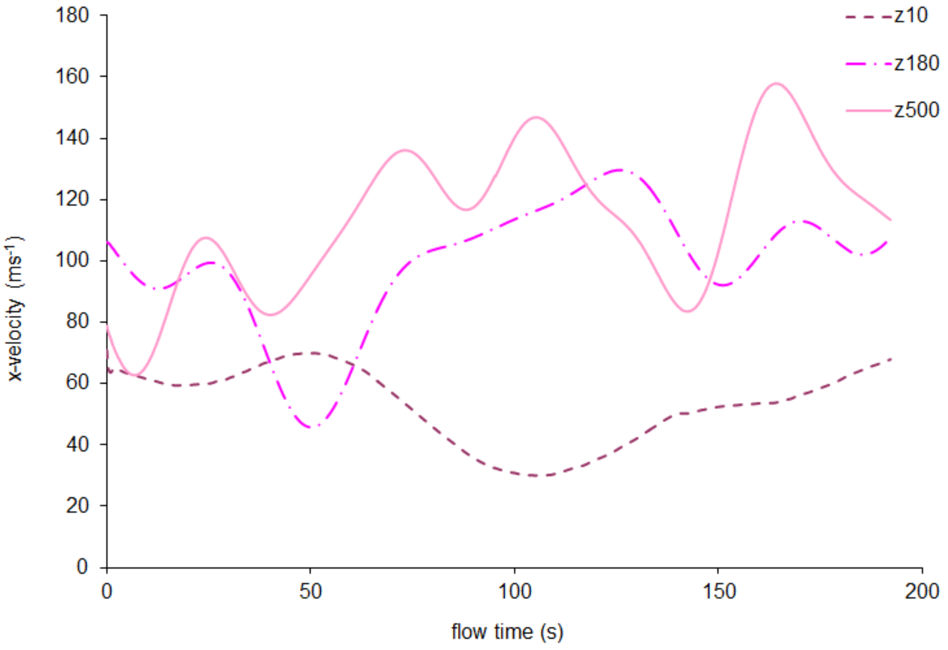

Figure 4.21. Time-history of inlet velocity using spectral synthesizer

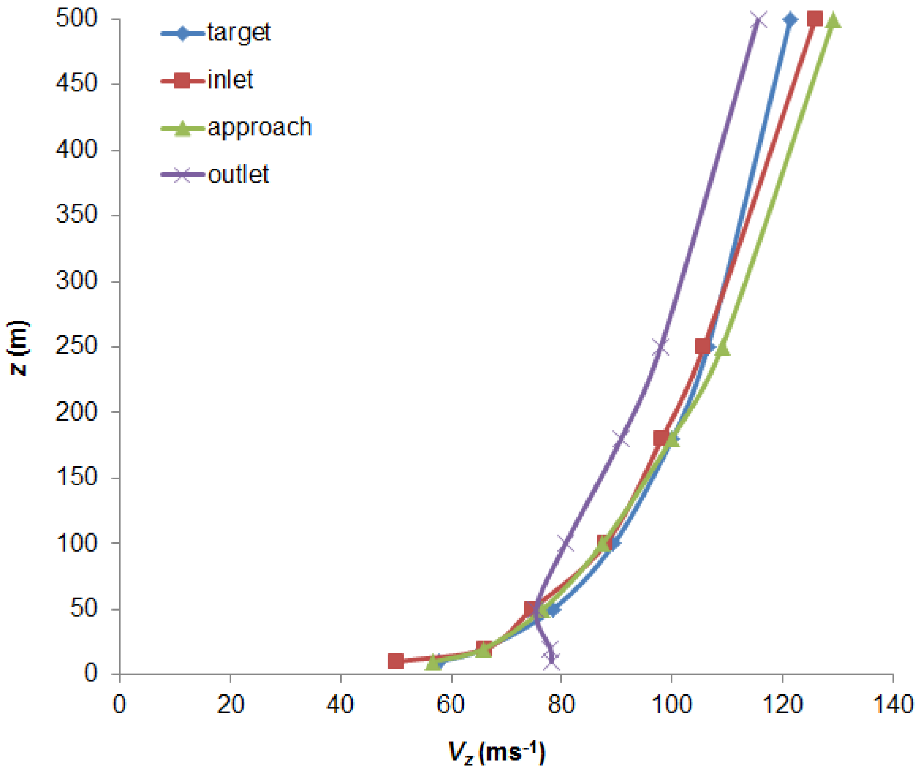

Figure 4.22. Mean x-velocity profiles for LES turbulence model with perturbations

4.5 CFD Simulations: CAARC Tall Building

To be directly comparable with the previous studies mentioned in Section 4.2, the results of the measured surface pressures had to be expressed in terms of the normalised mean and RMS pressure coefficients, C_P and C_{RMS}, which are given by

$$C_P = \frac{P - P_0}{0.5\rho V_{z=H}^2} \tag{4.7}$$

$$C_{RMS} = \frac{\sqrt{\dfrac{\sum (p' - P)^2}{(n-1)}}}{0.5\rho V_{z=H}^2} \tag{4.8}$$

where P is the mean pressure from the time history, P_0 is the static atmospheric pressure, p' is the instantaneous pressure component, and n is the number of sample points in the time history. The denominator $0.5\rho V_{z=H}{}^2$ in both equations represents the dynamic pressure, q, at the height of the tall building. The density of air was 1.226 kg/m^3 and the reference velocity at the building height was 100 ms^{-1}.

4.5.1 Domain Size

The initial set of CFD simulations that explicitly included the CAARC tall building were focused on confirming that the size of the computational domain was sufficiently large. The domain geometry that was used for the subsequent CFD simulations had to ensure that the flow was not overly-constrained at the building. Using the initial mesh detailed in Section 4.3.2, the smaller D1 domain contained approximately 2.59 million cells, while the larger D2 domain had approximately 2.96 million computational cells. The streamwise blockage ratio was 1.76% for D1 and 0.93% for D2. The geometry of D1 did not satisfy the recommendations of Revuz *et al.* (2010). However, it was hoped that this smaller alternative would be sufficient for the future CFD simulations since it contained fewer computational cells, and hence it required a lower computational cost.

The CFD results were computed by the RNG k-ε turbulence model. A numerical time-step of 0.01 s was used and the statistical analysis was obtained from 240 s of flow time (i.e., 2.4 x 10^4 time steps). The CPU cost of one physical time step was 25.93 s for D1 and 29.88 s for D2. Therefore, the total computation time of D1 was 7.2 days and D2 was 8.3 days.

The measured mean pressure coefficients, C_p, across the building perimeter at 2/3H for the two domain sizes are shown in Figure 4.23. On the front face, there is a negligible difference in mean pressure coefficients between the two domain sizes. However, a significant difference can be seen at the side and back faces; these pressures are related to flow separation effects and the mean pressures predicted by domain D1 are as much as 70% more negative than those predicted by domain D2. This significant difference suggests that the flow is over constrained by the lateral boundaries of the domain as it passed the building. Also, the computational saving of using D1 rather than D2 was not as beneficial as expected. Therefore, the larger D2 domain was used for the subsequent CFD simulations.

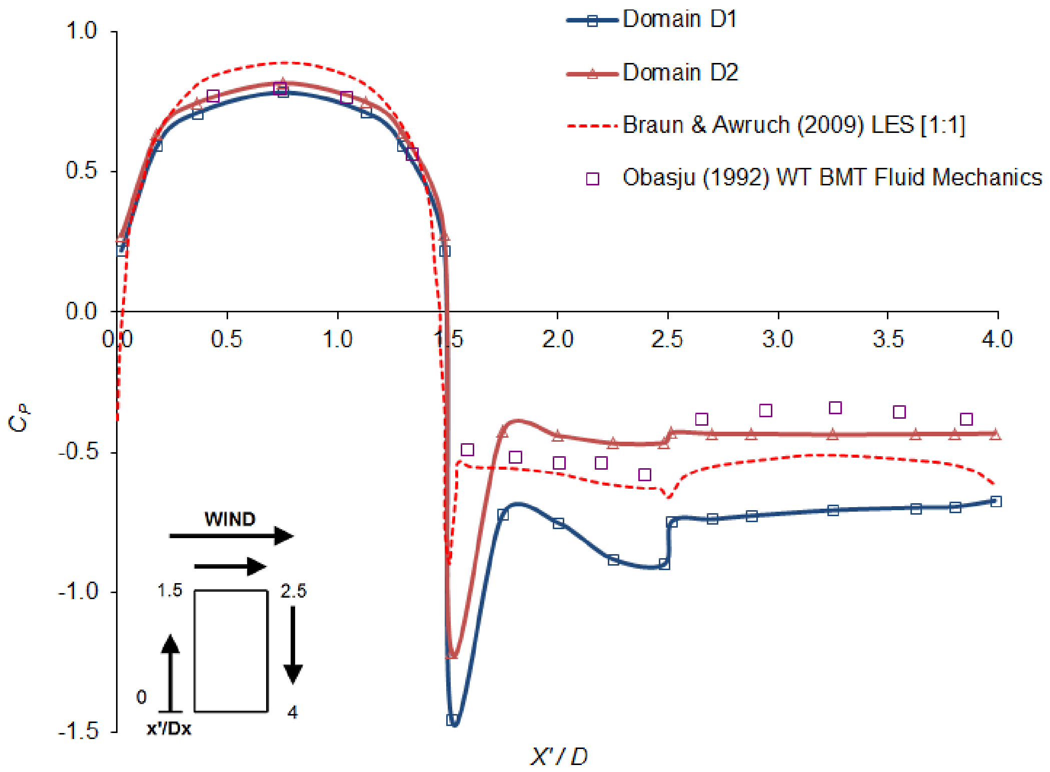

Figure 4.23. Mean pressure coefficients (C_p) at 2/3H showing effects of domain size

4.5.2 Near-wall Mesh Design

The mesh dependence of the predicted surface pressures was assessed by implementing the refinement strategy described in Section 4.3.2. CFD simulations using the RNG k-ε turbulence model were performed for each of the mesh refinement schemes listed in Table 4.4. The local surface pressures at $2/3H$ were measured throughout each simulation. The variation of the local surface pressure was assessed as the mesh was progressively refined to reduce gradient smearing. It was already known that complete mesh independence was impossible for such highly unsteady flows. Therefore, the refinement continued until a satisfactory agreement within the scatter of the results from previous numerical and wind tunnel studies was achieved. The calculated values in accordance with BS EN 1991-1-4:2005 (British Standards Institution, 2005) were also included in the comparison.

On the front face, it is clear from Figure 4.24 that the mean pressure coefficients, C_p, from the initial mesh showed a strong agreement to the previous numerical results by Huang *et al.* (2007) and Braun and Awruch (2009). As the mesh was refined for M1 and M2, the only notable difference appeared to occur at the monitors towards the edges of the front face. Relative to the initial mesh, C_p experienced a 16% reduction from refinement M1 and an 18% reduction from refinement M2. The variation at all other points on the front face was significantly less than -1%. However, the refinement M3 caused a notable reduction in the mean pressure coefficients at every monitor across the building face. The variation at the leading edge was approximately -28% relative to the initial mesh, while the maximum variance at all other points was -8%. The mean pressure coefficients provided by M3 showed a close agreement with the wind tunnel data by Obasju (1992). It is worth noting that the discrepancies among the previous studies are significantly lower on the front face than the side and back faces.

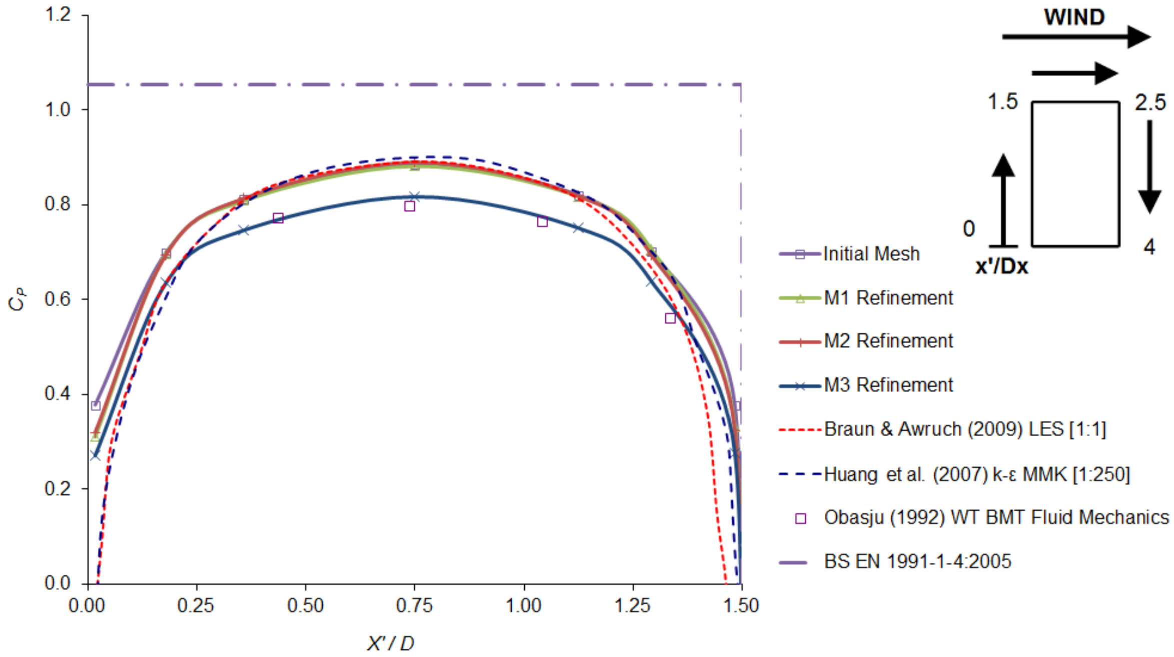

Figure 4.24. Mean pressure coefficients (C_p) at 2/3*H* on front face

As shown in Figure 4.25, the mean pressure coefficients on the side face were more responsive to the progressive mesh refinement. It was essential that the large suction effect caused by flow separation at the leading edge was adequately predicted since this can prove the dominant factor in the design of structural components and cladding. In all refinement cases, the predicted mean pressure coefficients at this point were more intense than those obtained by Huang *et al.* (2007) and Braun and Awruch (2009). However, the reductions in mean pressure coefficients at the downstream points were over-estimated by the initial mesh. As the mesh was refined, the mean pressure coefficients along the side face approached the values measured by Obasju (1992). Once again, the M3 refinement was considered to provide an acceptable agreement to these wind tunnel results.

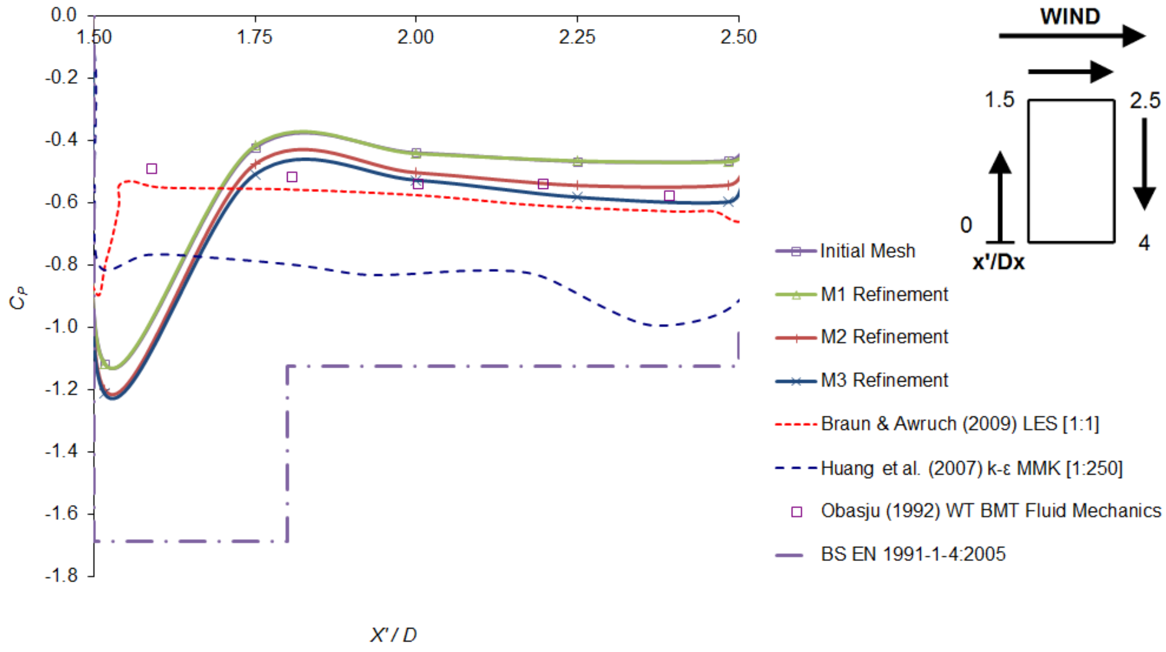

Figure 4.25. Mean pressure coefficients (C_p) at 2/3*H* on side face

Lastly, the mean pressure coefficients measured at 2/3*H* on the back face are shown in Figure 4.26. The negative mean pressure coefficients from the initial mesh were larger than those measured in the wind tunnel test by Obasju (1992). As the mesh was progressively refined, the intensity of the mean pressure increased towards the values measured by Huang *et al.* (2007) and Braun and Awruch (2009). It is evident from Figure 4.26 that the pressure distribution measured from each mesh refinement across the back face did not display the same symmetrical curvature measured by previous studies. This suggests that the vortex shedding associated with the full-scale wind speeds were so disorganised and fragmented that this pressure distribution seen from scaled wind characteristics did not occur.

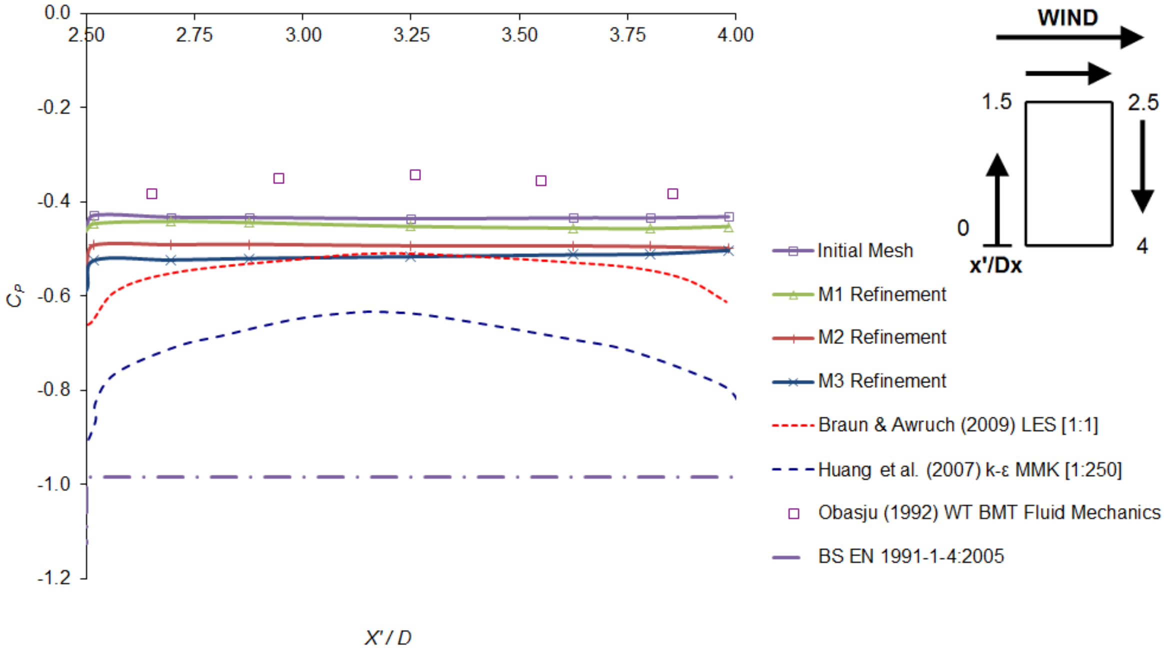

Figure 4.26. Mean pressure coefficients (C_p) at 2/3*H* on back face

It should be noted that the pressure coefficients obtained from the gust peak factor model of BS EN 1991-1-4:2005 (British Standards Institution, 2005) were conservatively higher on the front, side and back faces. Such an outcome was expected since the pressure coefficients provided by BS EN 1991-1-4:2005 are used to determined quasi-static design pressures rather than mean pressures. The results offer additional assurance that the pressure coefficients provided by the code of practice are safe – provided the limits of applicability, as discussed in Section 2.5.2, are satisfied.

It is acknowledged that the mesh design could have been further improved by adjusting the interval spacing on the building faces so that the mesh was more refined at the leading edges where separation occurred. Similarly, more careful refinement could have been provided at local regions where the complex flow phenomena took place, such as the near wake. This refinement would inevitably increase the computation times. Therefore, the refined mesh M3 was used for the subsequent CFD simulations.

4.5.3 Turbulence Model

The final and perhaps main stage of the CFD validation study was to assess the performances of the RANS and LES turbulence models for determining the wind loads on the CAARC standard tall building. The corresponding mean and RMS pressure coefficients at 1/3H and 2/3H were compared against previous data derived by numerical simulations and wind tunnel experiments. The literature reviewed in Section 2.7 and the empty channel studies performed in Section 4.4 both suggested that the LES turbulence model would provide a much closer agreement to the previous wind tunnel results than RANS. However, the extreme computational demand of full LES was also identified.

The spectral synthesizer using the reference I_u and ${}^{x}L_u$ values was used for generating perturbations in the incoming wind field in the CFD simulations using the LES model. The relevant solver settings for RANS and LES were specified as stated in Section 4.3.5. The numerical time-step of the RNG k-ε model was increased to 0.05 s and the CPU cost for a single physical time-step was 29.96 s. The numerical time-step of the LES dynamic SGS kinetic energy model was increased to 1 x 10^{-3} s to reduce the computation times and the cost of a single physical time-step was 31.97 s. The statistical analyses of the measured pressure quantities were based on flow records of 240 s. Therefore, a total of 4.8 x 10^{3} steps were computed by RANS and 2.4 x 10^{5} steps were required for LES. The computation time using 8 CPUs in parallel was 1.66 days for RANS and 88.8 days for LES.

The significant contrast in computation times highlighted that the implementation of full LES was not practical for the PBWE study, even when using the high performance parallel processing available to this project. Therefore, the assessment of the following results was focused on identifying what aspects of the loading would be lost by using RANS as opposed to LES for the PBWE framework. It was hoped that the RANS results would sufficiently predict the dominant loading features.

The mean pressure coefficients at 2/3*H* over the building perimeter are shown in Figure 4.27. It has already been detailed that the RNG *k-ε* turbulence model with domain D2 and mesh refinement M3 achieved a very strong agreement within the scatter of the previous data, with particularly close agreement to the wind tunnel results by Obasju (1992). Only a slight difference exists between the RANS and LES results on the front face, with the LES results typically less than 5% greater than RANS. A more notable difference occurs between the two results at the leading edge of the side face. The 12% larger pressure drop computed by the LES model is 12% larger than the mean pressure coefficients computed by the RANS model. The mean pressure coefficients determined by RANS and LES at the downstream region of the side face converge to a tolerance of 4.1%. The most significant difference occurs on the back face. The suction effects determined by the LES model are over 20% stronger than the pressures on the back face computed by the RANS model. The almost horizontal pressure distribution on the back face computed by RANS is also computed by LES. A similar situation occurs for the mean pressure distribution measured across the perimeter of the building at 1/3*H*, as shown in Figure 4.28.

For the LES turbulence model with random perturbations, the mean velocity measured in the approach flow during the empty channel studies at 2/3*H* was 5.4% greater than the target profile. The corresponding variance between RANS and the target profile was less than 1%. It should be noted that this would have partially contributed to the general increase in mean pressure coefficient computed by LES.

Overall, the mean pressure coefficients computed by the RANS model achieve adequate accuracy within the scatter of the previous numerical and wind tunnel results. The encouraging results suggest that the RANS model is capable of modelling the general mean pressure distribution on the CAARC tall building envelope for use in the PBWE framework.

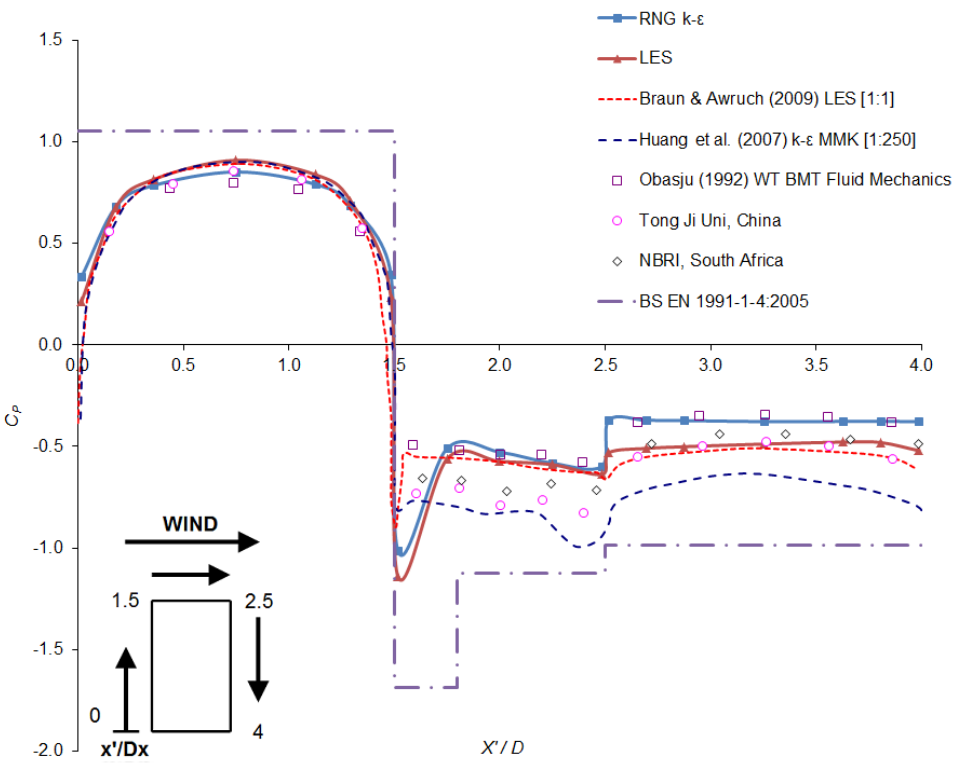

Figure 4.27. Mean pressure coefficients (C_p) at 2/3*H*

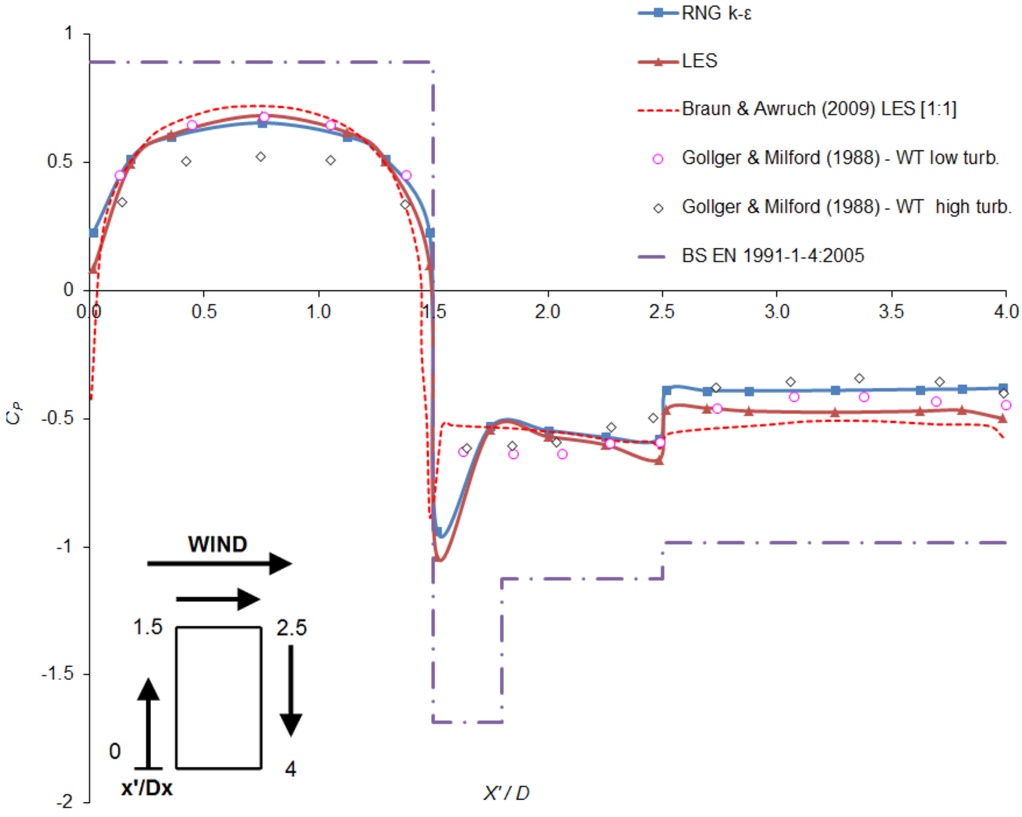

Figure 4.28. Mean pressure coefficients (C_p) at 1/3*H*

The RMS pressure coefficients, C_{RMS}, from previous numerical and wind tunnel studies show quite significant scatter, as shown in Figures 4.29 and 4.30 for 2/3*H* and 1/3*H*, respectively. In both cases, the computed LES results from the present study provide adequate accuracy within the broad scatter of the previous measurements. However, although the typical distribution pattern is similar, the fluctuating components computed by the RANS model are considerably less than the lowest C_{RMS} values determined by Obasju (1992). The failure of RANS to sustain the high atmospheric turbulence in the ABL wind field is considered to be a main reason for this shortcoming. In addition, the RANS model did not generate low-frequency velocity perturbations at the inlet. The results indicate that the RMS component is extremely sensitive to the turbulence in the incident wind field rather than the structure-induced turbulence, particularly on the front face.

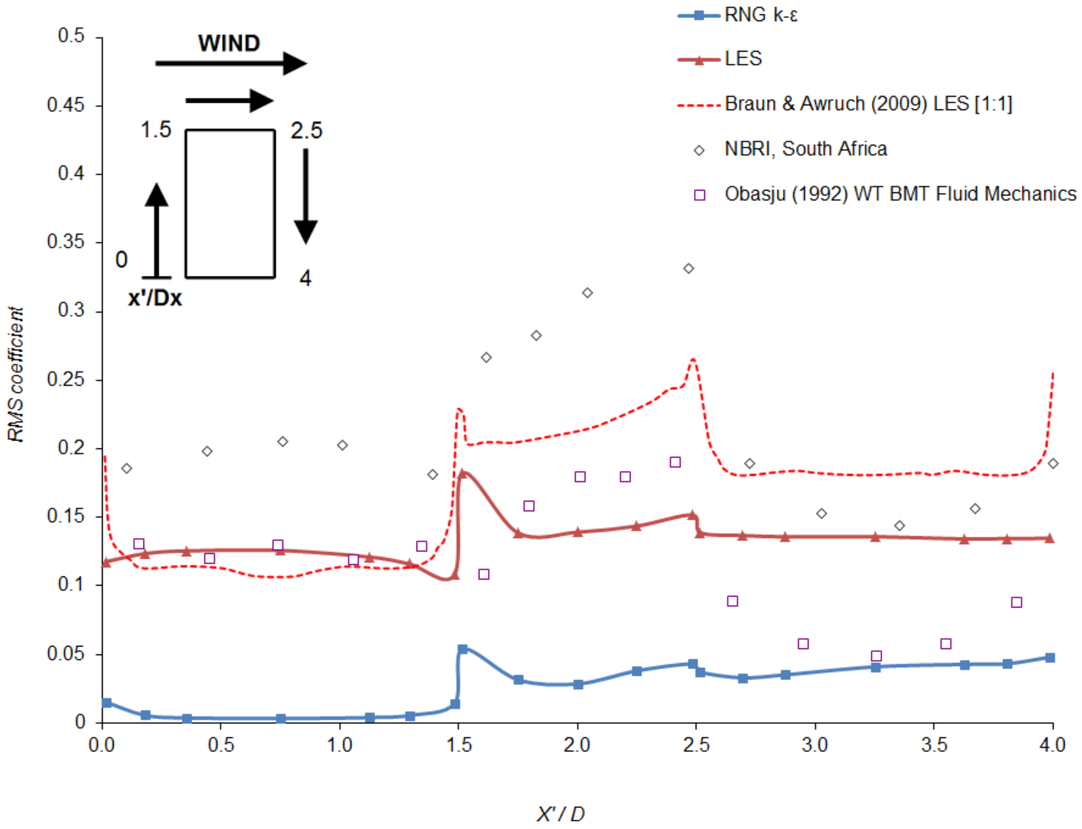

Figure 4.29. RMS pressure coefficients (C_{RMS}) at 2/3*H*

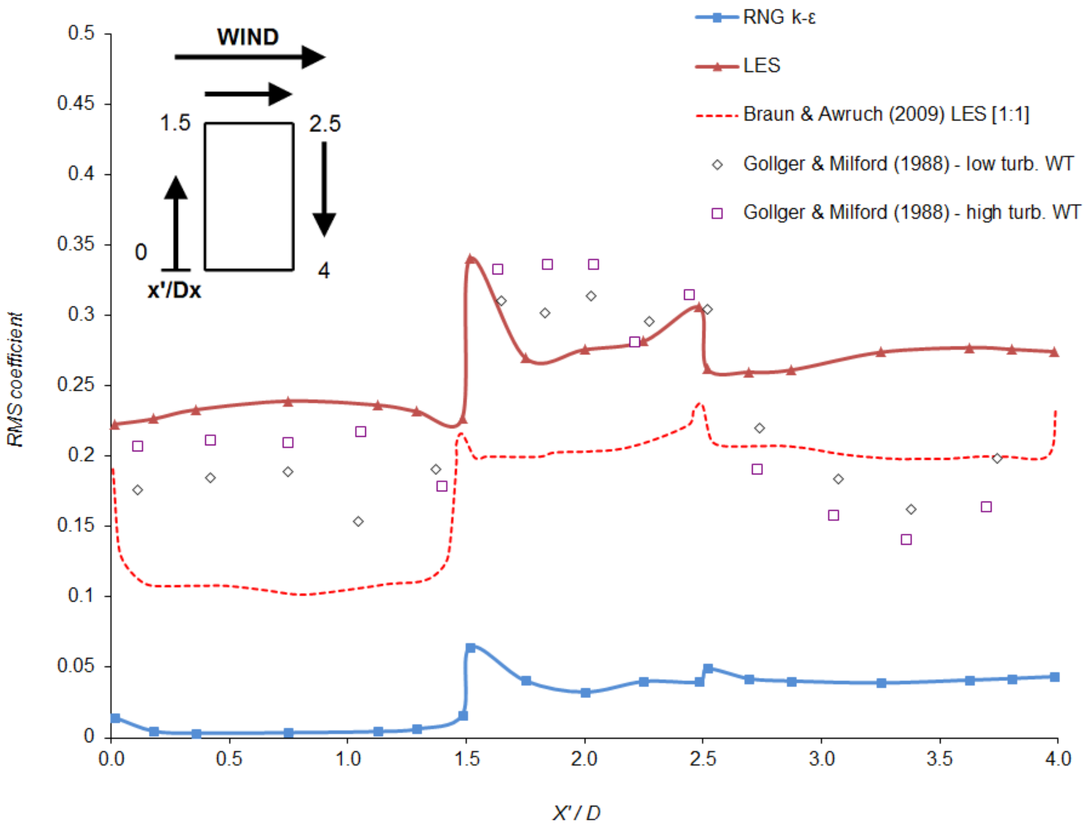

Figure 4.30. RMS pressure coefficients (C_{RMS}) at 1/3*H*

Furthermore, the peak values measured by RANS were as much as 40% lower than those determined by the LES model. This significant difference was expected since the LES model used the spectral synthesizer to generate large amplitude, low-frequency velocity perturbations, whereas the RANS model did not offer such a feature. The results support the Architectural Institute of Japan (AIJ) recommendations (Tamura *et al*, 2008), as illustrated by Figure 2.9, that using RANS to obtain alongwind design wind loads should be supplemented by an appropriate gust-peak factor.

4.5.4 Mean Pressure Contours and Flow Field Computed by RANS Turbulence Model

An assessment of the RNG *k-ε* results was performed to check if the broad flow features in the domain and the general pressure distribution on the building envelope were adequately modelled. This was necessary as the RANS model was the only practically manageable and feasible option to be adopted for the PBWE framework. The results were qualitatively assessed based on the flow fields and pressure contours described by Huang *et al.* (2007) and Braun and Awruch (2009), as detailed in Section 4.2.

The instantaneous velocity contours throughout the entire domain are illustrated in Figure 4.31 for various planes. The alternate vortex shedding is evident in the downstream wake in the *X*-*Y* plane both at 2/3*H* and 1/3*H.* The dissipation of the vortices in the far wake toward the domain outlet is captured. Furthermore, the disorganised nature of the vortex shedding is shown in the *X*-*Z* plane.

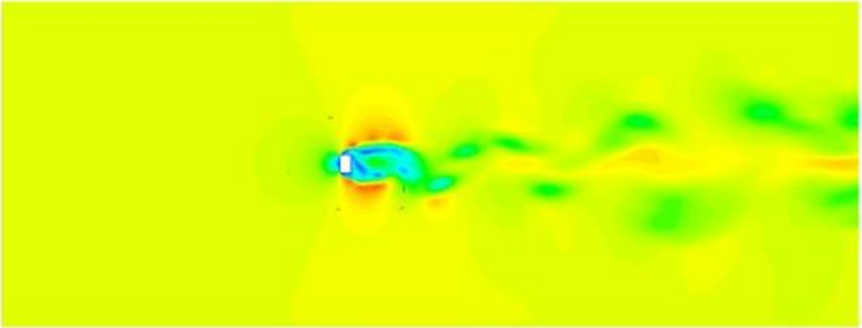

(a) *X*-*Y* plane at *z* = 2/3*H* = 120 m

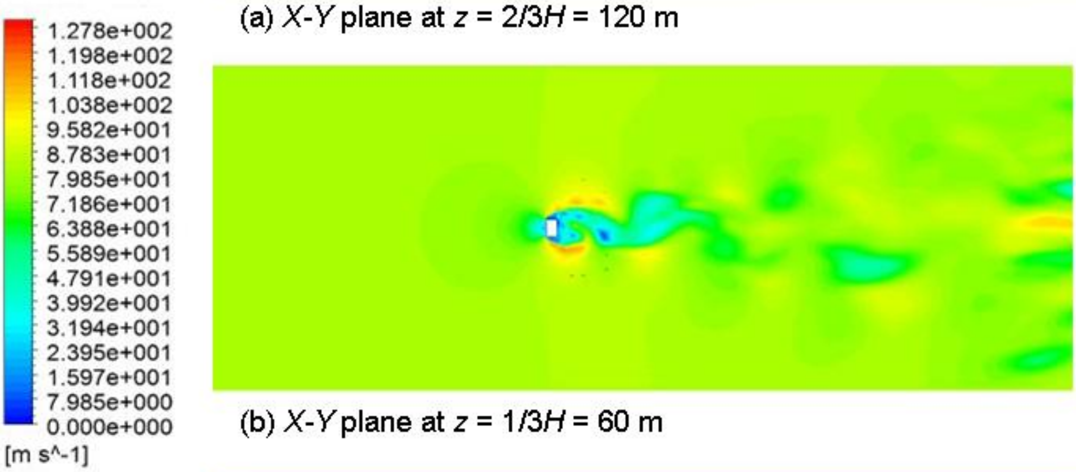

(b) *X*-*Y* plane at *z* = 1/3*H* = 60 m

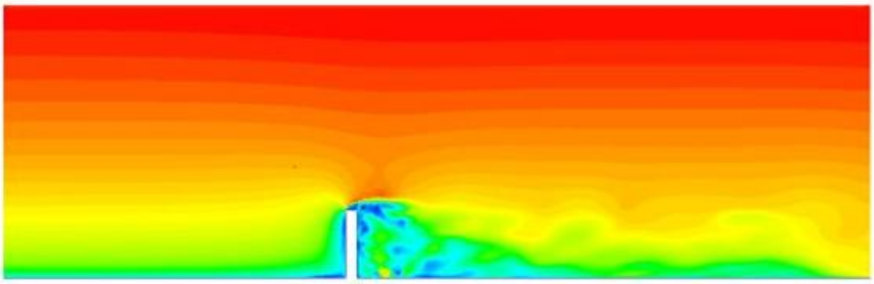

(c) *X*-*Z* plane at *y* = 0 m

Figure 4.31. Instantaneous velocity contours for RNG *k*-*ε* turbulence model

Closer detail of the local flow regime is given by the instantaneous velocity vectors shown in Figure 4.32 and 4.33. The Figures show that a good representation of the fundamental flow field features is achieved by RANS. The separated flow at the leading corners on the side walls and roof and the subsequent near-wake turbulent region are seen. In addition, the vertical fragmentation of the arch vortex in the wake and the alternate shedding phenomena are displayed. Finally, the streamlines in Figure 4.34 display the highly turbulent wake and the horseshoe vortex which forms upwind and is swept round the sides of the building.

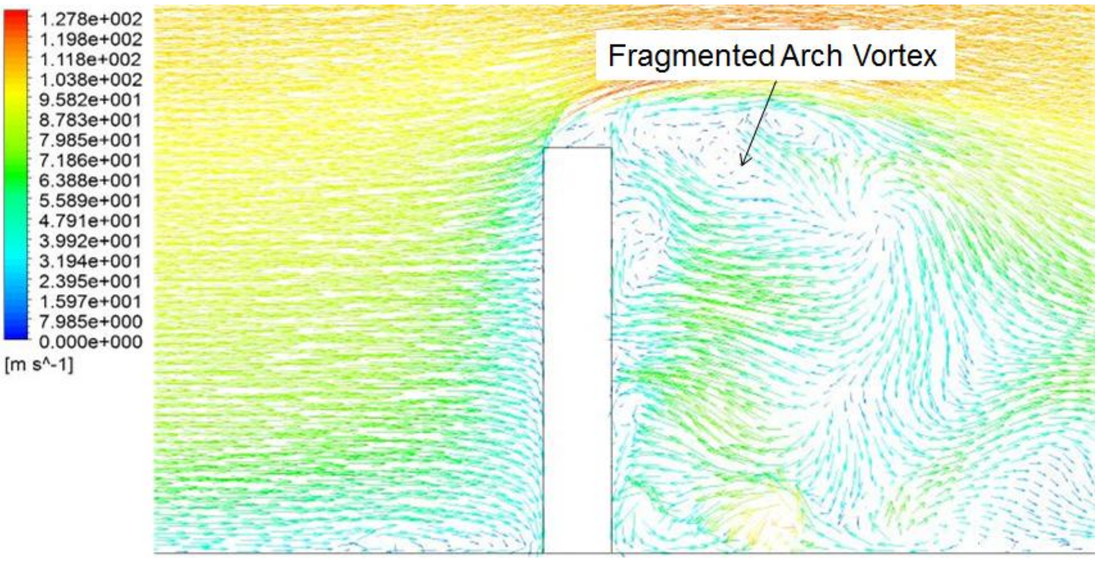

Figure 4.32. Instantaneous velocity vectors (*t* = 120 s) on *X*-*Z* plane at *y* = 0 m

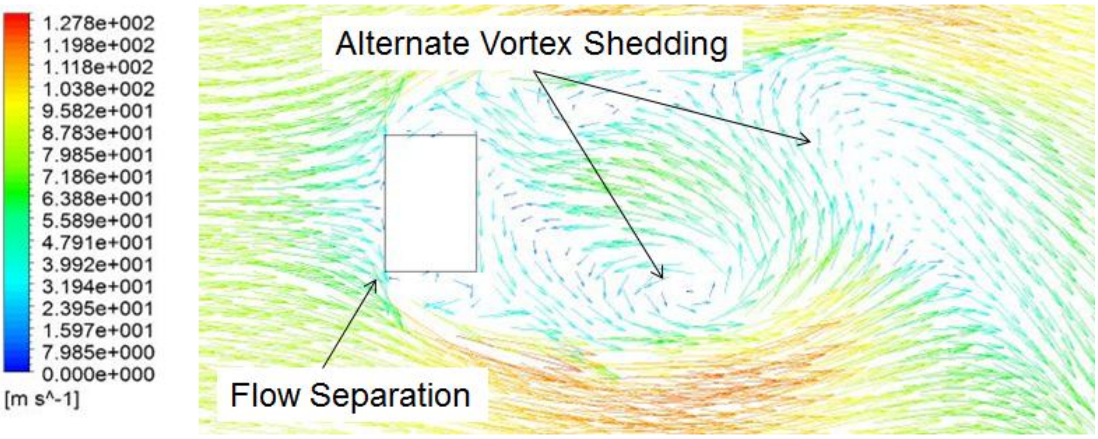

Figure 4.33. Instantaneous velocity vectors (*t* = 120 s) on *X*-*Y* plane at *z* = 2/3*H*

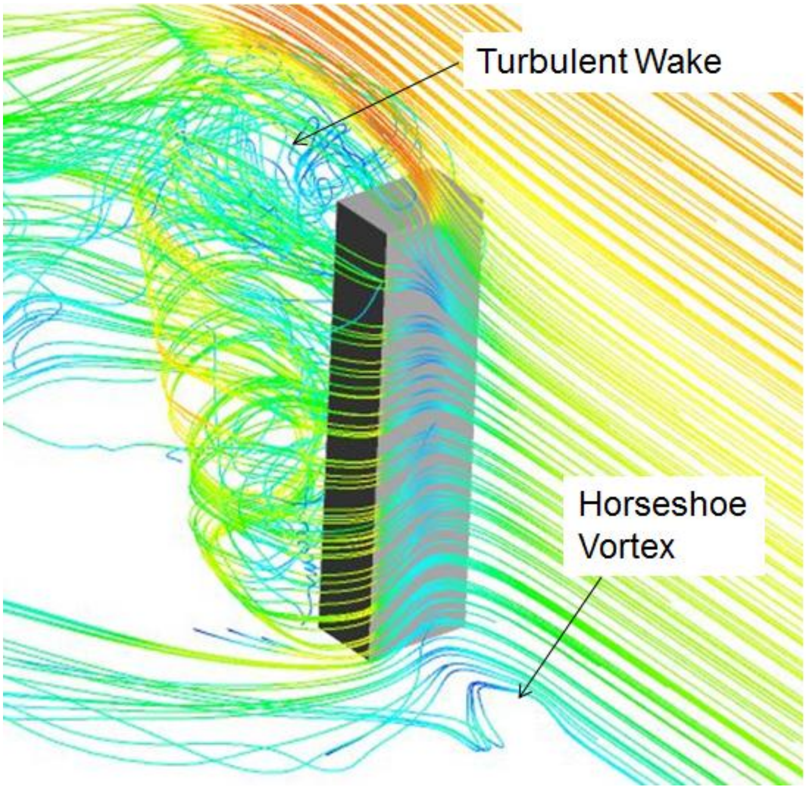

Figure 4.34. Streamlines of flow regime around CAARC building at *t* = 120s

The good qualitative representation of the principal flow features suggested that RANS could also provide a sufficient approximation of the general pressure over the CAARC tall building envelope. The corresponding mean pressure contours are illustrated in Figure 4.35.

On the front face, the mean pressure distribution showed the desired symmetry along the vertical centreline. The maximum drag pressure is exerted at the stagnation point, which occurred in this case at approximately 3/4*H.* This corresponds to the point where the flow was brought to rest. Above this point the flow was displaced over the top of the CAARC building. Below this point the flow was displaced downwards until it meets the ground. The increased pressure at the lower region of the front face due to the phenomena leading to the formation of this horseshoe vortex is evident.

On the side face, the vertical variation of the pressure is much more uniform. It has already been demonstrated from the mean pressure coefficients at 1/3*H* and 2/3*H* that the high suction zones at the leading edge are adequately computed. The fragmented vortex shedding in the near-wake creates the slightly asymmetric pressure distribution on the back face. However, these pressure differences on the back face are very small.

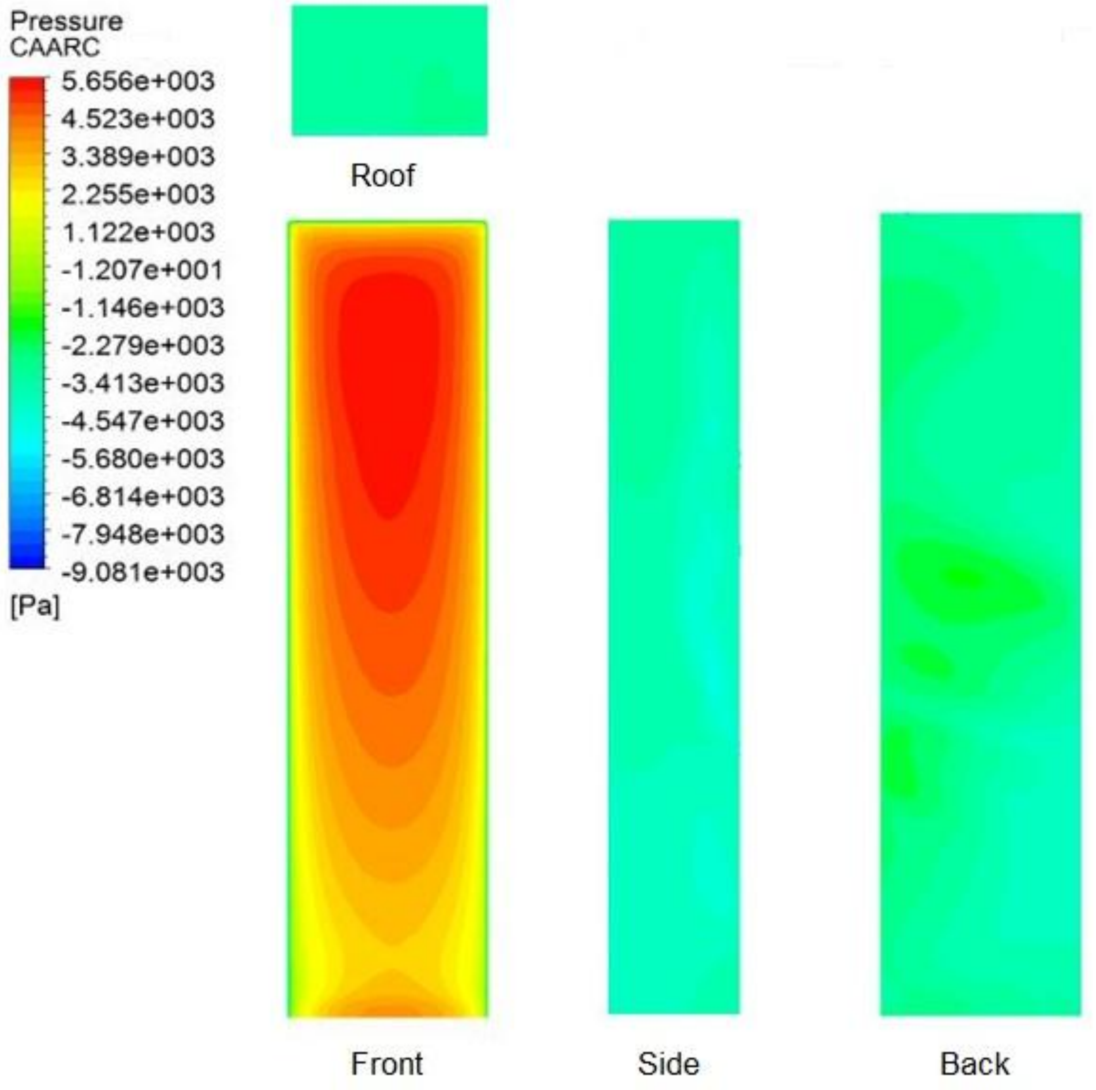

Figure 4.35. Mean pressure contours on CAARC tall building

Ultimately, this qualitative investigation identified that the RNG *k*-*ε* turbulence model provided a good prediction of both the fundamental flow field features and the overall pressure distribution. These results also demonstrate the importance of the quality of the nested mesh design.

4.6 Concluding Remarks

A comprehensive CFD validation study has been performed considering the CAARC standard tall building. The computational analyses demonstrated both the capabilities and practical limitations of RANS and LES turbulence models. The results were assessed in the context of their applicability for the proposed PBWE framework. The turbulence model used for the PBWE methodology was required to provide a sufficient representation of the ABL wind field for modelling the intensity measure (IM) wind events. This was investigated through a series of empty channel studies. It addition, it was necessary that the chosen turbulence model gave a good prediction of the main loading characteristics for the interaction parameter (IP). Therefore, the mean and RMS pressure coefficients predicted by RANS and LES around the perimeter of the tall building at heights of $1/3H$ and $2/3H$ were compared against previous numerical studies, wind tunnel experiments and codes of practice.

The RANS results successfully modelled the target mean velocity profile. Consequently, the overall mean wind pressures were adequately predicted, including the high suction effect due to flow separation at the leading edge on the side face. Knapp (2007) documented problems regarding the calculation of this suction effect on the Silsoe Cube using RANS. It appears that this was due to the near-wall treatment, i.e., using standard wall functions instead of enhanced wall treatment which is default with LES. However, the peak and RMS components of the wind loading were under-estimated by RANS. This was a direct consequence of the poor representation of the turbulence characteristics in the incident wind field.

As expected, the LES results offered the closest agreement to the measured wind tunnel data. However, the associated computational cost makes its implementation for the proposed PBWE framework extremely impractical. The IM wind events have to be simulated for the two tall building case studies, and hence a total of 20 CFD simulations are required since only one incident wind direction is assessed. If full LES was used with an approximate computation time of 88 days per simulation, then the total time to complete all the simulations would be nearly 5 years using 8 CPUs in parallel on the HPC available to this project. This is clearly not acceptable.

The implementation of LES would have been more feasible if the number of available FLUENT licenses was not a limitation. In addition, Section 2.7.4 discussed the promising potential for future improvements in CWE. However, based on the available computational resources it seemed necessary to accept the limitations of RANS for this study in order to conceptually develop the proposed PBWE framework.

5

Site Hazard Analysis

5.1 Preamble

In this Chapter the procedure for the site hazard analysis is detailed. The derived IM wind events are used for the subsequent PBWE assessment of the two tall building case studies. The discretisation process for the probability distributions of the two considered variables v_b and z_0 is demonstrated in their respective Sections. The formation of the Latin Hypercube sampling space is then illustrated. This includes a description of the sampling procedure that is followed to obtain the ten samples of variable sets v_b and z_0. These combinations are then used for Equations 3.3 to 3.7 to express the vertical variation of the mean wind velocity and turbulence properties. The resulting profiles of the IM wind events are illustrated. It is these derived IM profiles which are specified as inlet boundary conditions for the subsequent series of CFD simulations.

5.2 Basic Wind Velocity

According to the wind speed map in the National Annex to BS EN 1991-1-4:2005 (British Standards Institution, 2008a), shown in Figure 3.2, the basic wind speed in country terrain for Glasgow is approximately 25.4 ms^{-1} at an elevation of 10 metres. This corresponds to a Q = 0.02 annual risk of exceedance (50-year return period). The risk of exceedance distribution can be plotted by applying the probability factor, c_{prob}, from Equation 3.1 for a range of Q values to this basic wind velocity. The resulting risk of exceedance distribution for Glasgow is shown in Figure 5.1.

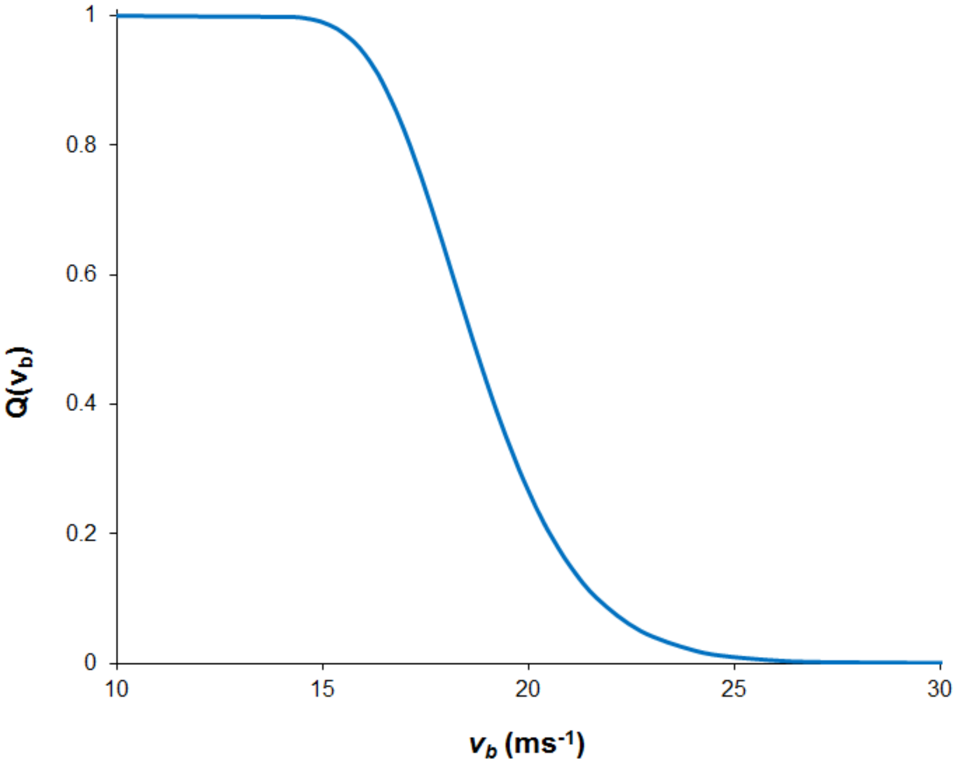

Figure 5.1. Risk of exceedance distribution for Glasgow

The cumulative distribution function is simply the reciprocal of the risk of exceedance distribution and is given in Figure 5.2. The steepest gradient of the cumulative distribution function represents the most likely value of the basic wind velocity, i.e., the mode.

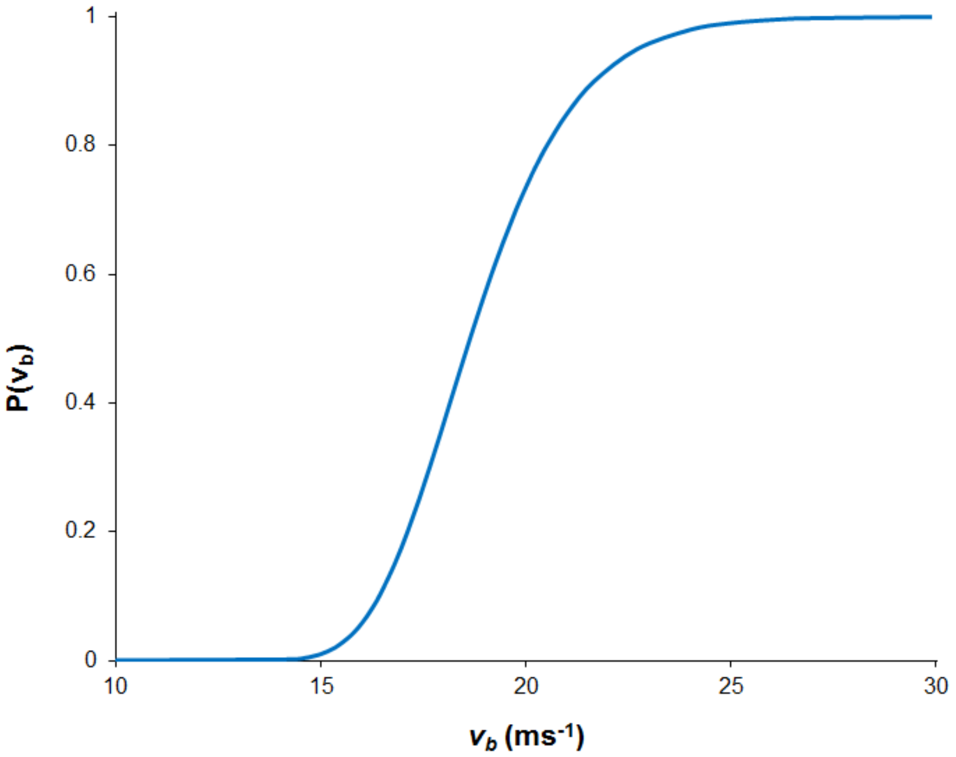

Figure 5.2. Cumulative probability distribution for Glasgow

The data of Figure 5.2 was fitted to the FTI distribution given by Equation 2.1 in MATLAB using the curve fitting command, *cftool*, to quantify the specific values of the mode, U, and dispersion, $1/\alpha$. This was necessary since the combination of the basic wind speed map and Equation 3.1 provided by NA to BS EN 1991-1-4:2005 did not allow a direct solution for the mode and dispersion to be derived. The best-fit analysis determined the mode was U = 18.3 ms^{-1} and the corresponding reciprocal of the dispersion was $\alpha = 0.56$. Therefore, the probability density function of v_b in Glasgow country terrain (z_0 = 0.03 m) is expressed by

$$p(v_b) = \exp\{-(0.56(v_b - 18.3))\}\exp[-\exp\{-(0.56(v_b - 18.3))\}] \qquad (5.1)$$

The resulting probability density function is shown in Figure 5.3. Deriving this explicit description is essential for forming the Latin Hypercube sampling space.

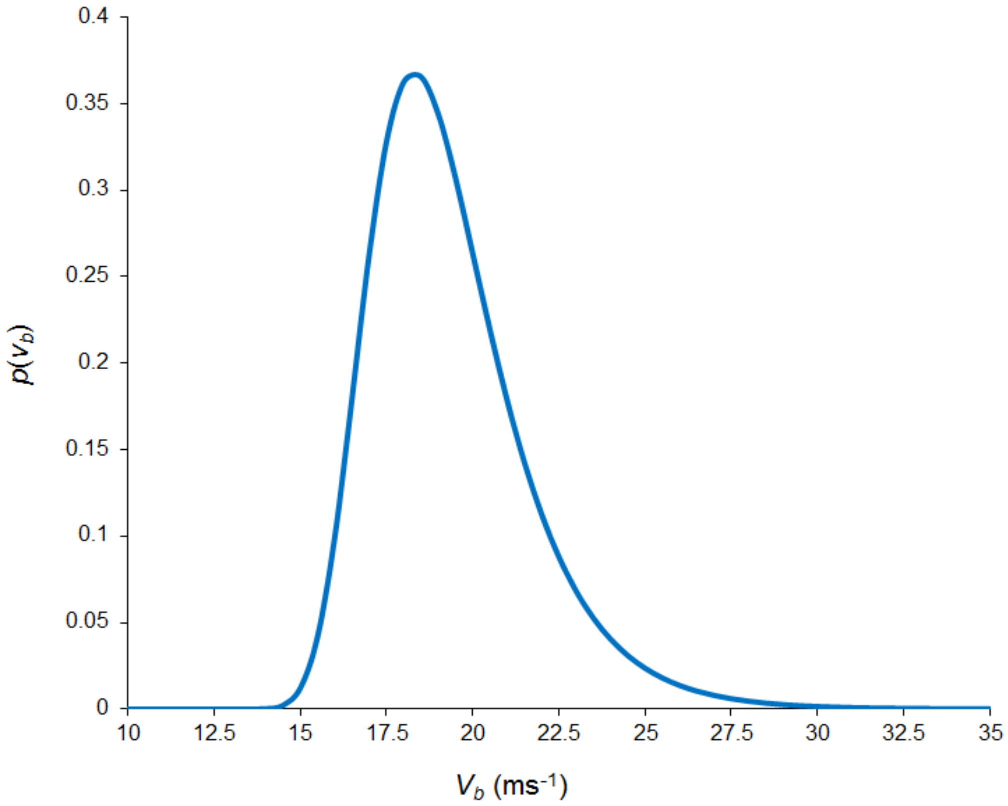

Figure 5.3. FTI probability distribution for Glasgow v_b

The next stage requires the distribution of Figure 5.3 to be normalised and subdivided into N equally probable intervals. The chosen number of samples is ten, i.e., $N = 10$. The reduced variate, using the mode and reciprocal of dispersion values 18.3 and 0.56 respectively, $y_{Vb} = 0.56(v_b - 18.3)$ is used to normalise the distribution and is substituted into Equation 5.1, which reduces the expression to

$$p(y_{V_b}) = \exp(-y_{V_b})\exp\left(-\exp(-y_{v_b})\right) \tag{5.2}$$

As the integral of the probability density function is equal to unity, then the integral of each equally probable interval must be equal to 0.1. The integral of Equation 5.2 was created in MathCAD and the upper and lower limits for each interval were determined iteratively. The resulting discretised probability distribution is illustrated in Figure 5.4. This reduced probability density function is ready to be used to form the grid of the Latin Hypercube sampling space.

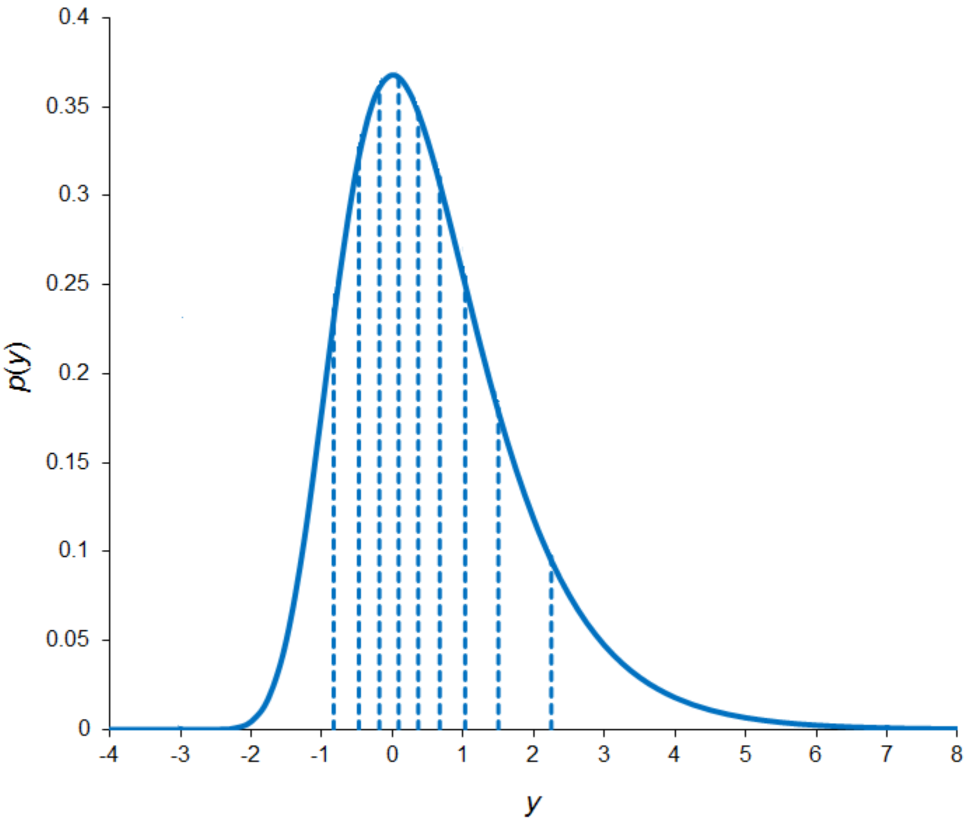

Figure 5.4. Normalised distribution for y_{vb} divided into 10 equally probable intervals

5.3 Aerodynamic Roughness Height

A similar discretisation procedure was followed for the Gaussian probability distribution of the aerodynamic roughness height, z_0. As mentioned in Section 3.2.1, the mean of the distribution is 0.3 m which corresponds to the general z_0 for town terrain categories. The integral of the Gaussian probability density function given by Equation 3.2 was set up in MathCAD. The prerequisite was to ensure that the determined variance σ enclosed 97.5% probability within the limits of 0.2 m and 0.4 m. This derived variance was $\sigma^2 = 2 \times 10^{-3}$. The resulting probability density function used for z_0 in Glasgow town terrain is shown in Figure 5.5.

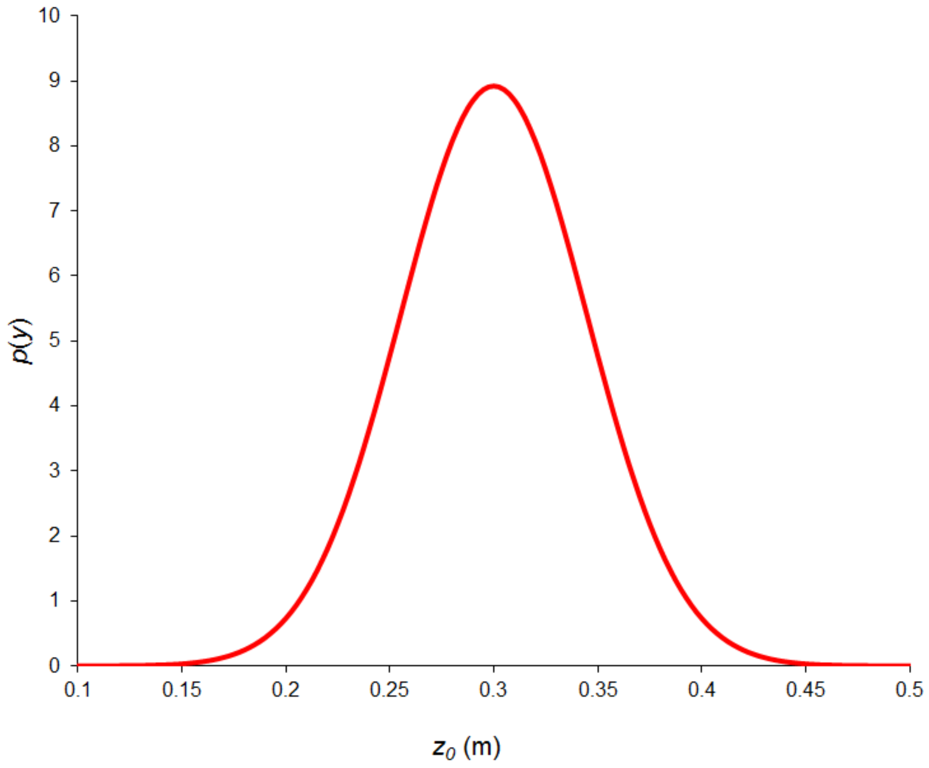

Figure 5.5. Gaussian probability distribution for Glasgow z_0

The probability distribution illustrated in Figure 5.5 was normalised by substituting the mean and variance values in the expression for y_{Zo} which is given by

$$y_{Zo} = \frac{z_0 - \overline{z_0}}{\sigma} = \frac{z_0 - 0.3}{\sqrt{0.002}} \tag{5.3}$$

The same process as Section 5.2 was followed to subdivide the normalised probability distribution into ten equally probable intervals for Latin Hypercube sampling. The completed discretisation is shown in Figure 5.6.

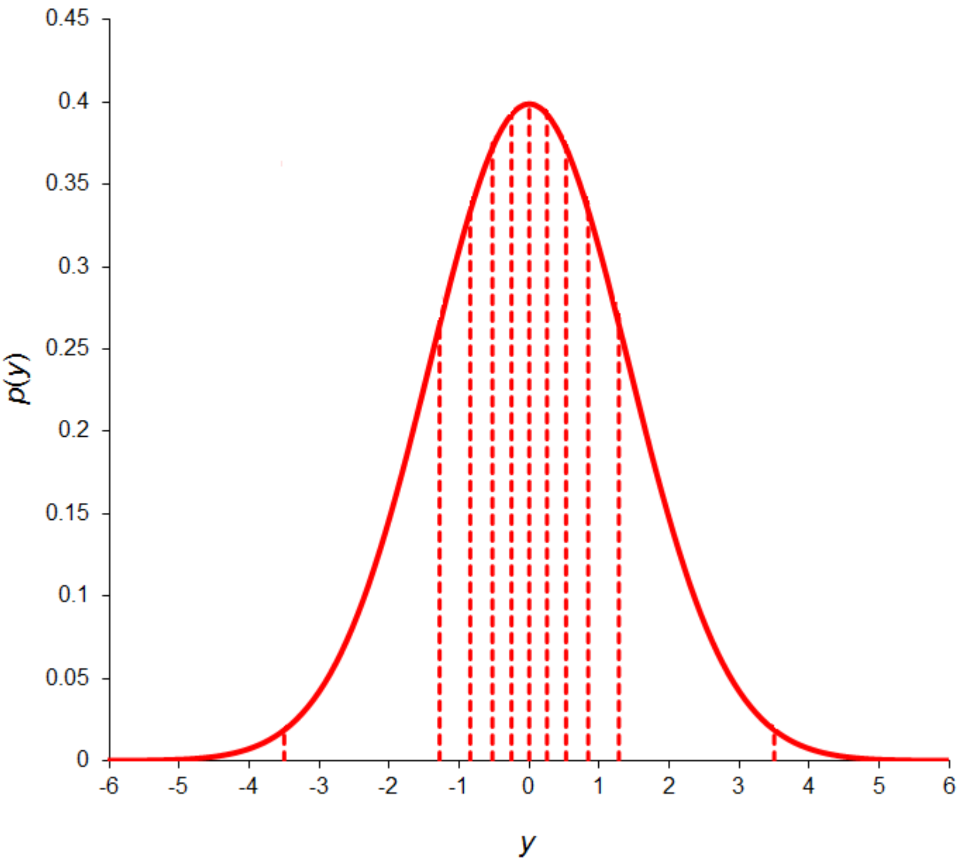

Figure 5.6. Normalised distribution for z_0 divided into 10 equally probable intervals

5.4 Latin Hypercube Sampling Space

The reduced variables of v_b and z_0 form the two-dimensional Latin Hypercube sampling space. The resulting sampling grid is shown in Figure 5.7. The normalised z_0 variable is plotted on the vertical axis and the equal probability intervals are shown in red. The normalised variable v_b is plotted on the horizontal axis and the equally probable boundaries are mapped in blue. This sampling grid shown in Figure 5.7 highlights the contrast in shape between the symmetrical probability density function of z_0 and the skewed probability density function of v_b.

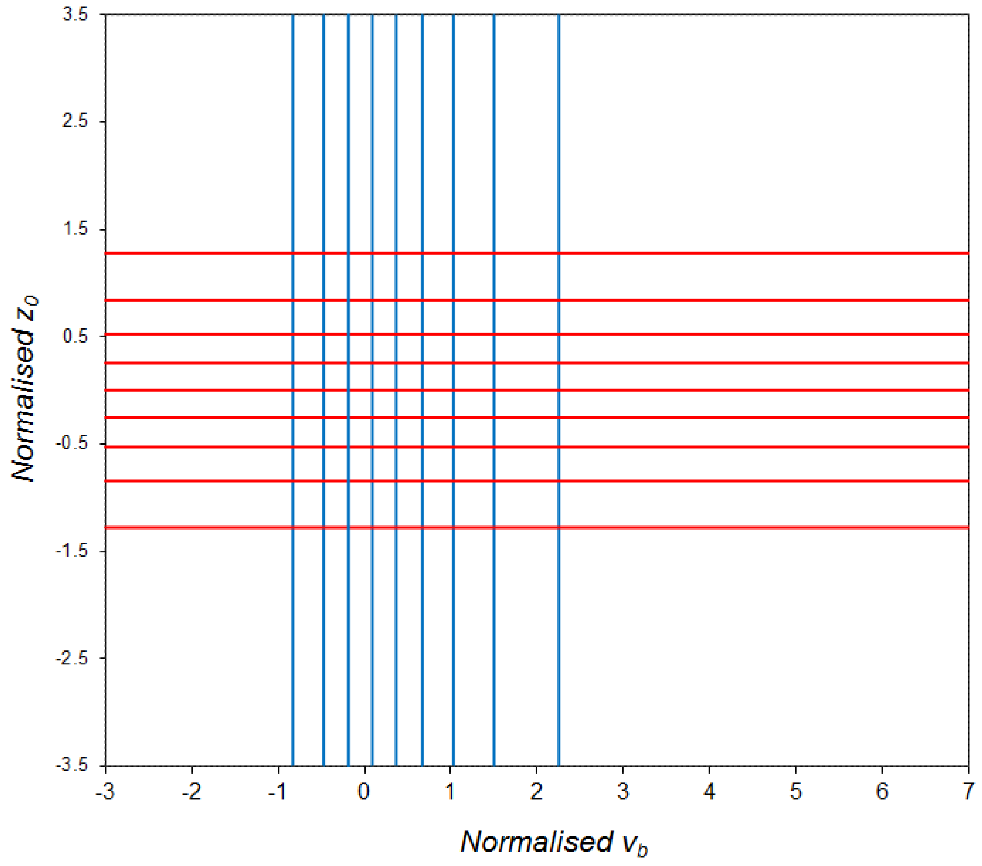

Figure 5.7. Hypercube sampling space for 10 realisations of v_b and z_0

The first stage requires the sampling cells to be determined. This is based on the fundamental principle that only one sample is taken within the axis-aligned hyperplane containing it. The 10 x 2 matrix *P* was formed for this initial sampling phase. The random permutation tool in MATLAB was used to form the columns of the *P* matrix and the result is shown in Equation 5.4. The first column represents the grid number for the normalised v_b intervals, while the second column is the grid number for the normalised z_0 intervals.

$$P = \begin{bmatrix} 1 & 7 \\ 2 & 9 \\ 3 & 2 \\ 4 & 10 \\ 5 & 4 \\ 6 & 3 \\ 7 & 8 \\ 8 & 1 \\ 9 & 6 \\ 10 & 5 \end{bmatrix} \tag{5.4}$$

The P sampling space is illustrated in Figure 5.8. The shaded cells correspond to the grid combinations determined by the P matrix. The grid cells are numbered in ascending order from left to right and bottom to top. It is evident that the basic requirement for only one sample to be taken from each row and column is satisfied.

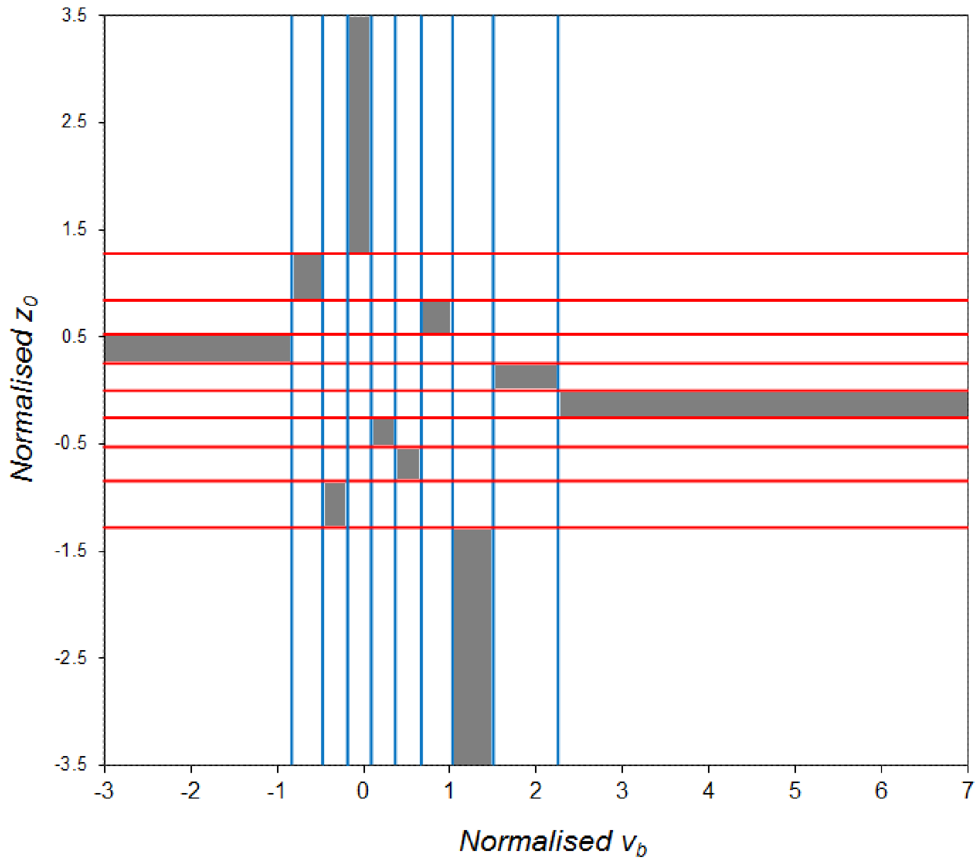

Figure 5.8. P sampling space for 10 realisations of v_b and z_0

The specific values of v_b and z_0 must be determined from within these sampling cells. This requires the 10 x 2 matrix R of random numbers from the uniform (0,1) distribution to be formed. Again, the research utilised the random permutations function in MATLAB to create the following R matrix

$$R = \begin{bmatrix} 0.759 & 0.599 \\ 0.509 & 0.658 \\ 0.075 & 0.747 \\ 0.385 & 0.439 \\ 0.320 & 0.588 \\ 0.184 & 0.546 \\ 0.758 & 0.606 \\ 0.672 & 0.442 \\ 0.413 & 0.727 \\ 0.256 & 0.292 \end{bmatrix} \tag{5.5}$$

It was mentioned in Section 3.2.3 that this matrix R represents the ratio of where the sample point lies between the lower and upper limits of the relevant sampling cell from the matrix P. The resulting S matrix was then calculated as

$$S = \begin{bmatrix} -1.355 & +0.416 \\ -0.650 & +1.130 \\ -0.453 & -0.953 \\ -0.080 & +2.255 \\ +0.177 & -0.365 \\ +0.422 & -0.669 \\ +0.943 & +0.717 \\ +1.346 & -2.518 \\ +1.810 & +0.184 \\ +3.466 & -0.179 \end{bmatrix} \tag{5.6}$$

The values from this S matrix are mapped on the Latin Hypercube sampling grid in Figure 5.9. These normalised values of v_b and z_0 must then be transformed to obtain their real parametric values.

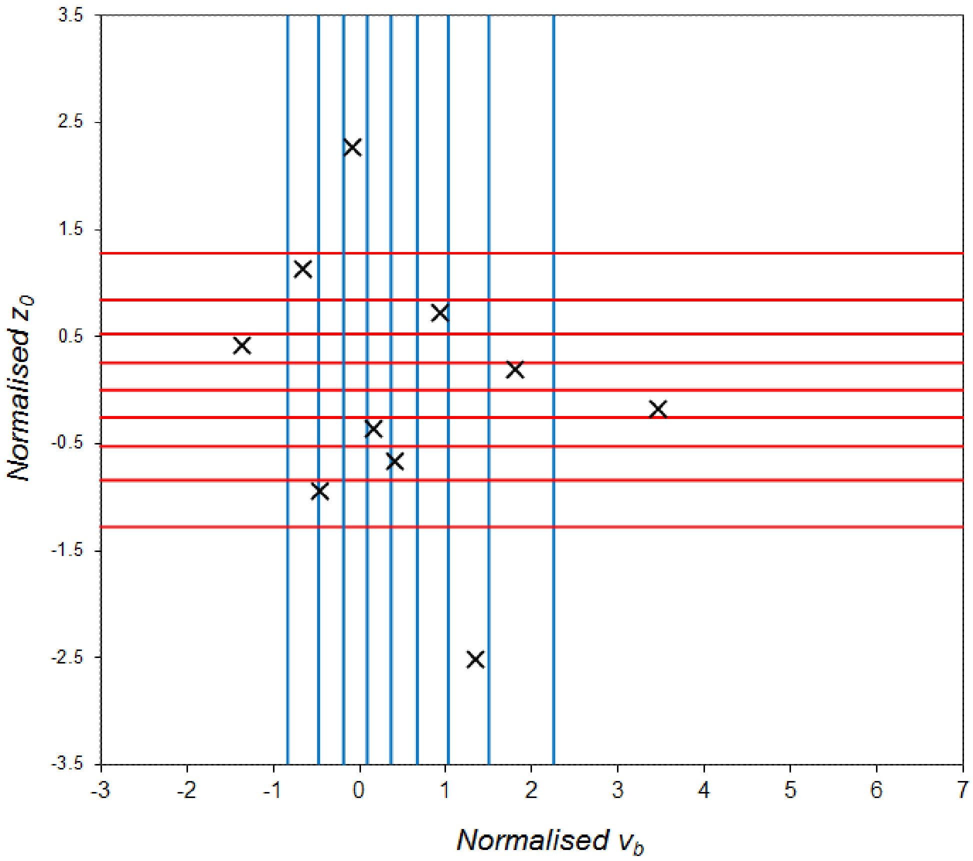

Figure 5.9. The final *S* sampling space for 10 realisations of v_b and z_0

5.5 Intensity Measure Wind Events

The parametric combinations of v_b and z_0 determined by the Latin Hypercube sampling method to describe the IM wind events are listed in Table 5.1. The values are accompanied by the corresponding frictional velocity u_* for each IM wind event. These parameters are used for Equations 3.3 to 3.7 to form expressions of the vertical variation of the mean wind velocity, the turbulence intensity and the turbulence length scale. The resulting profiles of these atmospheric boundary layer (ABL) characteristics are shown in Figures 5.10 to 5.12.

The K_x factor in Equation 3.3 considers the transition due to a step change from upwind country terrain where v_b is measured (z_0 = 0.03 m) to the town terrain where z_0 is sampled. The mean wind velocity measured at 10 metres at the site in town is less than the sampled v_b since the increased roughness of the town terrain exerts a greater retardation effect to the mean wind speed. In addition, this effect requires more momentum to be transferred from the smooth gradient wind to overcome the surface friction, which increases the depth of the ABL. The kinetic energy removed in the mean velocity from the increased roughness appears as turbulence. Thus, the step-change in surface roughness also increases the intensity of the atmospheric turbulence.

The mean wind velocity profile for the IM10 wind event is presented in Figure 5.13 along with the equilibrium profiles for the upwind country terrain and the site town terrain. It is evident that this transition state produces a higher mean wind velocity than would have been provided if a horizontally homogeneous ABL for the town terrain had been assumed. This would affect the structural wind loads since the pressure is directly related to the velocity.

Table 5.1. Summary of the IM wind event parameters

IM	v_b **(ms^{-1})**	z_0 **(m)**	u_* **(ms^{-1})**
1	15.86	0.313	1.820
2	17.13	0.336	2.006
3	17.49	0.270	1.924
4	18.16	0.371	2.190
5	18.62	0.288	2.086
6	19.06	0.279	2.117
7	20.00	0.323	2.315
8	20.72	0.220	2.159
9	21.56	0.306	2.457
10	24.54	0.294	2.765

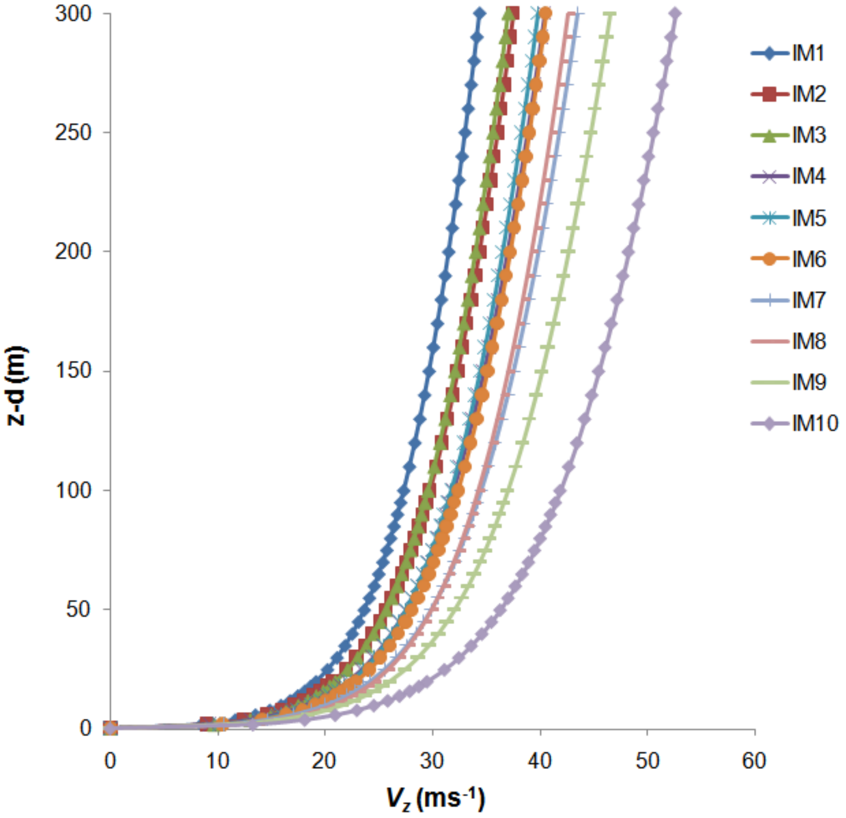

Figure 5.10. Vertical profiles of 10-minute mean wind velocity for the IM wind events.

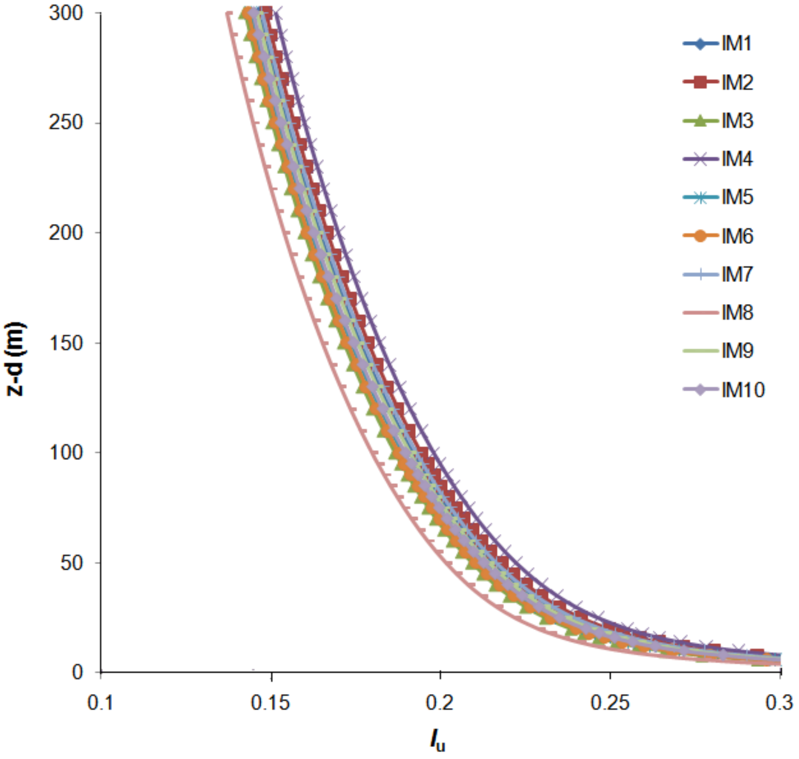

Figure 5.11. Streamwise turbulence intensity profiles for the IM wind events.

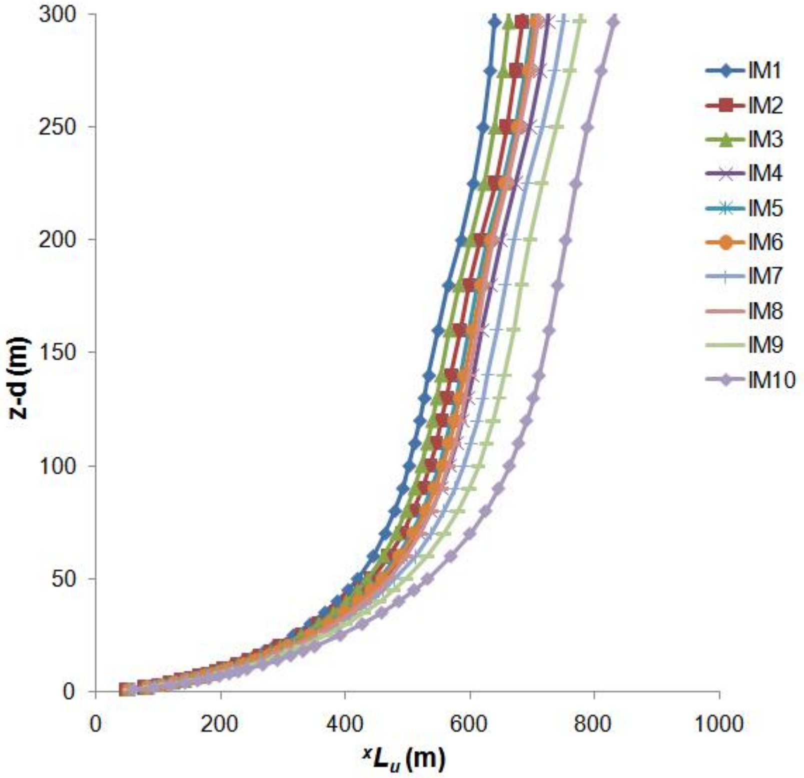

Figure 5.12. Streamwise turbulence length scale profiles for the IM wind events.

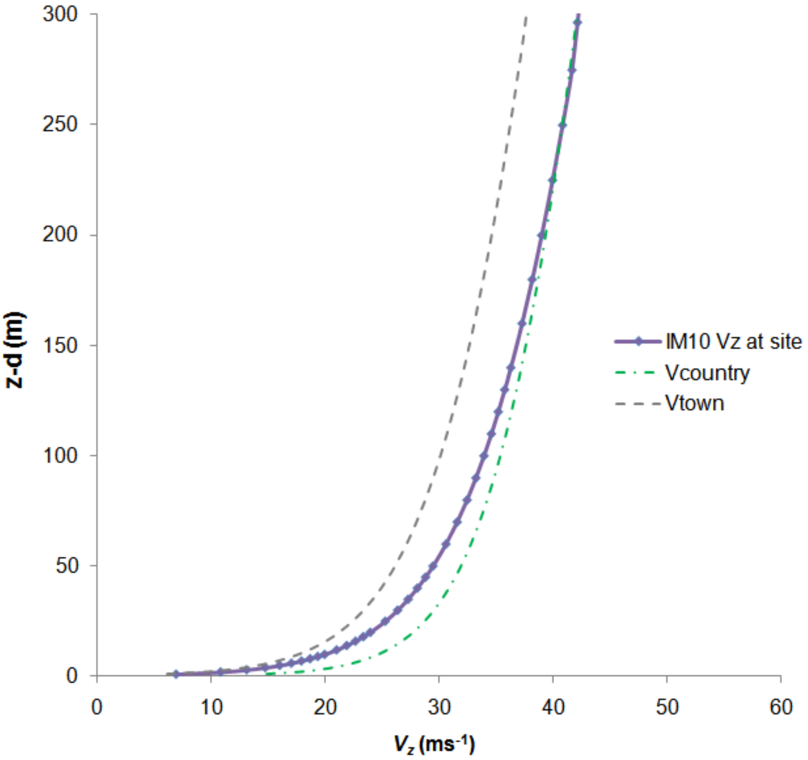

Figure 5.13. 10-minute mean wind velocity profile for the IM10 event showing transition state

5.6 Concluding Remarks

The Chapter has detailed the Latin-Hypercube sampling procedure used for the first stage of the PBWE framework: the site hazard analysis. The two tall building case studies are proposed for the same site wind environment, Glasgow. Therefore, the IM wind events derived from this site hazard analysis are used for the PBWE assessment of both tall building designs.

The influence of the transition factor, K_x, on the mean wind velocity was also demonstrated. Equilibrium atmospheric boundary layer (ABL) flow is an idealisation that will never occur due to the proximity of the UK coastline. Therefore, this factor helps improve the representation of the mean wind velocity due to a single step change in surface roughness.

The ten IM wind events derived from the site hazard analysis are specified as the inlet boundary conditions for the subsequent CFD simulations. However, it was shown in Chapter 4 that successful modelling of the ABL wind field depends on the chosen turbulence model. The CFD simulations using the LES turbulence model can be expected to provide a sufficiently accurate representation of both the mean wind velocity and the turbulence characteristics. Meanwhile, the empty channel study performed in Chapter 4 identified that the RANS turbulence model fails to sustain the characteristics of the atmospheric turbulence specified at the inlet. Therefore, the CFD simulations using the RANS model can only be expected to adequately model the mean wind velocity profile of each IM wind event. This limitation is important for assessing the results in Chapters 6 and 7.

6

PBWE Analysis for Regular Tall Building

6.1 Preamble

This Chapter follows the remaining stages of the simulation framework for the PBWE assessment of a regular tall building. The computational models for the fluid and structure domains are detailed. Two PBWE assessment strategies are considered. The initial PBWE assessment is based on modelling the IM wind events using the RANS turbulence model. The results from the structural analyses indicate that the structure is sensitive to load fluctuations on the front face. This raises concerns regarding the adequacy of the RANS model for the PBWE assessment for a structure of this form; it fails to adequately model the atmospheric turbulence in the incident wind field.

An alternative PBWE simulation strategy is then proposed. The LES turbulence model is used to calculate the pressure histories for the IM10 event only. The load histories from this reference event are then scaled for the remaining IM1 to IM9 events by using the corresponding mean pressures predicted by the RANS model; it was concluded from Chapter 4 that RANS can compute the mean pressures to an adequate level of accuracy. Such a simulation strategy does not explicitly consider the variation of turbulence length scale, turbulence intensity and excitation frequency between the wind events. The results show that the response of the regular tall building design is much more sensitive to the incoming atmospheric turbulence (including low-frequency perturbations) than the structure-induced turbulence.

6.2 Fluid Domain: Computational Model in ANSYS FLUENT

The CFD simulations of the regular tall building are based on the incident wind field acting normal to the wider building face, as indicated in Figure 6.1. The decision to base the principal geometry of the regular tall building on the CAARC standard tall building meant the adoption of the optimum domain geometry and near-wall mesh arrangement which had already been developed within Chapter 4. Details of the D2 domain and the M3 mesh refinement are reproduced in Table 6.1.

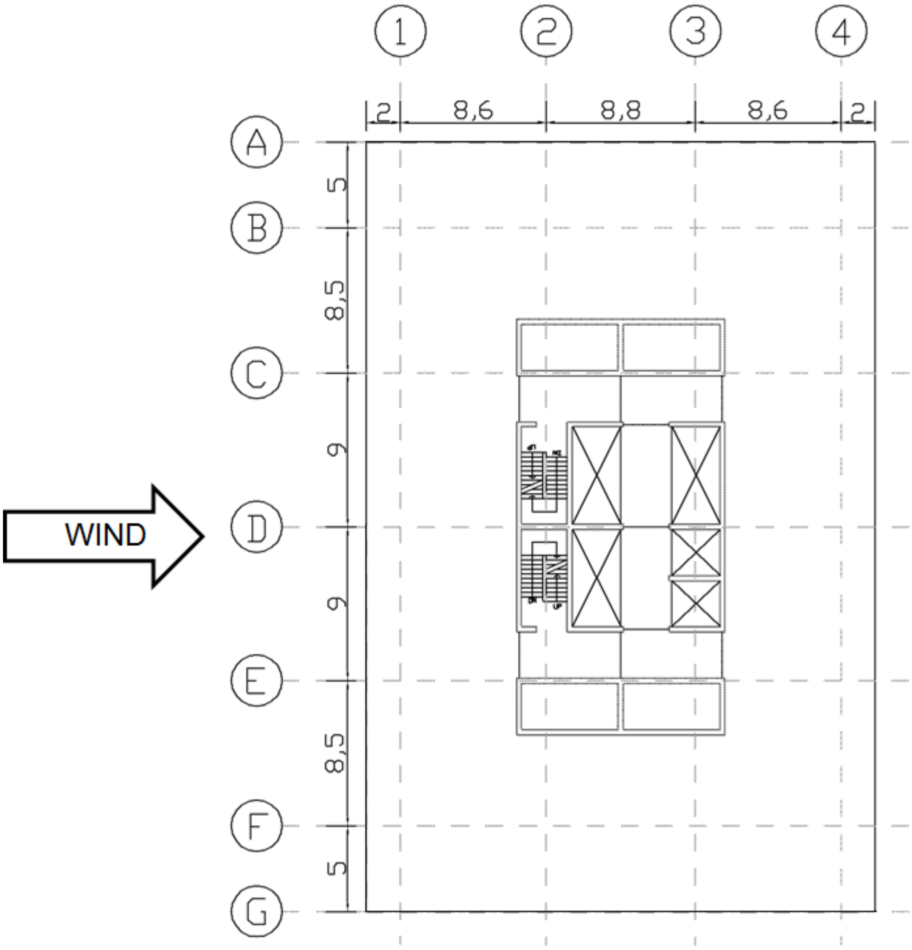

Figure 6.1.Orientation of the regular tall building relative to the incident wind

Table 6.1. Details of the domain geometry and mesh interval sizes

	DX (m)	DY (m)	DZ (m)
D2	900 + *D* + 1350	585 + *B* + 585	720
M3	0.54	0.60	1.20

The resultant surface mesh for the entire computational domain is shown in Figure 6.2. It should be noted that the surface mesh at the inlet and the top planes of the domain are omitted to increase clarity. The surface mesh at the near-wall region in FLUENT is shown in Figure 6.3. The inflated boundary layer mesh expanding from the building faces is clearly evident. Further detail of the computational mesh is provided in Sections 4.3.2 and 4.5.2. The CFD model using this mesh design contained a total of 2.97 million computational cells and provided a streamwise blockage ratio (area of windward face / area of inlet plane) of 0.94%.

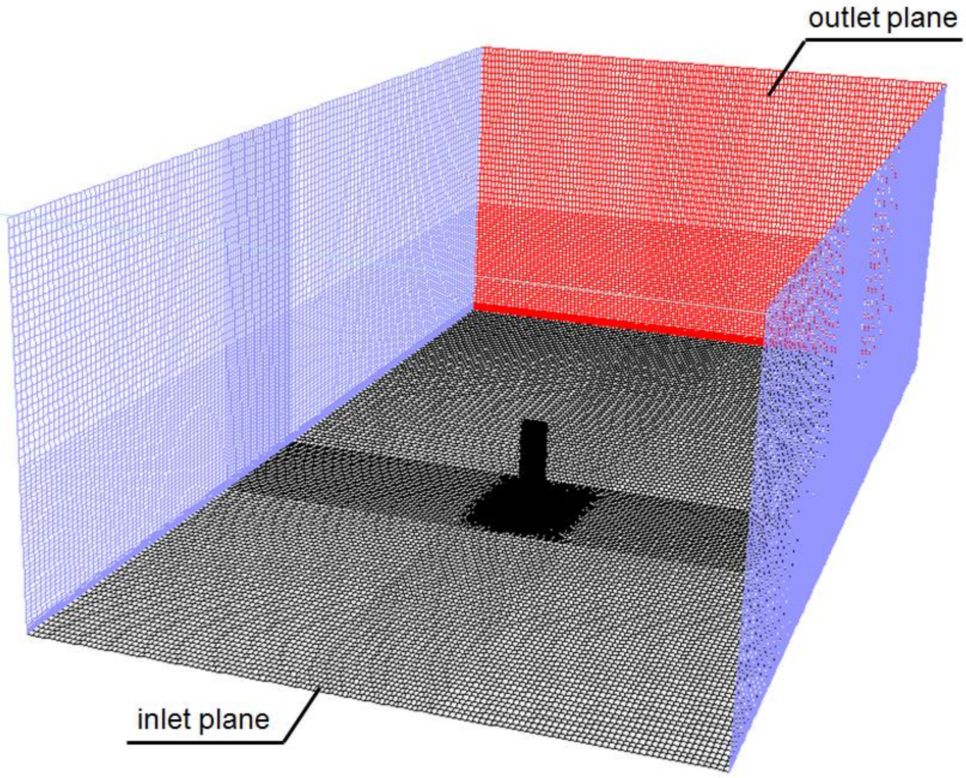

Figure 6.2. Fluid domain and surface mesh of regular tall building CFD model

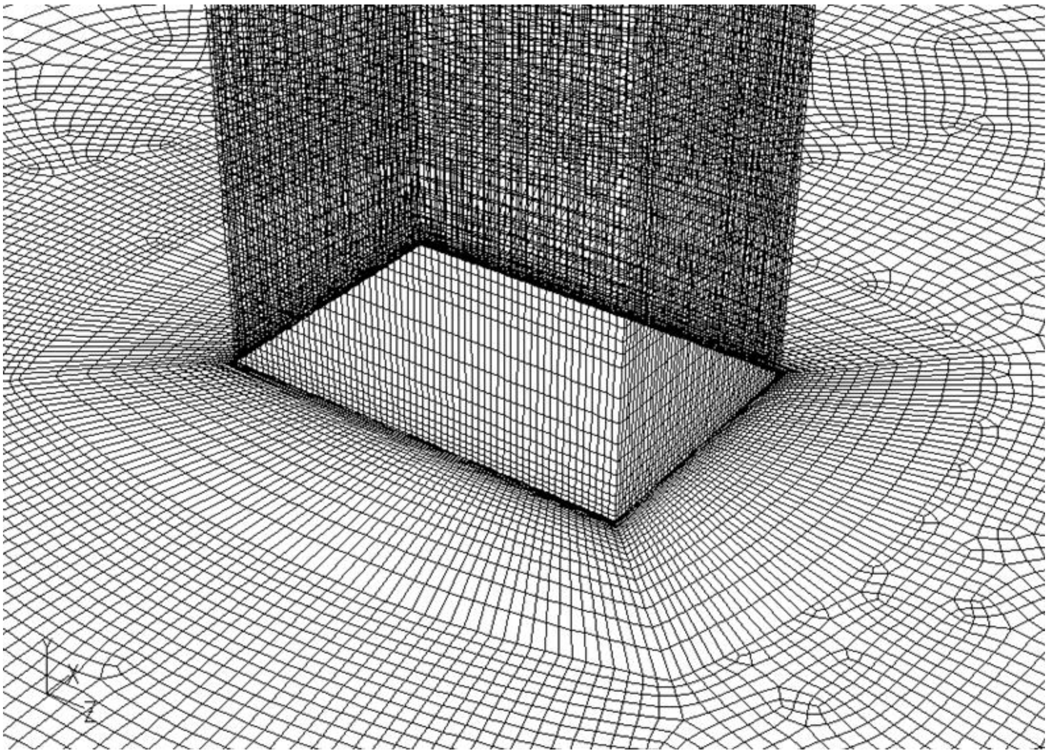

Figure 6.3. Near-wall surface mesh for the regular tall building CFD model

This computational mesh was used for separate CFD simulations for each of the ten IM wind events, as discussed in Chapter 5. The vertical profiles of the mean wind velocity, turbulence kinetic energy and turbulence dissipation rate associated with these IM wind events were formulated as UDFs (User-defined functions, written in C) to be interpreted by FLUENT. The inflow boundary condition was set as a velocity inlet and the relevant IM parameters were specified. As in Chapter 4, the top and side boundary conditions were also defined as velocity inlets with corresponding streamwise flow components only. The outflow was defined as a pressure outlet as detailed in Section 4.3.4. The building surfaces and domain floor were again modelled as wall boundaries with the no-slip condition.

A series of monitors were created across the building envelope to measure pressure histories during each CFD simulation. To position logically the array of pressure monitors, the total surface area of the regular tall building was subdivided into smaller areas based on the column grid and floor levels of the tall building design. A pressure monitor was created at the centroid of each of the discretised surface areas and the measured pressures were subsequently assumed constant over this small region. A total of 22 monitors were created around the perimeter at 25 intervals throughout the span of the tall building. In addition, 28 monitors were distributed on the roof level. This arrangement provided a total of 578 pressure monitors on the tall building, shown in Figure 6.4. The original intention to create monitors around the building perimeter at every level proved impractical; the HPC installation of FLUENT software could not accommodate so many pressure monitor locations. This was found to be associated with writing output data for more than 1000 monitors rather than a limitation of the HPC platform itself. In addition, there was not enough RAM available on the standard desktop PC to solve the Strand7 model with more than 800 wind load cases. Therefore, the strategy was revised and monitors were created at every second level to reduce the number of monitors to a manageable number.

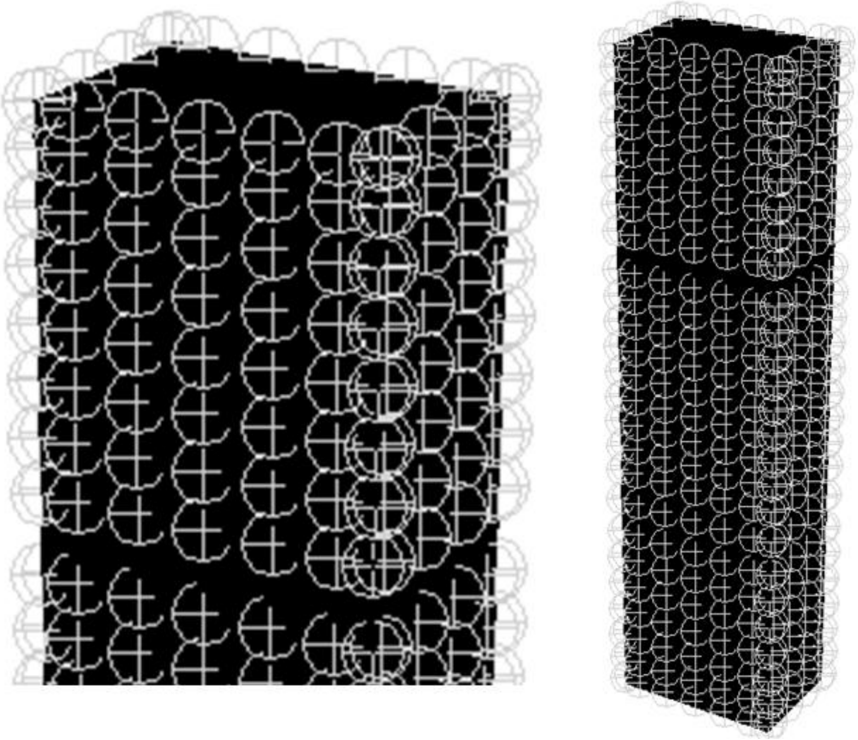

Figure 6.4. Pressure monitors created on the regular tall building in the CFD domain

The data from these 578 pressure monitors were written to separate external output (.out) files. The one-way coupling interface was developed to open and extract the data from these individual files into a Microsoft Excel Workbook. Furthermore, a separate VBA code was developed to translate the measured point pressures to forces by multiplying pressure histories by the corresponding discretised surface area. This data was then ready to be read into Strand7 as distinct load histories (factor vs. time load tables).

6.3 Structure Domain: Computational Model in Strand7

The structural domain was modelled in the commercially-available Finite Element (FE) package Strand7. Two different FE models of the regular tall building were created in Strand7 to establish the level of complexity required in the structural domain for the PBWE assessment. As with the CFD validation study in Chapter 4, the results of this structural identification study were assessed in terms of computational cost vs. accuracy. It should be noted that the labels of the vertical and crosswind axes swap between the fluid and structural domains. In the structural domain the *y*-axis refers to the vertical plane and the *z*-axis refers to the crosswind plane; the opposite was true in the fluid domain.

The design of the regular tall building features a core of 400 mm thick grade C50 reinforced concrete. It is the core that provides the primary lateral stability. Meanwhile, the floors are designed as 275 mm thick flat slabs of grade C40 reinforced concrete. The maximum column size is 2.8 m x 1.2 m at the outrigger level on the 11th floor. The minimum column size is 0.6 m x 0.8 m at the top floor. An edge beam around the outer perimeter of each floor has dimensions of 0.3 m x 0.75 m. Coupling beams connect the parts of the concrete core separated for the corridor openings and these members have dimensions of 0.5 m x 0.9 m.

Model 1 represented the more detailed FE model of the two. The beams and columns were modelled as beam elements, whilst the core and floor slabs were explicitly modelled as plate elements. The computational mesh comprised 12318 beam and 40581 plate elements connecting 43736 nodes, as shown in Figure 6.5. The edge beams and coupling beams were offset from the connecting nodes. This attribute ensured the top of the beams were positioned level with the floor plate and was responsible for generating additional bending moments due to axial forces in beams. From experience, the modelling approach followed for Model 1 has become industry-standard for FE analyses of such high-rise structures. The level of complexity is comparable to the final FE model resulting from the structural identification study by Kim *et al.* (2009), as described in Section 2.2.2.

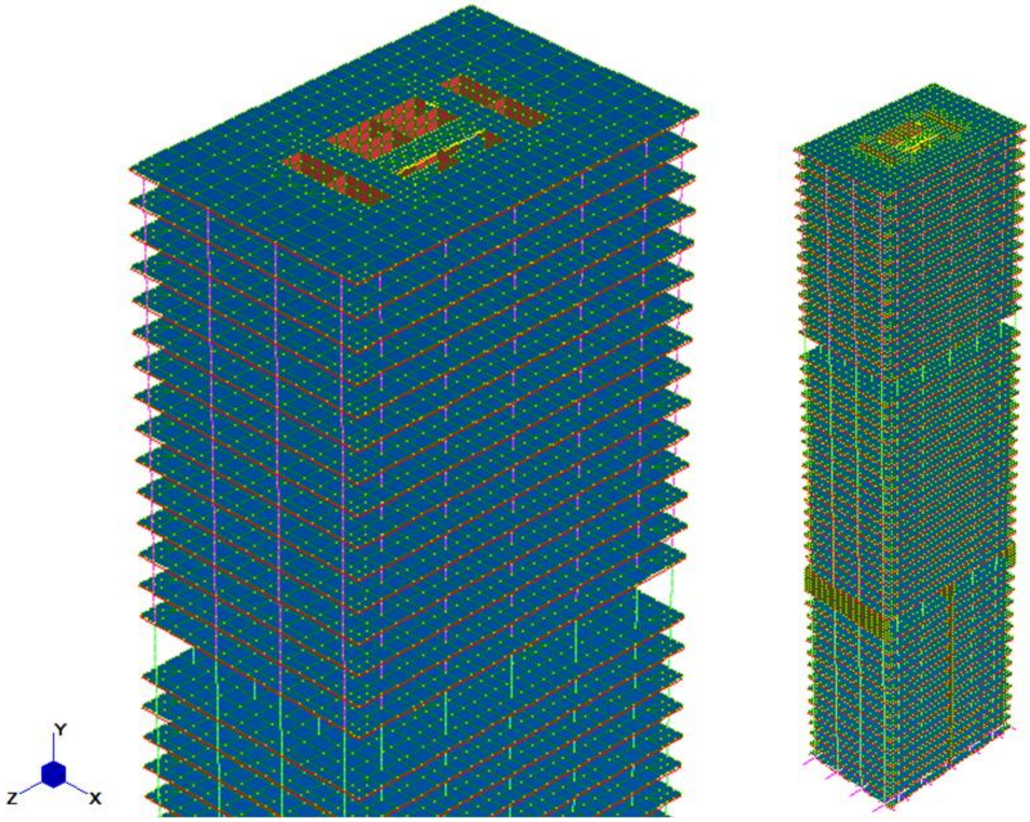

Figure 6.5. Strand7 FE Model 1 of the regular tall building

The level of complexity was reduced for Model 2 by simplifying the representation of the floor slabs. The plate elements comprising the floor were not explicitly modelled. Instead, the total mass of the floor slab was distributed at each level as a series of non-structural lumped masses at the columns and core of the modelled diaphragm. The core, columns and beams were modelled as per Model 1. The nodes at each floor level were rigidly linked in the horizontal *XZ* plane only, allowing different vertical movement between the vertical elements. This approach significantly reduced the number of plate elements in the model, subsequently reducing the computational cost required for structural analyses. The computational mesh involved the same number of beam elements as Model 1 but only 15787 plate elements and 26486 nodes, as shown in Figure 6.6. The number of plates and nodes in Model 2 are 61% and 39% less than those included in Model 1, respectively. The total number of all elements in Model 1 and Model 2 are summarised in Table 6.2

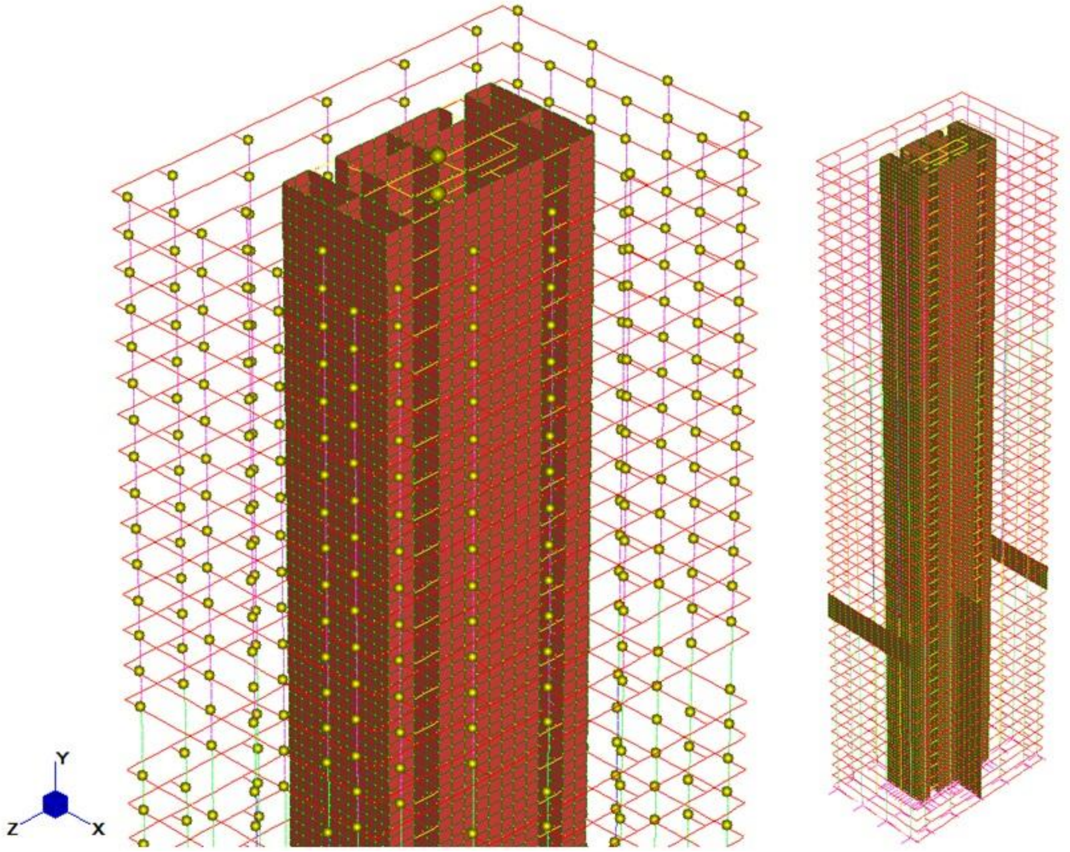

Figure 6.6. Strand7 FE Model 2 of the regular tall building

Table 6.2. Summary of elements in the Strand7 FE models of the regular tall building

Element	Model 1	Model 2	Ratio (M2/M1)
Beams	12318	12318	1
Plates	40581	15787	0.39
Nodes	43736	26486	0.61

For both Strand7 models, structural details were explicitly modelled only above the ground level; foundation details were ignored and assumed rigid. The nodes of the columns and core were restrained against translation and rotation at ground level. Fully fixing the nodes at the boundary implied that the entire model acts as an enclosed box during dynamic events. During dynamic analysis, any energy that is introduced into the computational model therefore stays within the model, propagating towards the free-end at the top of the tall building, reflected towards the bottom boundary and subsequently reflected upwards again. In reality, the energy waves arriving at the bottom boundary would partially reflect back (depending on the change of stiffness and mass density at ground level), but would also radiate into the basement levels (not included in the model) and be transmitted through the foundations, so some energy would be lost due to so-called radiation damping.

The boundary conditions implemented for these finite element models do not account for this radiation damping effect. Instead, it is assumed that the pile foundations of the structure are socketed into an extremely stiff rock and the energy is reflected back towards the top boundary, which justifies the assumption of the fully fixed boundary. Therefore, the energy is contained within the system and any dissipation is associated entirely with structural damping. The same boundary conditions were applied by Kim *et al.* (2009) and the calculated wind-induced response provided a good correlation to full-scale measured data. In addition, ESDU 83009 (Engineering Sciences Data Unit, 1990) states that it is difficult to quantify the amount of energy dissipated to soil-structure interaction and it is often relatively small compared with structural damping for tall buildings, as these are typically built on very firm foundations.

The Strand7 natural frequency solver was set to calculate the first 50 eigenvalues of the undamped dynamic system for both Model 1 and Model 2. The iteration limit was increased to allow all of the eigenvalues to converge to a minimum tolerance of 1×10^{-5}. The resulting natural frequencies and mode shapes were then compared to identify any differences induced by simplifying the representation of the floor slabs.

The mode shapes for the first three natural frequencies of Model 1 are illustrated in Figures 6.7 to 6.9. It should be noted that the contours shown in these Figures do not represent actual physical displacements; these are normalised values representing the deformed shape. Despite the modelling simplifications of Model 2, the FE model was able to produce very similar mode shapes to those computed for Model 1. However, as shown in Table 6.3, there were differences between the corresponding natural frequencies. For all modes of the dynamic system, Model 2 computed a lower frequency than Model 1. This comparison identifies that the modelling simplifications of Model 2 did not fully account for the additional stiffness provided by the floor slabs. This occurred because the *XZ* linkage does not account for any connectivity out of the floor plane. The most significant differences occurred for the predominantly crosswind modes of vibration (i.e. modes 2 and 5). Full *XYZ* linkage in the simplified model would have ensured plane sections remained plane. This would have overestimated the stiffness, resulting in higher natural frequencies and lower building response(s) than from Model 1. The dynamic characteristics are discussed in more detail below.

Table 6.3. First 6 natural frequencies from the Strand7 FE models of the regular tall building

Mode	Model 1 (Hz)	Model 2 (Hz)	Ratio (M2/M1)
1	0.267	0.233	0.87
2	0.312	0.243	0.77
3	0.432	0.411	0.95
4	1.013	0.928	0.91
5	1.150	0.994	0.86
6	1.240	1.166	0.94

The fundamental natural frequency of Model 1 was 0.267 Hz, which corresponds to a fundamental period of vibration T = 3.75 s. It is shown in

Figure 6.7 that the mode shape for this fundamental frequency was predominantly a classical first-order flexural mode in the direction of the *X*-axis. The fundamental mode was expected to oscillate in this direction since it represents the most flexible plane of the concrete core. Low frequency wind loading components below this fundamental natural frequency of vibration contribute to the background response of the structure. At 0.233 Hz, the fundamental frequency of Model 2 was 13% lower than Model 1.

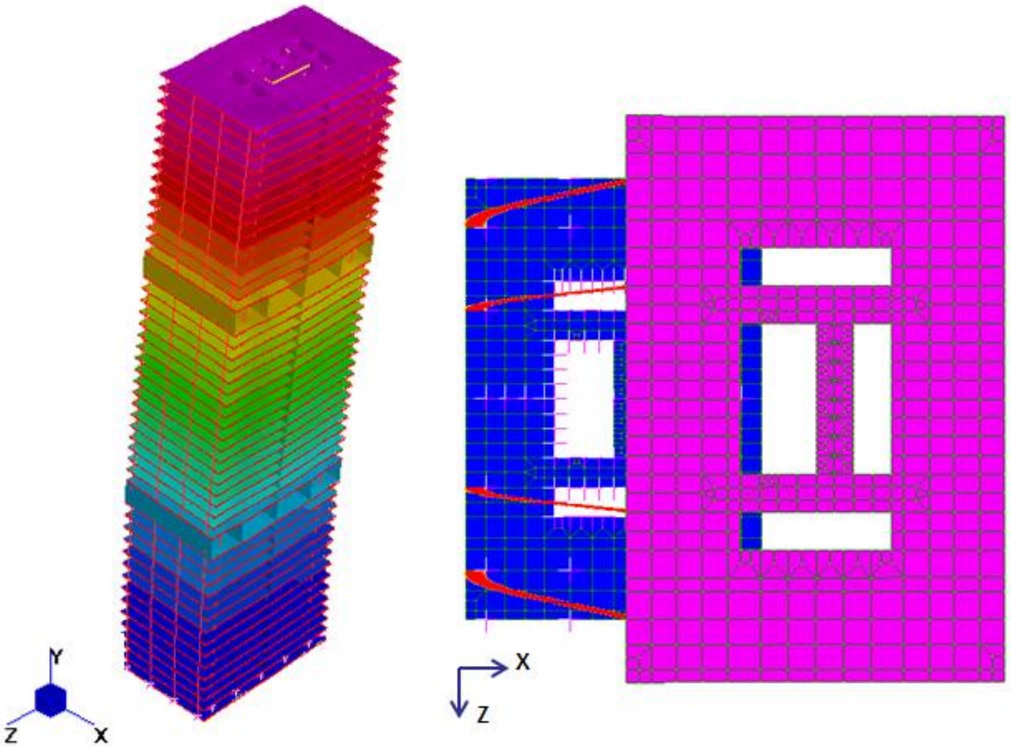

Figure 6.7. First mode of vibration of regular tall building, *f* = 0.267 Hz

The second natural frequency of Model 1 was 0.312 Hz (*T* = 3.21 s) and the computed mode shape, shown in Figure 6.8, is predominantly a first-order translational mode in the *Z*-axis. However, a small torsional contribution is clearly evident. This is a consequence of the slight eccentricity between the centre of mass and the centre of stiffness in the dynamic system. Model 2 was also able to capture this small torsional contribution, indicating the series of lumped masses were adequately distributed around the diaphragm at each level. It should be noted that this would not have been possible if only a single lumped mass was applied at each level. However, at 0.243 Hz, the second natural frequency of Model 2 is approximately 23% lower than that from Model 1 and is in very close proximity to the fundamental frequency of Model 2 (0.233 Hz). This discrepancy suggests that the floor slab provides significant additional lateral stiffness in the *Z*-axis. The floor slabs above and below the two outrigger levels would act as flanges to the shear walls and stiffen the structure. The simplifications of Model 2 are unlikely to adequately account for these Vierendeel effects. Similarly, explicitly modelling the floor slab in Model 1 ensures the shear deformation and shear linkage provided by the coupling beams across the core is sufficiently captured.

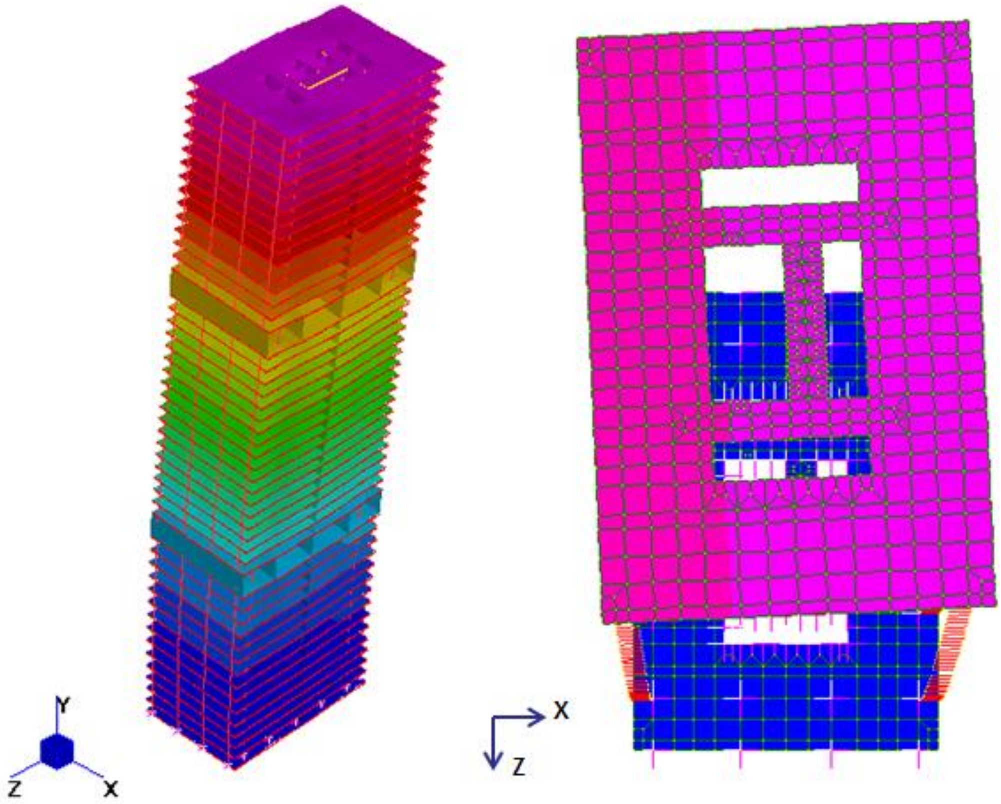

Figure 6.8. Second mode of vibration of regular tall building, *f* = 0.312 Hz

Finally, the third natural frequency of Model 1 was calculated as 0.432 Hz (*T* = 2.31 s) and the corresponding mode shape is illustrated in Figure 6.9. It is clearly seen that this mode displays predominantly the classic first-order torsional mode of vibration. The third natural frequency of Model 2 was 0.411 Hz, only 5% less than Model 1. This identifies that the mass distribution and torsional stiffness are adequately modelled by the simplified approach of Model 2 for the regular tall building. However, this may not be the case for irregular-shaped buildings.

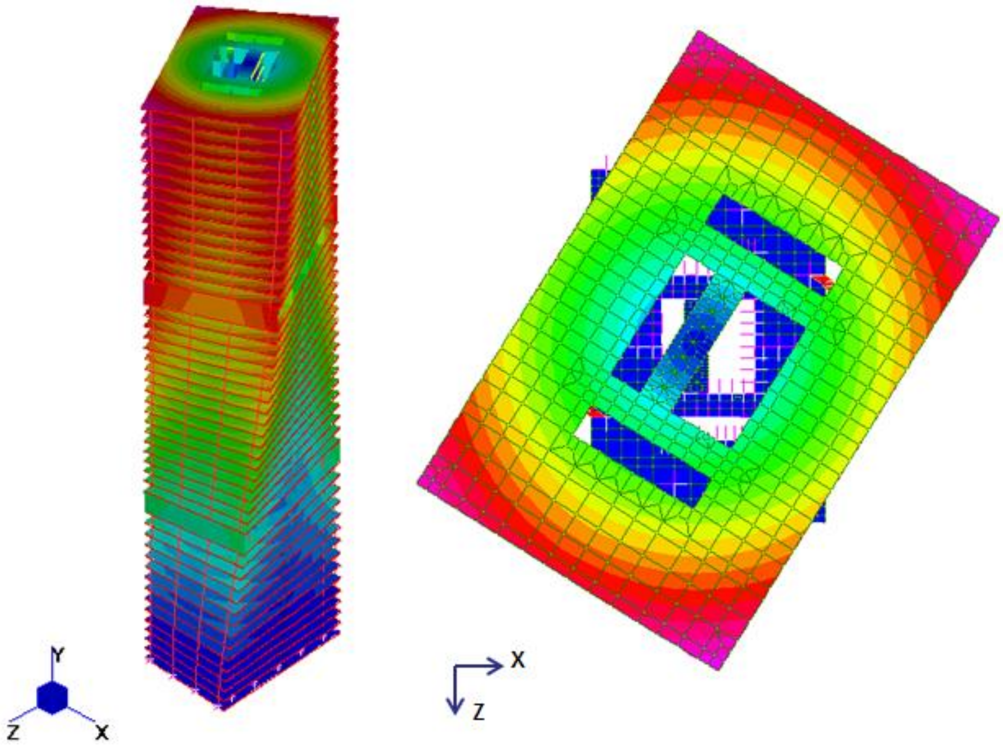

Figure 6.9. Third mode of vibration of regular tall building, *f* = 0.432 Hz

The effects of the mass-stiffness eccentricity cause the higher order frequencies to be associated with similarly complex coupled mode shapes. It is obvious that such coupled modes of vibration would not have been captured if the tall building was simply assumed to behave like an idealised ‘stick’ cantilever. Asymmetric loading on the side face from flow separation and vortex shedding were highlighted in Chapter 4 and such flow instabilities can excite torsional modes of vibration. The increased presence of a torsional component in the mode shapes could have a significant bearing on human perception of vibration since it was argued in Section 2.9 that occupants are extremely sensitive to torsional excitations.

The natural frequency comparison suggests that using Model 2 as opposed to Model 1 for the PBWE assessment would result in an increased dynamic response because Model 2 is more flexible, particularly in the crosswind direction. Adopting this simplified model would be conservative; the increased complexity of Model 1 would provide a more realistic representation of the wind-induced response of the physical structure. The resulting top floor accelerations from Model 1 and Model 2 are compared for one set of Interaction Parameter (IP) load histories, IP10, in Section 6.4.2 and a decision is made regarding which Strand7 FE model of the regular tall building is implemented for the full PBWE assessment. It also sets a prerequisite for the level of complexity required for the PBWE assessment of the irregular tall building.

The one-way coupling interface developed in Microsoft Excel VBA made use of the Dynamic Link Library in Strand7 to create 578 wind load cases. Strand7 required the wind loads to be applied as factor vs. time load tables which scale a specific load case. Therefore, each load case contained a nominal 1 kN point load at a distinct location corresponding to the position of the associated CFD pressure monitor. The coupling algorithm then created factor vs. time load tables and assigned these tables to the relevant wind load case. The nominal 1 kN load was scaled by the factor vs. time table to furnish the instantaneous wind load histories at each time-step throughout the linear transient dynamic analyses.

The models also considered the following vertical load cases: self-weight; dead load; and imposed load. These vertical loads were constant throughout the dynamic analyses. The dead and imposed loads on each floor were calculated for office buildings from BS EN 1992-1-1.2004 (British Standards Institution, 2004a) as 3.0 kN/m^2 and 3.5 kN/m^2, respectively.

6.4 PBWE Assessment: RANS Simulation Strategy

6.4.1 Interaction Analysis

The interaction analysis determines the interaction parameter (IP) wind loads imposed on the tall building for each intensity measure (IM) wind event in the time domain. The flow field and pressure distributions for a building of this form and the incident wind direction were discussed in detail in Chapter 4.

This provided an appreciation and better understanding of the expected load characteristics.

In this PBWE assessment the RNG k-ε turbulence model was adopted to calculate the wind pressures for the ten IM wind events. The limitations of this RANS turbulence model were well documented in Chapter 4. However, it was established that the use of the full LES model for the entire range of IM wind events was not practical due to its prohibitive computational demand. The relevant solver settings for the RANS turbulence model were specified, as detailed in Section 4.3.5. The computational time-step was 0.05 s and the CPU cost for a single physical time-step was 29.9 s using 8 CPUs on the HPC facility at the University of Strathclyde.

The highest mean velocity profile from the IM wind events was the one associated with the IM10 event. However, these wind speeds were notably less than those used for the CFD validation case, as presented earlier in Chapter 4. The initial reference wind speed for the validation case was 100 ms^{-1}, while the corresponding value at the building height for the IM10 event was 47.17 ms^{-1}. The initial 'warm-up' phase, which allows the unsteady flow to develop, is dependent on the velocity of the air travelling through the domain. Therefore, the 'warm-up' phase was considerably longer than for the validation case. In Chapter 4, statistical analysis of transient results was made after 60 seconds of flow time. However, the PBWE simulations using the characterised IM wind events required 120 seconds of flow time before representative results could be assessed. The upwind dimension of the fluid domain could have been reduced to shorten the transit times. However, the recommendations by Revuz *et al.* (2010) suggest that the adequate fluid domain size is not a function of mean wind velocity. Therefore, the domain geometry was constant for each IM wind event to avoid creating questions about consistency when evaluating the measured wind pressure histories.

The assessment of the wind-induced response of a tall building is typically based on the acceleration time histories over 600 seconds (Campbell *et al.*, 2005). The limitation on the number of CPUs that could be used for the CFD simulations for this study meant that providing such long wind load histories from each of the ten IM wind events would have taken a total computation time of 50 days when using the RANS turbulence model. The wind pressures were monitored for 120 seconds of flow time only and it is assumed that these measured 120-second load histories contain the most severe loading conditions for the considered IM wind event.

The mean wind pressures and their distribution across the building envelope depend on the vertical profile of the incident mean wind velocity. The predicted mean pressures from each of the IM wind events are compared at 2/3*H* in Figures 6.10 to 6.12. The key features of the mean loading distribution already described in Chapter 4, such as the high pressure at the centre of the windward face and the suction effects at the leading edge, are clearly evident.

On the front face, the computed pressure distribution is shown in Figure 6.10. The highest mean pressures are associated with the most intense mean wind velocity profile, the IM10 wind event (v_b = 25.5 ms^{-1}, z_0 = 0.29 m). The measured mean pressure values are approximately 30% greater than those mean pressures appearing during the IM9 wind event. This case represents the largest mean pressure increase between successive IM wind events. In general, the measured mean pressure values increase with each subsequent IM wind event. However, the mean pressures measured from IM4 are greater than IM5 and the same occurs between IM7 and IM8. This apparent anomaly arose because of differences in the vertical profiles of the mean wind speed.

The following interpretation can be given for the apparent above discrepancy. The magnitude of v_b increased for each subsequent IM wind event. However, this corresponded to an elevation of 10 metres in open country and did not represent the wind speed at 2/3*H* in town terrain, where z_0 was treated as a variable. The procedure to derive the mean velocity profiles is described in Chapter 5. The mean wind speed at this height was found to be greater for IM4 than IM5 and, likewise, IM7 was greater than IM8. Similar patterns occur on the side face and the leeward face, as seen in Figures 6.11 and 6.12, respectively.

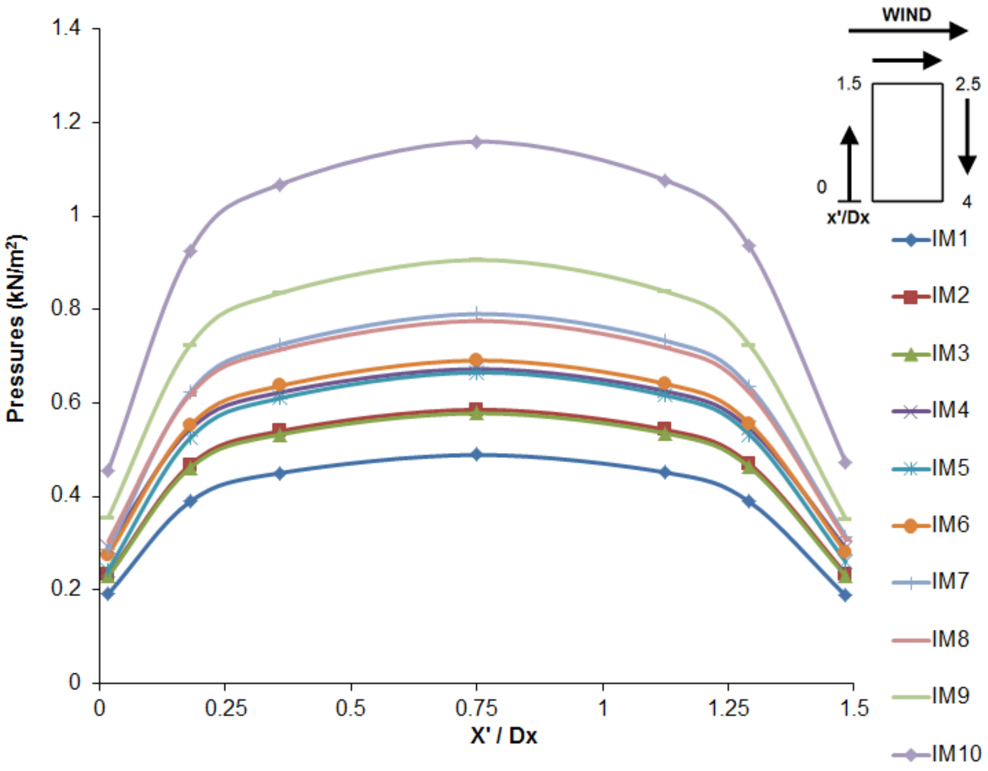

Figure 6.10. Mean pressures calculated on the front face at 2/3*H* for the IM wind events

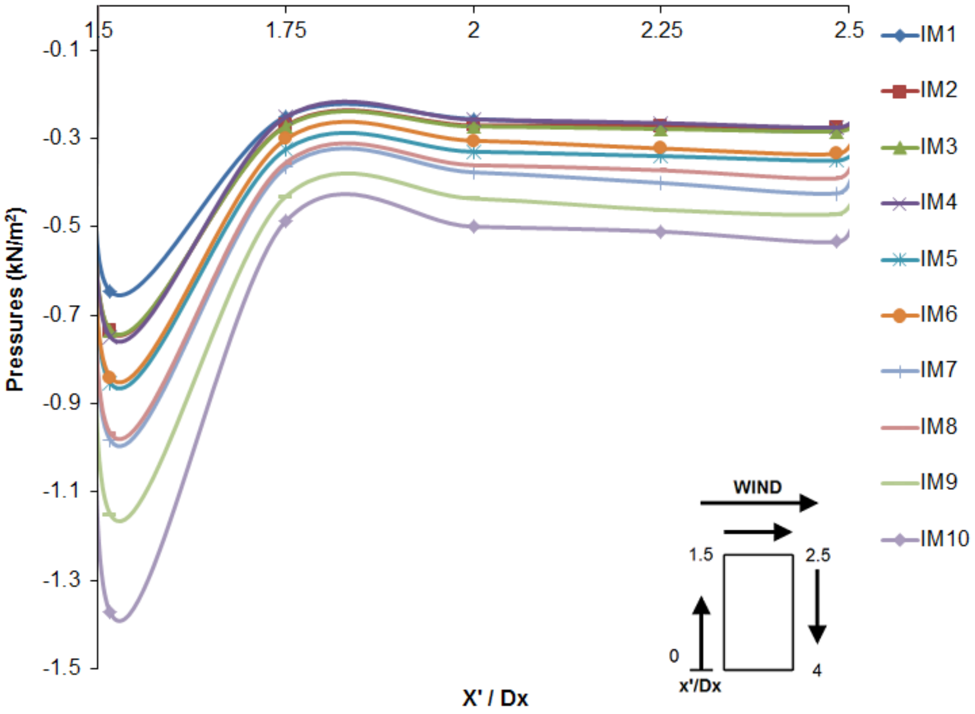

Figure 6.11. Mean pressures calculated on the side face at 2/3*H* for the IM wind events

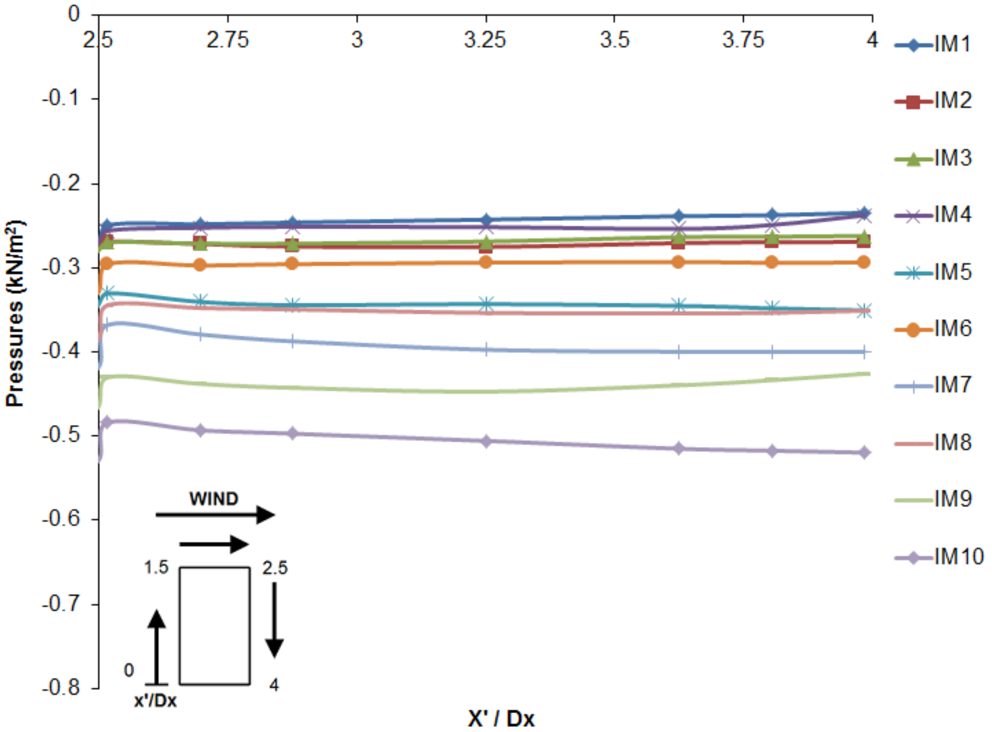

Figure 6.12. Mean pressures calculated on the back face at 2/3*H* for the IM wind events

The limitations of the RANS model in failing to sustain the high levels of turbulence specified at the inlet, as discussed in Chapter 4, meant the turbulence in the incident wind field was significantly lower than desired. Therefore, the fluctuations in the transient pressure histories were generated almost entirely from the structure-induced turbulence. The unsteady pressures measured on the centre of the front face at 2/3*H* (Level 29) are shown in Figure 6.13 for the IM1, IM5 and IM10 events. This point approximately corresponds to the stagnation point where the flow is brought to a rest. The failure to adequately model the turbulence in the incident wind field is the reason why the magnitudes of the fluctuations are extremely small.

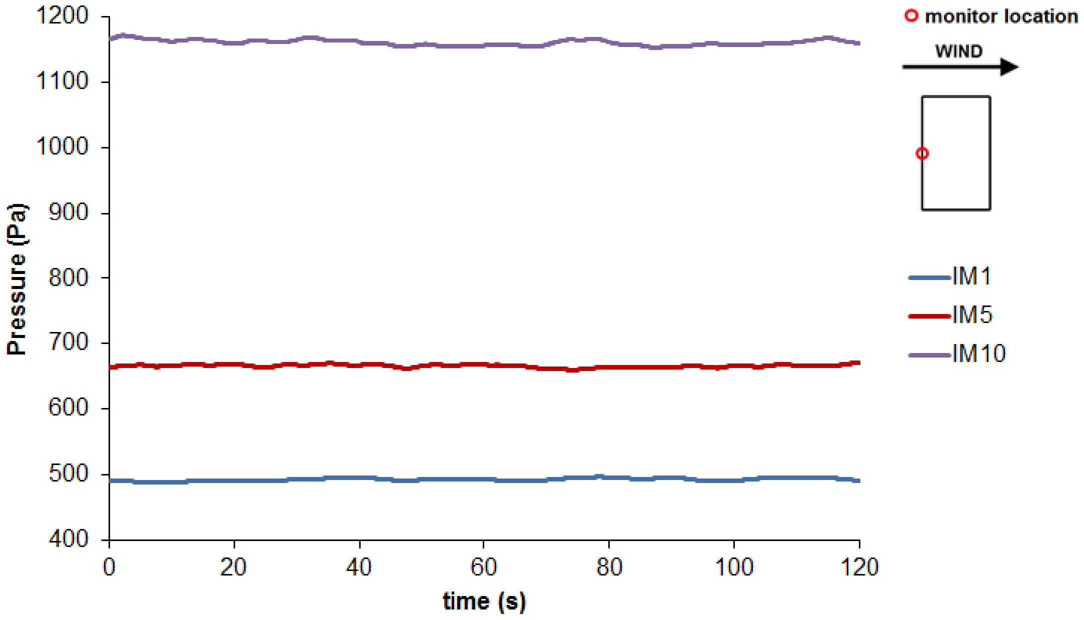

Figure 6.13. Pressure histories calculated by RANS at the centre of the front face at 2/3*H*

The pressure histories at the leading edge of the side face at 2/3*H* for the same three IM wind events are shown in Figure 6.14. The flow separation at this leading edge creates a crosswind suction effect and generates a much more unsteady loading condition than was seen on the front face.

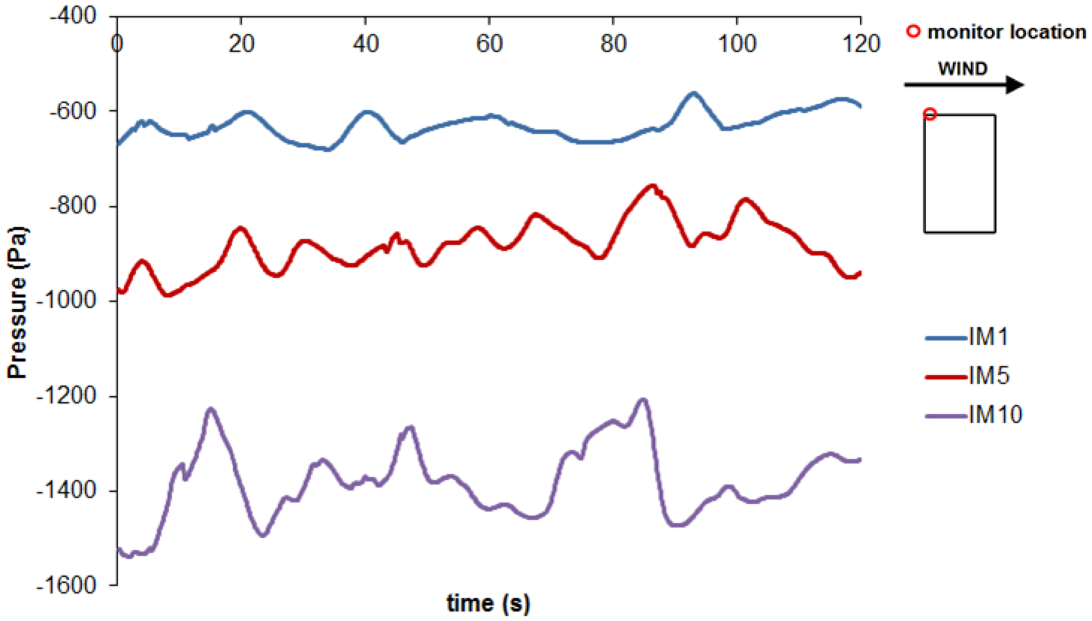

Figure 6.14. Pressure histories calculated by RANS at the leading edge of the side face at 2/3*H*

The fluctuations on the back face are principally generated from the vortex shedding phenomenon in the near-wake. The measured pressures at 2/3*H* on the centre of the back face display noticeable fluctuations, as shown by Figure 6.15. The broadband alternate shedding frequency of the twin vortices can excite both crosswind and torsional modes of vibration. The extremely small fluctuations seen on the front face suggested that the alongwind dynamic building response would be governed by the fluctuations on the back face.

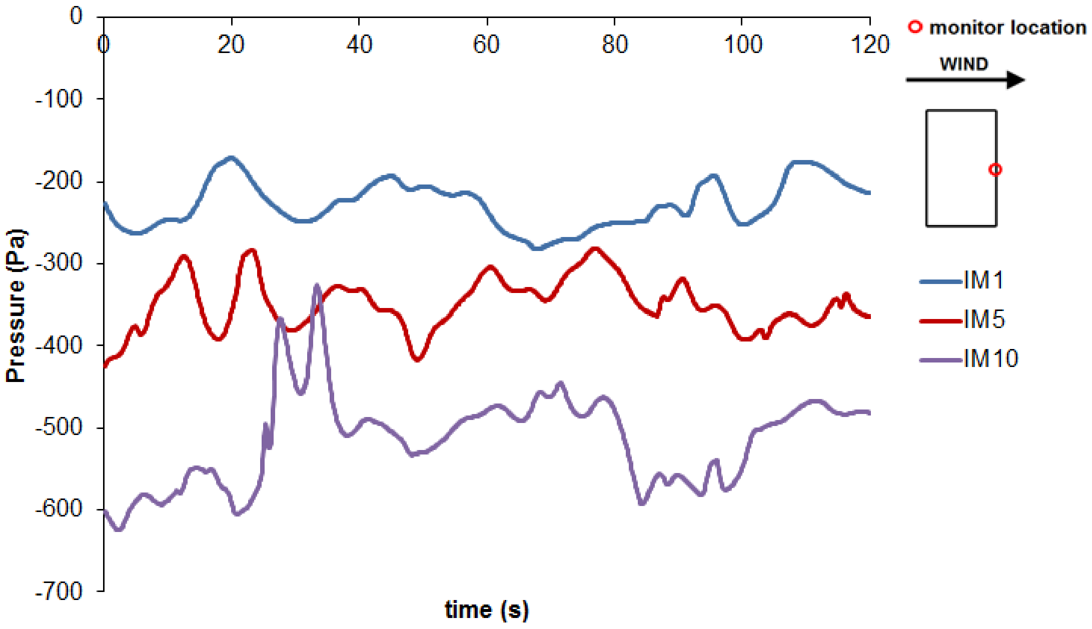

Figure 6.15. Pressure histories calculated by RANS at the centre of the back face at 2/3*H*

6.4.2 Structural Analysis

The structural analysis calculates the wind-induced response of the structure for each set of IP wind load histories in the time domain. The engineering demand parameter (EDP) monitored during the transient Strand7 simulations was the top floor acceleration. The total of 578 ‘factor vs. time’ load tables as calculated by the RANS turbulence model were created in Strand7 and attached to the associated load case by the one-way coupling algorithm, as described in Section 6.3. This procedure was repeated for each of the ten probabilistic wind events. If the building design failed the PBWE assessment then the design would have to be revised and the Strand7 simulations repeated. Therefore, it was practical to optimise the computational times of the Strand7 analyses. It should be noted that the building was modelled as a fixed rigid obstacle in CFD so these simulations would not need to be repeated unless the outer form of the building is changed.

The static displacement under self-weight was 10.1 millimetres in the direction of the alongwind *x*-axis due to the slight eccentricity between the centre of mass and centre of stiffness. The linear transient dynamic analyses required an initial set of time-steps to dampen the inertial effects and allow the structure to settle to its ‘quasi-static’ equilibrium state. This stage was an essential prerequisite before the wind loading could be applied. Therefore, the linear dynamic solver first calculated 120 seconds of simulation time with only the self-weight and constant dead and imposed vertical load cases included. The results file from this single simulation was used as the restart condition for all PBWE structural analyses.

Furthermore, the wind loads were conveniently ramped in time by the coupling algorithm to ensure they did not act as sudden blast-type loadings and adversely influence the calculated dynamic response. A ramping time of 60 seconds was chosen arbitrarily before the wind loads became fully active. The dynamic response of the structure to the 120 second wind load time histories was then calculated by the solver.

An initial set of Strand7 linear transient analyses were computed to complete the FE structural identification study from Section 6.3. These simulations were run for one of the ten wind load conditions, IP10. Firstly, a sensitivity study was performed using FE Model 1 to assess the influence of increasing the number of modes included in the dynamic analysis from 20 to 50. The modal superposition method solves the modal equilibrium equation for each mode considered in dynamic analysis. Therefore, an increase in the number of modes causes an increase in the computation time. For a MDOF finite element model with thousands of nodes and elements, such as the tall building models used in the present study, the CPU times can increase significantly depending on the number of additional modes included in the analysis. Therefore, it was practical to include the minimum possible number of modes while still capturing the key modal contributions.

The modal damping ratio, described in Section 2.2, of the fundamental natural frequency was determined using the ESDU 83009 (Engineering Sciences Data Unit, 1990) guidance and set as $\zeta = 0.016$. This is the same as the value recommended for concrete structures by Annex F of BS EN 1991-1-4:2005 (British Standards Institution, 2005). The damping ratio for the remaining modes was assumed to follow Rayleigh damping, as described in Section 3.3.2. No guidance was available for damping ratios of higher-order modes of vibration. An upper limiting damping ratio of 0.08 was specified and assumed to be valid for the highest frequency included in the modal superposition dynamic analysis. The natural frequencies for the 20th and 50th modes of vibration were 5.22 Hz and 10.18 Hz, respectively. The Rayleigh damping models for these two different upper limiting frequencies are shown in Figure 6.16.

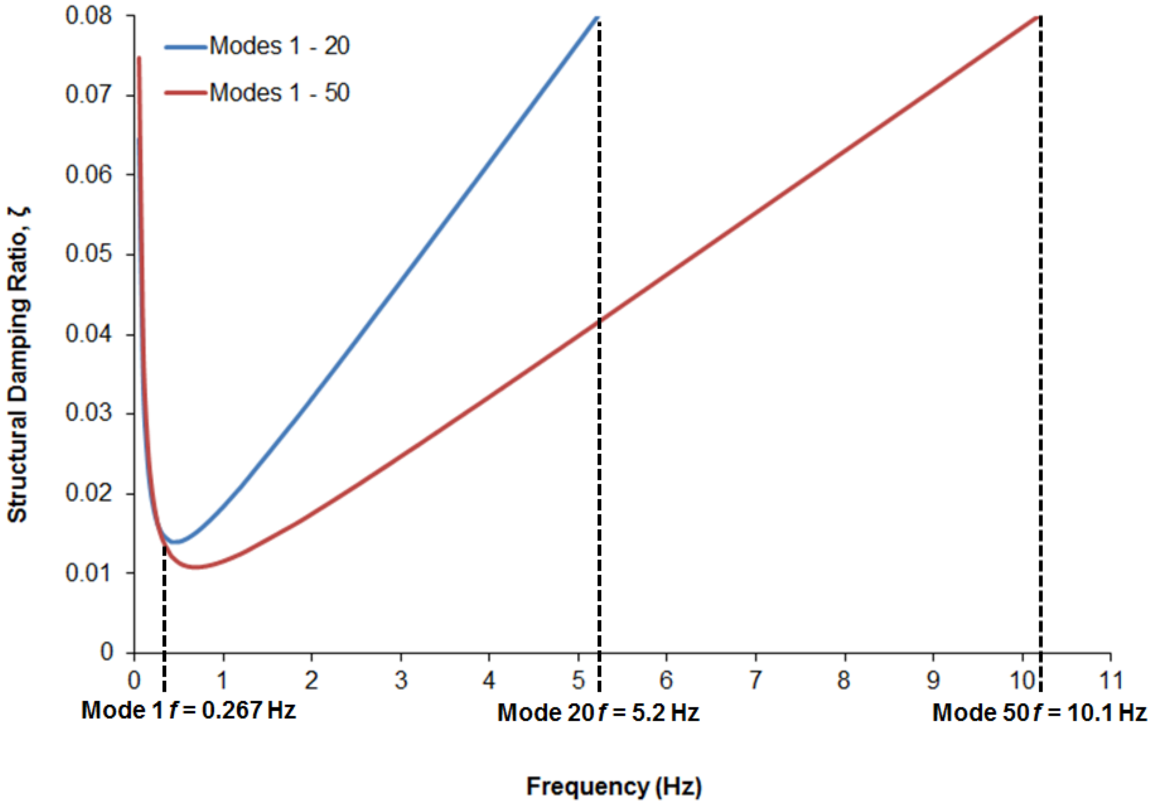

Figure 6.16. Rayleigh damping used for the structural analyses in Strand7

For the simulations including modes 1 to 20, the computational time-step was set to 0.05 s. This corresponded directly to the time-step used in the CFD simulations and was approximately four times smaller than the fundamental period of vibration of the 20th mode (T_{20} = 0.19 s) included in the linear transient dynamic analyses. It should be noted that decreasing the time-step for modes 1 to 20 was found to have a negligible effect on the calculated accelerations. A total of 3600 time-steps were computed. The total CPU time on a standard desktop PC with a 3.00 GHz dual-core processor was 2600 seconds (43 minutes 20 seconds).

The computational time-step that was specified for the modal superposition analysis involving modes 1 to 50 was 0.02 s. This time-step was five times smaller than the fundamental period of mode 50 (T_{50} = 0.10 s). A total of 9000 time-steps provided the 60 second load ramping time and the 120 second wind-induced response time. The total CPU time for the additional time-steps and the increased number of included eigenmodes was 5809 seconds (1 hour 37 minutes). This computation cost was more than a factor of 2.2 greater than was required for the analysis restricted to modes 1 to 20 only. However, it was still an order of magnitude smaller than the CPU time required by RANS to calculate the same number of time-steps in the CFD domain (71760 seconds).

An assessment of the calculated EDP top floor acceleration histories revealed that there was an almost negligible difference between the modal superposition analyses involving modes 1 to 20 and modes 1 to 50. This indirectly showed that the wind excitation did not induce noticeable response from the higher-order structural modes (modes 21 to 50). In addition, the natural frequency solver revealed that the sum of the effective modal masses for modes 1 to 20 amounted to more than 90% of the total mass of the structure. This is the criterion specified by BS EN 1998-1:2004 (British Standards Institution, 2004b) for the number of modes to include in the modal response analysis of structures for earthquake resistance. The results described herein are for the wind-induced response involving modes 1 to 20.

The absolute top floor accelerations (AXZ) from FE Models 1 and 2 were then compared as the final stage of the FE structural identification study. As shown in Figure 6.17, these 120-second time histories show a complex response. This can be attributed to both the unsteadiness of the wind loading and interference between different natural frequencies.

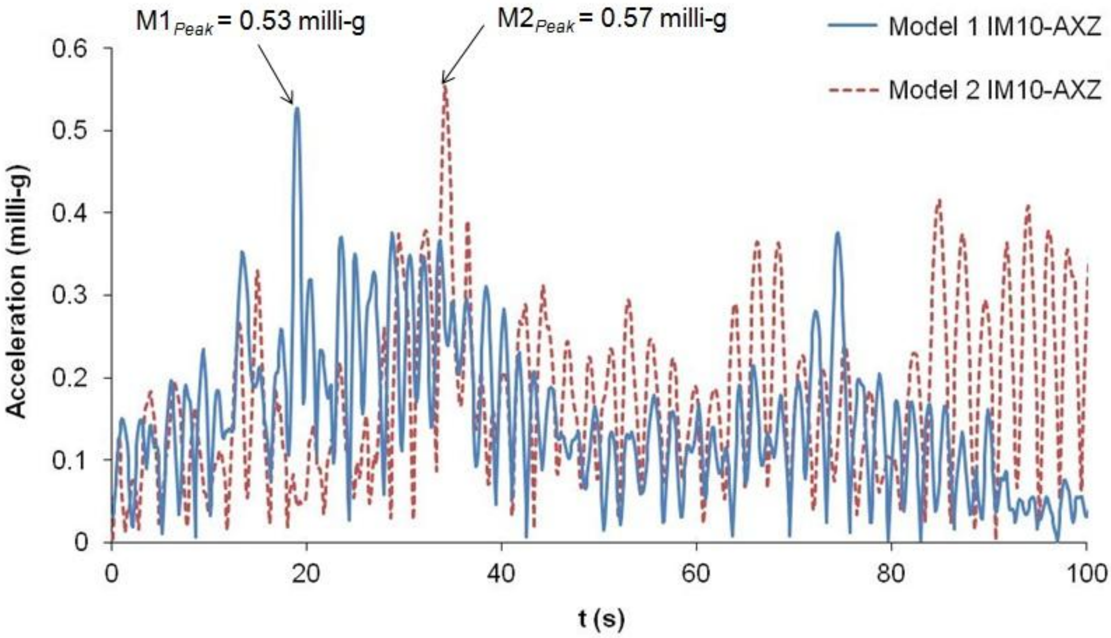

Figure 6.17. Absolute top floor accelerations (AXZ) from FE Models 1 and 2 during IP10 wind load conditions based on the RANS model

The RMS and peak from the absolute acceleration response of Model 1 are 0.21 milli-g and 0.53 milli-g, respectively. The time history of Model 1 shows two low frequency cycles and the peak of the building response is measured within the first cycle from 0 to 50 seconds. As mentioned above, the total CPU time for the Model 1 simulation was 2600 seconds (43 minutes 20 seconds). Meanwhile, due to the increased flexibility, the RMS and peak from the corresponding absolute acceleration response of Model 2 are 0.29 milli-g and 0.57 milli-g, respectively. The total CPU time for the Model 2 simulation was 1487 seconds (24 minutes 47 seconds). The differences between the two FE models are summarised in Table 6.4.

It is assumed that, beyond both 120-second building responses, the subsequent peaks do not exceed the computed values. Given the inherent unsteadiness of the loading and the stochastic nature of the response amplitudes, the appropriateness of this assumption is perhaps uncertain. A statistical approach may have been more appropriate to estimate the likely peak acceleration during the considered IM wind event.

Table 6.4. Summary of dynamic response properties and CPU times from the Strand7 FE models of the regular tall building

Property	**Model 1 (Hz)**	**Model 2 (Hz)**	**Ratio (M2/M1)**
Peak Response (milli-g)	0.53	0.57	1.08
RMS Response (milli-g)	0.21	0.29	1.38
CPU time (s)	2600	1487	0.57

Despite the distinct contrast in model complexity, the difference between the peak responses from the two FE models is only 8% under RANS-IP10 load conditions. This correlation was encouraging given that there was a significant saving in CPU cost from using the less complex Model 2 rather than Model 1. However, there was a more notable discrepancy between the RMS components of the two absolute acceleration signals. The RMS response of Model 2 was 38% greater than Model 1. This was caused by an increased crosswind (AZ) response from Model 2. The natural frequency comparison in Section 6.3 revealed that the natural frequencies in the (predominantly) crosswind mode shapes were significantly lower for Model 2 from underestimating the additional stiffness provided by the floor slabs. Therefore, this discrepancy was somewhat expected.

The Engineering Demand Parameter (EDP) for the PBWE framework is based on the peak top floor accelerations during each IM wind event. On the evidence of the structural identification study, it is acknowledged that the rigid-plate assumption of Model 2 may be adequate to use for the remaining structural analyses. It would provide conservative results for the regular tall building by overestimating the wind-induced response. Nonetheless, the discrepancy between the two FE models may have increased under more unsteady (and realistic) loading conditions than could be provided by the

RANS model. There is also uncertainty regarding the adequacy of the rigid-plate assumption for more irregular building geometries, such as an ‘L’-shaped building with a re-entrant corner. The major advantage of using Model 2 as opposed to Model 1 is the significant saving in CPU cost. However, the CPU time to run a linear transient dynamic analysis of FE Model 1 in Strand7 is still over a magnitude smaller than the CPU time to solve the preceding CFD simulation that generates the wind load histories. Ultimately, in the context of the whole PBWE framework, the CPU cost of Model 1 is considered to be acceptable and it will provide the more accurate solution of the two FE modelling approaches. Hence, Model 1 is used herein to determine the EDP response under the remaining IP wind load conditions. The same modelling techniques are implemented for the PBWE assessment of irregular-shaped building in Chapter 7. The decision may have been different if an alternative, quicker technique was used to generate the load histories and/or if the process involved many more structural analyses than the ten specified for this PBWE assessment.

Referring back to the AXZ response of Model 1, the peak within the second low-frequency cycle is approximately 40% less than the peak within the first. A closer inspection of the loading showed that the mean overall alongwind drag force acting on the structure during 0 to 50 seconds is 9220 kN, while the mean drag force from 50 to 100 seconds is 9050 kN. This small reduction in mean wind force is likely to be only slightly responsible for the reduced peak in the second cycle of the beat response. The main cause of this drop in peak response is considered to be directly related to the unsteadiness of the wind loading. It was found that the average RMS of the overall loading on the front face was 34.7% greater during the first 50 seconds than it was during 50 to 100 seconds. In addition, the average RMS component of the loading on the back face, due to the turbulent near-wake, was 51% greater from 0 to 50 seconds than during 50 to 100 seconds. This reflects the unsteadiness of the structure-induced turbulence.

The time histories of the alongwind (AX) and crosswind (AZ) acceleration components from FE Model 1 are plotted in Figure 6.18. The amplitudes of the response signals both show a distinct modulation due to a beat frequency with a period of approximately 40 seconds ($f_{beat,1}$ = 0.025 Hz). It is this predominant beat frequency that creates the two low-frequency cycles seen in the absolute acceleration response. Furthermore, there appears to be a second beat in the AZ acceleration response that modulates the amplitudes of successive local response cycles. Each cycle has a period of approximately 3.3 seconds, which suggests that the beat has a period of 6.6 seconds ($f_{beat,2}$ = 0.15 Hz).

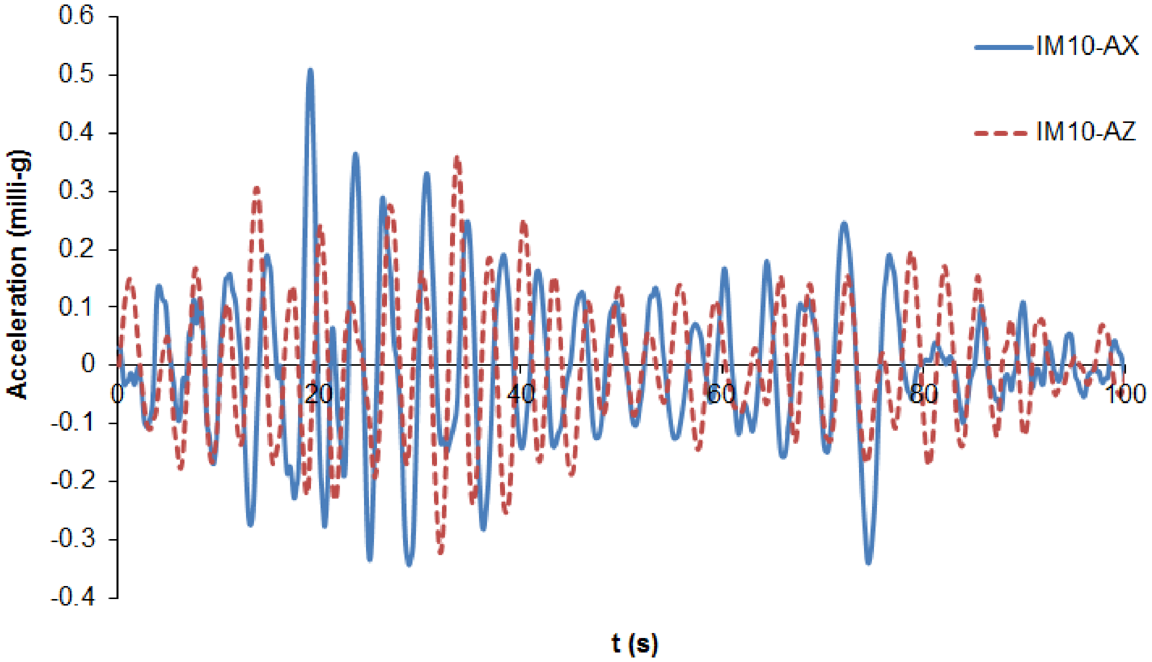

Figure 6.18. AX and AZ components of top floor acceleration response from Model 1 during IP10 wind load conditions based on the RANS model

The Pearson product-moment correlation coefficient between the AX and AZ response time histories of Model 1 is 0.02. This measure is defined as the covariance of the two variables divided by the product of their standard deviations. This calculated value represents an extremely weak correlation between the alongwind AX and the crosswind AZ components of acceleration. This is reflected in the scatter of the acceleration trace for the IP10 wind loading event based on the RANS wind pressures, shown in

Figure 6.19. This shows that neither the alongwind nor the crosswind responses to wind loading are dominant.

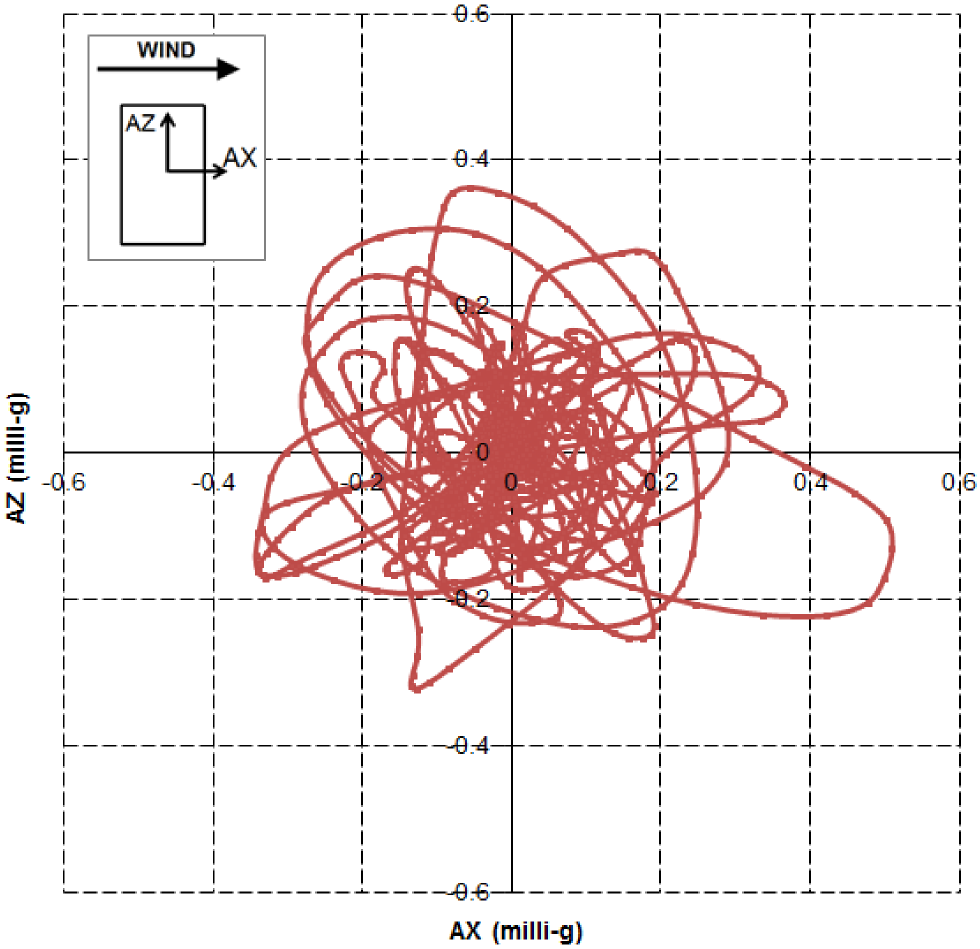

Figure 6.19. Acceleration trace of Model 1 during IP10 load conditions based on the RANS model

Fast-Fourier Transform (FFT) analyses were performed in MATLAB to obtain the frequency spectrum of the AX and AZ acceleration time history response signals. This identified the modes of vibration that were responding during the transient analysis. The frequency spectra in Figures 6.20 to 6.22 identify various interference frequencies within the complex wind-induced response of the building. The spectra may also include a small number of artificial frequency peaks, occurring due to the discretisation process of FFT and the relatively short time history.

It is evident from Figure 6.20 that the AX alongwind building response was predominantly in the fundamental mode of vibration (f_1 = 0.267 Hz). A distinct peak is also visible for the 3rd mode of vibration (f_3 = 0.432 Hz), although the magnitude is approximately 60% less than the fundamental frequency. In addition, there appears to be a small contribution measured in the 4th mode of vibration (f_4 = 1.01 Hz). However, this response is only 5% of the fundamental frequency response. The FFT analysis did not identify any notable modal contributions for frequencies greater than 2 Hz.

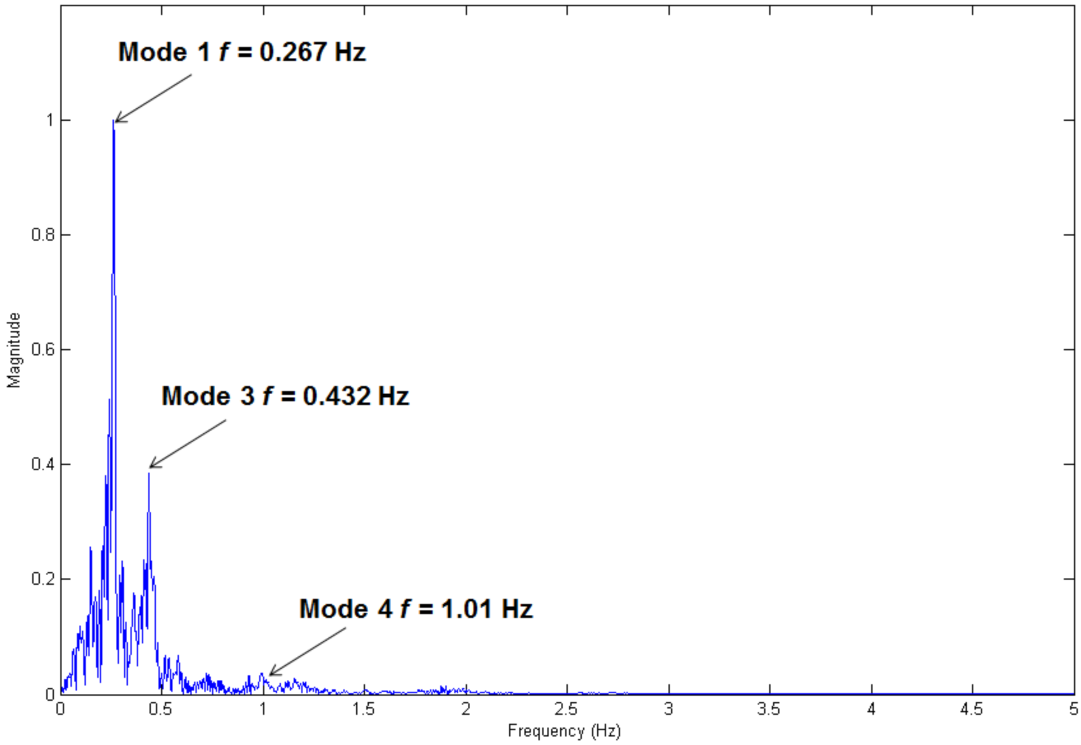

Figure 6.20. Frequency spectrum of AX time history during the IP10 load conditions based on the RANS model

Figure 6.21 clearly shows that the crosswind acceleration response was primarily in the 2nd mode of vibration, which corresponds to the translational mode shape in the *Z* axis. A less distinct peak can be observed for the 3rd mode of vibration. This modal contribution is over 80% less than the fundamental crosswind mode. There is also a slight response measured over the frequency range corresponding to the 6th mode of vibration. However, this contribution is approximately 2.5% in relation to the 2nd mode of vibration. No distinct responses are observed for frequencies greater than 1.5 Hz.

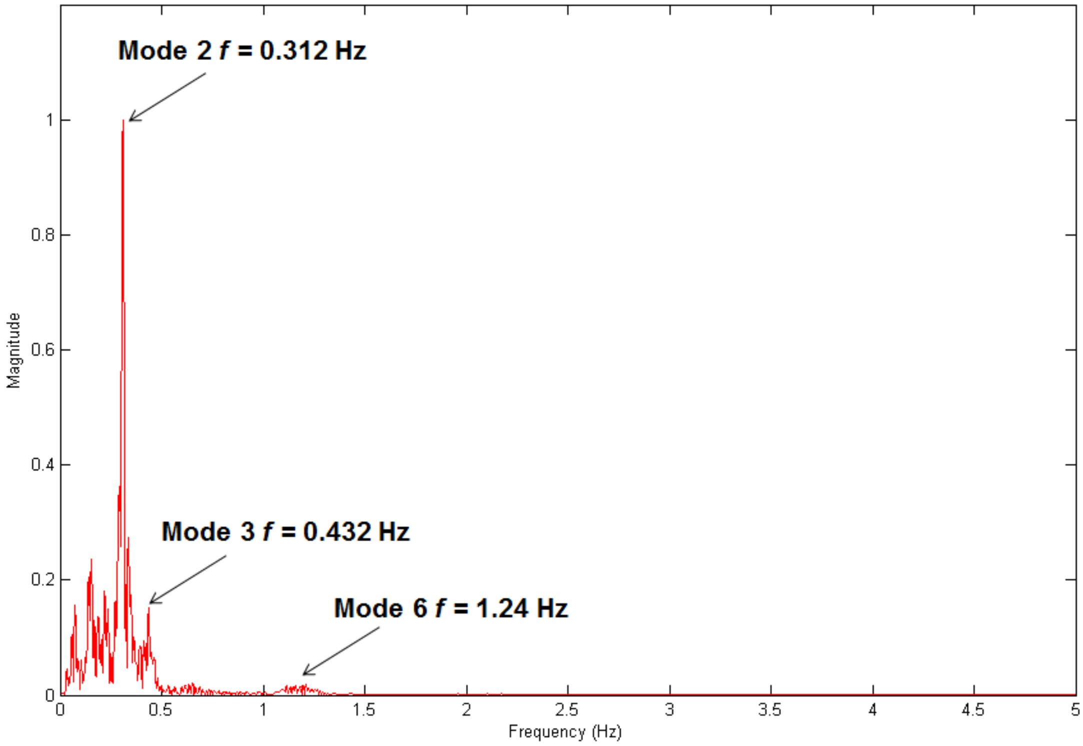

Figure 6.21. Frequency spectrum of AZ time history during the IP10 load conditions based on the RANS model

The AX and AZ frequency content below 0.5 Hz is shown in Figure 6.22 to identify the possible frequencies that are ‘beating’ to create the observed amplitude modulation. In addition to the dominant natural frequencies, it is evident that both the AX and AZ acceleration response signals contained a range of interference frequencies. The peak corresponding to the second beat frequency, $f_{beat,2}$, at 0.15 Hz is visible. In comparison the magnitude of the first distinct beat frequency peak, $f_{beat,1}$, is relatively small since the acceleration signal contained only two complete cycles of this low-frequency interference component during the 120 seconds of response time history. The frequency of a beat is equal to the difference between two closely-spaced interfering frequencies. The frequency spectrum shown in Figure 6.22 suggests that $f_{beat,1}$ involves the 1st mode (f = 0.267 Hz) and a notable interference frequency (f_i = 0.242 Hz). Similarly, $f_{beat,2}$ is likely to be caused by interference between the 1st mode (f = 0.267 Hz) and the 3rd mode (f =

0.312 Hz). The time-histories do not appear to involve as many interference frequencies. Hence, the FFT spectra are likely to become smoother if the time-history records are increased, with many of the apparent interference frequencies converging to form fewer, more distinct peaks.

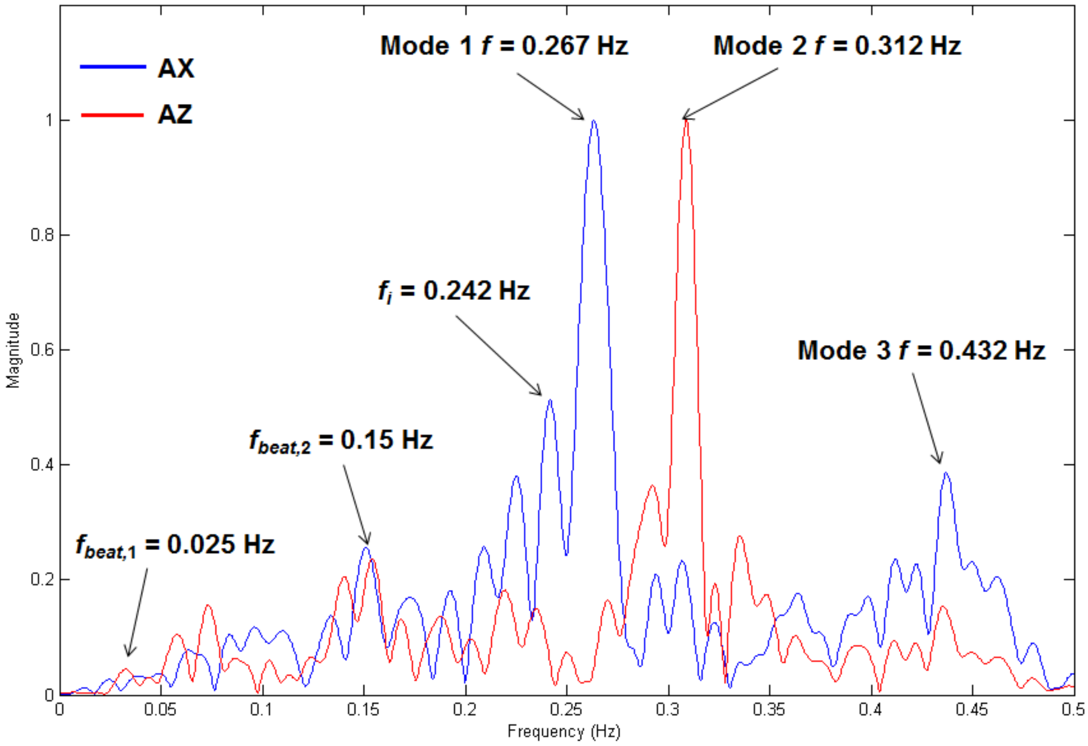

Figure 6.22. Frequency spectrum between 0 Hz to 0.5 Hz during the IP10 load conditions based on the RANS model

The linear transient dynamic solver was run for the remaining IP1 to IP9 wind load conditions. As mentioned earlier, it was deemed adequate to limit the number of modes included in these subsequent Strand7 analyses to the first 20. The Microsoft Excel VBA code extracted the EDP transient results of the top floor alongwind, crosswind and rotational accelerations that were calculated from each of these Strand7 dynamic analyses. An analogous post-processing procedure similar to that detailed above was performed to assess the building response associated with each wind event.

A graph of the relationship between the calculated EDP (top floor peak acceleration) and the mean wind velocity at the top building height for each wind event is plotted in Figure 6.23 and a summary of the peak values is provided in Table 6.5. In general, the peak top floor accelerations are very low for such a flexible tall building. This was considered to be a direct consequence of the inability of RANS to sustain atmospheric turbulence in the incident wind field, as identified in Chapter 4. Distinct exceptions are the EDP peak accelerations associated with the IM7 and IM9 wind events. The magnitude of the peak accelerations associated with these two wind events are more representative of the expected wind-induced response of the regular tall building. The possible reasons for these exceptions are discussed below.

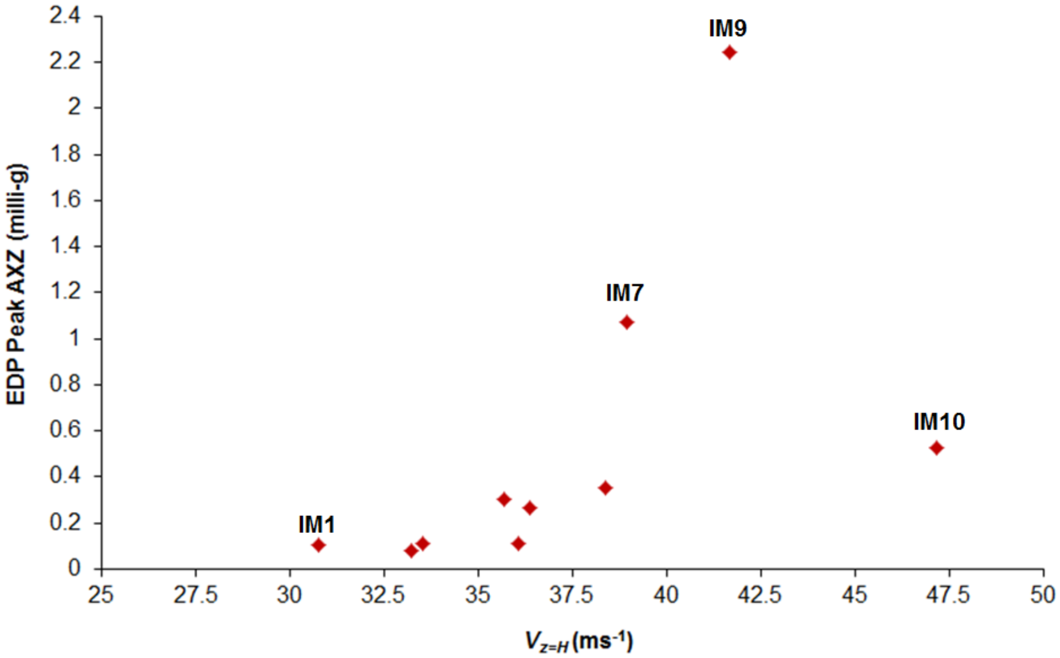

Figure 6.23. EDP peak acceleration vs. IM mean wind velocity at building height based on the RANS model

Table 6.5. Summary of EDP peak top floor accelerations based on the RANS model

IM	$V_{z=H}$ (ms^{-1})	A_{peak} (milli-g)
1	30.75	0.104
2	33.55	0.110
3	33.23	0.079
4	36.08	0.107
5	35.69	0.304
6	36.38	0.267
7	38.94	1.069
8	38.39	0.353
9	41.67	2.242
10	47.17	0.527

The AX and AZ acceleration histories revealed that the building was responding predominantly in the direction of the alongwind *X* axis during both the IP7 and the IP9 wind load conditions. This trend was in distinct contrast to the typical uncorrelated building response experienced from the other IP wind loading events. Statistical analysis of the IP loading histories revealed the IP7 and the IP9 load conditions showed unexpected increases in RMS pressure components on the front face at the top floor. The load histories at the centre of the front face on the top floor for the IP7, IP9 and IP10 load conditions are shown in Figure 6.24. The measured RMS components from IP7 and IP9 are approximately 30% and 36% greater than the RMS component from IP10, respectively. The reason for this notable difference is that the first 40 seconds of the IP7 and IP9 load histories contain unsteady structure-induced sweeps of pressure as the flow was displaced upwards and over the top of the building; this characteristic was not as intense in the IP10 load history during the 120 seconds of flow-time.

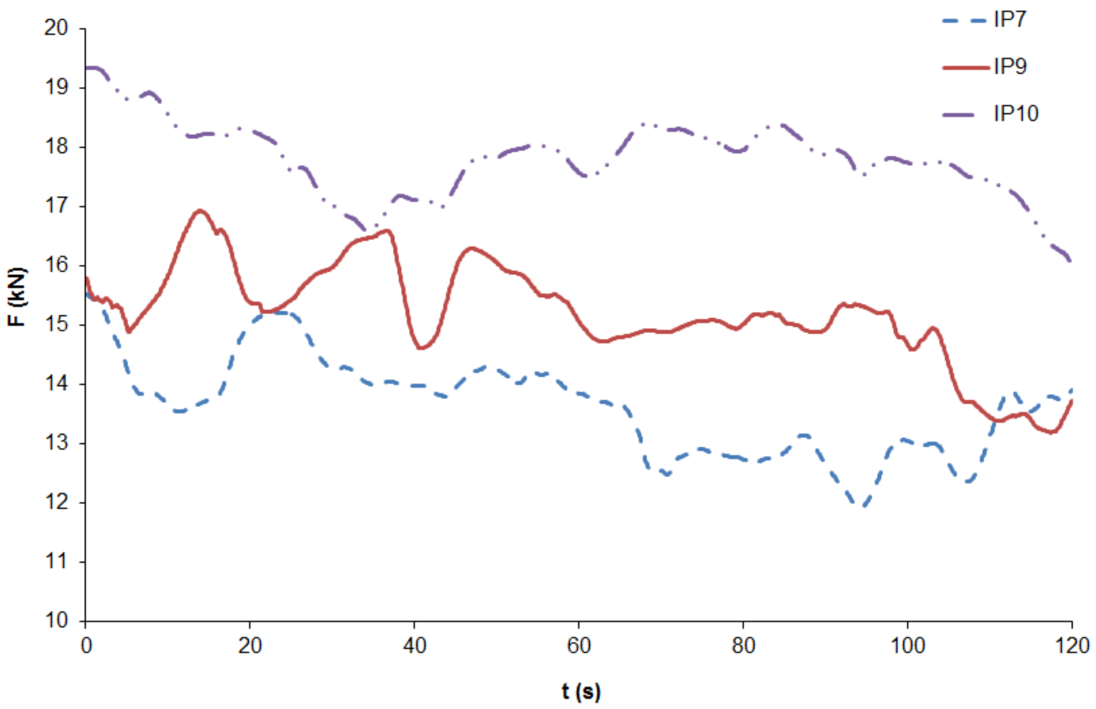

Figure 6.24. Time-history of force at the centre of the windward face on the top floor

The sensitivity of this structure to loading fluctuations on the windward face suggests that the atmospheric turbulence in the incident wind field could be the dominant excitation phenomenon. This raises concerns regarding the adequacy of the use of the RANS model for assessing the wind-induced response of this regular building design since it fails to sustain the inflow turbulence in the incident wind field.

Nonetheless, the best-fit engineering demand parameter (EDP) fragility curve was determined in MATLAB based on the related conditional probabilities of the v_b variable. The reciprocal of the dispersion, α, and the mode, U, for the Fisher-Tippett Type 1 distribution, as given by Equation 2.1, were 6.067 and 0.168 milli-g, respectively. Hence, the expression for the cumulative distribution function (CDF) becomes

$$P(a_{peak}) = \exp\left[-\exp\left\{-\left(6.067(a_{peak} - 0.168)\right)\right\}\right] \qquad (6.1)$$

This equation provided a narrow-banded, low range of accelerations as seen from the CDF in Figure 6.25. The CDF indicates that there is almost 100% probability that the peak top floor acceleration will not exceed 1 milli-g.

However, the peak EDP accelerations determined from the IP7 and IP9 loads both surpassed this threshold simply by capturing more structure-induced unsteadiness in the loading on the windward face towards the top of the building during the 120-second time-history. Since the response from these two wind events are valid for a structure of this form, the fragility curve is considered to be poorly estimated by this PBWE simulation strategy.

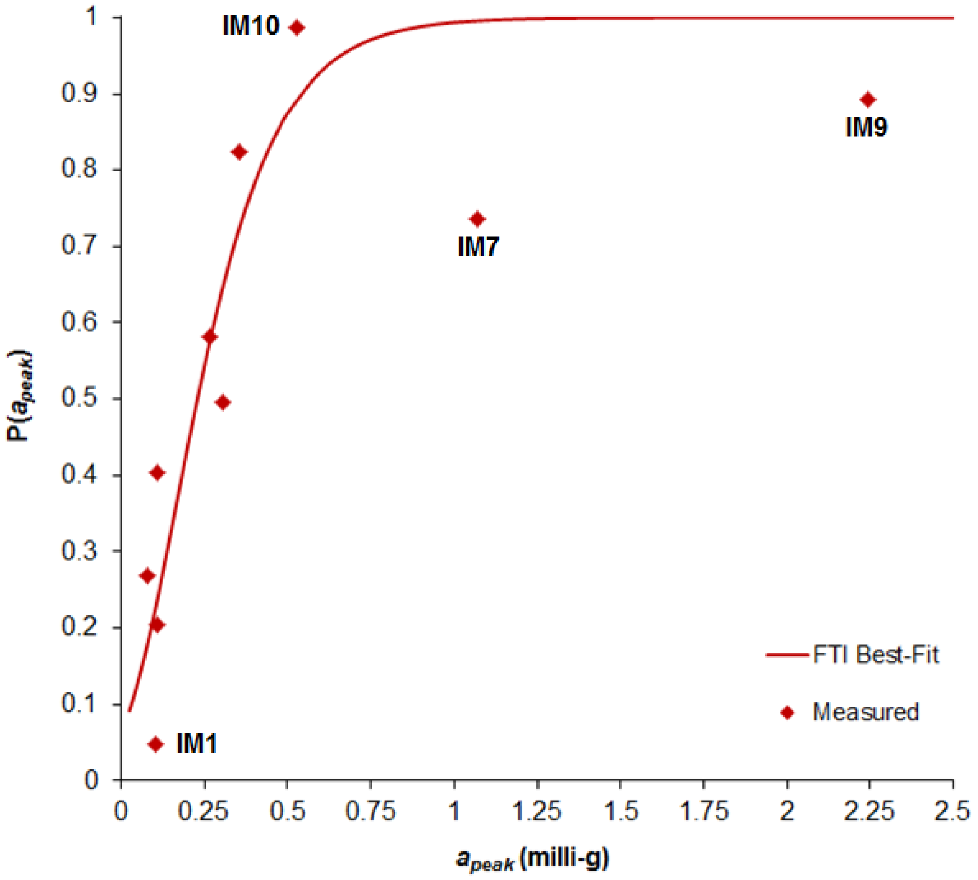

Figure 6.25. EDP fragility curve for the regular tall building based on the RANS model

Furthermore, the scatter from the ten EDP peak results inevitably affects the goodness of the fit to the data. The R-square value is 0.786 and the Sum of Squares due to Error (SSE) value is 0.19. An R-square value much closer to 1 and an SSE value much closer to zero were desired, which would have been improved by increasing the number of sampled IM wind events to provide more data points. However, this would further increase the already extensive CPU requirements of the CFD simulations.

6.4.3 Damage Analysis

The low accelerations provided by the poorly represented EDP fragility curve for the regular tall building were expected to easily satisfy the three DM performance expectation levels. The Melbourne and Palmer equation, given by Equation 2.10, was used to determine the limiting peak acceleration criteria for occupant comfort. The parameters that were specified for this equation were f = 0.267 Hz and T = 120 seconds. The resulting peak acceleration design limits for the three return periods in Section 3.4 are listed in Table 6.6. The peak acceleration values obtained from the EDP fragility curve are also included in Table 6.5. These peak values are significantly below the peak acceleration limits for the three return periods, and hence the damage criteria are satisfied.

Table 6.6. Damage analysis based on the RANS simulation strategy

Damage Measure (Complaint)	**Limiting Exceedance Probability**	**Peak Acceleration Limit (milli-g)**	**Peak Acceleration from PBWE (milli-g)**
Minor	20%	12.01	0.42
Moderate	5%	15.34	0.66
Major	2%	17.53	0.81

It was established in Chapter 4 that the RANS model fails to adequately sustain the atmospheric turbulence in the incident wind field. It is the atmospheric turbulence which would generate the major fluctuations on the windward face for such a regular tall building. Since the building response was found to be very sensitive to loading fluctuations on the windward face, it would have been very concerning if the accelerations from this RANS simulation strategy exceeded the well-established Melbourne and Palmer thresholds.

6.5 PBWE Assessment: RANS-LES Hybrid Simulation Strategy

6.5.1 Interaction Analysis

Due to the limitations of the RANS model, the following RANS-LES hybrid-type simulation strategy was developed as an alternative. In this approach the LES dynamic SGS kinetic energy model (ANSYS Inc, 2009a) was used to calculate the unsteady pressures for the IM10 wind event only, as a reference event. The transient wind loads were measured at the same 578 monitor positions as described in Section 6.3. A Microsoft Excel VBA algorithm was created to normalise the monitor data by dividing the instantaneous LES pressure results from IM10 by the corresponding mean LES pressure. Therefore, the 578 LES pressure histories were expressed as a function of the mean wind pressure.

The mean wind pressures for the IM1 to IM9 events were obtained from the RANS model detailed in the preceding Section. The mean pressure distribution is dependent on the vertical profile of the mean wind velocity. It was established in Chapter 4 that RANS can determine the mean surface pressures on the tall building to a sufficient level of accuracy. The transient wind load histories for the IP10 structural analysis were obtained directly from the LES simulation, whereas the corresponding wind load histories for the IP1 to IP9 events were created by up-scaling the normalised LES results for the reference IP10 event by the relevant mean pressures predicted by the RANS based analyses.

The procedure to adapt the 578 load histories from the reference IM10 wind event, which was calculated explicitly using the LES model, for the IM1 to IM9 events can be summarised by the following expression

$$P(t)_{IM(n)} = \left(\frac{P_{LES,IM10}(t)}{\overline{P}_{LES,IM10}} \right) \cdot \overline{P}_{RANS,IM(n)} \tag{6.2}$$

where *n* represents the considered IM wind event (*n* = 1 to 9).

In this alternative model the mean pressure distributions are representative of the considered IM wind event. However, the linear scaling from this simulation strategy obviously does not explicitly consider the variation of turbulence length scale, turbulence intensity and excitation frequency between the wind events. Nonetheless, it is believed that the adopted simplification provides a credible indication of the importance of atmospheric turbulence for the PBWE assessment of the regular tall building. The IM10 event represents the most intense wind event. Therefore, the results from the adapted IM1 to IM9 events were expected to be conservative.

For the LES turbulence model, the spectral synthesizer function was used to generate perturbations in the velocity field at the inflow boundary condition. The turbulence intensity and turbulence length scale were chosen as the specification method for generating the fluctuating velocity components, with values of 16.7% and 166 metres at building height, respectively. The computational time-step of the LES model was 1×10^{-3} s and the CPU cost for a single time-step was 32.0 s using 8 CPUs in parallel. Therefore, the total CPU time which was spent computing both the 120-second 'warm-up' period and the 120-second IP load histories for this reference IM wind event was 89 days.

The visible contrast between the pressure histories measured by the RANS and the LES models is illustrated by Figure 6.26 to 6.28. It is evident that the pressure histories determined by these two turbulence models produce approximately the same mean pressure. However, the LES wind loadings on the front, side and back face are all driven by the low-frequency velocity perturbations as generated by the spectral synthesizer at the inlet. In addition, the wind pressures predicted by the LES model also contain high-frequency fluctuations, which are components of atmospheric turbulence and structure-induced turbulence. In contrast, the fluctuations measured by the RANS model are almost entirely attributable to structure-induced turbulence.

It was believed that the low-frequency perturbations would act as gradual changes to the mean wind loading since the frequency content (f = 0.017 Hz) is considerably lower than the natural frequencies of the tall building (f_1 = 0.267 Hz). The structural analysis of the tall building was expected to be more dependent on the higher frequency fluctuations generated by both the atmospheric turbulence and the structure-induced turbulence.

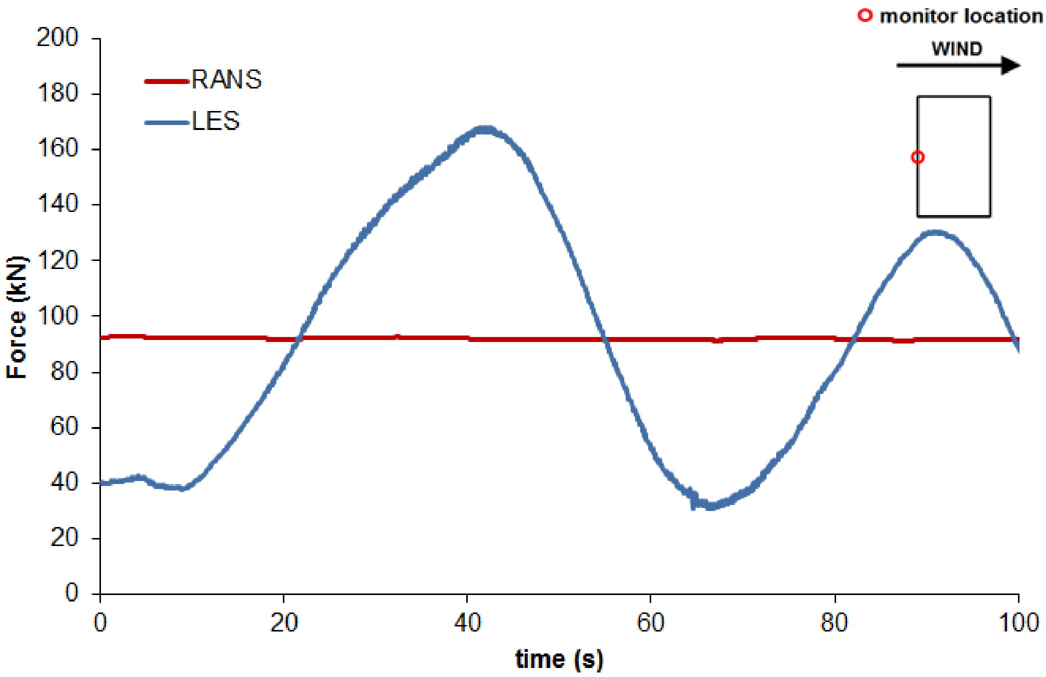

Figure 6.26. Comparison of pressure histories on the centre of the front face at 2/3*H*

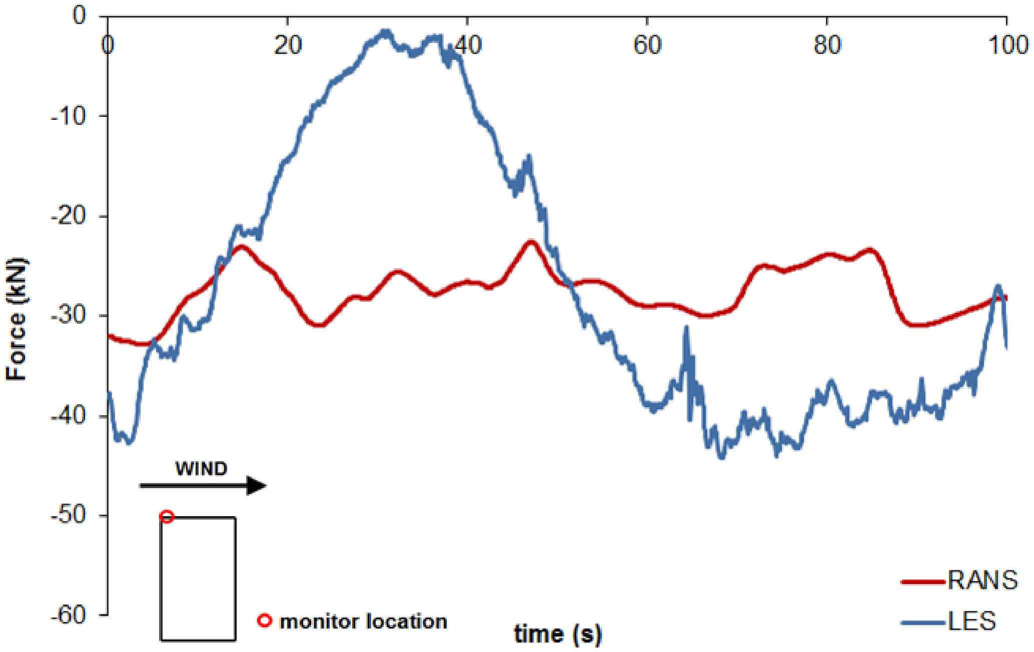

Figure 6.27. Comparison of pressure histories at the leading edge of the side face at 2/3*H*

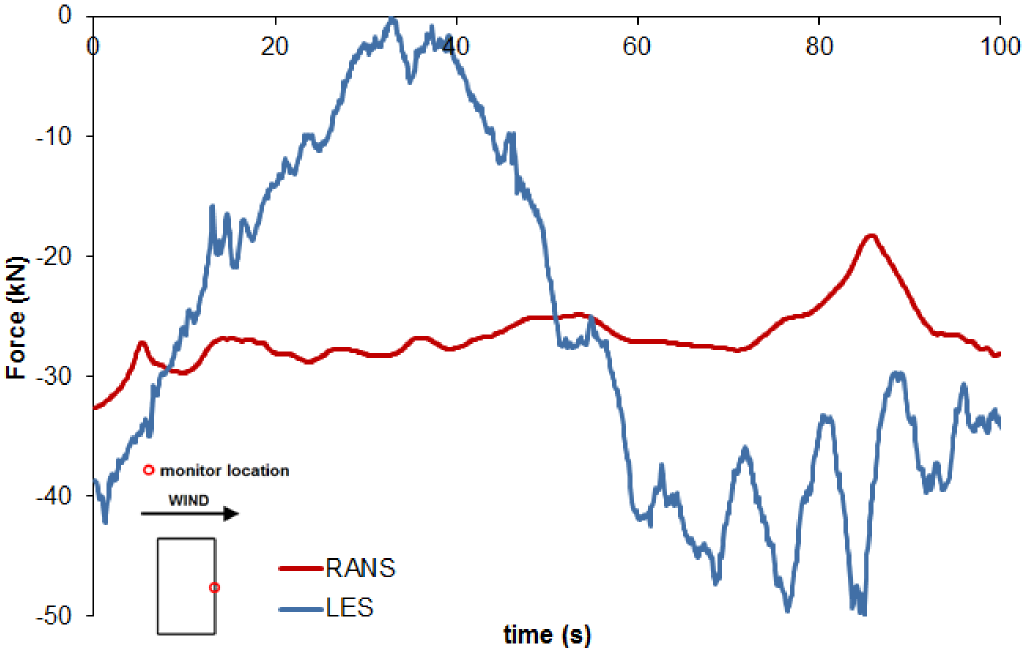

Figure 6.28. Comparison of pressure histories on the centre of the back face at 2/3*H*

6.5.2 Structural Analysis

The procedure for the structural analysis was repeated to determine the wind-induced response for each set of IP load conditions from the RANS-LES hybrid-type simulation strategy. The specifications for the linear transient dynamic solver were consistent with those applied for the Strand7 analyses in the preceding Section. As shown in Figure 6.16, the modal damping ratios for modes 1 (f_1 = 0.267 Hz) to 20 (f_{20} = 5.22 Hz) were formulated as Rayleigh damping.

The alongwind AX acceleration and crosswind AZ acceleration response histories on the top floor from the IP10 load conditions calculated by the LES model (LES-IP10) are shown in Figure 6.29. The response of the structure to the LES-IP10 load histories is clearly more complex than the response from IP10 load conditions calculated by the RANS model (RANS-IP10), shown in Figure 6.18. The distinct low-frequency beat modulation, which was a prominent response feature from the RANS-IP10 loads, is not evident in Figure 6.29. Instead, the stochastic response histories from the LES-IP10 wind loads appear to contain several interference frequencies. These complex acceleration histories are a consequence of the increased unsteady fluctuations from the atmospheric turbulence produced by the LES model. In addition, the amplitudes of both the AX and AZ response histories show a notable increase during the last 40 seconds. The increased responses are caused by increased unsteadiness of the wind loading on both the side and back faces of the building during this time, as shown in Figures 6.27 and 6.28, respectively.

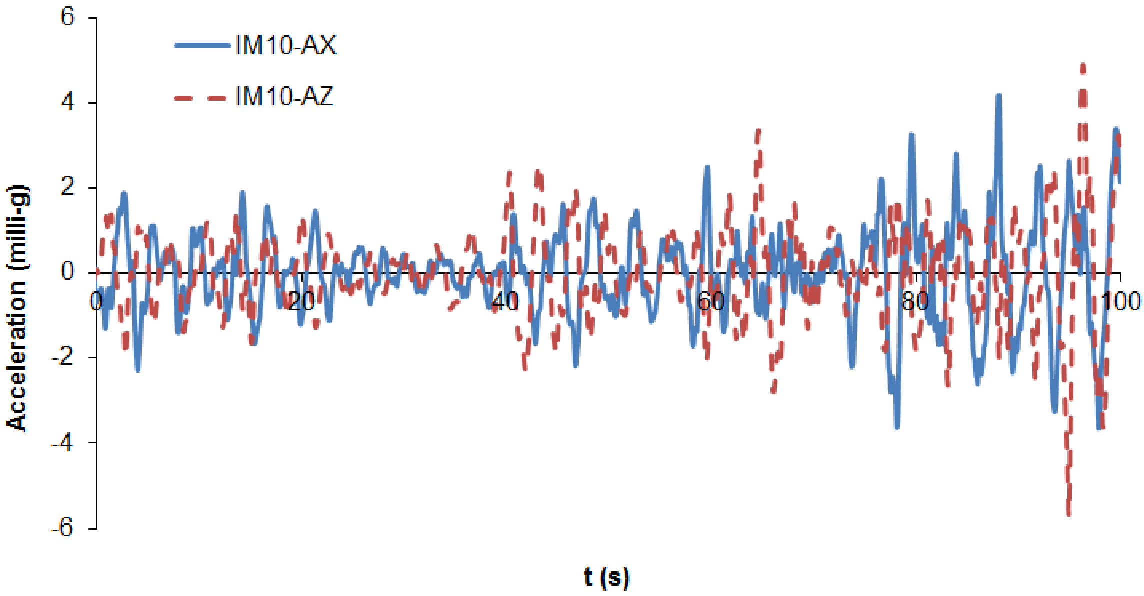

Figure 6.29. AX and AZ components of top floor acceleration response during the IP10 wind load conditions based on the LES model

The absolute top floor acceleration histories resulting from the RANS-IP10 and the LES-IP10 load conditions are shown in Figure 6.30. The standard deviation from the LES-IP10 load conditions is 2.43 milli-g, while the absolute peak acceleration is 6.83 milli-g. These two statistical parameters are both over an order of magnitude greater than the corresponding values from the RANS-IP10 load conditions. In general, the absolute response history appears to gradually increase, particularly during the last 40 seconds. Once again, this is a consequence of more unsteady loading fluctuations on both the side and back faces during this time. The peak is measured towards the end of the 120-second time history at 94.9 seconds. It can be seen that this maximum peak is notably larger than the preceding peaks in the response history. This raises concerns regarding the adequacy of only considering a 120-second response history from the wind event as opposed to the typical 600-second duration. However, the computational demands of the LES model dictated that providing a longer IP load history was completely impractical.

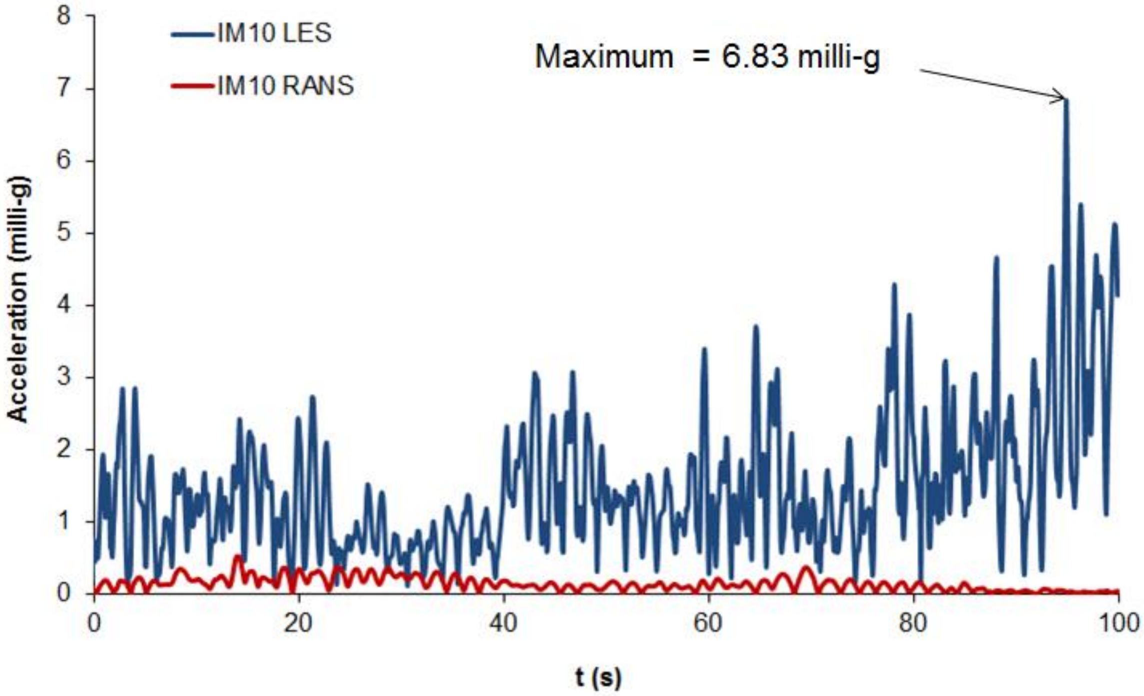

Figure 6.30. Absolute top floor acceleration during the IP10 load histories from the RANS and the LES models

The Pearson product-moment correlation coefficient for the AX and AZ top floor response histories from the LES-IP10 load histories is -0.21. This value suggests that the AX and AZ response components are more correlated than the corresponding AX and AZ response histories from the RANS-IP10 load histories. However, it still represents a fairly weak linear correlation and suggests the regular tall building is not responding in any one dominant direction of motion. This is supported by the resulting acceleration trace from the LES-IP10 wind loading event, as shown in Figure 6.31.

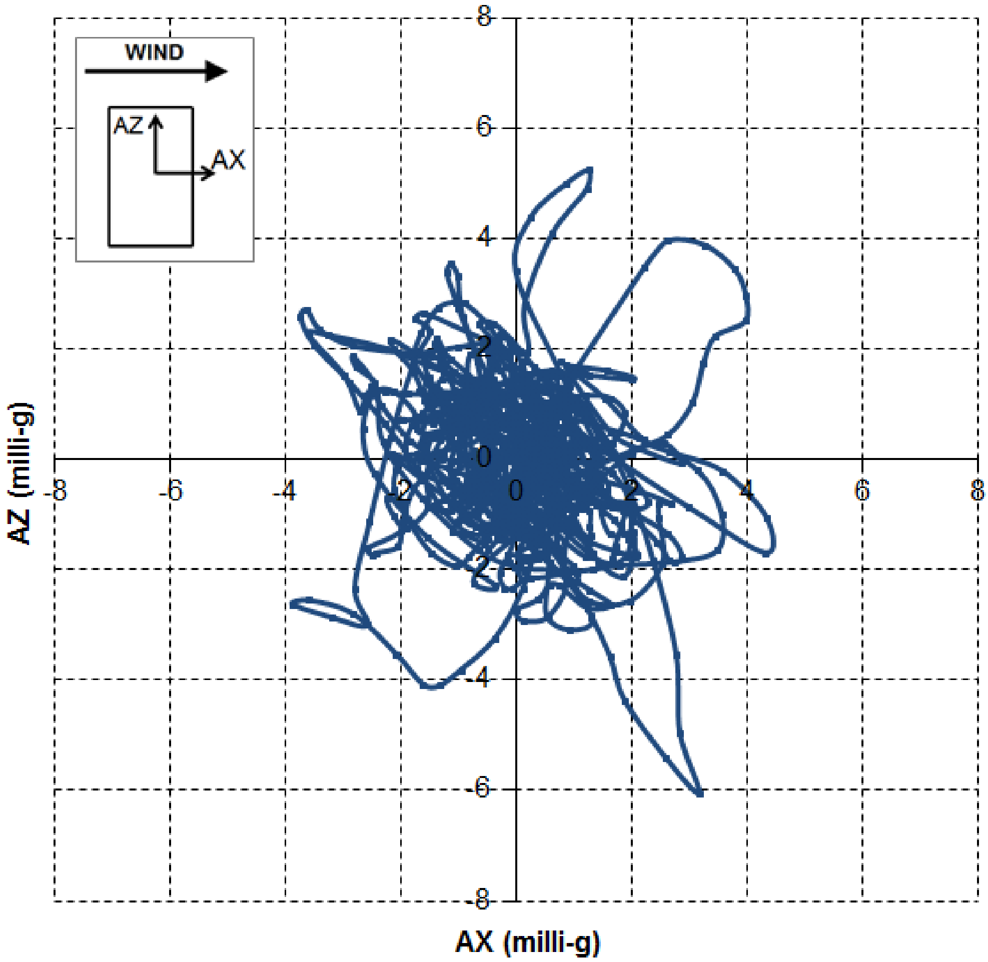

Figure 6.31. Acceleration trace during IP10 load conditions based on LES model

FFT analyses were again performed in MATLAB to obtain the frequency spectrum of the AX and AZ time histories from the LES-IP10 loading conditions. It is evident from Figure 6.32 that the lower frequency range of the AX time history from the LES-IP10 loading is similar to the corresponding AX time history from the RANS-IP10 loading. However, the AX frequency spectrum from the LES-IP10 loading contains much more notable contributions from the higher-order natural frequencies. The contribution of the 4th mode of vibration is almost 3 times greater than was measured from the RANS-IP10 load conditions. In addition, a distinct peak is observed at the 7th mode of vibration (f = 2.25 Hz), while the frequency spectrum from the RANS-IP10 loading did not display any notable responses at frequencies greater than 2 Hz. The FFT spectrum also displays a broader and more prominent range of interference frequencies than was experienced during the

AX response history from RANS-IP10 loading. A similar contrast is observed between the AZ frequency spectra from the RANS-IP10 and the LES-IP10 load conditions, as shown in Figure 6.33. The FFT response spectra from the LES-IP10 load conditions are also likely to become smoother if the time-history durations are increased.

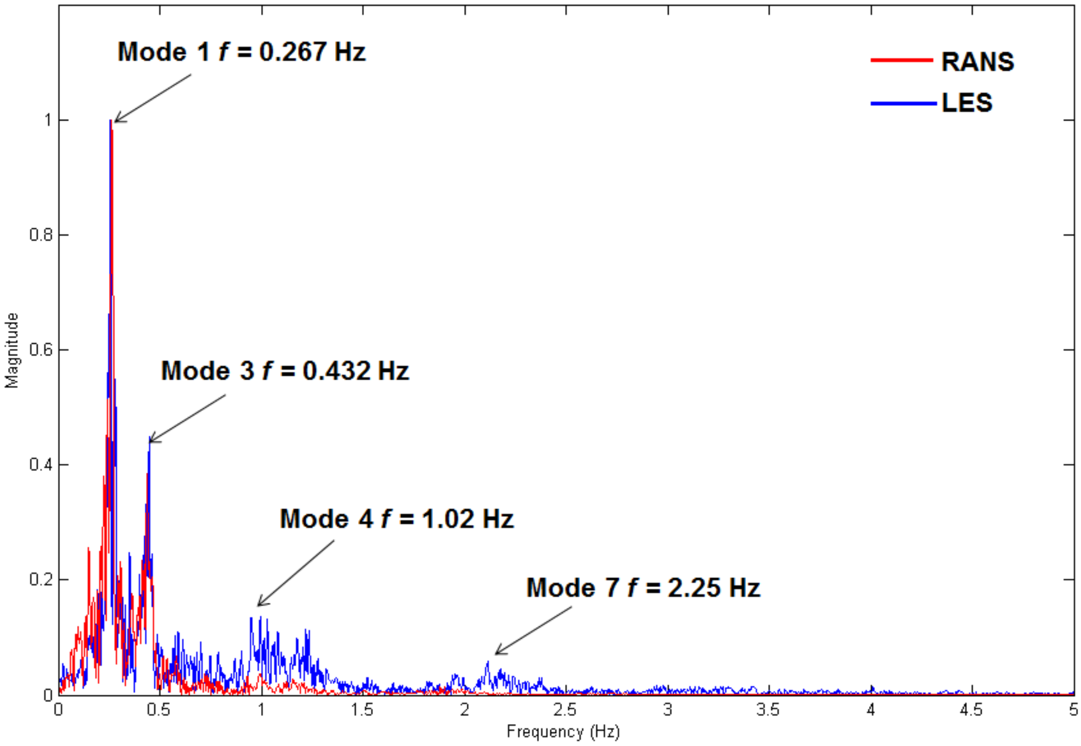

Figure 6.32. Frequency spectrum of AX time history during the LES-IP10 and the RANS-IP10 wind loading

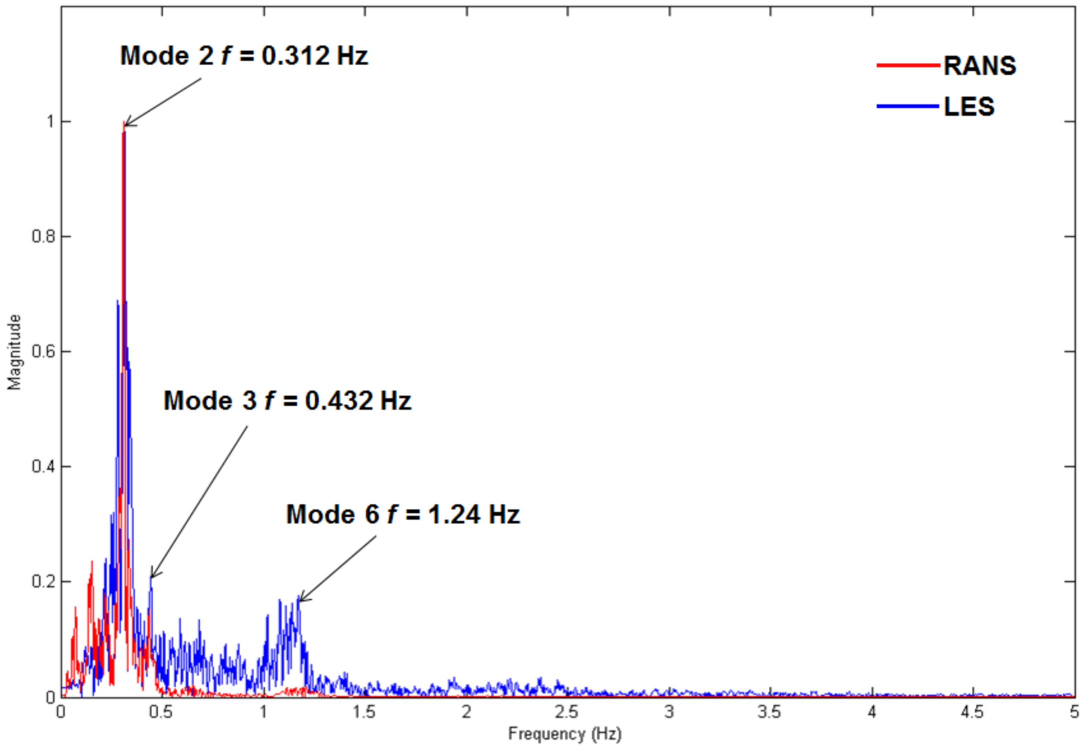

Figure 6.33. Frequency spectrum of AZ time history during the LES-IP10 and the RANS-IP10 wind loading

The peak top floor accelerations (chosen as EDPs) from the adapted IP1 to IP9 wind load conditions were identified using the post-processing algorithm developed in Microsoft Excel VBA. The relationship between these calculated EDP peak top floor accelerations and the mean wind velocity at building height for each wind event is plotted in Figure 6.34 and a summary of the peak values is provided in Table 6.7. The results from the RANS-LES hybrid simulation strategy are significantly greater than the results from the RANS solution alone. This highlights the sensitivity of the structure to atmospheric turbulence (including low-frequency perturbations), which were not present in the RANS model. Due to the assumptions contained within the proposed RANS-LES hybrid simulation strategy, the scatter of these results is attributable to the variations in the mean pressure distributions. The trend of the results shows a gradual increase in EDP acceleration with increasing IM mean wind velocity at building height; it does not display the distinct increases from the IP7 and the IP9 load conditions, as was observed from the RANS-based solution.

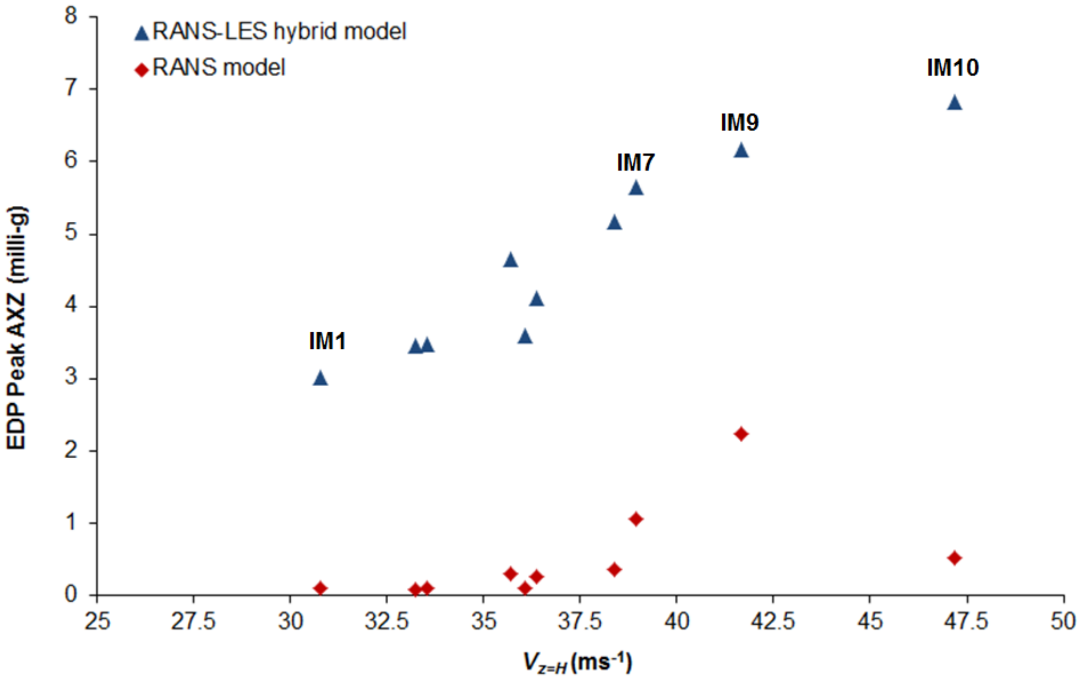

Figure 6.34. EDP top floor acceleration vs. IM mean wind velocity at building height predicted by the RANS and the RANS-LES hybrid models

Table 6.7. Summary of EDP peak top floor accelerations based on RANS-LES hybrid model

IM	$V_{z=H}$ (ms^{-1})	A_{peak} (milli-g)
1	30.75	3.021
2	33.55	3.478
3	33.23	3.458
4	36.08	3.595
5	35.69	4.650
6	36.38	4.121
7	38.94	5.645
8	38.39	5.162
9	41.67	6.173
10	47.17	6.834

The best-fit engineering demand parameter (EDP) fragility curve was again determined in MATLAB based on the related conditional probabilities of the v_b variable. The reciprocal of the dispersion, α, and the mode, U, for the Fisher-Tippett Type 1 distribution, as given by Equation 2.1, were 0.91 and 3.8 milli-g, respectively. Hence, the expression for the cumulative distribution function (CDF) becomes

$$P(a_{peak}) = \exp\left[-\exp\left\{-\left(0.91\left(a_{peak} - 3.8\right)\right)\right\}\right] \tag{6.3}$$

The resulting CDF is shown in Figure 6.35. The R-square value is 0.924 and the Sum of Squares due to Error (SSE) value is 0.067. These goodness-of-fit statistics indicate that the fit adequately describes the variation of the peak acceleration data and the results have a small random error component. This represents a significantly better fit than was achieved from the EDP fragility curve based on the RANS model. However, it cannot be overlooked that the extent of this goodness-of-fit is likely to be aided by the IP scaling procedure which underlies the RANS-LES hybrid model.

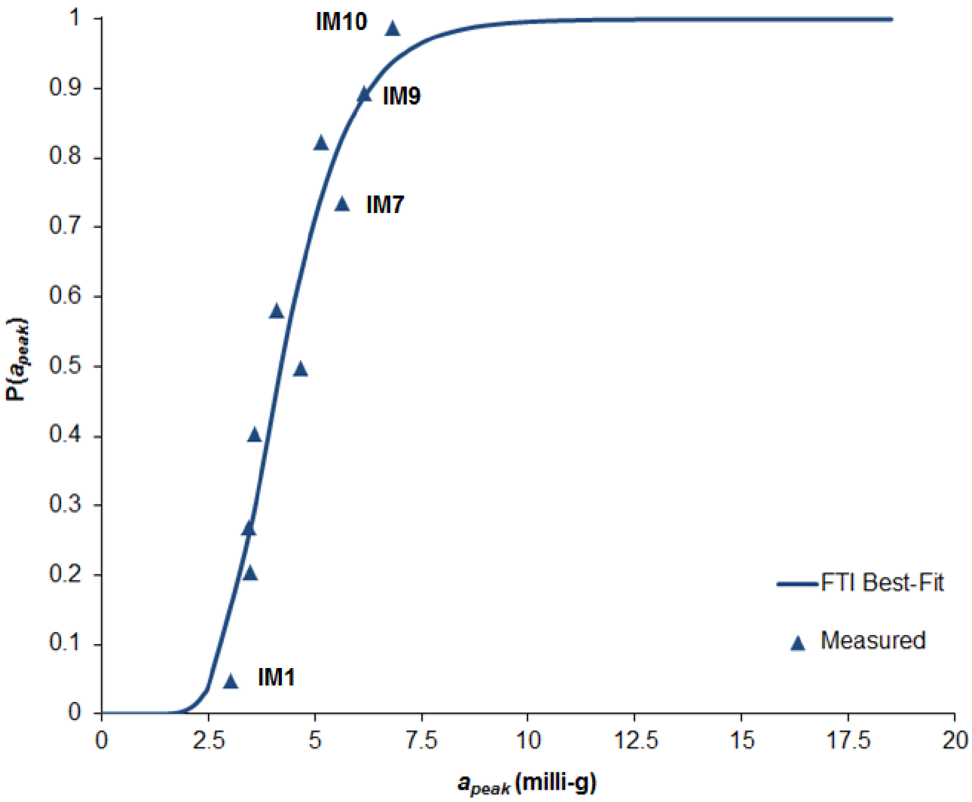

Figure 6.35. EDP fragility curve for regular tall building based on RANS-LES hybrid model

As shown in Figure 6.36, the RANS-LES hybrid simulation strategy produced an increased and broader range of accelerations than was determined from the RANS model alone. Despite its underlying assumptions, this alternative solution is considered to provide a more realistic representation of the structural response for the PBWE assessment. The contrast from this comparison further emphasises that the fragility curve derived from the RANS simulation strategy provides a very poor representation of the probabilistic performance of the regular tall building.

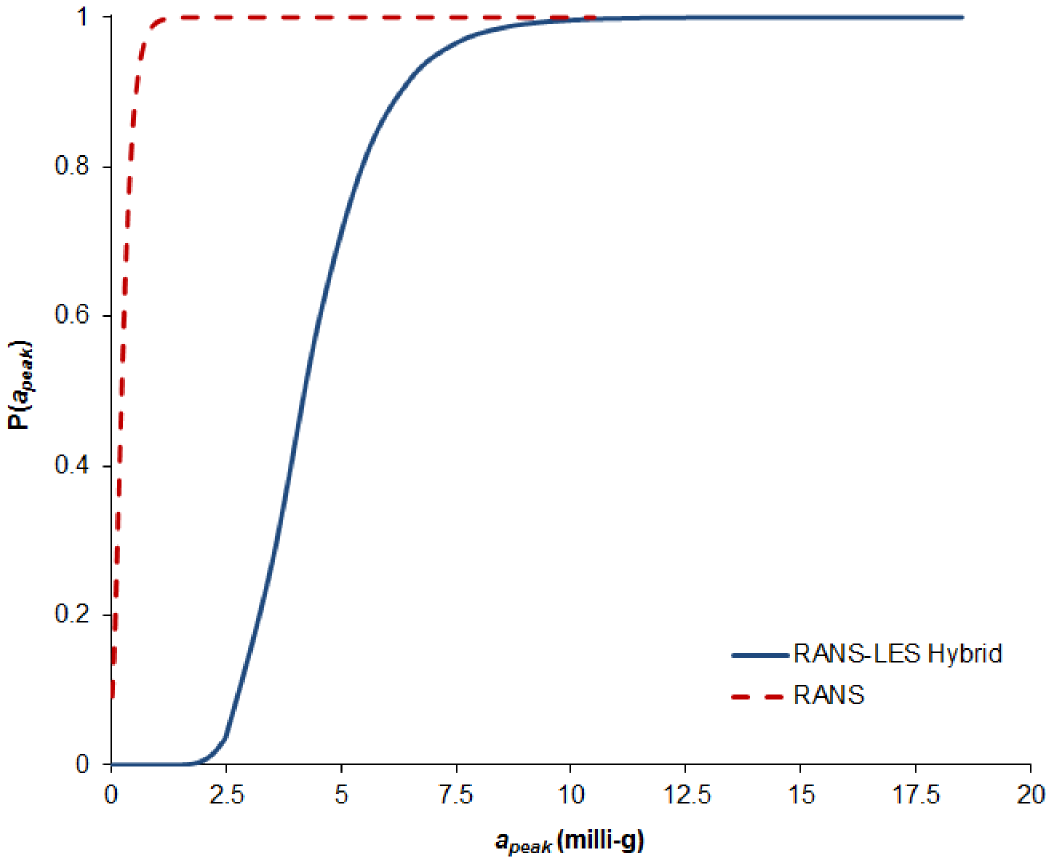

Figure 6.36. Comparison of the EDP fragility curves from the RANS and the RANS-LES hybrid solution strategies

6.5.3 Damage Analysis

The fragility curve from the alternative simulation strategy was compared against the calculated Melbourne and Palmer peak acceleration limits for occupant comfort. The peak accelerations from the EDP fragility curve which relate to the specified limiting exceedance probabilities are listed in Table

6.8. It can be seen that these accelerations are all safely below the Melbourne and Palmer peak acceleration limits. Therefore, the performance of the regular tall building design is satisfactory according to this proposed PBWE framework. However, it should be noted that the limiting exceedance probabilities were almost arbitrarily specified for the three return periods. The structure may not have satisfied the damage criteria if more stringent limiting exceedance probabilities were defined for such short return periods.

Table 6.8. Damage analysis based on the RANS-LES hybrid simulation strategy

Damage Measure (Complaint)	**Limiting Exceedance Probability**	**Peak Acceleration Limit (milli-g)**	**Peak Acceleration from PBWE (milli-g)**
Minor	20%	12.01	5.45
Moderate	5%	15.34	7.06
Major	2%	17.53	8.07

6.6 Concluding Remarks

The stages of the PBWE framework have been followed to assess the performance of the regular tall building design based on two solution strategies. The results showed that the regular tall building was significantly more sensitive to the incoming atmospheric turbulence (including low-frequency velocity perturbations) than to the structure-induced turbulence. On this evidence, it was clearly unacceptable to use the RANS turbulence model alone for determining the wind-induced response of a tall building of this form since it fails to adequately model the atmospheric turbulence in the incident wind field.

The RANS-LES hybrid simulation strategy used the LES model to calculate the wind histories for a reference IM wind event, here the IM10 event was chosen. The reference results were scaled for the remaining IM1 to IM9 events via mean pressures. This strategy does not explicitly consider the variation of turbulence length scale, turbulence intensity and excitation frequency between the wind events. Nonetheless, it was considered to provide a more realistic representation of the wind-induced response of the tall building than was offered by the RANS model alone. The resulting performance of the regular tall building satisfied the PBWE damage criteria that were specified in terms of occupant comfort.

The wind load histories calculated by the LES model were clearly driven by the low-frequency velocity perturbations generated at the inlet boundary condition. Therefore, the level of accuracy achieved by the LES model was dependent on the boundary conditions specified at the inlet. This emphasised the importance of specifying boundary conditions that adequately represent the considered site. It is difficult to satisfy this requirement since there is a general lack of field data available of wind flow within densely built-up town terrains.

There was evidence to suggest that the 120-second dynamic response histories from each of the wind events may not have been sufficiently long enough. The wind-induced response of a tall building is typically assessed over 600 seconds. However, the computational demands of CFD, particularly when using the LES model, dictated that providing a longer IP load history was impractical in the context of this thesis. In addition, the complexity of the observed building response implied that it may be more appropriate to assess the acceleration histories within each structural analysis by using suitable statistical methods rather than simply obtaining the maximum peak as was done here.

7

PBWE Analysis for Irregular Tall Building

7.1 Preamble

This Chapter follows the remaining stages of the simulation framework for the PBWE assessment of an irregular tall building. The computational models for the fluid and structure domains are detailed. The previous Chapter concluded that the RANS-LES hybrid simulation strategy offered a more realistic representation of the wind-induced response for the regular tall building. Within the time-scale of the thesis, however, it was too impractical to perform the reference CFD simulation using the LES model for the irregular tall building (as has been done in Chapter 6 for a regular tall building) due to its prohibitive computational demand, i.e., approximately 100 days. Rather, the PBWE assessment included in this Chapter is based on modelling the IM wind events using the RANS turbulence model only. The resulting performance of the irregular tall building is then compared against the performance of the regular tall building also based on the RANS model.

The results show that the structure-induced turbulence has a more significant and consistent effect on the wind-induced response of the irregular tall building. This is because the irregular geometry induces more complex flow patterns and unsteady loading conditions than the regular tall building design. The RANS model appears more suited to the PBWE framework as the level of structure-induced turbulence increases for irregular buildings. However, it is nevertheless concluded that this model is not fully appropriate to be applied as a stand-alone model for computing the IP wind load histories.

7.2 Fluid Domain: Computational Model in ANSYS FLUENT

The series of CFD simulations for the irregular tall building considers the wind acting normal to the most flexible axis of the tall building, as indicated in Figure 7.1. The corresponding crosswind width *B* is 60 m and the alongwind depth *D* is 46 m. The domain geometry was created following the recommendations by Revuz *et al.* (2010). The guidelines for the size of the domain are based on the crosswind width and height of the considered tall building. The width of the irregular tall building (*B* = 60 m) is notably larger than the regular tall building (*B* = 45 m). Therefore, the domain volume was 40% larger than the domain used for the CFD simulations of the regular tall building. This provided the same 0.93% streamwise blockage ratio (area of windward face / area of inlet face). The geometry of the computational domain is detailed in Table 7.1.

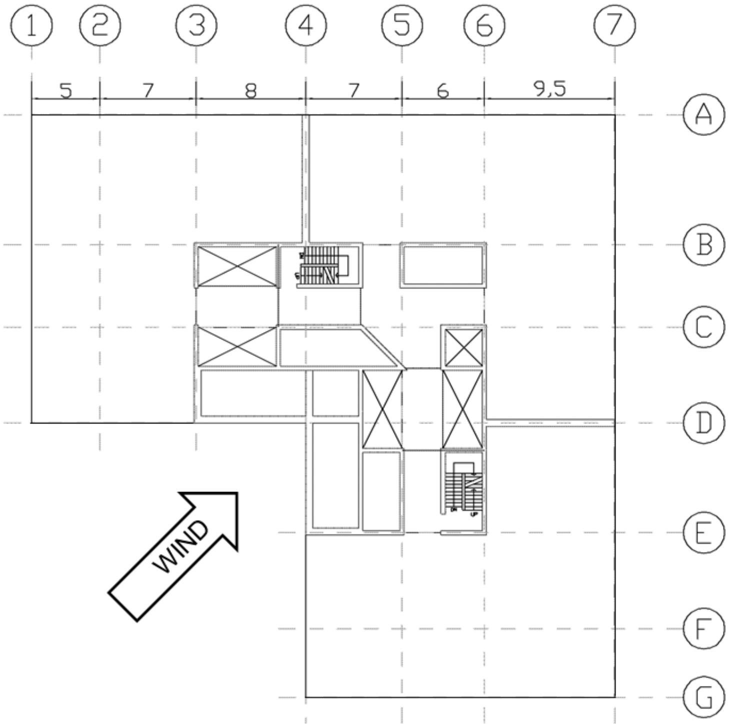

Figure 7.1.Orientation of the irregular tall building relative to the incident wind

Table 7.1. Details of the domain geometry for the irregular tall building

	DX (m)	DY (m)	DZ (m)
D1	900 + *D* + 1500	780 + *B* + 780	720

The same nested mesh technique as for the regular tall building study was implemented for the mesh design. Unfortunately, the mesh generation within the nest was an extremely challenging task due to the re-entrant corner of the irregular ‘L’-shaped building. It was further complicated since the angle of attack meant none of the six building faces ran parallel with the outer faces of the domain. The inflated boundary layer tool in the pre-processing software GAMBIT (FLUENT Inc, 2007) can be used to define the spacing of mesh node rows in the regions immediately adjacent to building surfaces; this feature was used for the regular tall building mesh design. However, the automatic meshing algorithm in GAMBIT consistently produced highly skewed and inverted computational cells when the inflated boundary layer tool was used for the irregular tall building. Therefore, the near-wall fluid regions that would have been occupied by the inflated boundary layer had to be discretised into a series of individual fluid volumes and meshed manually.

In addition, the orientation of the building meant the faces could not be distinctly classified as windward, side and leeward. Therefore, a mesh interval size, which is used to specify the number of intervals on an edge, of 0.54 m was applied to all the horizontal edges of the building face. The regular tall building mesh had this 0.54 m refinement for the side faces and a coarser interval size of 0.60 m for the windward and leeward faces. A reduced vertical interval size of 1.10 m was used for the irregular tall building mesh to decrease the skewness at the re-entrant corner.

The final near-wall mesh design for these discretised fluid volumes consisted of 1.625×10^6 hexahedral cells. This is 63% more cells than was contained within the boundary layer of the regular tall building. This is almost entirely attributable to the re-entrant corner and ensuring the mesh within this region was not overly skewed. The near wall mesh in the horizontal *X*-*Y* plane is shown in Figure 7.2 and a closer inspection of the mesh design at the re-entrant corner is shown in Figure 7.3. Finally, the unstructured mesh design that was automatically generated in the nest is shown in Figure 7.4. The total number of computational cells within the nest is 2.65 x 10^6.

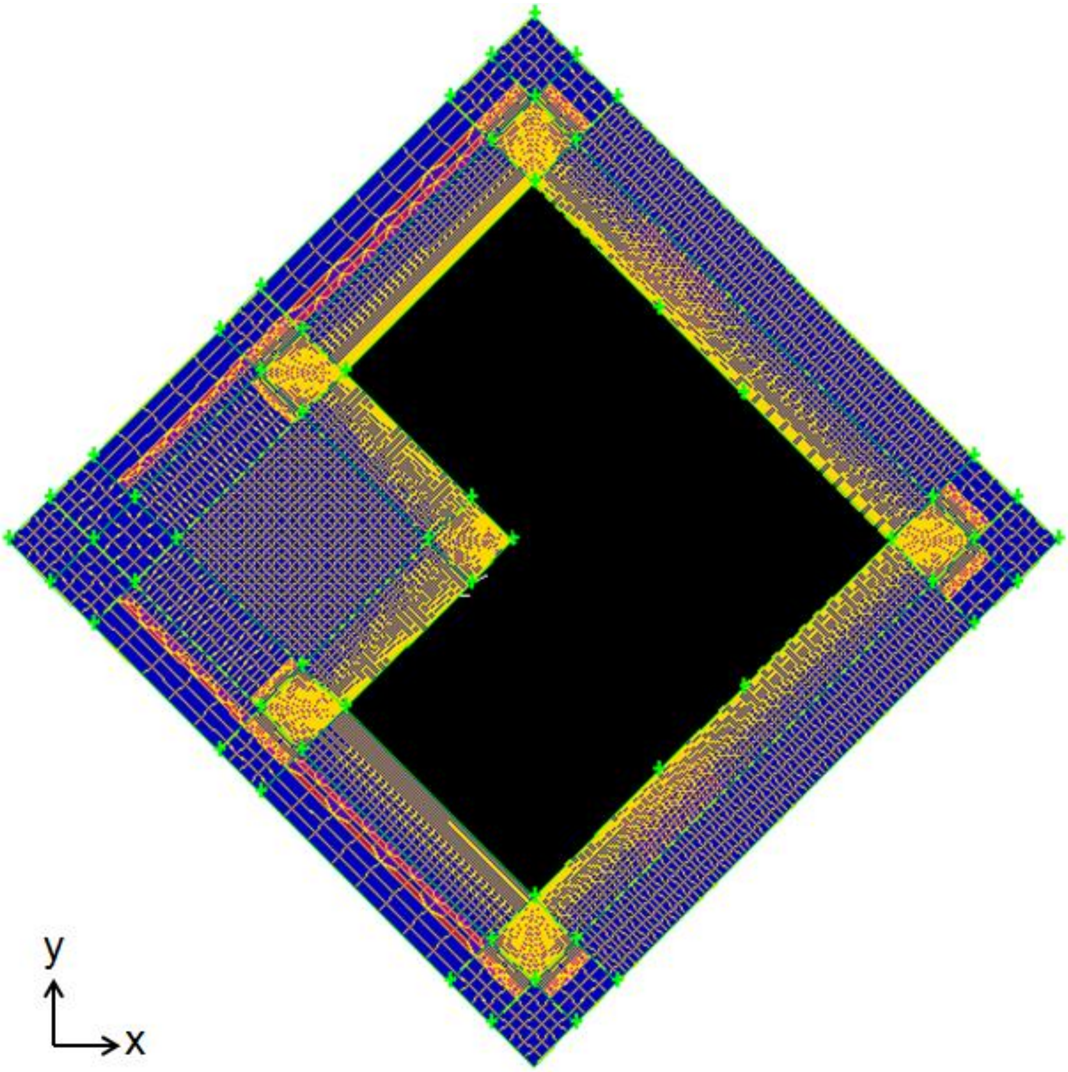

Figure 7.2. Near-wall mesh in *X*-*Y* plane showing subdivided regions (flow is from left to right)

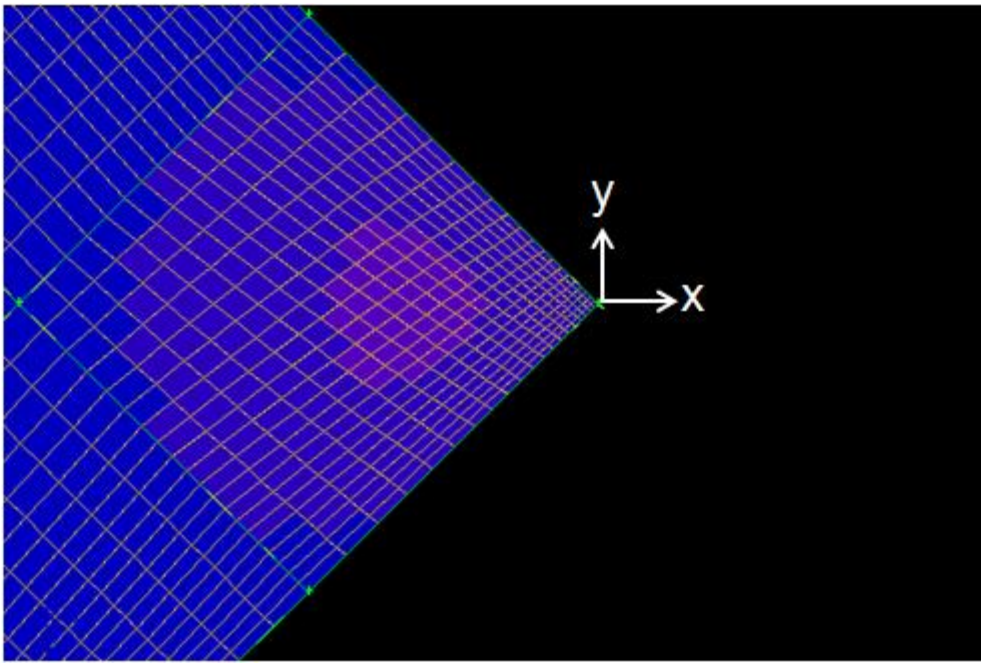

Figure 7.3. Near-wall mesh at the re-entrant corner in *X-Y* plane (flow is from left to right)

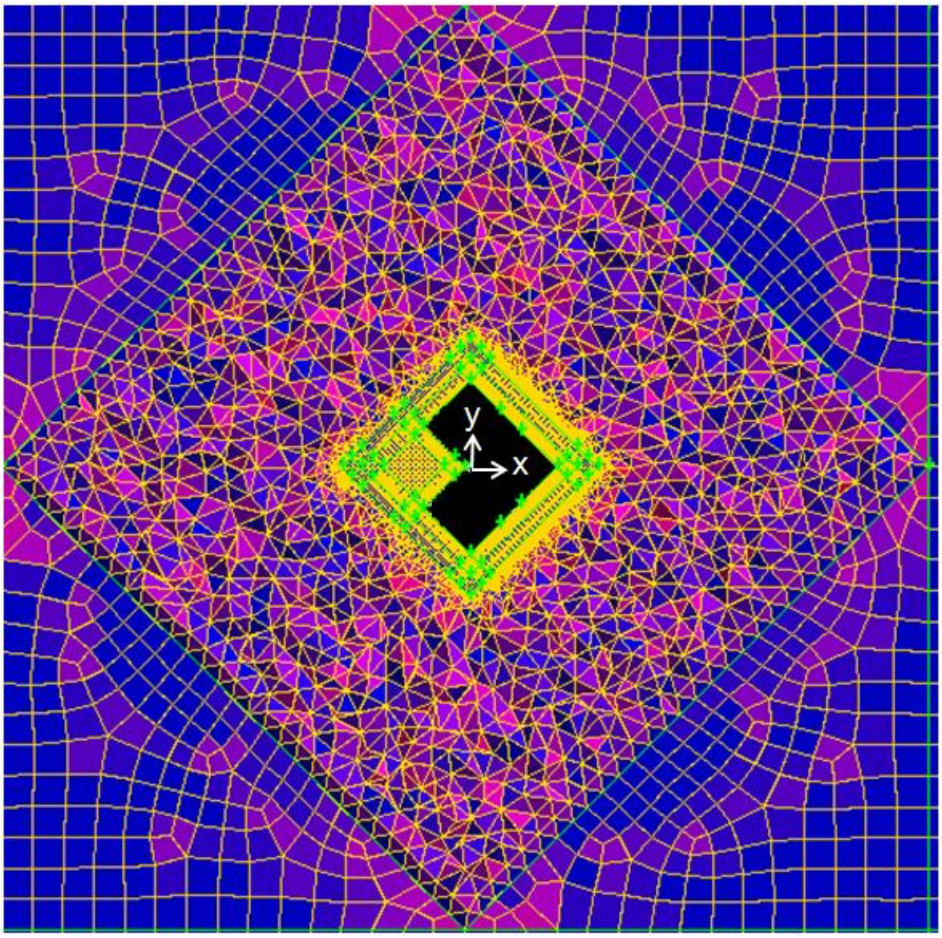

Figure 7.4. Unstructured mesh in the nest in *X-Y* plane (flow is from left to right)

The meshed domain in the horizontal *X-Y* plane for the entire domain is shown in Figure 7.5. This CFD model consists of 3.70 million computational cells and represents a 25% increase on the total number of cells contained within the CFD domain for the regular tall building. With this mesh design, almost 40% of the total computational cells are concentrated within the nest and approximately 28% of the total number is contained within the subdivided near-wall volumes.

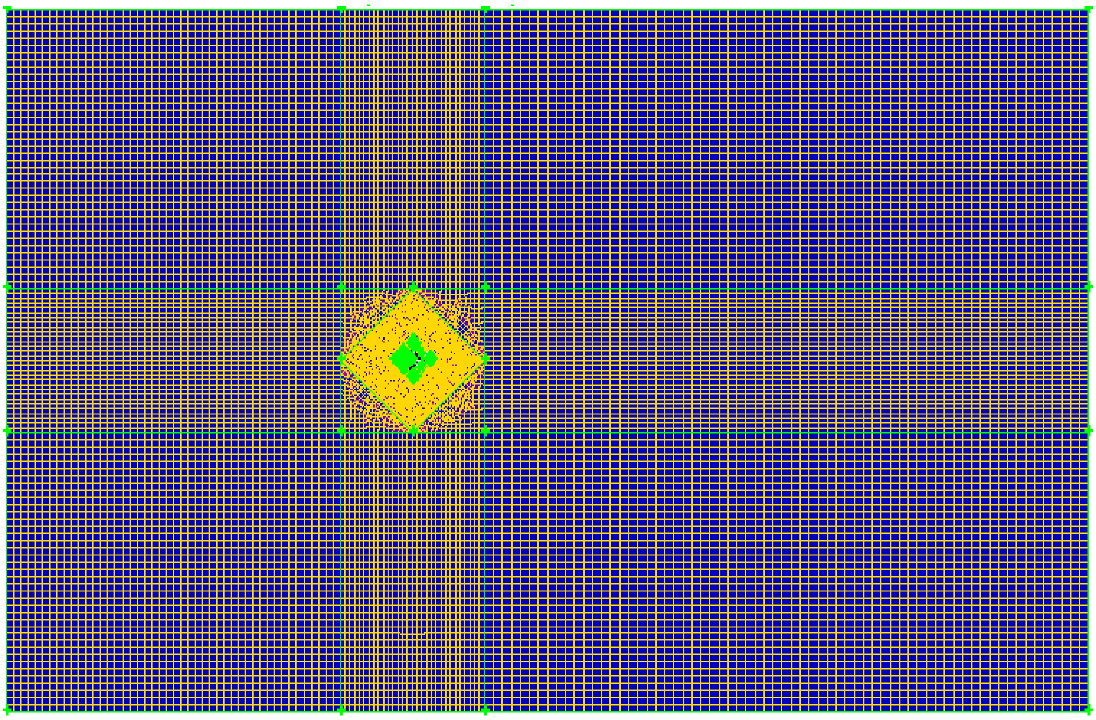

Figure 7.5. Domain mesh in *X-Y* plane for irregular building (flow is from left to right)

The boundary conditions used for these CFD simulations were consistent with those specified for the regular tall building. In summary, the inflow boundary condition was defined as a velocity inlet with the vertical profiles of the atmospheric boundary layer (ABL) wind characteristics for each IM wind event. The top and side boundary conditions were defined as velocity inlets with corresponding streamwise velocity components to better maintain the ABL flow. The outlet boundary condition was defined as a pressure outlet with 0 Pa gauge pressure. The boundary conditions on the building faces and domain floor were set as no-slip condition walls.

The pressure monitors on the irregular building were created using the same discretisation strategy as detailed for the regular tall building in Section 6.2. A total of 30 monitors were created around the perimeter at 25 intervals throughout the building span. An additional 41 monitors were created to measure the pressure on the building roof. Therefore, a total of 791 pressure monitors were generated. This is approximately 37% more than the regular building. This increase in monitors was simply due to the increased surface area of the irregular building. Figure 7.6 shows the monitor arrangement.

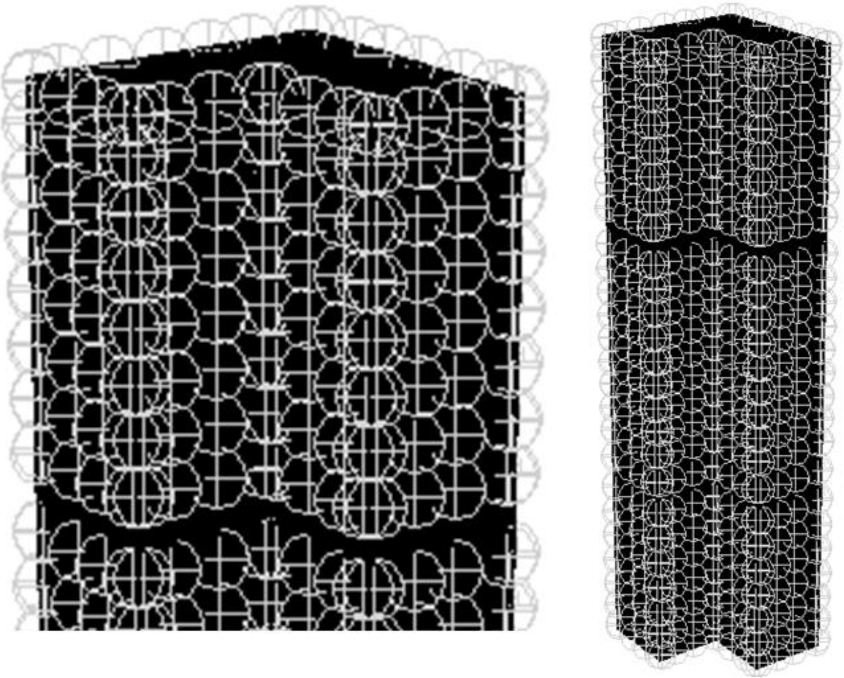

Figure 7.6. Pressure monitors created on the irregular tall building in the CFD domain

The initial task of the one-way coupling algorithm was to access the 791 separate output files and translate the measured point pressure histories into forces by multiplying the values by the associated surface area. These adjusted values were then created as separate factor vs. time load tables for the Strand7 structural domain finite element model.

7.3 Structure Domain: Computational Model in Strand7

The finite element model of this irregular tall building in Strand7 comprised 47155 nodes, connected by 11239 beam and 45329 plate elements, as shown in Figure 7.7. As with the regular tall building, the labels of the vertical and crosswind axes swap between the fluid and structural domains. In the structural domain the *y*-axis refers to the vertical plane and the *z*-axis refers to the crosswind plane; the opposite was true in the fluid domain.

Structural members of the irregular tall building were designed to furnish a fundamental natural frequency that was approximately equal to the regular tall building dynamic system (i.e. $f = 0.267$ Hz). The core and shear walls at the outrigger levels are 400 mm thick and use reinforced concrete with a 50 MPa compressive strength. The same 275 mm thick flat slab design is adopted. The edge beams and coupling beams have the same dimensions and material properties as used by the regular tall building design. The maximum and minimum column sizes are consistent with those used in the previous tall building structural model. However, the design consists of a broader range of column sizes and these dimensions are typically larger than those featuring in the regular tall building design.

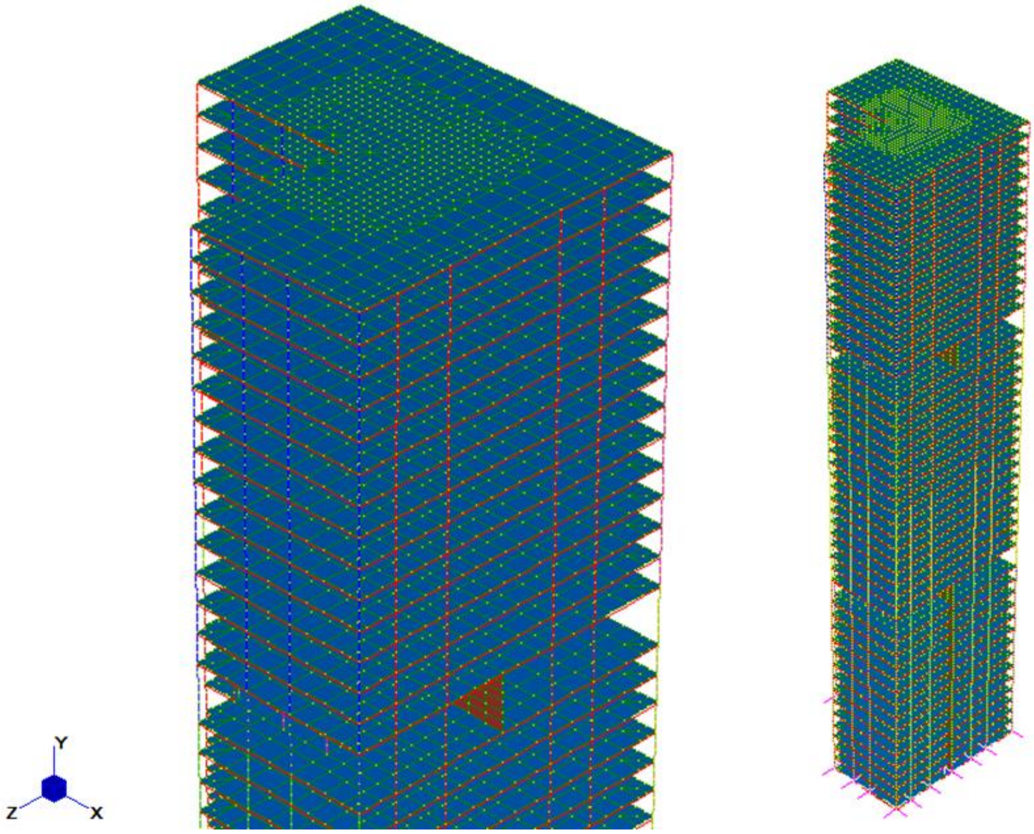

Figure 7.7. Strand7 finite element model of irregular tall building

The same fully-fixed boundary conditions were defined at the base of the computational model. The natural frequency solver then determined the first 50 eigenvalues and corresponding mode shapes for this structural system. The calculated natural frequencies are listed along with those for the regular tall building in Appendix A. The mode shapes for the first three natural frequencies of the system are displayed in Figures 7.8 to 7.10.

The fundamental natural frequency of the structural system is 0.264 Hz (period T = 3.79 s). As intended, this value is very close to the fundamental frequency of the regular tall building (only 1% smaller). The corresponding mode shape is presented in Figure 7.8. The displacement of the top floor relative to the ground floor shows that this is predominantly a first-order translational mode in direction of the most flexible plane of the structure. This direction of motion is parallel to the angle of attack of the incident wind field. The IM wind flow arriving in the re-entrant bay will exert a high drag force on the building. The high pressure gradient within this region creates unsteady structure-induced turbulence.

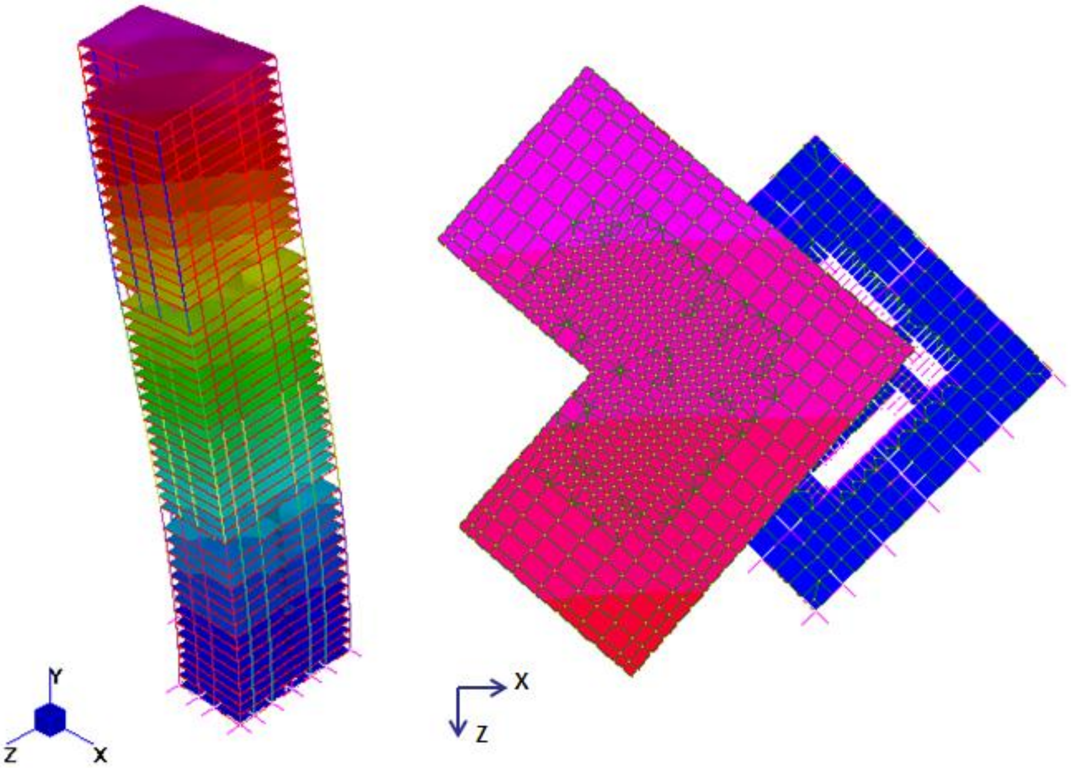

Figure 7.8. First mode of vibration of irregular tall building, f = 0.264 Hz

The second natural frequency is 0.327 Hz (*T* = 3.06 s) and its associated mode shape is shown in Figure 7.9. The displacement of the top floor plate relative to the ground floor shows that this mode of vibration is clearly a complex coupled mode shape with components of translation in the crosswind direction and torsion. This highlights the increased sensitivity of this structural shape to torsional excitations.

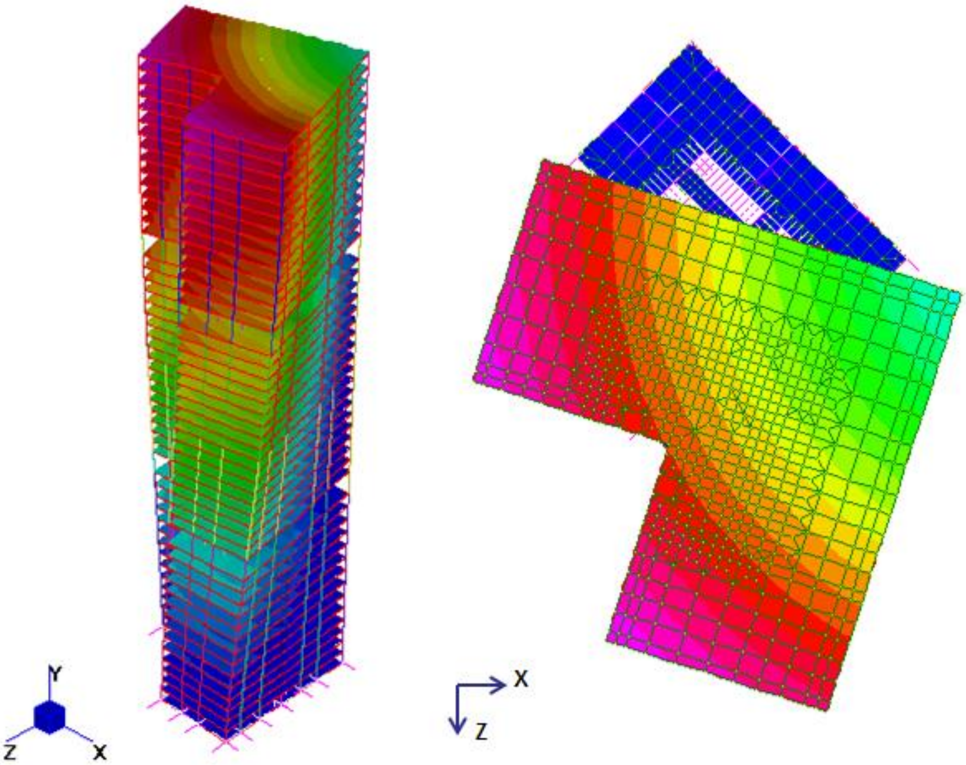

Figure 7.9.Second mode of vibration of irregular tall building, *f* = 0.327 Hz

The first-order torsional mode of vibration occurs at a frequency of 0.362 Hz and its displaced mode shape is shown in Figure 7.10. This torsional mode of vibration appears at a notably lower frequency than for the regular tall building. Furthermore, the intervals separating the second and third natural frequencies are smaller for the irregular structure. This further emphasises the sensitivity of the design to complex responses and torsional excitation. The contribution of the torsional component is also a predominant feature for the higher-order modes of vibration.

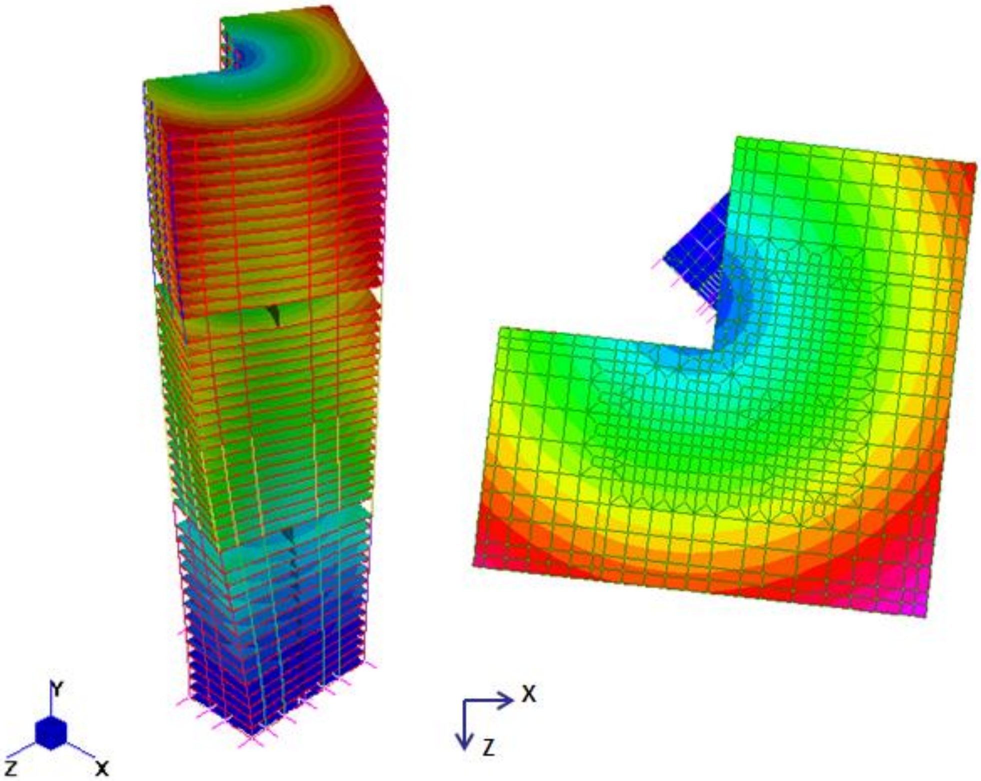

Figure 7.10. Third mode of vibration of irregular tall, *f* = 0.362 Hz

The vertical load cases for the self-weight, dead load and imposed load were created with the same attributes as the regular tall building on each floor. The coupling algorithm followed the same strategy to generate the 791 individual wind load cases and 1 kN nominal point loads. The factor vs. time load tables were then generated from the pressure histories measured during the CFD simulation of the considered IM wind event.

7.4 PBWE Assessment: RANS Simulation Strategy

7.4.1 Interaction Analysis

The RNG *k-ε* turbulence model was implemented for the PBWE assessment of the irregular tall building. It was concluded in Chapter 6 that the limitations of the RANS model meant the use of the RANS model for the regular tall building design was unacceptable. However, the complex flow patterns associated with both the geometry of irregular tall building and the relative angle of attack of the wind were expected to induce more unsteady structure-induced turbulence loading conditions than the regular tall building design, which may increase the adequacy of the RANS model. The relevant solver settings for the RANS turbulence model were specified, as detailed in Section 4.3.5, to provide consistency and allow direct performance comparison with the RANS model implemented for the regular tall building. The computational time-step was 0.05 s and the CPU cost for a single physical time-step was 51.8 s using 8 CPUs on the HPC facility at the University of Strathclyde. This represents a 73% increase on the computation time required for the CFD simulations of the regular tall building using the RANS model, which occurs due to the increased number of computational cells in the fluid domain.

The CFD simulations were performed for the same 240 seconds of flow time, which satisfied the 120-second ‘warm-up’ requirement and provided the 120-second wind load histories. The total computation time of the RANS model for each IM wind event was 2.88 days. The rise in computation time emphasises the impracticality of performing the RANS-LES hybrid simulation strategy; a 75% increase in computation time for the reference IM event using the LES model would have taken approximately 160 days to complete using 8 CPUs in parallel on the HPC facility.

An adequate prediction of the flow features around the tall building was required in order to obtain the desired level of accuracy for the mean wind loads. The local flow features around the irregular tall building for the IM10 wind event are shown in Figures 7.11 to 7.13. The qualitative assessment of the flow regime is based on the broad flow features described for the CAARC tall building in Section 4.5.4. The instantaneous velocity vectors on the *X-Y* plane at 2/3*H* (120 metres) show flow separation at the downwind edge of the ‘wings’ of the tall building, as illustrated in Figure 7.11. The shear layers from the separated flow enclose a turbulent near-wake. The formation of vortices in the near-wake and the alternate shedding process can also be observed in Figure 7.11. The fragmented arch vortex in the wake is apparent from the velocity vectors in the *X-Y* plane, as shown in Figure 7.12. The streamlines in Figure 7.13 display the highly turbulent wake and the horseshoe vortex which forms upwind and is swept round the sides of the building. Overall, it appears that the main characteristics of the flow regime were adequately captured by the RANS model.

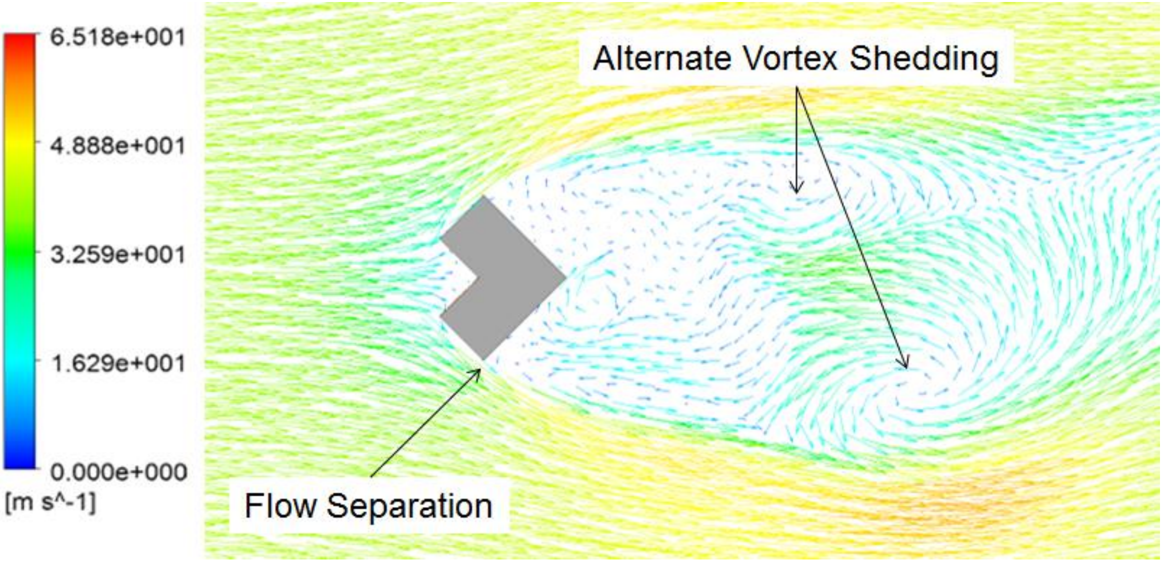

Figure 7.11. Instantaneous velocity vectors (*t* = 120 s) on *X*-*Y* plane at *z* = 120 m during the IM10 wind event

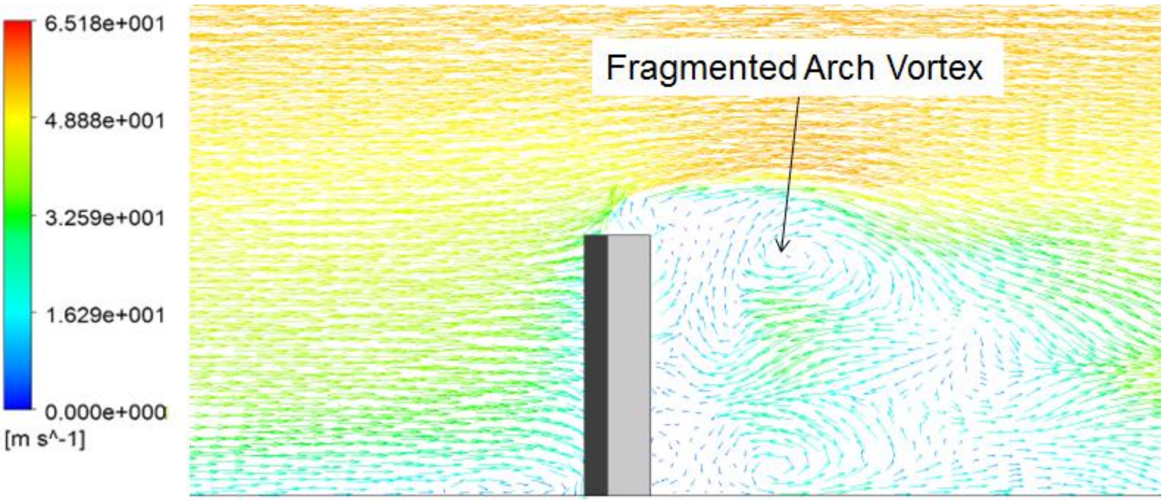

Figure 7.12. Instantaneous velocity vectors (*t* = 120 s) on *X*-*Z* plane at *y* = 0 m during the IM10 wind event

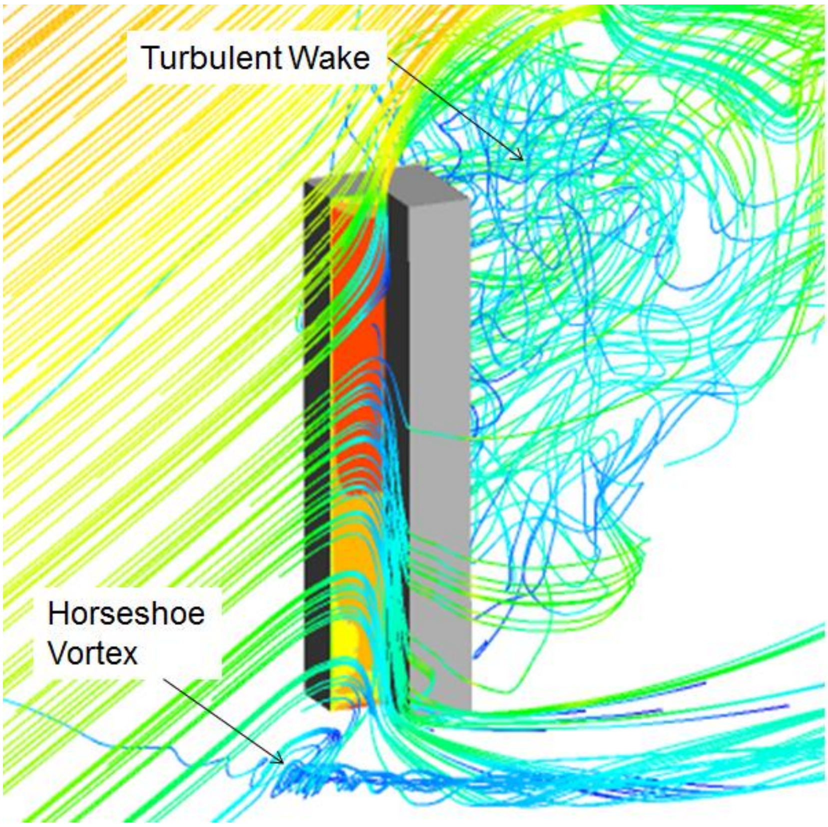

Figure 7.13. Streamlines of flow regime during the IM10 wind event

The mean pressure contours for the IP10 event are shown in Figure 7.14. The re-entrant corner is facing directly into the wind, and hence the highest drag pressures appear within the re-entrant bay. The mean pressure within the re-entrant bay showed the expected distribution due to the vertical variation of the mean velocity profile. The maximum drag pressure is exerted at the stagnation point at approximately 3/4*H.* The increased pressure region towards the base of the structure is present due to the boundary of the domain floor and the phenomena leading to the formation of the horseshoe vortex. The pressure distribution indicates that the flow separates at the upwind edge of the building ‘wings’ and reattaches on the front face of the ‘wings’. The reattached flow separates again at the downwind edge to create the suction effect on the back faces of the building ‘wings’.

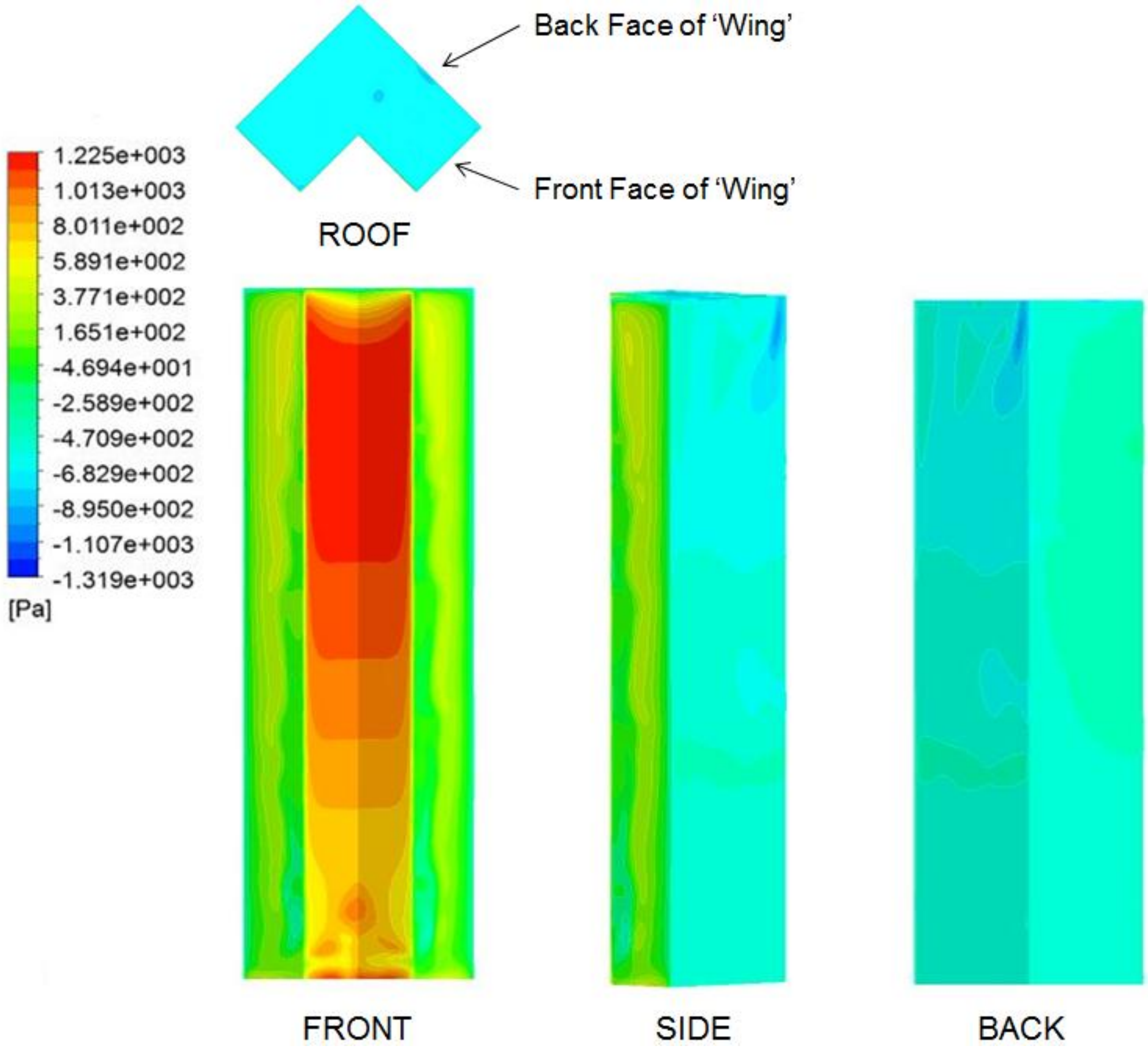

Figure 7.14. Mean pressure contours on the irregular tall building during the IM10 wind event

The adopted geometry of the irregular tall building design meant there was no reference literature, such as previous wind tunnel tests or numerical studies, available for comparison. Therefore, the mean pressure distribution at 2/3*H* for the IM10 wind event was compared against the wind pressures calculated using BS EN 1991-1-4:2005 (British Standards Institution, 2005), as shown in Figure 7.15. The magnitude of the gust-peak factor pressures from BS EN 1991-1-4:2005 were conservatively greater than the mean wind pressures from the RANS model. It should be noted that the BS EN 1991-1-4:2005 values are quasi-static design values; they do not represent the mean wind pressures. Therefore, they were expected to be notably greater than the mean pressures from the RANS model.

The mean pressure appears almost constant within the re-entrant bay; it does not display the curvilinear symmetry that was seen on the front face of the regular tall building. The mean pressure from the RANS model at the leading edge of the building 'wing' is close to zero because the pressure history was periodically separating and reattaching at this point. The flow reattachment further downwind on the front face of the 'wing' causes a gradual increase in mean wind pressure. The second flow separation occurs at the downwind edge of the building 'wing' which creates the suction effect on the back face. The suction effect is not as intense as was observed with the flow separation at the leading edge of the regular tall building. This is due to the different orientation of the building faces relative to the direction of the incident wind field.

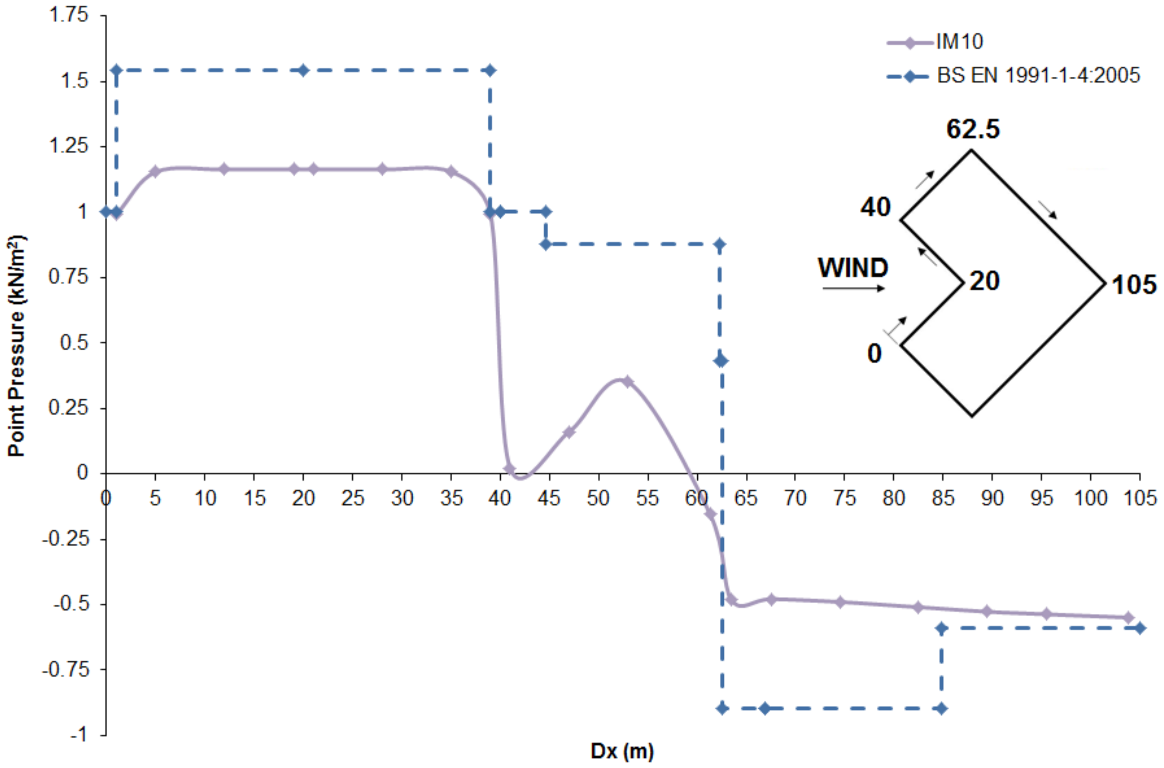

Figure 7.15. Comparison of wind pressures at 2/3*H* calculated using the RANS model and the BS EN 1991-1-4:2005 gust-peak factor model

The mean pressure distribution around the perimeter of the irregular tall building at 2/3*H* is shown for the range of IM wind events in Figure 7.16. The mean pressure differences between each of the IM wind events follow a similar pattern to what was observed for the regular tall building. The most intense mean surface pressures are associated with the IM10 wind event. In general, the intensity of the measured mean pressures increases with each subsequent IM wind event. The same apparent anomaly as with the regular tall building occurred between both the IM4 and IM5 events and the IM7 and IM8 events; it was already identified in Section 6.4.1 that this was attributable to the mean velocity profiles for these wind events.

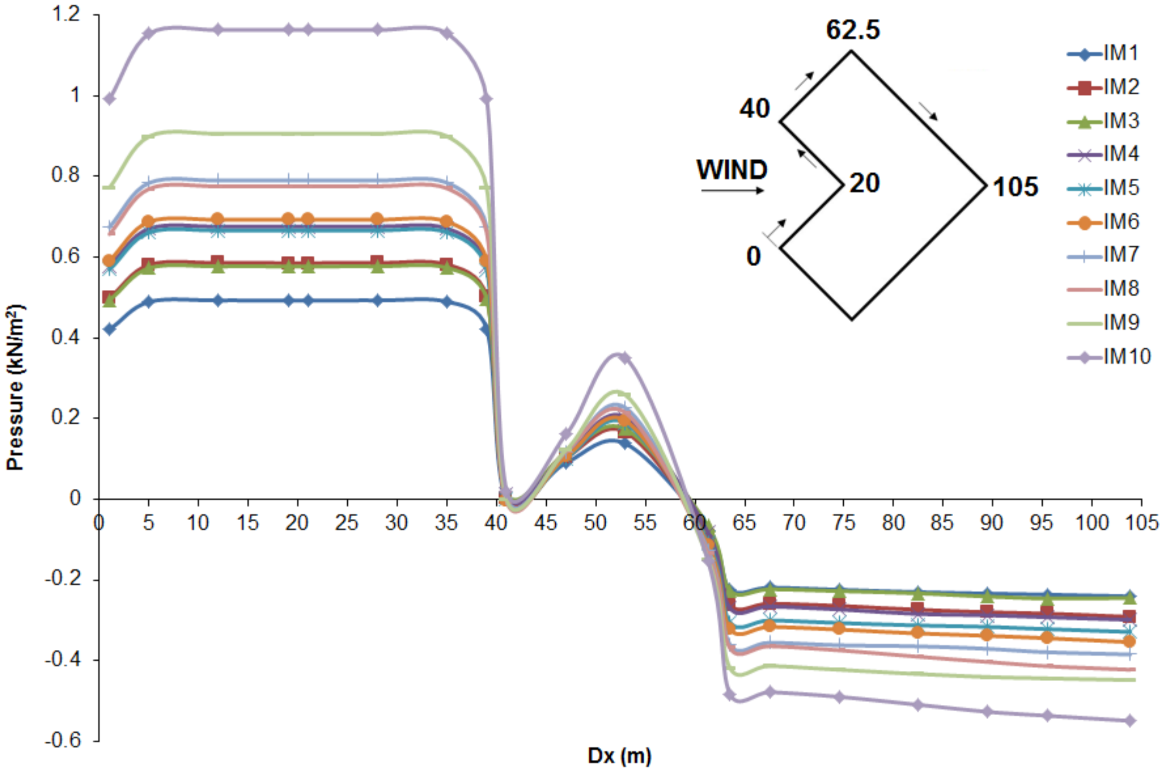

Figure 7.16. Mean pressure calculated on the irregular tall building at 2/3*H* for the IM wind events

The limitations of the RANS model meant the fluctuations in the pressure histories were generated only from structure-induced turbulence. The pressure histories monitored towards the re-entrant corner at 2/3*H* for the IM1, IM5 and IM10 wind events are shown in Figure 7.17. The time histories display an almost harmonic-type loading, which is notably more unsteady than the loading fluctuations observed on the windward face of the regular tall building. This periodicity occurs as the flow contained within the re-entrant bay is displaced round the sides and over the top of building.

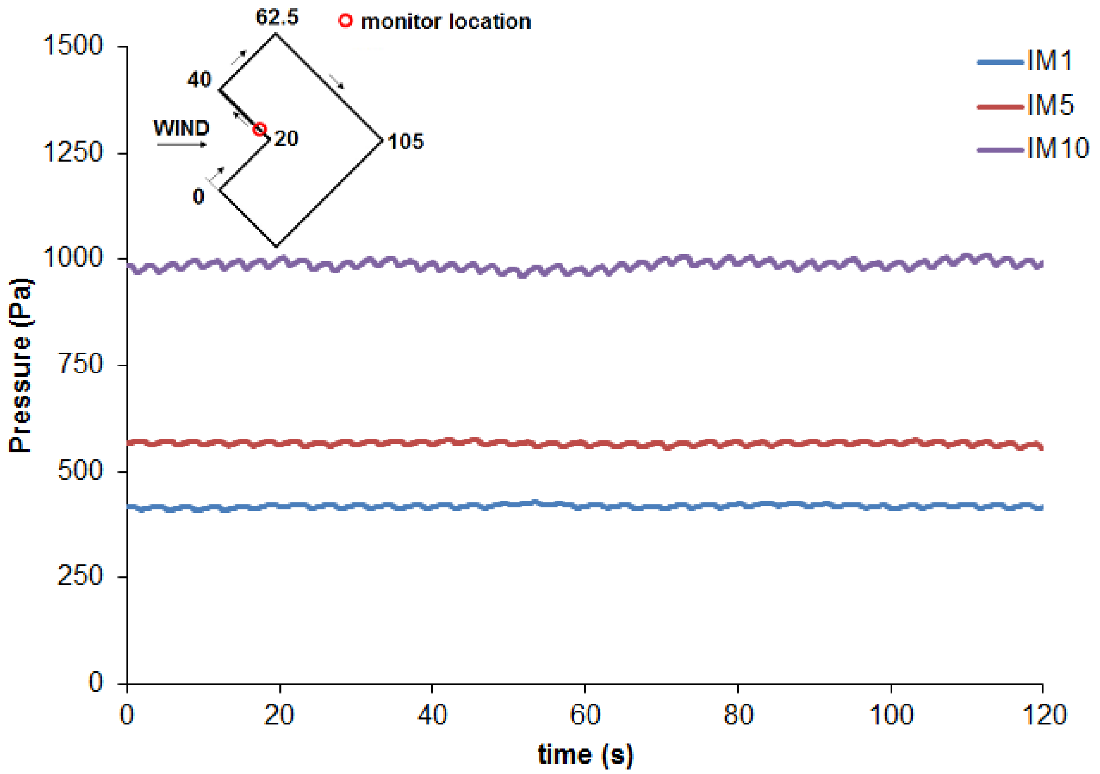

Figure 7.17. Pressure histories calculated by RANS towards the re-entrant corner at 2/3*H*

Figure 7.18 displays the corresponding time histories measured at the leading edge of the building 'wing'. In all cases, the flow can be seen to switch between a reattached and separated state. The pressure time history appears to contain two dominant frequencies; a low frequency component with a period of approximately 70 seconds (0.014 Hz) and a higher frequency component with a period of approximately 2.9 seconds (0.35 Hz). The complex pressure history emphasises the increased structure-induced turbulence generated by the irregular geometry and the angle of attack of the incident wind field.

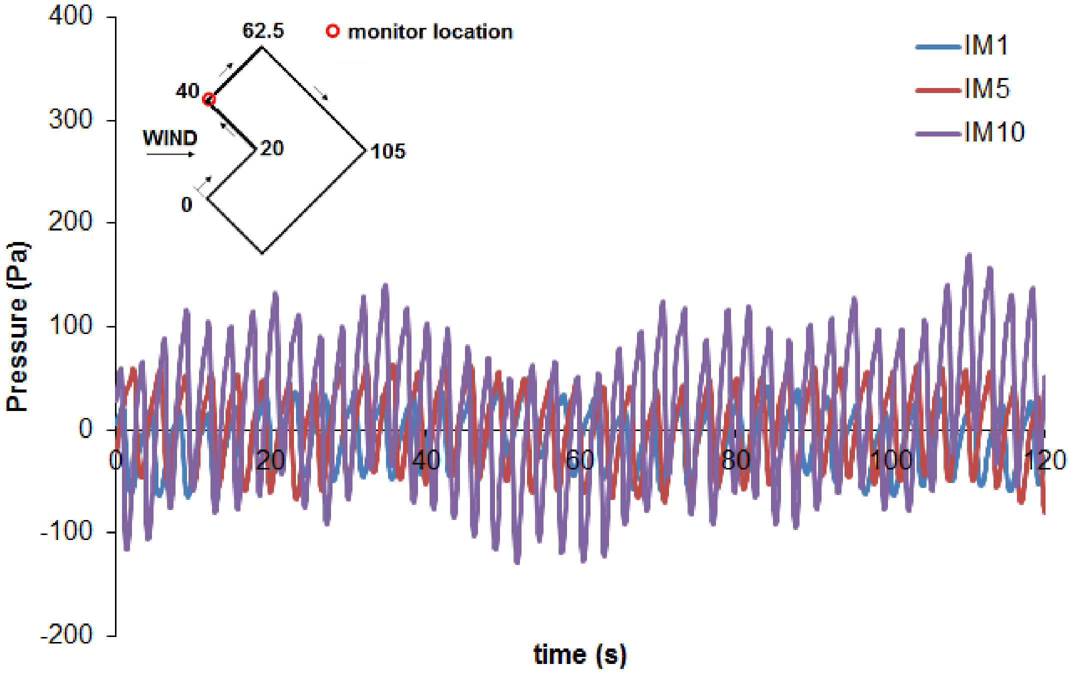

Figure 7.18. Pressure histories calculated by RANS at the upwind wing at 2/3*H*

The corresponding pressure fluctuations on the back face of the building 'wing' are shown in Figure 7.19. The unsteadiness in the loading histories is principally generated by vortex shedding in the near-wake. The frequency content of the loading on the back face is directly related to the vortex shedding frequencies. It has already been noted that the alternate shedding frequency of the twin vortices can excite both crosswind and torsional modes of vibration. The latter response is particularly relevant for the irregular building since 'L'-shaped cross-sections are sensitive to torsional excitations. In this case, no dominant shedding frequency is evident. This is a consequence of the cross-sectional shape of the building and its orientation with respect to the incident wind. A more distinct shedding frequency could occur for other incident wind directions.

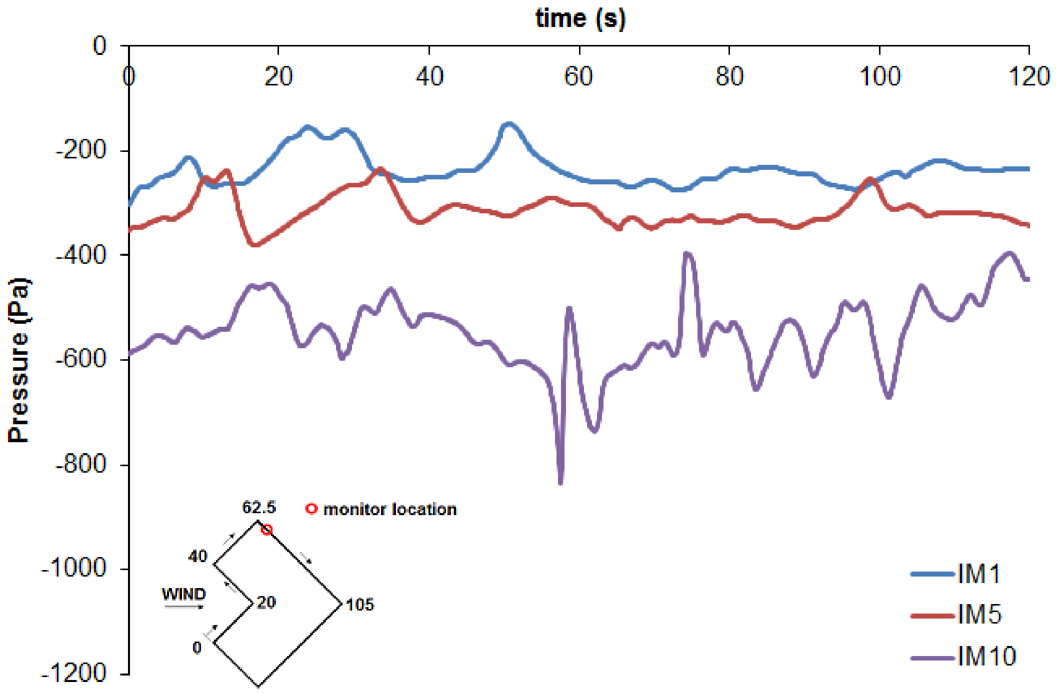

Figure 7.19. Pressure histories calculated by RANS at the leading edge of the back face at 2/3*H*

7.4.2 Structural Analysis

The structural analysis was performed to obtain the wind-induced response of the irregular tall building design for the ten IP load conditions computed by the RANS simulation strategy. The 791 factor vs. time load tables corresponding to the considered IM load conditions were created in Strand7 and attached to the associated load case by the one-way coupling algorithm, as described in Section 7.3. The specifications for the linear transient dynamic solver were consistent with those applied for the regular tall building in the preceding Chapter.

The static displacement under self-weight was 18.5 mm in the direction of the alongwind *x*-axis and 6.4 mm in the direction of the crosswind *z*-axis due to eccentricity between the centre of mass and centre of stiffness. The structure required an initial set of time-steps to settle to its ‘quasi-static’ equilibrium. The procedure detailed for the regular tall building was followed to obtain the restart conditions for the subsequent PBWE structural analyses.

In addition, the wind loads were conveniently ramped over 60-seconds, as chosen arbitrarily for the regular tall building.

The natural frequency solver revealed that the sum of the effective modal masses for modes 1 to 20 amounted to more than 90% of the total mass of the structure. Therefore, the modal superposition analyses were set to include the first 20 modes of vibration. As the fundamental natural frequency for the irregular tall building was very similar to the regular tall building, the damping ratio adopted for the fundamental mode of vibration (f = 0.264 Hz) was 0.016. The damping ratio for the remaining modes was again assumed to follow Rayleigh damping. An upper limiting damping ratio of 0.08 was specified for the 20th mode of vibration (f = 4.8 Hz). The Rayleigh damping model for the modal superposition dynamic analyses is shown in Figure 7.20.

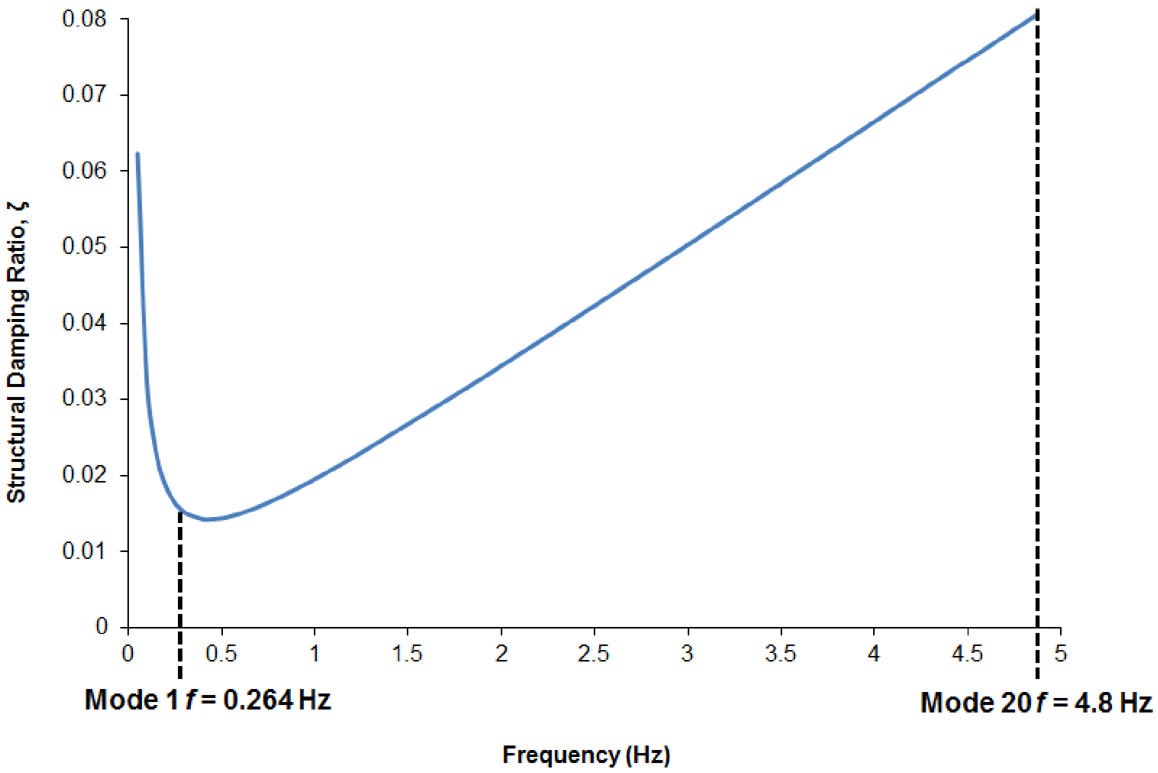

Figure 7.20. Rayleigh damping used for the structural analyses in Strand7

The computational time-step was set to 0.05 s and a total of 3600 time-steps were computed. The total CPU time on a standard desktop PC with a 3.00 GHz dual-core processor was 7380 seconds (2 hours 3 minutes), which is almost 3 times longer than the corresponding computation time for the regular tall building. The rise is due to both the increased number of wind loads associated with the structural analysis and the increased number of elements in the FE model of the irregular tall building.

The alongwind AX acceleration and crosswind AZ acceleration histories on the top floor from the IP10 load conditions are plotted in Figure 7.21. The complex response of the structure to the UP10 load histories can be seen to involve several interference frequencies, although the modulation is not as distinct as the beat frequency observed for the regular tall building in Figure 6.16.

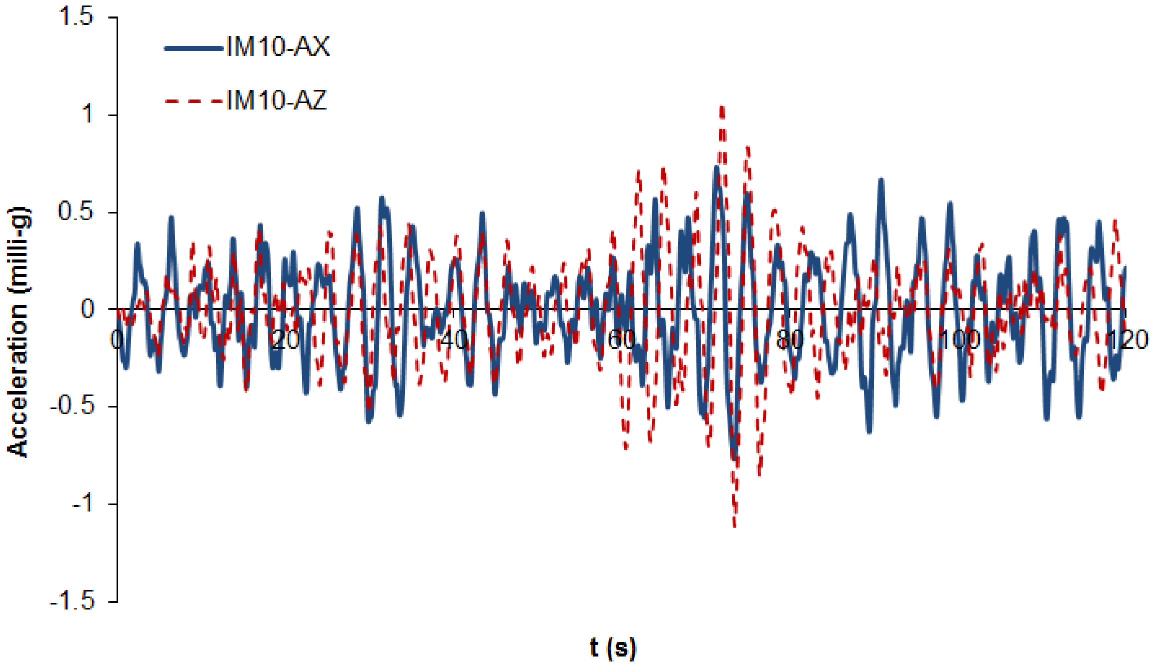

Figure 7.21. AX and AZ components of top floor acceleration response during the IP10 wind load conditions based on the RANS model

The corresponding absolute acceleration response is shown in Figure 7.22. The standard deviation for the 120-second absolute acceleration time history is 0.65 milli-g, which is 3 times greater than the corresponding value measured for the regular tall building from the same IM event. The absolute peak acceleration is 1.46 milli-g and occurs in the time history response at 73.4 seconds. This statistical parameter is 2.75 times greater than was measured for the regular tall building from the same IM event. The results indicate that the structure-induced turbulence has clearly a more pronounced effect on the irregular tall building than the regular tall building. However, the building response is still considerably lower than the response observed for the regular tall building from the LES-IP10 load conditions. This indicates that the absence of atmospheric turbulence is still causing a significant underestimation of structural response.

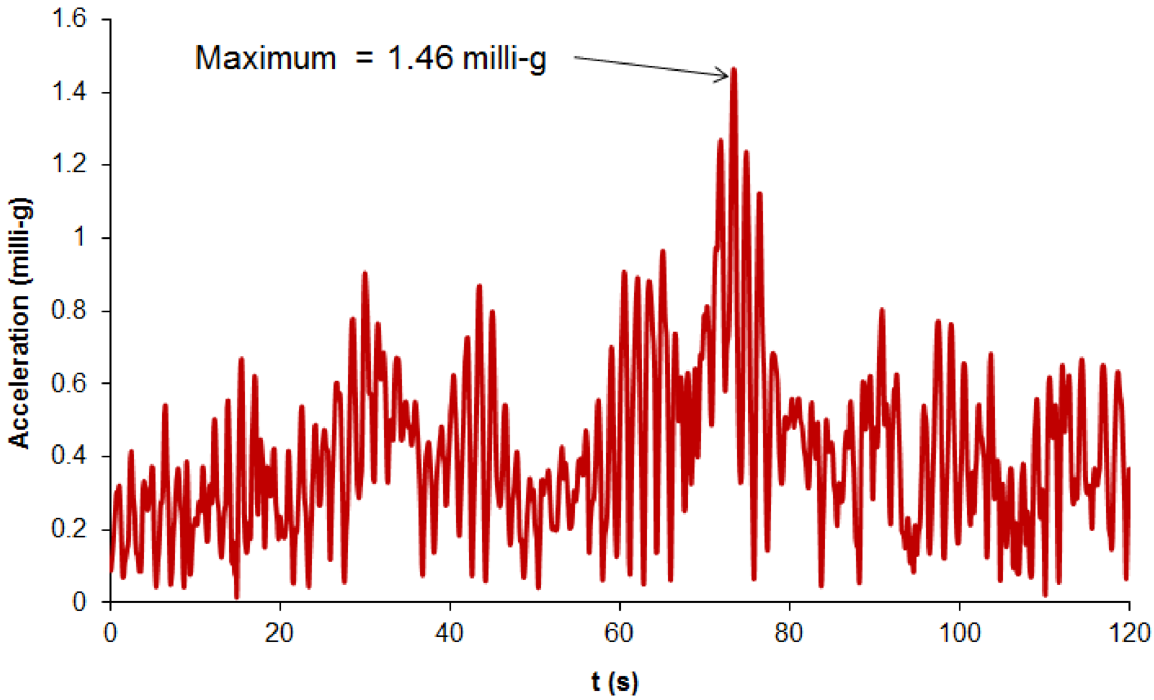

Figure 7.22. Absolute top floor acceleration comparison for the IP10 wind load conditions based on the RANS model

The Pearson product-moment correlation coefficient for the AX and AZ top floor response histories from the LES-IP10 load histories is 0.31. This value suggests that the AX and AZ response components are better correlated than the corresponding AX and AZ response histories than the ones obtained from the regular tall building analysis. However, a value much closer to 1 would be required to suggest the building was responding in a dominant direction of motion. The corresponding acceleration trace from the IP10 wind loading event is shown in Figure 7.23.

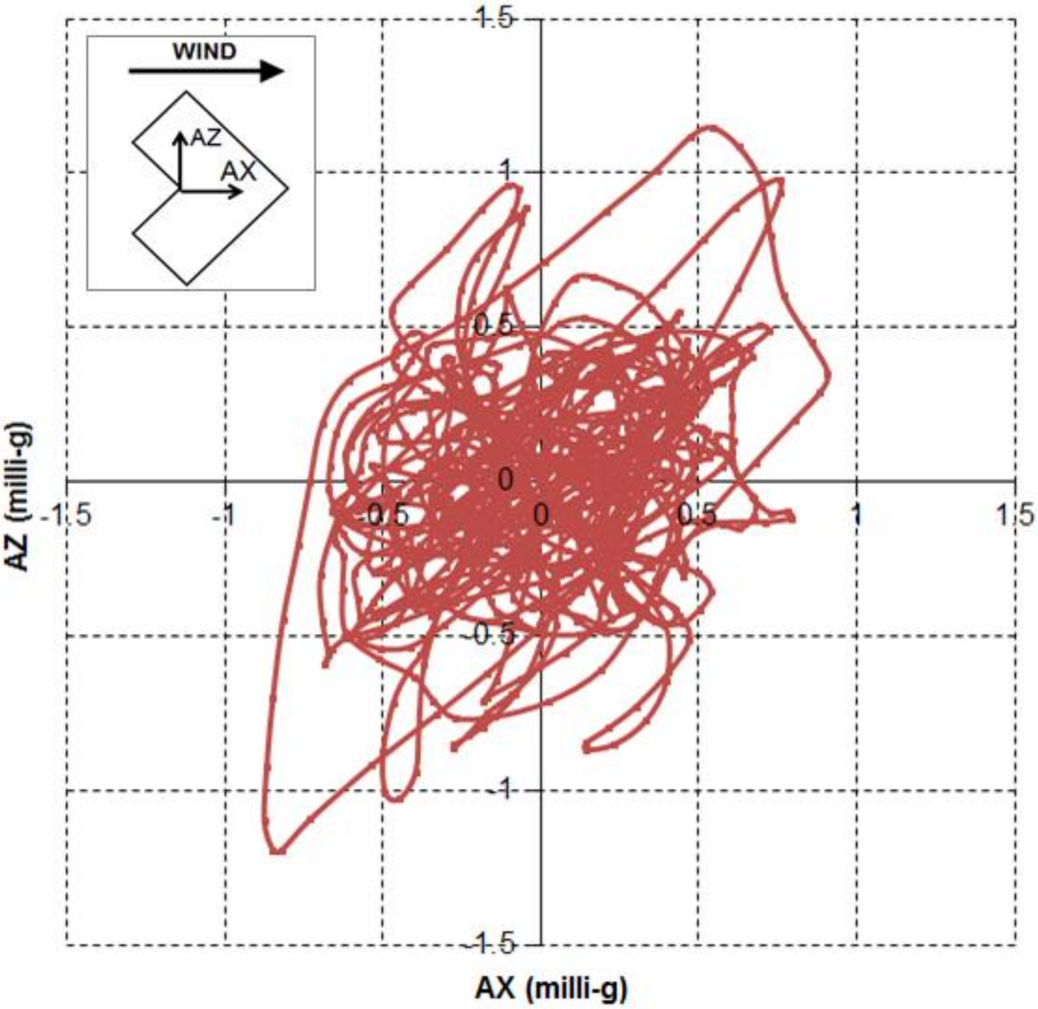

Figure 7.23. Resultant acceleration trace during the IP10 wind load conditions based on the RANS model

FFT analyses were performed in MATLAB to identify the frequencies involved in the building response. The resulting frequency spectrum for the AX response history is shown in Figure 7.24 and it is evident that the response is predominantly in the fundamental mode of vibration (f_1 = 0.264 Hz). The contribution from the 3rd mode of vibration is approximately 65% less than the fundamental frequency response. However, the range of notable interference frequencies between the 1st and 3rd modes of vibration makes it slightly difficult to identify a distinct peak for the 3rd mode. A considerable contribution is measured in the 4th mode of vibration (f_4 = 0.974 Hz), which is notably larger than the 4th mode response from the regular tall building response using the RANS model. There appears to be a small contribution measured in the 8th mode of vibration (f_8 = 2.19 Hz). The FFT analysis did not identify any notable modal contributions for frequencies greater than 2.5 Hz.

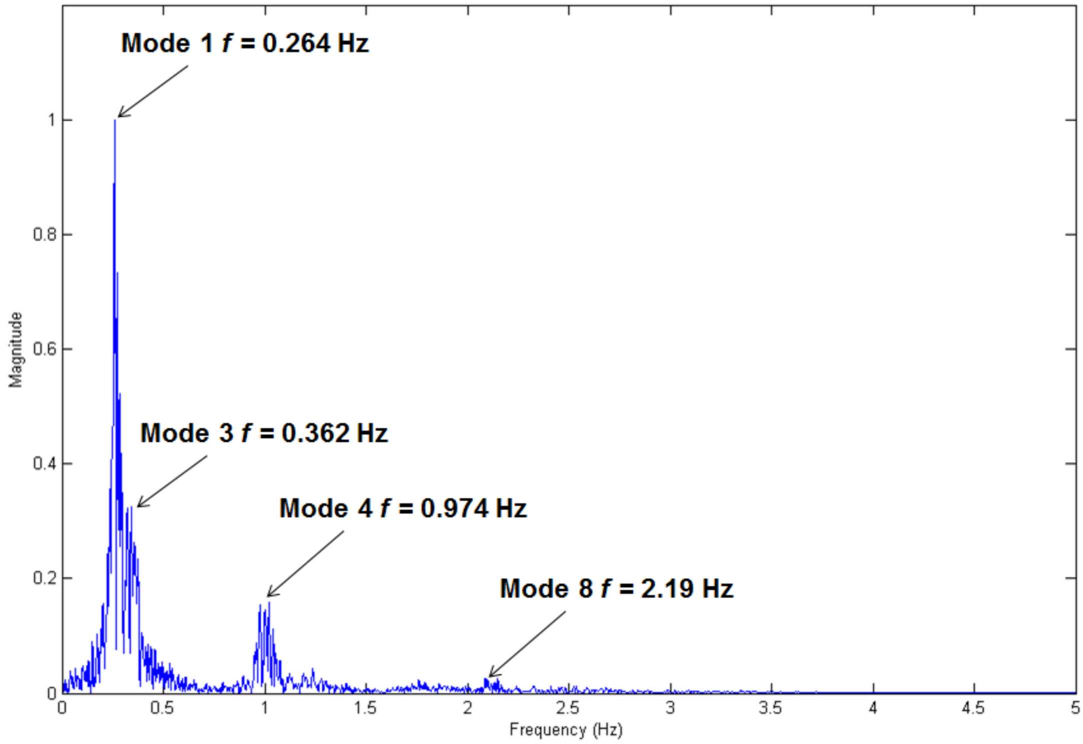

Figure 7.24. Frequency spectrum of AX time history during the IP10 load conditions based on the RANS model

It is evident from the frequency spectrum shown in Figure 7.25 that the AZ building response is predominantly vibrating in the 2nd mode of vibration. The proximity of the natural frequencies associated with the 2nd and the 3rd modes of vibration is too close to distinguish a peak for the 3rd mode from the frequency spectrum. A notable response is measured in the 5th mode of vibration. This identifies that the higher-order modal response from the irregular tall building is much greater than was seen for the regular tall building using the same simulation strategy. Once again, the FFT analysis did not identify any notable response frequencies greater than 2.5 Hz.

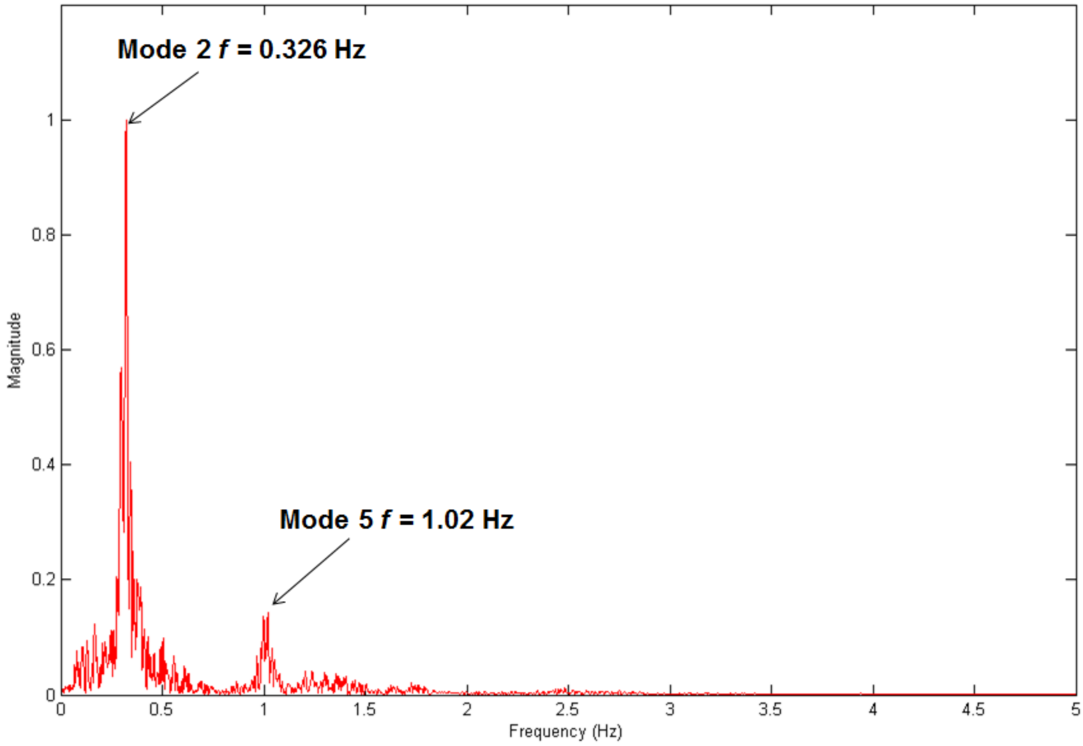

Figure 7.25. Frequency spectrum of AZ time history during the IP10 load conditions based on the RANS model

The FFT spectra from 0 Hz to 0.5 Hz are shown in Figure 7.26 to help identify the contribution of the 3rd mode of vibration in both the AX and AZ responses. The modal contribution is very low for both cases, which suggests either the building is genuinely not responding in this mode or, perhaps more likely, the AX and AZ response signals fail to capture the response from this predominantly torsional mode of vibration. As noted for the regular tall building response, the FFT spectra are expected to become smoother if the time history record was increased. However, there is little to suggest that the 3rd mode response will become more pronounced as a result of this process.

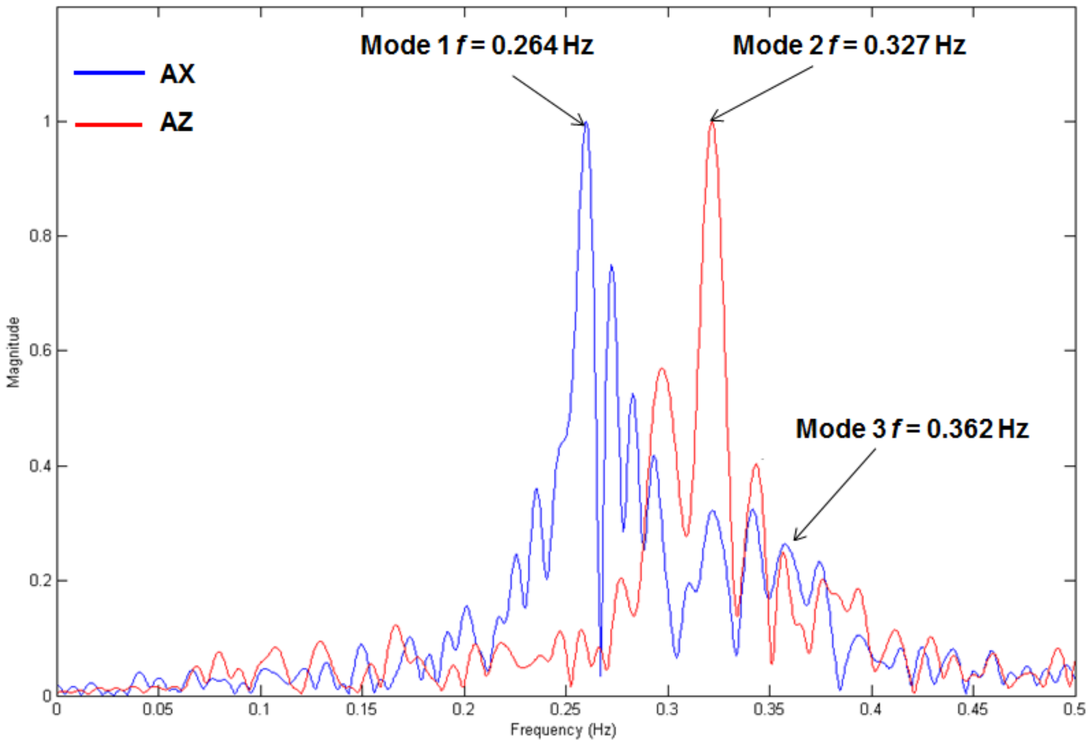

Figure 7.26. Frequency spectrum between 0 Hz to 0.5 Hz during the IP10 load conditions based on the RANS model

The relationship between the calculated EDP (top floor peak acceleration) and the mean wind velocity at the top building height for each wind event is shown in Figure 7.27 and a summary of the peak values is provided in Table 7.2. The trend of the results shows a steady increase in the EDP acceleration with increasing IM mean velocity at building height; it does not display the distinct increases from the IP7 and the IP9 load conditions, as was observed for the regular tall building from the RANS-based solution. In general, the EDP responses of the irregular tall building are notably greater than the results for the regular tall building using the same simulation strategy. Exceptions are the EDP peak accelerations associated with the IP7 and IP9 load conditions due to the sensitivity of the regular tall building to fluctuations on the windward face, as discussed in Section 6.4.2.

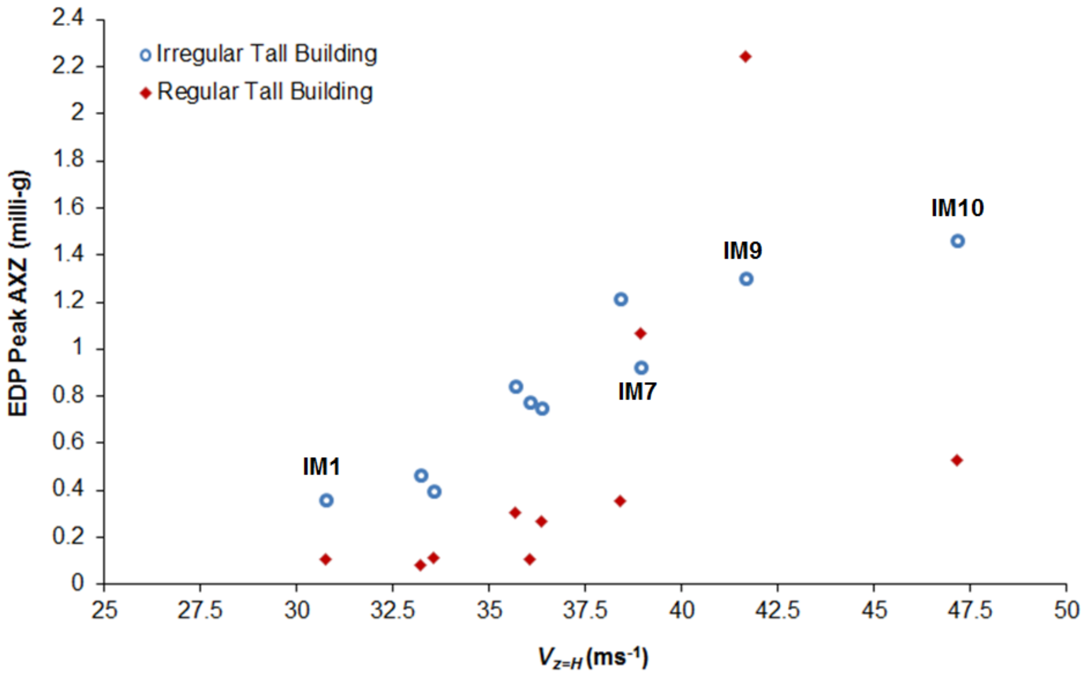

Figure 7.27. EDP peak acceleration vs IM mean wind velocity at building height based on the RANS model

Table 7.2. Summary of EDP peak top floor accelerations based on RANS model

IM	$V_{z=H}$ (ms^{-1})	A_{peak} (milli-g)
1	30.75	0.360
2	33.55	0.396
3	33.23	0.464
4	36.08	0.779
5	35.69	0.847
6	36.38	0.751
7	38.94	0.927
8	38.39	1.213
9	41.67	1.306
10	47.17	1.465

The best-fit engineering demand parameter (EDP) fragility curve was determined in MATLAB. The values calculated for the reciprocal of the dispersion, α, and the mode, U, for the Fisher-Tippett Type 1 distribution were 2.89 and 0.62 milli-g, respectively. Hence, the expression for the cumulative distribution function (CDF), given by Equation 2.1, becomes

$$P(a_{peak}) = \exp\left[-\exp\left\{-\left(2.89(a_{peak} - 0.62)\right)\right\}\right] \tag{7.1}$$

The resulting cumulative distribution function (CDF) is shown in Figure 7.28. The R-square value is 0.938 and the Sum of Squares due to Error (SSE) value is 0.055. These goodness-of-fit statistics indicate that the fit adequately describes the variation of the peak acceleration data and the results have a small random error component. This represents a significantly better fit than was achieved from the EDP fragility curve of the regular tall building based on the same RANS simulation strategy.

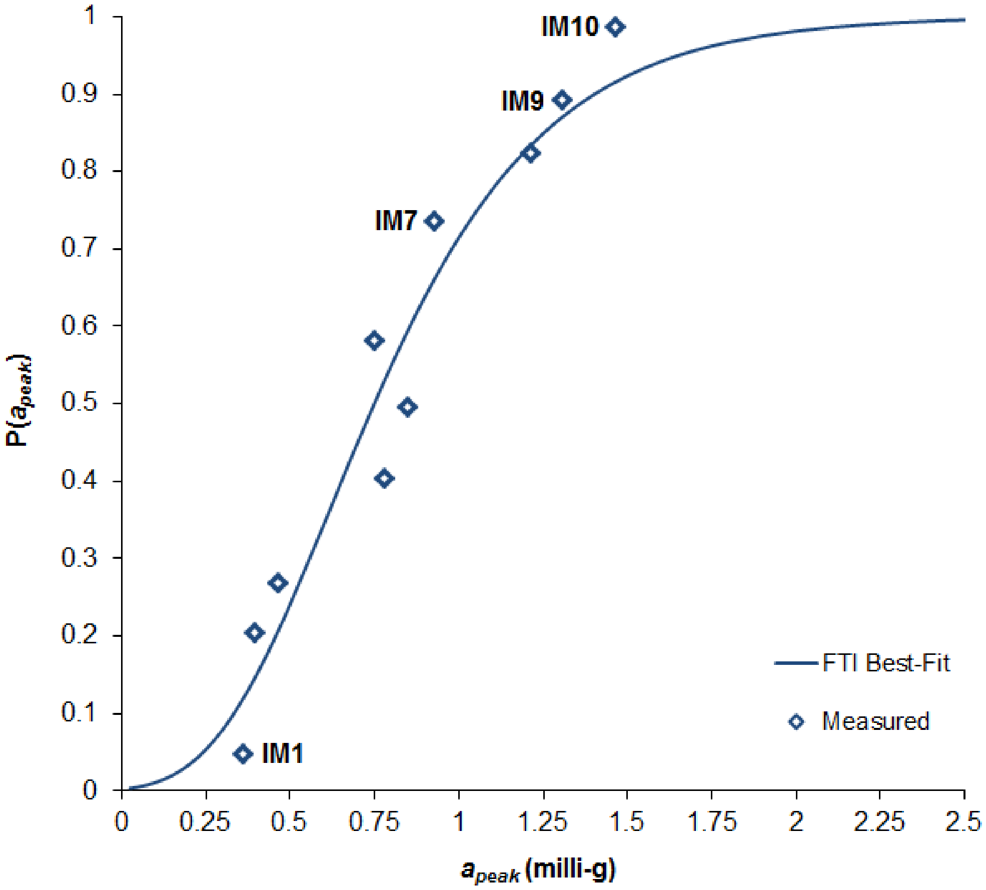

Figure 7.28. EDP fragility curve for the irregular tall building based on the RANS model

The CDF contains a broader range of accelerations in comparison to the EDP fragility curve for the regular tall building using the same simulation strategy, as shown in Figure 7.29. However, the acceleration range is still considerably lower than was observed for the regular tall building when using the RANS-LES simulation strategy.

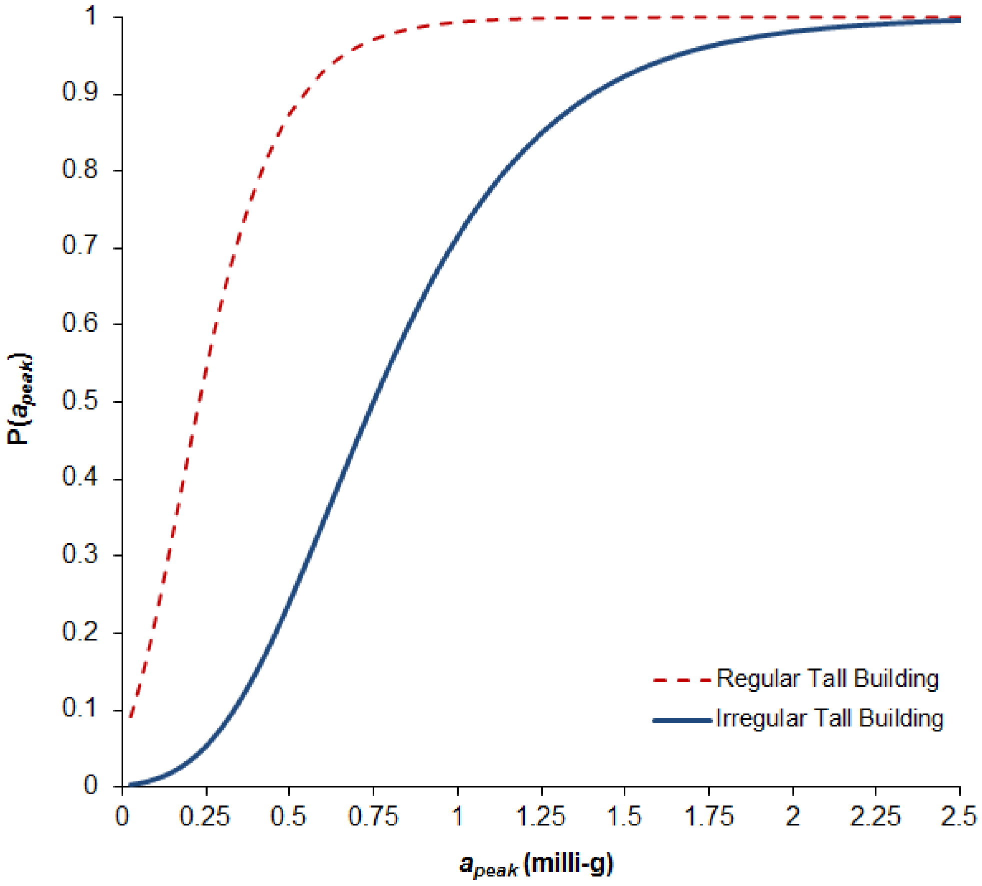

Figure 7.29. Comparison of the EDP fragility curves for the regular tall building and the irregular tall building based on the RANS model

For the regular tall building, the increase in building response from the RANS model to the LES model identified that the atmospheric turbulence (including low-frequency perturbations) contributed approximately 92% of the total response for that particular building form and structural characteristics. This relationship provides little indication of the corresponding increase in response for the irregular tall building, since the irregular geometry induces different flow patterns and the structural system possesses different dynamic properties. The relative increase in response due to atmospheric turbulence may not have been as significant for the irregular tall building since the structure-induced turbulence alone had a more notable effect. However, such irregular 'L'-shaped buildings are generally more sensitive to wind-induced excitation than regular prismatic buildings (Taranath, 1998). Therefore, it is expected that the peak response of the irregular tall building from the RANS-LES simulation strategy would have been at least equal to that computed for the regular tall building.

The goodness-of-fit to the data is potentially misleading as to the applicability of this RANS simulation strategy. Due to the reasons described above, the resulting fragility curve is still considered to be a poor representation of the probabilistic performance of the irregular tall building. Designing the structure on the basis of these results could cause serious serviceability problems after the building is constructed. Significant costs would then be incurred from designing and implementing an effective retrofit solution.

7.4.3 Damage Analysis

Despite the differences seen for the PBWE analysis of an irregular tall building as compared to a regular one, the irregular structure comfortably satisfies the specified DM performance criteria when the RANS simulation strategy is implemented. The low accelerations are considered to be physically unrealistic; this discrepancy can be attributed mostly to the limitations of the RANS model in generating more adequate pressure histories.

Table 7.3. Damage analysis based on the RANS simulation strategy

Damage Measure (Complaint)	**Limiting Exceedance Probability**	**Peak Acceleration Limit (milli-g)**	**Peak Acceleration from PBWE (milli-g)**
Minor	20%	12.01	1.14
Moderate	5%	15.34	1.64
Major	2%	17.53	1.97

7.5 Concluding Remarks

The irregular tall building has been subjected to the proposed PBWE framework using the RANS simulation strategy only. The computational cost of LES meant it was too impractical to use the alternative RANS-LES hybrid simulation strategy within the time-scale of the thesis.

The results from the RANS simulation strategy showed that the structure-induced turbulence alone had a greater, and more consistent, effect on the structural response of the irregular tall building than was seen for the regular tall building. Unlike the regular tall building, there were no distinct outliers in the EDP fragility curve data. This implies that the RANS model may become more useful in cases where the structure-induced turbulence dominates the response. However, the accelerations from the RANS simulation strategy for the irregular building were still significantly less than the accelerations from the RANS-LES simulation strategy for the regular building. Since it is well known that such L-shaped geometries are generally more sensitive to wind-induced excitation than regular prismatic geometries, the resulting fragility curve from the RANS simulation strategy was considered to offer a poor representation of the physical performance of the irregular building.

The differences between the structural responses from the RANS simulation strategy for the irregular building and the alternative RANS-LES simulation strategy for the regular building suggested that, even with increased structure-induced turbulence, the atmospheric turbulence would also govern the response of an irregular tall building. Therefore, achieving the correct input of atmospheric turbulence and controlling its propagation through the model are imperative to competent PBWE analyses of tall buildings. The latter is a condition which the RANS turbulence model cannot satisfy.

8

Discussion and Conclusions

8.1 Preamble

Overall, the results from the present research have identified the adequacy and applicability of the proposed PBWE framework for tall building design. The PBWE framework involves the following five clearly-defined analysis steps: Hazard Analysis; Interaction Analysis; Structural Analysis; Damage Analysis; and Loss Analysis. This Chapter begins by reviewing the methodology for the Hazard Analysis to determine whether it indeed addresses the weaknesses from previous applications of PBWE. Attention is then focused on the appropriate choice of complexity and the application of CFD as a tool for generating the transient wind loads as part of the PBWE assessment. There is a particular emphasis on the significance of the choice of turbulence model as the limitations of the proposed PBWE framework were primarily associated with CFD. The value of the developed one-way coupling algorithm is then discussed. This is followed by summarising the key structural response characteristics which were identified from the PBWE assessments of two tall buildings case studies; a regular rectangular-shaped tall building and an irregular ‘L’-shaped tall building. The Chapter concludes by stating the key conclusions that are drawn from this Thesis.

8.2 Strategy for the Hazard Analysis

The methodology for the Hazard Analysis was formulated with the intention of addressing weaknesses from previous research in terms of characterising the Intensity Measure (IM) wind events. These IM wind events are the foundation on which the PBWE assessment is based, and hence it was important that the strategy for the proposed framework was robust and adequately represented the incident wind at the site.

The general methodology for the Hazard Analysis can be deemed appropriate and valid. The probability distribution of the extreme mean wind speed, v_b, was based on extreme value analysis that is endorsed in the UK codes of practice. In addition, the Gaussian distribution of the terrain roughness parameter z_0 allowed the uncertainty of quantifying this parameter for the site to be addressed. Latin hypercube sampling was an efficient method for determining the parametric combinations of v_b and z_0. These combinations were then used in conjunction with the well-established ESDU equations to form expressions for the wind characteristics for each IM wind event.

However, one of the main issues was deciding how many samples would provide a statistically robust representation of the performance of the tall building, whilst ensuring the PBWE assessment would be computationally feasible. The decision to derive only ten parametric combinations of v_b and z_0 (i.e. ten probabilistic IM wind events) was governed by the computational cost required for the subsequent CFD simulations – even when using the RANS turbulence model. The goodness-of-fit statistics for the resulting fragility curves suggested that the number of samples was insufficient. This was particularly apparent for the PBWE assessment of the regular tall building using the RANS simulation strategy.

Furthermore, the variation of wind directionality was not explicitly considered due to the significant increase in computational cost this would have incurred from running the additional CFD simulations. The prevailing winds in the UK arrive from the west-south-west due to frontal depressions from the Atlantic Ocean. By only considering a single wind direction, it was assumed that the considered tall building was orientated such that its most flexible axis was aligned parallel to the prevailing winds and the effects in all other wind directions were negligible. This idealised condition would not suffice for tall building design. The proposed methodology could be applied just as effectively for a full range of wind directions. A detailed terrain analysis would be required to identify changes in terrain category relative to each wind direction and establish whether there are any significant topographic features.

8.3 Application of CFD for PBWE of Tall Buildings

The CFD simulations performed as part of this research are amongst the few to be computed using full-scale geometries and flow characteristics. Previous similar CFD studies have largely been computed at model-scale to directly coincide with a wind tunnel model, where the flow characteristics are scaled according to the scale of the model. In addition, previous results are primarily assessed only in terms of pressure without progressing to determine the specific effects on the resulting structural response.

Overall, the results from the research support the general view that CFD is not currently in a position to be used instead of wind tunnel testing, which was not unexpected. However, there is some encouraging evidence which suggests CFD can be used as a complementary tool for a limited range of applications – provided it is used within its capabilities.

The use of CFD as a method for generating the transient wind loads was the most apparent weakness of the proposed PBWE framework. Also, as described in Section 8.2, the computational demands of CFD enforced a number of limitations for the Site Hazard Analysis. A considerable amount of development is required if CFD is to become adequate and appropriate for this type of application. The quality of the results was shown to be strongly dependent on the chosen turbulence model. The capabilities and limitations of both RANS and LES turbulence models are summarised below.

8.3.1 RANS Turbulence Model

The validation study performed in Chapter 4 identified that the RANS model was able to sustain the inlet mean velocity profile throughout the domain. As a result, the mean pressure coefficients acting on the benchmark CAARC tall building were computed with good agreement with previous wind tunnel data. Previous research had raised concerns regarding the adequacy of RANS for computing the suction effect towards the leading edge of a bluff body. However, the results from the validation study identified that these past under-predictions were not caused by any failure from the turbulence model. This study overcame the perceived problem by providing a sufficiently fine near-wall mesh.

However, the RANS model was found to be incapable of modelling an equilibrium atmospheric boundary layer when turbulence in the flow is high (which occurs during all strong winds). The turbulence specified at the domain inlet could not be sustained and had almost completely dissipated by the time the flow reached the building. This meant that the turbulence characteristics determined from the Site Hazard Analysis had a negligible effect on the measured load histories; any fluctuations were generated almost entirely from structure-induced turbulence. The results from the validation study showed that the RMS component of the wind loading on the CAARC tall building was considerably under-predicted by the RANS model. This was a direct consequence of the model failing to sustain the atmospheric turbulence in the wind field when it arrived at the tall building. This shortcoming meant the wind-induced structural responses of the tall building case studies were unrepresentatively low. The structural responses are discussed in more detail in Section 8.5.

Ultimately, the results from the PBWE assessments show that the RANS model is not suited to competent PBWE applications. However, it could perhaps be used in combination with wind tunnel testing for problems where mean velocity or pressure is the main measure for the assessment criteria. Such applications include environmental wind studies, which assess the wind conditions due to a new development for pedestrian comfort and safety as a function of mean wind speed at ground level.

8.3.2 LES Turbulence Model

The results showed that the LES turbulence model offers the closest alternative to wind tunnel testing in terms of accuracy. The validation study in Chapter 4 identified that the LES model was able to adequately compute both the mean and RMS pressure coefficients around the perimeter on the benchmark CAARC tall building at heights of 1/3*H* and 2/3*H*, even during full-scale, high Reynolds number flow . The RMS component was successfully computed because the LES model was able to sustain the atmospheric turbulence from the inflow to the building. Subsequently, the corresponding load histories induced a much greater structural response for the regular tall building than was seen from the RANS load histories. This is discussed in more detail in Section 8.5.

The major limitation of applying the LES model for the proposed PBWE framework was the computational cost needed to generate the load histories. The enforced restriction on the number of FLUENT licenses limited the number of processors that could be used in parallel for the CFD simulations to 8. This meant that the study could only utilise 0.7% of the total computational power of the HPC facility at the University of Strathclyde (1088 CPUs). For the regular tall building, a total of 88 days were required to compute the LES results for a single reference IM wind event. There was also evidence from the resulting building response histories that suggested the 120 s load histories may not have been long enough to characterise the wind-induced response of the tall building. The computation costs would have increased even further if the duration of the loading histories were increased. This would not have been feasible within the timescale of the thesis.

Provided the scalability of the software is efficient, increasing the number of processors would reduce the computation cost of implementing the LES model. If the HPC offered an alternative free and open source CFD software (e.g. OpenFoam) then it would overcome the limitation regarding the licenses. This would then allow more processors to be used in parallel for the simulations.

In addition, a technique which could have slightly reduced the computation times would have been to manually partition the mesh for parallel processing rather than relying on the auto-partition feature available in FLUENT. This would have ensured that the computational resources were concentrated within the nest of the computational domain, which contained the large majority of the computational cells.

Although these measures would improve the computational efficiency, the computation times would not reduce by several orders of magnitude. Such a decrease would be necessary for LES to ever genuinely compete with wind tunnel testing for such applications. This is unlikely to happen in the near future and requires a significant research effort.

8.3.3 RANS-LES Hybrid Model

The RANS-LES hybrid model was developed as part of this research to achieve an adequate level of accuracy and a manageable computation cost. The aim was to utilise the capabilities the RANS model and avoid the need to use full LES for all ten IM wind events, since this was not computationally feasible. The RANS model was used to determine the mean wind loads from each monitor on the surface of the tall building for all ten IM events. The LES model was used to determine the transient load histories from each monitor for a single reference IM event, IM10. This IM10 event represented the event with the lowest probability of occurrence. The procedure to generate transient wind loads for all ten IM events is described in Section 6.5.

The resulting wind load histories for IM1 to IM9 were based on certain assumptions regarding the turbulence properties of the wind, namely the hybrid model does not explicitly account for variation of turbulence length scale, turbulence intensity and excitation frequency between the wind events. Nonetheless, this approach was considered to offer an adequate representation of the wind loading on the structure by adapting loading fluctuations induced from the strongest wind within the set of IM events. It can be considered a successful compromise between RANS and LES for use with the proposed PBWE framework. The key aspect is minimising the computation time required for the single reference LES simulation.

8.4 One-Way Wind-Structure Coupling Algorithm

The one-way coupling interface developed in Microsoft Excel VBA performed very effectively for post-processing the data files from FLUENT and generating the load histories in Strand7 for the structural analysis. The Application Programming Interface (API) in Strand7 was a key component of the algorithm. The algorithm was developed to be flexible and robust. Therefore, it could be easily adapted if wind tunnel testing was used to generate the load histories rather than CFD. In this case, the first stage would involve post-processing the raw data measured by each pressure tap on the wind tunnel model. The interface would then follow an almost identical procedure to create the resulting load histories and apply them to the Strand7 structural model. However, it must be emphasised again that this model does not explicitly account for aero-elastic effects.

8.5 Structural Response of Tall Building Case Studies

8.5.1 Regular Tall Building

The regular tall building was subjected to two separate PBWE studies in Chapter 6, with each using different solution strategies to derive the transient structural wind loads. The results from the RANS simulation strategy displayed quite significant scatter between the ten peak accelerations. There were two distinct outlying events, IP7 and IP9, which induced notably higher peak accelerations. There was no reason to suggest that these structural responses occurred due to the inflow boundary conditions. It was found that these apparent anomalies were caused by only slight increases in load fluctuations on the windward face. The results from the RANS-LES strategy induced notably higher accelerations which were much more likely for such a tall building. There were also no distinct outliers such as those found from the RANS simulation strategy. Overall, it was concluded that the RANS-LES hybrid simulation strategy offered a better representation of the wind-induced response than the RANS model alone. Despite the increase in response seen from the RANS-LES model, the regular tall building satisfied the prescribed probabilistic performance objectives for both the simulation strategies.

The resulting building responses from RANS and LES load histories were directly compared for the single reference wind event, IM10. This provided an indication of the contributions of atmospheric turbulence and structure-induced turbulence for regular prismatic tall buildings. The RANS model was only able to capture structure-induced turbulence due to its inability to sustain the turbulence properties specified at the inlet. Conversely, the LES model was able to simulate both the atmospheric turbulence and the structure-induced turbulence. Since the reference event had the lowest probability of occurrence, it should have induced the highest structural response. The results showed that the building response was very sensitive to atmospheric turbulence – contributing approximately 92% of the total response. The structure-induced turbulence alone induced a very low response (approximately 8% of total) which was clearly a completely inadequate representation of the wind-induced response of the tall building. Ultimately, it was proved that the deficiencies of the RANS model were too significant to be used for competent PBWE studies.

The load histories computed by the LES model were primarily driven by the low frequency component of the atmospheric turbulence. The spectral synthesizer in FLUENT provides a method for generating these perturbations at the inlet when using LES, with the intention that these fluctuations are adequate for the considered site. However, it is difficult to validate this for built-up urban terrains since there is a lack of field data available for such purposes.

8.5.2 Irregular Tall Building

The PBWE assessment of the irregular tall building is detailed in Chapter 7. An initial set of time-steps were computed for the irregular tall building using the LES model. The average CPU time for a single time-step revealed that it would have taken approximately 100 days to compute sufficiently long data for a single IM wind event. Due to this prohibitive computational demand, the PBWE assessment of the irregular tall building was only based on load histories from the RANS simulation strategy. The geometry of the irregular tall building increased the level of structure-induced turbulence, which was expected to improve the adequacy of the RANS model.

The resulting accelerations were notably higher than those computed from the structural analysis of the regular tall building when using the same RANS simulation strategy. This was due to increased unsteadiness in the loading from structure-induced turbulence. However, these accelerations were considerably lower than those obtained from the RANS-LES simulation strategy for the regular tall building. Since the geometry of the irregular tall building is typically more sensitive to wind-induced excitation, the probabilistic fragility curve from the RANS simulation strategy was considered to offer a poor representation of the physical performance of the irregular tall building. These results suggested that the atmospheric turbulence would also govern the response of an irregular tall building.

8.6 Summary of Conclusions

- The proposed PBWE framework is shown to offer great potential but its progress relies on the next generation of CFD turbulence models overcoming the existing limitations. Future development of CFD turbulence models should aspire towards achieving adequate accuracy at a practical computation cost.

- The RANS turbulence model can be applied to external flow problems where the results are governed by the mean velocity profile.
- The RANS turbulence model can be used as useful visualisation tool for illustrating mean flow fields and pressure contours – provided its limitations are understood.
- The RANS turbulence model can adequately compute the mean suction effect caused by flow separation at the leading edge of a prismatic bluff body if a sufficiently fine near-wall mesh is provided and enhanced wall treatment is used.
- The LES model may offer the closest alternative to wind tunnel testing but its computational cost is completely impractical, particularly if the analysis needs several CFD simulations to be computed. This requirement applies to the proposed PBWE framework.
- In the context of the proposed PBWE framework, the RANS-LES simulation strategy provides an adequate representation of the wind-induced response of tall buildings.
- A considerable flow record is required to determine the peak structural response during a strong wind event. Given the complexity of the building response, the peak value within a finite statistical set does not necessarily represent the peak response during the wind event unless the flow record is comparable to the duration of the wind storm.
- The contribution of atmospheric turbulence must be adequately included in any assessment of the wind-induced response of a tall building, irrespective of its geometry. Considering structure-induced turbulence alone is not enough and will produce results which are physically unrealistic.

9

Recommendations for Future Work

It has been demonstrated from this research that the proposed PBWE framework for tall building design offers great potential. However, in order to further progress the development of PBWE for tall building design, there are specific aspects of the currently proposed framework that can be improved by future research based on the lessons learnt from the present study.

The most evident weakness was associated with using CFD as a simulation tool for the Interaction Analysis stage. This could be overcome if wind tunnel testing was used as a direct replacement to generate the load histories. Although it was noted in Chapter 2 that wind tunnel testing has its own limitations, it currently provides the most accurate method of determining structural wind loads in the absence of full scale results. The flexibility of the PBWE framework would ensure that this change from CFD to wind tunnel testing would have a negligible impact on the other stages. This would improve the accuracy and efficiency of the proposed framework. It would also enable the directionality of the wind to be explicitly considered as part of the PBWE assessment. However, this obviously requires a wind tunnel testing facility to be readily available.

In terms of the application of CFD, it would be useful to assess whether turbulence could be generated within the domain of interest using the RANS model by following a similar method to that performed in wind tunnel testing.

This would involve creating an array of artificial roughness blocks in the upwind region of the domain to disturb the incoming flow. This could improve the performance of the RANS model for such applications and allow the user to take full advantage of its relatively low computational cost. However, it could become quite a time consuming process to establish the correct inlet boundary conditions and roughness block configuration for each IM wind event. This iterative process would also be needed if wind tunnel testing was used. However, due to the high computational cost of CFD, the procedure in the wind tunnel would be several of orders of magnitude quicker than CFD.

The adequacy of the RANS model may also improve if the tall building was explicitly modelled along with its surroundings rather than as an isolated obstacle in the CFD domain.

The results emphasised the need to properly consider the influence of atmospheric turbulence when determining the wind-induced response of tall buildings. Addressing the need for wind data in built-up urban terrains would help validate that the IM wind characteristics used to determine the loading and resulting building response are representative for the considered site.

Given the uncertainty regarding structural damping, it may be appropriate to incorporate the damping ratio for the fundamental mode of vibration as an additional variable for the Latin Hypercube sampling space. This would mean the Rayleigh damping used for the Structural Analysis would vary between each IM wind event, which would introduce additional scatter in the EDP results. A Gaussian distribution similar to that used for sampling z_0 should be adequate. This would be sampled over quite a narrow range of values so the impact would have to be assessed to determine whether it is worthwhile.

A question which emanated from the present study was how to adequately establish the peak wind-induced structural response within a finite statistical set. Solving this issue would be very beneficial for future assessments of wind-induced response of buildings in the time domain.

The Damage Analysis was based on a simple method similar to that used by van de Lindt and Dao (2009). This stage of the PBWE framework could be assessed by future research to determine whether the methodology for specifying the performance levels is appropriate or whether there is scope for improvement. There is a need for universally accepted occupant comfort criteria. A probabilistic approach appears to be the most appropriate solution given the subjectivity and uncertainty surrounding this subject.

The development of the proposed PBWE framework would greatly benefit from overcoming these issues. It is hoped that the continuation of this work by future research will lead to the eventual transition from academia to practical implementation for tall building design.

References

Allsop, A., 2009a. *BS EN 1991-1-4 Tall Buildings.* New Eurocode for Wind Loading, Institution of Civil Engineers, London, 11th May 2009. [Lecture]

Allsop, A., 2009b. *BS EN 1991-1-4 Wind Responses*. New Eurocode for Wind Loading, Institution of Civil Engineers, London, 11th May 2009. [Lecture]

ANSYS Inc., 2009a. *ANSYS FLUENT 12.0 Theory Guide*.

ANSYS Inc., 2009b. *ANSYS FLUENT 12.0 User Guide*

Augusti, G., Borri, C., Niemann, H.J., 2001. Is Aeolian risk as significant as other environmental risks? *Reliability Engineering and System Safety*, Elsevier, 74 pp 227-237.

Augusti, G. and Ciampoli, M., 2008. Performance-Based Design in risk assessment and reduction, *Probabilistic Engineering Mechanics,* Elsevier, 23 pp 496-508.

Bashor, R., Kijewski-Correa, T., Kareem, A., 2005. On the Wind-Induced Response of Tall Buildings: The Effect of Uncertainties in Dynamic Properties and Human Comfort Thresholds. In: *10th Americas Conference on Wind Engineering*. Baton Rouge, Louisiana 31 May – 4 June 2005.

Beneke, D.L. and Kwok, K.C.S., 1993. Aerodynamic effect of wind induced torsion on tall buildings. *Journal of Wind Engineering and Industrial Aerodynamics*, Elsevier 50 pp 271-280.

Blocken, B., Stathopoulos, T., Carmeliet, J., 2007. CFD simulation of the atmospheric boundary layer: wall function problems. *Atmospheric Environment.* Elsevier 41 pp 238-252.

Braun, A.L. and Awruch, A.M., 2009. Aerodynamic and aeroelastic analyses on the CAARC standard tall building model using numerical simulation. *Computers and Structures,* Elsevier 87 pp 564-581.

Breeze, G., 2011. *Dynamic comfort criteria for structures: A review of UK codes, standards and advisory documents*. Bracknell: HIS BRE Press.

British Standards Insitution, 1985. *BS 6611:1985 Guide to evaluation of the response of occupants of fixed structures, especially buildings and offshore structures, to low-frequency horizontal motion (0.063 Hz to 1 Hz).* London: BSI.

British Standards Institution, 1987. *BS 6841:1987 Guide to measurement and evaluation of human exposure to whole-body mechanical vibration and repeated shock.* London: BSI.

British Standards Institution, 2002. *BS 6399-2:1997 Loadings for buildings – Part 2: Code of practice for wind loads.* London: BSI.

British Standards Institution, 2004a. *BS EN 1992-1-1.2004 Design of concrete structures – Part 1-1: General rules and rules for buildings.* London: BSI.

British Standards Institution, 2004b. *BS EN 1998-1:2004 Design of structures for earthquake resistance – Part 1: General rules, seismic actions and rules for buildings.* London: BSI.

British Standards Institution, 2005. *BS EN 1991-1-4:2005 Eurocode 1: Actions on structures – Part 1-4: General actions – Wind actions.* London: BSI.

British Standards Institution, 2008a. *NA to BS EN 1991-1-4:2005 UK National Annex to Eurocode 1: Actions on structures – Part 1-4: General actions – Wind actions.* London: BSI.

British Standards Institution, 2008b. *BS 6472-1:2008 Guide to evaluation of human exposure to vibration in buildings – Part 1: Vibration sources other than blasting.* London: BSI.

British Standards Institution, 2009. *PD 6688-1-4:2009 Published Document. Background information to the National Annex to BS EN 1991-1-4 and additional guidance.* London: BSI.

Campbell, S., Kwok, K.C.S., Hitchcock, P.A., 2005. Dynamic characteristics and wind-induced response of two high-rise residential buildings during typhoons. *Journal of Wind Engineering and Industrial Aerodynamics*, Elsevier 93 pp 461-482.

Castro, I.P., 2003. CFD for External Aerodynamics in the Built Environment. *The QNET-CFD Network Newsletter.* Vol. 2: No. 2 – July 2003, pp 4-7.

Chan, C.-M. and Chui, J.K.L., 2006. Wind-induced response and serviceability design optimization of tall steel buildings. *Engineering Structures,* Elsevier 28 pp 503-513.

Chen, X. and Huang, G., 2009. Evaluation of peak resultant response for wind-excited tall buildings. *Engineering Structures,* Elsevier 31 pp 858-868.

Chopra, A.K., 2007. *Dynamics of Structures: Theory and Applications to Earthquake Engineering*, 3rd Edition, New Jersey: Pearson Prentice Hall.

Ciampoli, M., and Petrini, F., 2010. Performance-based design of offshore wind turbines. In: *12th International Conference on Engineering, Science, Construction, and Operations in Challenging Environments.* Hawaii, USA 14-17 March 2010.

Ciampoli, M., Petrini, F., Augusti, G., 2010. A procedure for Performance-Based Wind Engineering. *Safety, Reliability and Risk of Structures, Infrastructures and Engineering Systems.* Taylor & Francis Group pp 1843-1850.

Cochran, L. and Derickson, R., 2011. A physical modeler's view of Computational Wind Engineering. *Journal of Wind Engineering and Industrial Aerodynamics,* Elsevier 99 pp 139-153.

Colls, J., 2002. *Air Pollution.* 2nd Edition, London: Spon Press.

Cook, N.J., 1982. Towards better estimation of extreme winds. *Journal of Wind Engineering and Industrial Aerodynamics*, Elsevier 9 pp 295-323.

Cook, N.J., 1985. *The designer's guide to wind loading of building structures Part 1: Background, damage survey, wind data and structural classification*. London: Butterworths Scientific.

Davenport, A.G., 1998. What makes a structure wind sensitive? In: *The Jubileum Conference on Wind Effects on Buildings and Structures*. Porto Alegre, Brazil 25-29 May 1998, A.A. Balkema, Rotterdam, Netherlands.

Deierlein, G.G., Krawinkler, H., Cornell, C.A., 2003. A framework for performance-based earthquake engineering. In: *Pacific Conference on Earthquake Engineering.* Christchurch, New Zealand 13-15 February 2003.

Engineering Sciences Data Unit, 1990. *IHS ESDU 83009 Damping of structures. Part1: tall buildings.*

Engineering Sciences Data Unit, 2001. *IHS ESDU 86010 Characteristics of atmospheric turbulence near the ground. Part 3: variations in space and time for strong winds (neutral atmosphere).*

Engineering Sciences Data Unit, 2002a. *IHS ESDU 83045 Strong winds in the atmospheric boundary layer. Part 2: discrete gust speeds.*

Engineering Sciences Data Unit, 2002b. *IHS ESDU 82026 Strong winds in the atmospheric boundary layer. Part 1: hourly-mean wind speeds.*

Engineering Sciences Data Unit, 2010. *IHS ESDU 74030 Characteristics of atmospheric turbulence near the ground. Part 1: definitions and general information.*

FLUENT Inc, 2007. *GAMBIT 2.4.6 User Guide.*

Gething, B., 2010. Design for future climate – Opportunities for adaptation in the built environment. Technology Strategy Board.

Gu, M. and Quan, Y., 2004. Across-wind loads of typical tall buildings. *Journal of Wind Engineering and Industrial Aerodynamics*, Elsevier 92 pp 1147-1165.

Ghobarah, A., 2001. Performance-based design in earthquake engineering: state of development. *Engineering Structures,* Elsevier 23 pp 878-884.

HAZUS, 2012. *HAZUS – MH 2.1 Technical Manual: Multi-hazard loss estimation methodology.*

Heil, M., 2004. An efficient solver for the fully coupled solution of lasrge-displacement fluid-structure interaction problems. *Computer Methods in Applied Mechanics and Engineering,* Elsevier 193 pp 1-23.

Hicks, S.J. and Devine, P.J., 2004. Design guide on the vibration of floors in hospitals. *The Steel Construction Institute Publication 331*, Ascot: SCI.

Holmes, J.D., 2002. Fatigue life under along-wind loading – closed-form solutions. *Engineering Structures,* Elsevier 24 pp 109-114.

Holmes, J.D., 2007. *Wind Loading of Structures*, 2nd Edition. London: Taylor & Francis.

Huang, S., Li, Q.S., & Xu, S., 2007. Numerical evaluation of wind effects on a tall steel building by CFD. *Journal of Constructional Steel Research*, Elsevier 63 pp 612-627.

International Organization for Standardization, 1984. *ISO 6897:1984 Guidelines for the evaluation of the response of occupants of fixed structures, especially buildings and offshore structures, to low-frequency horizontal motion (0.063 to 1.0 Hz).* Geneva, Switzerland: ISO.

International Organization for Standardization, 1997. *ISO 2631-1:1997 Mechanical vibration and shock – Evaluation of human exposure to whole-body vibration – Part 1: General requirements.* Geneva, Switzerland: ISO.

Irwin, P.A., 2009. Wind engineering challenges of the new generation of super-tall buildings. *Journal of Wind Engineering and Industrial Aerodynamics,* Elsevier 97 pp 328-334.

Joosten, M.M., 2007. *Analysis of Gauβ-Seidel solution strategy for coupled problems based on a one-dimensional model problem*, M.Res. Swansea University.

Kareem, A., 2008. Numerical simulation of wind effects: A probabilistic perspective. *Journal of Wind Engineering and Industrial Aerodynamics*, Elsevier 96 pp 1472-1497.

Kim, J.Y., Yu, E., Kim, D.Y., and Kim, S.D., 2009. Calibration of analytical models to assess wind-induced acceleration responses of tall buildings in serviceability level. *Engineering Structures,* Elsevier 31 pp 2086-2096.

Knapp, G., 2007. *Improved methods for structural wind engineering.* Ph. D. University of Nottingham.

Kwok, K.C.S., 2007. *Wind-induced vibrations of structures – with special reference to tall building aerodynamics*. Effects on Buildings and Urban Environment. Tokyo Polytechnic University, Tokyo, Japan, March 2007. [Lecture]

Kwok, K.C.S., Hitchcock, P.A., Burton, M.D., 2009. Perception of vibration and occupant comfort in wind-excited tall buildings. *Journal of Wind Engineering and Industrial Aerodynamics*, Elsevier 97 pp 368-380.

Lee, C.K.L., Noguchi, H., Koshizuka, S., 2007. Fluid-shell structure interaction analysis by coupled particle and finite element method. *Computers and Structures,* Elsevier 85 pp 688-697.

Li, Q.S. *et al.*, 2000. Damping in buildings: its neutral network model and AR model. *Engineering Structures,* Elsevier 22 pp 1216-1223.

Liew, J.Y.R., 2003. Performance-based fire safety design of structures – A multi-dimensional integration. *Advances in Structural Engineering,* Multi-Science 7 pp 311-333.

Lu, Z. and Zhang, D., 2003. On importance sampling Monte Carlo approach to uncertainty analysis for flow and transport in porous media. *Advances in Water Resources,* Elsevier 26 pp 1177-1188.

Matthies, H.G. and Steindorf, J., 2002. Partitioned but strongly coupled iteration schemes for non-linear fluid-structure interaction. *Computers and Structures,* Elsevier 80 pp 1991-1999.

Mehta, K.C., 1998. Wind load standards. In: *The Jubileum Conference on Wind Effects on Buildings and Structures*. Porto Alegre, Brazil 25-29 May 1998, A.A. Balkema, Rotterdam, Netherlands.

Melbourne, W.H., and Palmer, T.R., 1992. Acceleration and comfort criteria for buildings undergoing complex motions. *Journal of Wind Engineering and Industrial Aerodynamics,* Elsevier 41-44 pp 105-116.

Moehle, J. and Deierlein, G.G., 2004. A framework methodology for performance-based earthquake engineering. In: *Proc. World Conference on Earthquake Engineering*, Vancouver, Canada 1-6 August 2004.

Morava, B., Haskett, T., Chadwick, A, Wates, E., 2010. Assessment of occupant comfort in wind-sensitive buildings using a six-degree-of-freedom motion simulator. In: *ASCE 2010 Structures Congress*, Orlando, Florida, USA 12-15 May 2010.

Murakami, S., 1997. Current status and future trends in computational wind engineering. *Journal of Wind Engineering and Industrial Aerodynamics,* Elsevier 67 & 68 pp 3-34.

Murakami, S., 1998. Overview of turbulence models applied in CWE-1997. *Journal of Wind Engineering and Industrial Aerodynamics,* Elsevier 74-76 pp 1-24.

Narayanan, R.S., 2009a. *Introduction to Structural Eurocode System*. New Eurocode for Wind Loading, Institution of Civil Engineers, London, 11 May 2009*.* [Lecture]

Narayanan, R.S., 2009b. *Calibration of BS EN 1991-1-4 & UK National Annex against BS 6399: Part 2*. New Eurocode for Wind Loading, Institution of Civil Engineers, London, 11 May 2009*.* [Lecture]

Nozu, T., Tamura, T., Okuda, Y., Sanada, S., 2008. LES of the flow and building wall pressures in the center of Tokyo. *Journal of Wind Engineering and Industrial Aerodynamics,* Elsevier 96 pp 1762-1773.

O'Sullivan, J.P., Archer, R.A., Flay, R.G.J., 2011. Consistent boundary conditions for flows within the atmospheric boundary layer. *Journal of Wind Engineering and Industrial Aerodynamics,* Elsevier 99 pp 65-77.

Obasaju, E.D., 1992. Measurement of forces and base overturning moments on the CAARC tall building model in a simulated atmospheric boundary layer. *Journal of Wind Engineering and Industrial Aerodynamics*, Elsevier 40 pp 103-126.

Olson, A., Sandberg, G., Dahlblom, O., 2003. On Latin hypercube sampling for structural reliability analysis. *Structural Safety,* Elsevier 25 pp 47-68.

Pagnini, L.C. and Solari, G., 2002. Gust buffeting and turbulence uncertainties. *Journal of Wind Engineering and Industrial Aerodynamics,* Elsevier 90 pp 441-459.

Paulotto, C., Ciampoli, M., Augusti, G., 2004. Some proposals for a first step towards a Performance-Based Wind Engineering. In: *1st International Forum on Engineering Decision Making.* Stoos, Switzerland 5-9 December 2004.

Petrini, F., Bontempi, F., Ciampoli, M., 2008. Performance-Based Wind Engineering as a tool for the design of the hangers in a suspension bridge. In: *4th International ASRANet Colloquium.* Athens, Greece 25-27 June 2008.

Petrini, F., 2009. *A probabilistic approach to Performance-Based Wind Engineeering (PBWE)*. Ph. D. Università degli Studi di Roma “La Sapienza”, Rome, Italy.

Petrini, F., Ciampoli, M., and Augusti, G., 2009. A probabilistic framework for Performance-Based Wind Engineering. In: *Proceedings of the 5th European and African Conference on Wind Engineering*. Florence, Italy 19-23 July 2009.

Pirnia, J.D. *et al.*, 2007. Full-scale validation of wind-induced response of tall buildings: investigation of amplitude-dependent dynamic properties. In: ASCE *2007 Structures Congress: New Horizons and Better Practices.*

Preveser, T. and Holding, J., 2002. Bluff body asymmetric flow phenomenon – real effect or solver artefact? *Wind and Structures,* Techno Press 5 pp 359-368.

Revuz, J., Hargreaves, D., Owen, J., 2010. Domain size for Computational Fluid Dynamics modelling of tall buildings. In: *9th UK Conference on Wind Engineering.* Bristol 20-22 September 2010.

Richards, P.J. and Norris, S.E., 2011. Appropriate boundary conditions for computational wind engineering models revisited. *Journal of Wind Engineering and Industrial Aerodynamics,* Elsevier 99 pp 257-266.

Richardson, G.M., and Surry, D., 1992. The Silsoe Building: a comparison of pressure coefficients and spectra at model and full-scale. *Journal of Wind Engineering and Industrial Aerodynamics,* Elsevier 41-44 pp 1653-1664.

Simiu, E. and Scanlan, R.H., 1986. *Wind Effects on Structures: an Introduction to Wind Engineering*, 2nd Edition, New York: John Wiley & Sons.

Solari, G. and Piccardo, G., 2001. Probabilistic 3-D turbulence modelling for gust buffeting of structures. *Probabilistic Engineering Mechanics,* Elsevier 16 pp 73-86.

Spallart, P.R., 2001. Young Person's Guide to Detached-Eddy Simulation, NASA.

Stansfield, K., 2006. Burj Dubai raises the tall building stakes. *The Structural Engineer*, 5 December 2006 pp 13-16.

Strand7, 2005a, *Strand7 Verification Manual: Verification tests for the Strand7 finite element analysis system.*

Strand7, 2005b. *Strand7 Application Programming Interface Manual.*

Suda, K, Satake, N., Ono, J., and Sasaki, A., 1996. Damping properties of buildings in Japan. *Journal of Wind Engineering and Industrial Aerodynamics,* Elsevier 59 pp 383-392.

Sun, D., Owen, J.S., & Wright, N.G., 2009. Application of the k-ω turbulence model for a wind-induced vibration study of 2D bluff bodies. *Journal of Wind Engineering and Industrial Aerodynamics*, Elsevier 96 pp 1974-1984.

Swaddiwudhipong, S. and Khan, M.S., 2000. Dynamic response of wind-excited building using CFD. *Journal of Sound and Vibration,* Elsevier 253(4) pp 735-754.

Tamura, T., 2008. Towards practical use of LES in wind engineering. *Journal of Wind Engineering and Industrial Aerodynamics*, Elsevier 96 pp 1451-1471.

Tamura, T., Nozawa, K., Kondo, K., 2008. AIJ guide for numerical prediction of wind loads on buildings. *Journal of Wind Engineering and Industrial Aerodynamics*, Elsevier 96 pp 1974-1984.

Taranath, B.S., 1998. *Steel, Concrete & Composite Design of Tall Buildings*, 2nd Edition, McGraw-Hill, New York.

Taylor, I. and Vezza, M., 2002. Aeroelastic stability analysis of a bridge deck with added vanes using a discrete vortex method. *Wind and Structures,* Techno Press 5 pp 277-290.

Tieleman, H.W., 2008. Strong wind observations in the atmospheric surface layer. *Journal of Wind Engineering and Industrial Aerodynamics*, Elsevier 96 pp 41-77.

Thepmongkorn, S. and Kwok, K.C.S., 2002. Wind-induced responses of tall buildings experiencing complex motion. *Journal of Wind Engineering and Industrial Aerodynamics*, Elsevier 90 pp 515-526.

Unanwa, C.O., McDonald, J.R., Mehta, K.C., Smith, D.A., 2000. The development of wind damage bands for buildings, *Journal of Wind Engineering and Industrial Aerodynamics*, Elsevier 84 pp 119-149.

van de Lindt, J.W., and Dao, T.N., 2009. Performance-Based Wind Engineering for Wood-Frame Buildings. *Journal of Structural Engineering,* ASCE 135 pp 169-177.

Wen, Y.K., 2001. Reliability and performance-based design, *Structural Safety*, Elsevier 23 pp 407-428.

Whittaker, A.S., Hamburger, R.O., Mahoney, M., 2003. Performance-based engineering of buildings for extreme events. In: *AISC-SINY Symposium on Resisting Blast and Progressive Collapse.* American Institute of Steel Construction, New York 4-5 December 2003.

Wilcox, D.C., 2002. *Turbulence Modeling for CFD,* 2nd Edition, DCW Industries, California.

Yang, Y., Gu, M., Chen, S., Jin, X., 2009. New inflow boundary conditions for modelling the neutral equilibrium atmospheric boundary layer in computational wind engineering, *Journal of Wind Engineering and Industrial Aerodynamics.* Elsevier 97 pp 88-95.

Zhang, L., Li, J., Peng, Y., 2008. Dynamic response and reliability analysis of tall buildings subject to wind loading. *Journal of Wind Engineering and Industrial Aerodynamics*, Elsevier 96 pp 25-40.

Zhao, Y.G., and Ono, T., 2001. Moment methods for structural reliability. *Structural Safety,* Elsevier 23 pp 47-75.

Appendix

First 50 Natural Frequencies of Tall Building Case Studies

	Regular Tall Building		Irregular Tall Building	
Mode	***f* (Hz)**	***T* (s)**	***f* (Hz)**	***T* (s)**
1	0.267	3.741	0.264	3.792
2	0.312	3.202	0.327	3.060
3	0.432	2.315	0.362	2.760
4	1.013	0.987	0.974	1.027
5	1.150	0.870	1.021	0.979
6	1.240	0.806	1.274	0.785
7	2.248	0.445	1.787	0.560
8	2.249	0.445	2.194	0.456
9	2.516	0.397	2.602	0.384
10	3.335	0.300	2.813	0.355
11	3.487	0.287	3.298	0.303
12	3.722	0.269	3.431	0.291
13	3.774	0.265	3.561	0.281
14	4.034	0.248	3.750	0.267
15	4.212	0.237	3.893	0.257
16	4.240	0.236	4.335	0.231
17	4.311	0.232	4.400	0.227
18	4.626	0.216	4.490	0.223
19	4.863	0.206	4.529	0.221
20	5.217	0.192	4.824	0.207
21	5.287	0.189	5.010	0.200

Mode	***f* (Hz)**	***T* (s)**	***f* (Hz)**	***T* (s)**
22	5.575	0.179	5.091	0.196
23	5.717	0.175	5.317	0.188
24	5.866	0.170	5.825	0.172
25	6.013	0.166	6.143	0.163
26	6.375	0.157	6.193	0.161
27	6.965	0.144	6.271	0.159
28	7.378	0.136	6.332	0.158
29	7.401	0.135	6.396	0.156
30	7.419	0.135	6.596	0.152
31	7.472	0.134	6.705	0.149
32	7.593	0.132	6.971	0.143
33	7.674	0.130	7.092	0.141
34	7.695	0.130	7.119	0.140
35	7.706	0.130	7.139	0.140
36	8.035	0.124	7.268	0.138
37	8.375	0.119	7.298	0.137
38	8.384	0.119	7.318	0.137
39	8.489	0.118	7.341	0.136
40	8.823	0.113	7.348	0.136
41	8.976	0.111	7.369	0.136
42	9.144	0.109	7.371	0.136
43	9.194	0.109	7.398	0.135
44	9.304	0.107	7.408	0.135
45	9.313	0.107	7.417	0.135
46	9.478	0.106	7.432	0.135

Mode	***f* (Hz)**	***T* (s)**
47	9.912	0.101
48	10.099	0.099
49	10.155	0.098
50	10.178	0.098

***f* (Hz)**	***T* (s)**
7.440	0.134
7.460	0.134
7.464	0.134
7.481	0.134